

Department of Physics and Astronomy

**Concentrated Solar Thermal Energy Storage using Metal Hydrides:
Fluorine Substitution in Metal Hydrides**

Mariana Soledad Tortoza

This thesis is presented for the Degree of Doctor of Philosophy of Curtin University

October 2023

Statement of Originality

To the best of my knowledge and belief, this thesis contains no material previously published by any other person except where due acknowledgment has been made. This thesis contains no material which has been accepted for the award of any other degree.

Mariana Soledad Tortoza

Statement of contribution by others

Chapter 1: Introduction to the context of this doctoral thesis and outline of the research directions of the project. Written by myself with included corrections from Prof. Craig Buckley, Assoc. Prof. Mark Paskevicius and Dr. Terry Humphries.

Chapter 2: Description of the experimental methods and methodology employed. Written by myself with contributions and corrections from Prof. Craig Buckley, Assoc. Prof. Mark Paskevicius and Dr. Terry Humphries.


Chapter 3: Research article published in the Journal of Physical Chemistry Chemical Physics in 2018 (<https://doi.org/10.1039/7ccp07433f>) presenting the thermodynamics and performance of the Mg–H–F system for thermochemical energy storage applications. Written by myself with contributions and corrections from Prof. Craig Buckley, Assoc. Prof. Mark Paskevicius, Dr. Terry Humphries, Dr. Drew Sheppard and Dr. Matthew Rowles, Dr. Veronica Sofianos, and Dr. Kondo-Francois Aguey-Zinsou.

Chapter 4: Research article published in the Journal of Physical Chemistry C 124 in 2020 (<https://dx.doi.org/10.1021/acs.jpcc.9b11211>) presenting fluorine substitution in magnesium hydride as a tool for thermodynamic control. Written by Dr. Terry Humphries with contributions and corrections from Prof. Craig Buckley, Assoc. Prof. Mark Paskevicius, Myself, Dr. Jack Yang, Dr. Richard Mole, Julianne Bird, Dr. Matthew Rowles, Dr. Veronica Sofianos, and Dr. Dehong Yu.

Chapter 5: Investigation and experimental results related to thermodynamics and performance of the Na–Mg–H–F system for thermochemical energy storage applications. Written by myself with contributions and corrections from Prof. Craig Buckley, Assoc. Prof. Mark Paskevicius and Dr. Terry Humphries.

Chapter 6: General conclusions of the research project and discussion of the perspectives. Written by myself with contributions and corrections from Prof. Craig Buckley, Assoc. Prof. Mark Paskevicius and Dr. Terry Humphries.

Detailed co-author contributions statement for each publication can be found in Appendix IV of this document.



Mariana Tortoza
(Ph.D. candidate's signature)



Professor Craig Buckley
(supervisor's signature)

Abstract

Humanity must alter the way energy is consumed and it is imperative that we stop consuming fossil fuels entirely and start using renewable energy sources. The most abundant of these renewable energy sources is solar and Concentrating Solar Power (CSP) has been reported to be the most efficient way to employ solar energy to generate electricity. One major advantage of CSP plants is that, when paired with a thermal energy storage (TES) module, electricity can be generated when the sun is not shining. Molten nitrate salts are commercially used as TES materials and are classed as the first generation of TES systems, but they have disadvantages including low thermal storage capacity (therefore requiring large volumes), high costs, and to avoid degradation the operating temperature is limited to 565 °C.

To overcome these disadvantages, metal hydrides can instead be employed as thermochemical energy storage (TCES) materials. This class of materials store heat, with an energy density of between 5 and 30 times higher than molten salts, and also have the potential to reduce heat storage costs. The system operates as follows: during the daytime, the temperature of the high temperature metal hydrides (HTMH) reactor will increase (due to CSP), and an endothermic chemical dissociation reaction is initiated in the TCES material. Hydrogen is released, and stored, causing the pressure of the system to increase. At night, the temperature of the HTMH decreases and the HTMH begins to reabsorb the hydrogen and releases heat (i.e. exothermic reaction) to run the turbine to produce electricity. Furthermore, the US Department of Energy's Sunshot program has defined that the next generation of CSP plants should operate between 600 and 800 °C. Therefore, it is evidently necessary to increase the operating temperature and stability of metal hydrides to operate them at the desired operating temperature range to be used as TES materials. In order to address this challenge, fluorine substitution of hydrogen atoms in the metal hydrides is proposed. This is possible due to the comparable ionic size of the hydride and fluoride ions and the structural similarity of their compounds. In this thesis, fluorine has been substituted for hydrogen in MgH_2 to form a range of $\text{Mg}(\text{H}_x\text{F}_{1-x})_2$ compounds ($x = 1, 0.95, 0.85, 0.70, 0.50, 0$) and in NaMgH_3 to form a range of $\text{NaMg}(\text{H}_{1-x}\text{F}_x)_3$ ($x = 0, 1, 2, 3$) solid solutions. These materials are designed to be potential thermal energy storage materials with higher operating efficiencies than their parent compounds MgH_2 and NaMgH_3 . $\text{Mg}(\text{H}_x\text{F}_{1-x})_2$, was analysed over two Chapters (chapter 3 and 4) in this thesis. In Stage I, *in situ* synchrotron powder X-ray diffraction was used as a characterisation technique to study the evolution and decomposition of crystallographic phases as a function of temperature. Thermal analysis such as differential scanning calorimetry, thermogravimetric analysis, temperature-programmed-desorption mass spectrometry, and Pressure–Composition–Isothermal (PCI) analysis were carried out on all $\text{Mg}(\text{H}_x\text{F}_{1-x})_2$ mixtures, concluding that as F content increases the thermal stability also increases, however, kinetics decreased compared to pure MgH_2 . The decomposition impact on

Mg(H_{0.85}F_{0.15})₂ shows, through DSC measurement, a maximum rate of H₂ desorption is achieved at 434 °C with a practical hydrogen capacity of 4.6 ± 0.2 wt.% H₂ (theoretical 5.4 wt.% H₂). PCI measurements have determined that the values of enthalpy and entropy of Mg(H_{0.85}F_{0.15})₂ are 73.6 ± 1.2 kJ mol⁻¹H₂ and 131.2 ± 2 J K⁻¹mol⁻¹H₂, respectively. Both values are lower than for MgH₂ with ΔH_{des} of 74.06 kJ mol⁻¹H₂ and ΔS_{des}= 133.4 J K⁻¹mol⁻¹H₂. After the decomposition of each Mg–H–F sample, it was observed that an Mg(H_{0.43}F_{0.57})₂ phase was formed being responsible for the H₂ not being released until T > 505 °C. Also, cycling studies of Mg(H_{0.85}F_{0.15})₂ were undertaken to evaluate the operating temperature and efficiency of the material. These were completed over six absorption/desorption cycles between 425 and 480 °C, which is ~ 80 °C higher than what can be achieved for bulk MgH₂. Therefore, this increases the cycling temperature compared to that of bulk MgH₂, thereby increasing efficiency.

Stage II, is a characterisation study of the Mg(H_xF_{1-x})₂ system by inelastic neutron spectroscopy, powder X-ray diffraction, and thermal conductivity measurements. After performing these analyses, the results were confirmed using density functional theory. A marked trend is observed across the series of solid solutions in each experiment, indicating that the tunability of the MgH₂ properties could be adjusted. As the F-substitution increases, the Mg-H(F) bond distance increases for the axial positions on the Mg-H(F) octahedra. Overall, this leads to an increase in Mg-H(F) bond strength and thermal stability, improving the viability of Mg-H-F as a potential TES material.

The NaMg(H_{1-x}F_x)₃ (x = 0, 1, 2, 3) system was analysed in the third study in Chapter 5 of this thesis to explore its potential use for hydrogen storage or as a thermal energy storage material. The NaMg(H_{1-x}F_x)₃ mixtures were formed using fluorine substitution to stabilise the parent NaMgH₃ material. To determine if this system would be viable as a TCES material it was examined by in situ synchrotron powder XRD, DSC-TGA-MS, and PCI analysis. After performing thermal studies on the NaMg(H_{1-x}F_x)₃ system it can be concluded that increasing the F content in these -NaMg(H_{1-x}F_x)₃- solid solutions the thermal stability increases. For the NaMgHF₂ material the measurements showed that the maximum H₂ desorption in DSC is reached in a single endothermic step at the temperature of 525 °C, while in TPD-MS the maximum hydrogen desorption temperature peak is observed at 545 °C. Also the in-situ synchrotron results show that the complete decomposition of NaMgHF₂ occurs at 595 °C forming NaMgF₃, NaF and MgO. The PCI measurements of NaMgHF₂ determined an enthalpy of decomposition of 89 ± 12 kJ/mol H₂ and entropy of 121 ± 16 J/K/mol H₂. In comparison with NaMgH₃, these values increased from 86.60 kJ/mol H₂ and decreased from 132.20 J/K/mol H₂, respectively. With regards to the cyclability of NaMgHF₂, a reduction of ~ 18 % of the practical hydrogen capacity was determined over four cycles at 508 °C.

Based on the information from the experimental work on the NaMgHF₂ sample, it is evident that NaMgHF₂ is an ideal candidate for solar thermal energy storage. This is due to its high enthalpy and high operating

temperatures, meaning less hydrogen is needed to generate electrical energy, compared to other hydrides for solar thermal storage.

Acknowledgment

Many thanks to Professor Craig Buckley, for the huge opportunity to be one of his students. Through these studies, I have learnt about science, the academic environment at Curtin, commitment, responsibility, solidarity, laboratory techniques, the importance of scholarly journals, for sure much more than I am detailing but learnings that will serve me for the rest of my life.

I wish to thank my supervisor, Dr. Terry Humphries for his teachings, patience, guidance, and support throughout the duration of my Ph.D. Thanks for your belief in me, for your constant motivation, and for your positivity. I am very grateful.

I would also like to thank the members of the Hydrogen Storage Research Group at Curtin University, Dr. Drew Sheppard, Dr. Mark Paskevicius, Dr. Veronica Sofianos, Dr. Mathew Rowles for introducing me into the scientific world and letting me work with you all. Your support and guidance is highly appreciated.

Thanks to the Ph.D. students who brightened my pathway at the University. I shared the office with Enrico Ianni, and Arnaud Griffond, they were my office mates. Thanks, Enrico, for the futbol games. Arnaud, you are a great friend of mine, thanks for all your memories. Thanks to Marcela Montserrat Landero Figueroa, and Payam Javadian, also other Ph.D. students I had the pleasure to spend time with.

I would also like to acknowledge the facilities, scientific and technical assistance of the Australian Synchrotron and specifically Dr. Helen Brand, and the Australian Microscopy & Microanalysis Research Facility at the Centre for Microscopy, Characterisation & Analysis at John de Laeter Research Center. I am specifically grateful to Veronica Avery for her assistance and Matthew Rowles for his expertise in X-ray analysis and crystallography.

I would like to acknowledge Prof. Kondo-Francois Aguey-Zinsou for his thermal analysis in an inert atmosphere at the University of New South Wales.

A special thanks to Martin Novillo and Cecilia D'Amico for informing me of the existence of this possibility. Also to Carolina Maggi who encouraged me in this process.

To my family; you have all been extremely supportive throughout this experience. A special mention goes to my daughter, Sienna Milena Cingolani, I love you all. Thank you for being who you are, encouraging me when I needed it most and being so adorable.

Finally, I would like to acknowledge the financial support of the Australian Research Council (ARC) for ARC Linkage LP150100730: "Metal hydride reactors for high-temperature thermochemical heat storage", Chief Investigators: Buckley, Prof Craig E; Chandratilleke, Prof Tilak, Sheppard, Dr. Drew, Davies, Dr. Ian, Allen, Kenneth.

Table of content

Statement of Originality	2
Abstract	4
Acknowledgment	7
List of Figures	11
List of Tables	14
1. Introduction	15
1.1. Energy in the world	15
1.2. Renewable Energy & Solar Thermal Energy	16
1.3. Solar energy storage	17
1.4. Thermal energy storage types and options for materials.	18
1.5. Metal Hydrides	21
1.5.1. Classification of hydride forming materials	24
1.6. Medium range temperature metal hydrides – TCES metal hydrides pair	26
1.7. Fluorine Substitution	29
1.8. Thesis outline	31
1.9. References	33
2. Experimental and Characterisation Techniques	37
2.1. Synthesis	37
2.1.1. Sample Preparation	37
2.1.2. Planetary Ball Milling	38
2.2. X-ray Diffraction	38
2.2.1. Ex situ X-Ray Diffraction (XRD)	39
2.2.2. In situ synchrotron X-ray Diffraction (SR-XRD)	40
2.3. Thermal Analysis	40
2.4. Sorption Analysis	42
2.4.1. The Sieverts' Method	42
2.4.2. Pressure Composition Temperature Isotherms	44
2.5. Inelastic neutron scattering (INS)	49
2.6. References	50

3.	<i>Thermodynamics and performance of the Mg–H–F system for thermochemical energy storage applications</i>	52
3.1.	<i>Introduction</i>	53
3.2.	<i>Experimental</i>	55
3.3.	<i>Results and Discussion</i>	58
3.3.1.	<i>Structure and Composition.</i>	58
3.3.2.	<i>Thermal analysis.</i>	60
3.3.3.	<i>Rehydrogenation studies</i>	67
3.3.4.	<i>Cycling studies</i>	69
3.4.	<i>Conclusions</i>	69
3.5.	<i>Acknowledgements</i>	70
3.6.	<i>References</i>	71
4.	<i>Fluorine Substitution in Magnesium Hydride as a Tool for Thermodynamic Control</i>	74
4.1.	<i>Introduction</i>	75
4.2.	<i>Experimental Section</i>	76
4.2.1.	<i>Sample Preparation</i>	76
4.2.2	<i>Synchrotron X-ray Characterisations</i>	77
4.2.3.	<i>Inelastic Neutron Scattering Characterisations</i>	77
4.2.2.	<i>Thermal Property Characterisation</i>	78
4.2.3.	<i>First-Principle Calculations</i>	78
4.3.	<i>Results and Discussion</i>	80
4.3.1.	<i>Powder X-ray diffraction</i>	80
4.3.2.	<i>Inelastic Neutron Spectroscopy</i>	83
4.3.3.	<i>Thermodynamics of Mg(H_xF_{1-x})₂</i>	84
4.3.4.	<i>Thermal Transport Properties of Mg(H_xF_{1-x})₂</i>	85
4.4.	<i>Conclusions</i>	87
4.4.	<i>References</i>	88
5.	<i>Thermodynamics and performance of the Na-Mg-H-F system for thermochemical energy storage applications</i>	91
5.1	<i>Introduction</i>	92

5.2	<i>Results and Discussion</i>	95
5.3	<i>Conclusions</i>	109
5.4	<i>References</i>	111
6.	<i>Summary and future work</i>	113
	<i>Appendix I. Electronic supplementary information of chapter 3</i>	120
	<i>Appendix II, Electronic supplementary information of chapter 4</i>	126
	<i>Appendix III. Ammonium chloride-metal hydride based reaction cycle for vehicular applications</i>	133
	<i>Appendix IV. Statement of contributions</i>	152

List of Figures

Figure 1.1. Evolution of world demand and supply (includes all varieties of fossil fuels; data available up to 2021) of crude oil in millions of barrels per day in recent decades [5].....	16
Figure 1.2. Schematic of a CSP plant using molten salts for thermal energy storage [19].	19
Figure 1.3. Schematic diagram of multiple PCM LHTES system [24].	20
Figure 1.5. Schematic representation of the construction of MgH ₂ /Mg heat stores. Part A: temporary storage of hydrogen in a pressure container; part B: temporary storage of hydrogen in a low-temperature metal hydride [12]....	26
Figure 1.6. PCT curves of 1-cycle at 300 °C for MgH ₂ powders obtained after reactive ball milling for 200 h [62].	28
Figure 2.1... X-ray diffraction as described by Bragg's Law [3].	39
Figure 2.2. Schematic of the Sievert's apparatus rig at Curtin University [8]. V ₁ , V ₂ , V ₃ , V ₄ , V ₅ and V ₆ are valves : V _{ref} : reference volume: V _{so} : ambient sample volume : V _{sn} : non-ambient sample volume, Sample Volume: V _s and calibration volume: V _{cv}	43
Figure 2.3. Hydrogen desorption pressure composition isotherms (PCT) for NaMgH ₃ performed at temperatures between 398 and 439 °C [11].....	46
Figure 2.4. Van't Hoff diagram of hydrogen desorption equilibrium pressures and linear fit to the data [11, 12]. The data points plotted come from the centre point of the plateaus from Fig 2.3.	46
Figure 3.1. In-situ SR-XRD at room temperature of Mg(H _x F _{1-x}) ₂ samples ball milled for 40 hours and annealed. * signifies Mg ₂ FeH ₆ , ● signifies Fe and ▲ signifies MgO. All other Bragg peaks are associated with the Mg(H _x F _{1-x}) ₂ mixtures. λ = 1.000389(1) Å.	57
Figure 3.2. Refined lattice parameters of Mg(H _x F _{1-x}) ₂ -L mixtures from room temperature in-situ SR-XRD. (a) Quadratic fit for lattice parameters a and c versus composition. a = -0.0762x ² - 0.0326x + 4.6236. c = -0.0239x ² - 0.0069x + 3.0521 (b) quadratic fit for unit cell volume and H occupancy versus composition. Unit cell volume V = -2.5527x ² - 1.1113x + 65.246. H Occupancy = 0.2073x ² + 0.7952x - 0.0064.	59
Figure 3.3. (a) In-situ XRD for Mg(H _{0.85} F _{0.15}) ₂ . λ = 1.000389(1) Å. Simultaneous thermal analysis of Mg(H _x F _{1-x}) ₂ samples by (b) DSC, (c) TGA and (d) MS. ΔT/Δt = 10 °C/min. DSC and MS data are normalised to the mass of the sample.	61
Figure 3.4. (a) Pressure–Composition–Isotherms (PCI) for Mg(H _{0.85} F _{0.15}) ₂ -S performed between 437 °C and 461°C. ◆ ln(P/P _o) _{461°C} = 0.02978 x + 3.7850, ● ln(P/P _o) _{450.1°C} = 0.0279 x + 3.6048, ■ ln(P/P _o) _{444.2°C} = 0.0256 x + 3.4978, ▲ ln(P/P _o) _{436°C} = 0.0227 x + 3.3731, where x = wt% H ₂ desorbed. (b) van't Hoff plot of respective H ₂ desorption equilibrium pressures, where T is temperature (K). P _o =1 bar.....	64
Figure 3.5. a) Ex-situ XRD of Mg(H _{0.85} F _{0.15}) ₂ ; (b) after PCI desorption at 450 °C; (c) after PCI absorption at 450 °C. λ = 1.5418 Å, at room temperature.	65
Figure 3.6. Figure 3.7. (a) Hydrogen desorption kinetic data for the PCI of Mg(H _{0.85} F _{0.15}) ₂ performed at 450 °C, (b) Hydrogen absorption kinetic data for the PCI of Mg(H _{0.85} F _{0.15}) ₂ performed at 450 °C; (c) Hydrogen desorption and absorption PCIs performed at 450 °C.....	67
Figure 3.7. (a) Cycling studies of Mg(H _{0.85} F _{0.15}) ₂ ; (b) XRD after cycling in the hydrogenated state. λ = 1.5418 Å, at room temperature.....	68

Figure 4.1. Representative views of $Mg(H_xF_{1-x})_2$; (a) $Mg-H(F)_6$ octahedral units viewed along the a -axis and (b) along the c axis. Mg atoms represented as red spheres, H(F) atoms as blue spheres and $Mg-H(F)_6$ octahedra represented with yellow faces.	81
Figure 4.2. Phase distribution in $Mg(H_xF_{1-x})_2$ solid solutions determined by SR-XRD as observed at the (110) Bragg peak. $T = 27$ °C.	81
Figure 4.3. Phonon density-of-states of $Mg(H_xF_{1-x})_2$ solid solutions determined by (a) INS (intensity is normalised) and (b) DFT-based lattice dynamic calculations. For calculated data the contributions from different constituent atoms are weighted by their corresponding inelastic neutron scattering cross-sections. For MgF_2 , there are no phonon branches beyond 80 meV. Insets show the enlarged low-energy part of the phonon density-of-states. (c-d) show the pattern of atomic vibrations for the B_{1g} , E_u and E_g phonon modes for MgH_2 and MgF_2	82
Figure 4.4. Formation energies for $Mg(H_xF_{1-x})_2$. Black squares correspond to DFT calculated formation energies, red triangles correspond to experimentally derived formation energies [7, 10, 44].	84
Figure 4.5. Thermal transport properties of $Mg(H_xF_{1-x})_2$. Thermal conductivity (black square), thermal diffusivity (blue triangle) and volumetric heat capacity (red circle) measured at RT under Ar atmosphere.	86
Figure 5.1. $NaMgH_3$ crystal structure, space group $Pnma$, $N^\circ. 62$. Lattice $a = 5.463 \text{ \AA}$, $b = 7.703 \text{ \AA}$, $c = 5.411 \text{ \AA}$ [16]. Na atoms are represented with the light blue spheres, Mg with orange and H with the blue spheres.	93
Figure 5.2. SR-XRD data at room temperature for $NaMg(H_{1-x}F_x)_3$ samples after ball milling and annealing. All other Bragg peaks are associated with the $NaMg(H_{1-x}F_x)_3$ mixtures. $\lambda = 1.000389(1) \text{ \AA}$	96
Figure 5.3. a) Represents the Crystallographic Density (g/cm^3) and Unit Cell volume (cm^3) of $NaMg(H_{1-x}F_x)_3$ solution and b) represents the lattice parameters a , b and c of the $NaMg(H_{1-x}F_x)_3$ series determined by Rietveld analysis of the SR-XRD data. Lattice a : $y = -0.0032x^2 + 0.018x + 5.46$. $R^2 = 0.9977$; Lattice b : $y = -0.0036x^2 - 0.00033x + 7.6985$. $R^2 = 0.9994$; Lattice c : $y = -0.0037x^2 - 0.0045x + 5.4097$. $R^2 = 0.9999$	97
Figure 5.4. Representation of the $NaMgHF_2$ crystal structure. Na atoms are represented with the light blue spheres, Mg with orange and H (and F) with the blue spheres.	98
Figure I.1. Ex-situ XRD data for samples ball milled for 40 hours (L) collected at room temperature. $\lambda = 1.5418 \text{ \AA}$. Red and black dot line's refers to main peaks of MgF_2 and MgH_2 respectively.	120
Figure I.2. In situ SR-XRD at room temperature of $Mg(H_xF_{1-x})_2-L$ samples ball milled for 40 hours and annealed. $\lambda = 1.0003896$	121
Figure I.3. Comparison between SR-XRD of samples ball milled for 10 and 40 hours and then annealed (A). $\bullet = Mg_2FeH_6$, $\blacklozenge = Si$. $\lambda = 1.5418 \text{ \AA}$, at room temperature	121
Figure I.4. In-situ XRD for $Mg(H_{0.70}F_{0.30})-L$ performed under vacuum using a heating rate of $10^\circ C/min$ before $200^\circ C$ and $5^\circ C/min$ after $200^\circ C$. $\lambda = 1.0003896 \text{ \AA}$	122
Figure I.5. In-situ XRD for $Mg(H_{0.50}F_{0.50})-L$ performed under vacuum using a heating rate of $10^\circ C/min$ before $200^\circ C$ and $5^\circ C/min$ after $200^\circ C$. $\lambda = 1.0003896 \text{ \AA}$	122
Figure I.6. In-situ XRD for $Mg(H_{0.95}F_{0.05})-L$ performed under vacuum using a heating rate of $10^\circ C/min$ before $200^\circ C$ and $5^\circ C/min$ after $200^\circ C$. $\lambda = 1.0003896 \text{ \AA}$	123

Figure I.7. Simultaneous thermal analysis of $Mg(H_{1-x}F_x)_2$ -L samples by (a) DSC, (b) TGA and (c) MS. Ramp rate = 10 °C/min. DSC and MS data are normalised to the mass of the sample.	124
Figure I.8. Simultaneous thermal analysis of $Mg(H_{0.50}F_{0.50})$ -L. by (a) MS and (b) TGA. Ramp rate = 10 °C/min.	125
Figure I.9. In-situ XRD for $Mg(H_{0.50}F_{0.50})$ -L. $\lambda = 0.7745419 \text{ \AA}$	125
Figure II.1. SR-XRD pattern, Phase distribution and Rietveld refinement plot of $Mg(H_xF_{1-x})_2$ solid solutions focused on the (110) Bragg peak. the Experimental data illustrated as black line, calculated diffraction pattern as blue squares, calculated phase distribution as multi-coloured lines and the difference plot in black at the bottom of the plot. T = 27 °C.....	129
Figure II.2. NEXAFS data collected near the magnesium K-edge for the $Mg(H_xF_{1-x})_2$ system.	132

List of Tables

<i>Table 1.1. Frequently used solid and liquid materials for the storage of sensible heat. Energy stored per mass of different storage materials [12, 13].</i>	18
<i>Table 1.2. Methods of storing hydrogen and their relevant properties [20, 22, 23, 24, 25, 26, 27].</i>	22
<i>Table 3.1. Decomposition temperatures and hydrogen capacities and values of $Mg(H_xF_{1-x})_2$-S mixtures measured by DSC-TGA up to 550 °C. $\Delta T/\Delta t = 10$ °C/min.</i>	63
<i>Table 3.2. Thermodynamic properties at 5 different hydrogen contents for $Mg(H_{0.85}F_{0.15})_2$-S</i>	64
<i>Table 4.1. Supercells and K-point meshes chosen for finite-displacement phonon calculations in VASP. Also shown is the Γ-centred K-point grids used for phonon density-of-states integrations. Note that the supercell for phonon simulations were specified with respect to the supercells for calculating the substitution formation energies, not the primitive MgH_2 unit cell.</i>	79
<i>Table 4.2. Structural properties of $Mg(H_xF_{1-x})_2$ ($x = 1, 0.95, 0.85, 0.70, 0.50, 0$) materials measured by SR-XRD at room temperature. Estimated standard deviations (esd's) are in parentheses.</i>	81
<i>Table 4.3. Thermal Transport Properties of $Mg(H_xF_{1-x})_2$ measured at room temperature under Ar atmosphere. λ_{TC} is thermal conductivity (W/m.K), k is thermal diffusivity (mm^2/s), and C is the heat capacity per unit volume ($MJ/m^3.K$).</i>	86
<i>Table 5.1. Mixing molar ratios and preparation conditions of $NaMg(H_{1-x}F_x)_3$. The compositions were determined by SR-XRD analysis and Rietveld refinement. Uncertainties are in parentheses.</i>	95
<i>Table 5.2. Peak positions for triplet at $2\theta = \sim 21.2$. I: left peak, II: middle peak, and III: right peak.</i>	96
<i>Table 5.3. Structural properties of $NaMg(H_{1-x}F_x)_3$ mixtures (Pnma) at room temperature. Estimated standard deviations (esd's) are in parentheses.</i>	97
<i>Table 5.4. Composition of $NaMgHF_2$ determined by SR-XRD as a function of temperature.</i>	99
<i>Table I.1. Summary of parameters and data collected from PCT desorption measurements of $Mg(H_{0.85}F_{0.15})_2$-S Pressure and H_2 wt% uncertainties</i>	123
<i>Table II.1. Quantitative Rietveld analysis of SR-XRD data for $Mg(H_xF_{1-x})_2$ solid solutions. Errors are in parentheses. The phases in shaded grey were used in the weight averaged calculations.</i>	126
<i>Table II.2. Atomic coordinates and thermal parameters of $Mg(H_xF_{1-x})_2$ solid solutions. Errors are in parentheses.</i>	128
<i>Table II.3. Crystallographic parameters for $Mg(H_xF_{1-x})_2$ compounds optimized by DFT calculations. Percentage difference compared to experimental values given in parentheses.</i>	130
<i>Table II.4. Thermodynamics of $Mg(H_xF_{1-x})_2$ compounds determined by DFT calculations and physical measurements. ΔH_{form} is the enthalpy of formation of $Mg(H_xF_{1-x})_2$ determined by DFT calculations. ΔH_{des} is the enthalpy of desorption determined experimentally.</i>	131

1. Introduction

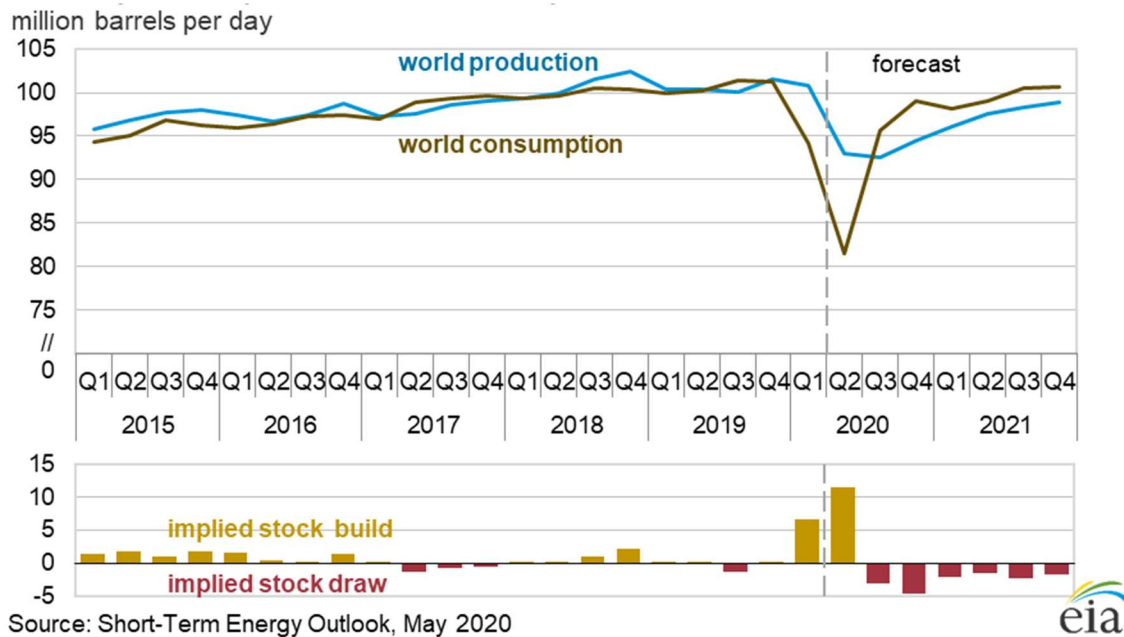
1.1. Energy in the world

The growing world population is depleting the world's energy resources and fossil fuels are no exception. For this reason, if the consumption of the world energy supplies continues in this trend, it will be unsustainable [1]. The fossil fuels (coal, oil, gas) will not cover the demand in the long term, as such, we cannot continue to burn these resources because they are vital for fossil-based industrial applications, in other words, for other processes and products that are critical for mankind. These products include plastics, paints, tyres, dyes, ammonia, glass, ammonium nitrate, soap, aspirin, petrochemicals, lubricants, rubber, creosote oil and solvents [2]. Therefore, it is evident that it is necessary to find a long-term energy solution, which should be sustainable, reliable, limitless, clean, and of course globally scalable.

It is necessary to move towards alternative forms of energy production, but nuclear fission and fusion also have some drawbacks, as such, they may not be taken into account as a solution. Firstly, nuclear energy has bad publicity, it is hazardous, and is not scalable. Secondly, it has many disadvantages such as the technology used is slow and it requires high temperatures.

This opens the door to new methods of energy production, with the focus on renewable energy sources. In this category of energy, we have several different sources including wave tidal, ocean thermal, wind, hydroelectric, biomass, geothermal, and solar power.

Over the past two centuries, energy supply has been based on secondary energy sources such as fossil fuels (natural gas, naphtha, gas oil, and coking coal) derived from primary energy sources such as oil and coal. Unfortunately, the use of these fuels has caused many problems, among which are: 1) global warming or the greenhouse effect caused mainly by the release of CO₂ and subsequent climate change; 2) deterioration of air quality in large cities where fossil fuel-based transportation, industry (such as agro-industry, cement manufacture), and electricity is used; 3) increase in fossil fuel prices as a result of the sustained increase in demand with a supply that in certain periods does not meet the demand. For example, in 2010 there was a demand of 88.3 million barrels per day against a supply of 87.5 million barrels per day (Fig. 1.1). In 2016, growth in emissions contrasts with the sharp reduction needed to meet the goals of the Paris Agreement on climate change [3]. According to the IEA (International Energy Agency) Global Energy & CO₂ Status Report 2017 [4], global energy demand increased by 2.1 % in 2017, compared to 0.9 % the previous year and 0.9 % on average over the previous five years. In fact, 72 % of this increase was met by fossil fuels, a quarter by renewables and the remainder by nuclear energy. For these reasons, in recent decades, different alternatives to fossil fuels have been researched.



Source: Short-Term Energy Outlook, May 2020

Figure 1.1. Evolution of world demand and supply (includes all varieties of fossil fuels; data available up to 2021) of crude oil in millions of barrels per day in recent decades [5].

1.2. Renewable Energy & Solar Thermal Energy

All renewable energy sources, in one way or another, are derived from the sun, geothermal being an exception. Moreover, all of them have efficiency losses, plus their total energy capacity is too low compared to traditional fossil fuel-based energy [1, 6] with the exception of solar that can delivered many times our requirements.

Compared to solar power, in terms of incident solar irradiation on the Earth surface, the other renewable energy sources supply less than 1% of energy [1]. This leaves us with solar power as the dominant solution for generating renewable energy it fulfils all requirements (with geography taken into account) and at the same time allows us to preserve fossil fuels for the production of industrial materials such as plastic and chemicals. The sun radiates the Earth with 10,000 times more energy than the actual total world energy consumption [2]. That means solar power can cover the entire world's energy consumption and future demand, plus it is a clean, sustainable, and reliable source. Studies show that the rate of energy consumption is higher during daytime hours and decreases at night-time and during cloudy weather [2]. Taking this into account, and because there is excess solar power during the day, it will be necessary, and wise, to store some power to be used during non-sunny periods.

My belief is that humankind needs a mixture of renewable sources of energy to be sustainable and for once stop the use of fossils. For example, use solar during the daytime, use the wind in windy places (this can also allow producing energy at night and during cloudy days). The ideal would be to study the geography, the climate of each place with its disadvantages and benefits because each place has its particular advantage, to

maximize the use of the most suitable energy source in order to build a specific plant according to the needs and properties of each place.

1.3. *Solar energy storage*

Much work has been conducted in the field of solar energy. Generally, there are two main methods to collect solar power, solar cells, and solar thermal:

Solar cells: convert the sun's energy into electricity by the photovoltaic effect. The conventional solar cell is made of crystalline silicon and is called photovoltaic (PV) cells. A positive aspect of PV use is that it allows energy collection in a decentralised approach. However, because of the low efficiency of the technology, it does not exploit the sun's energy perfectly. Efficiency is the ratio between energy output and energy input of a given system, for solar PV cells, this means the ratio of produced electrical energy to the amount of solar energy incident on the cell under standardized testing conditions. Although some experimental solar cells have achieved efficiencies of close to 50%, most commercial solar panels (silicon typically) reach an efficiency of 20% [7]. PV alone will not cover the world's energy demand due to collection inefficiencies, the present temperature limits of the materials (some materials are not able to work at high temperatures), and because this technology uses chemicals that will present an environmental impact (e.g. arsenic) [7].

Solar thermal: This solution is a low-tech method of concentrating solar energy. The system that is currently used is called concentrating solar power (CSP) and is the most efficient in terms of sunlight used to produce electricity [8]. The main concept is to set curved mirrors in such a position as to focus the sun and collect the energy (heat) and heat a substance (such as a heat transfer fluid). Electricity can then be generated by driving a turbine via a generator (Rankine cycle engine). Energy must be able to be supplied 24 hours a day to maintain industrial process that run 24/7. Although during daytime we will be able to use the heat of the sun directly, energy needs to be stored to use after sunset for producing electricity at night.

Although CSP has the convenience of thermal energy storage, solar PV is the most economical technique; to exploit both features thermal storage could be coupled to PV. The ideal CSP plant is an energy storage system capable of storing large amounts of heat (solar energy) for a long time and at a low cost. This can be achieved by using thermal energy storage (TES) materials [9]. TES is a technology that stores thermal energy by heating a storage medium so that the stored energy can be used later. The requirement for TES to allow storage of energy from the sun and be able to use it later in order to have energy available for 24 hours a day. To address this, a high energy density storage material will be necessary to minimise the volume of the material required to store this energy. At the same time, to reach higher energy conversion efficiencies a higher temperature thermal energy storage material (greater than 650 °C) will be required such as SrH₂ [10] and CaCO₃ [11]. However, the main driver is the cost of this technology.

1.4. Thermal energy storage types and options for materials.

The different kinds of thermal energy storage can be divided into three basic methods: sensible heat, latent heat, and thermo-chemical heat storage. Each of these has different advantages and disadvantages that determine their applications. A comparison of the different types of TES methods is described in table 1.1.

Table 1.1. Frequently used solid and liquid materials for the storage of sensible heat. Energy stored per mass of different storage materials [12, 13].

Method of thermal storage	Material	Density (kg.m ⁻³)	Specific heat capacity (kJ.kg ⁻¹)	Latent heat of fusion (kJ.kg ⁻¹)	Reaction enthalpy (kJ.molH ₂ ⁻¹)	Gravimetric energy density (kJ.kg ⁻¹)	Volumetric energy density (kWh m ⁻³)	Temperature (°C)
Sensible	Rock	2240	0.9	-	-	-	-	-
	Sandstone	2200	0.71	-	-	-	-	-
	Brick	1600	0.84	-	-	-	-	-
	Soil	1300	0.46	-	-	-	-	-
	Concrete	2240	1.13	-	-	-	-	-
	nitrate salts (60% NaNO ₃ + 40% KNO ₃)	1804	1.52	-	39	413	250	T _{hot} < 565
Latent	KNO ₃	2110	-	91.6	-	266	155	T _{melting} < 333
	paraffin wax	1802	-	174.4	-	174	-	64
	Fe-Cu (MGA)	-	-	205	-	-	-	1085 ^a
	Al-Sn (MGA)	-	-	59	-	-	-	232 ^a
	SiC-Si (MGA)	-	-	1926	-	-	-	1414 ^a
Thermochemical	$CaCO_3 \rightleftharpoons CaO + CO_2$	-	-	-	165.7	1657	-	890 ^b
	$2CaH_2 + 3CaSi \rightleftharpoons Ca_5Si_3 + 2H_2$	-	-	-	107.3	743.4	-	703 ^c
	$SrH_2 \rightleftharpoons Sr + H_2$	-	-	-	183	2041	-	1070 ^d
	$MgH_2 \rightleftharpoons Mg + H_2$	1380	-	-	74.06	2811	1110	T _{range} < 350 – 450 ^e
	$CaH_2 \rightleftharpoons Ca + H_2$	770	-	-	207.9	4939	-	1000 ^f

^a[14], ^b[11], ^c[15], ^d[10], ^e[16], ^f[17]

The most popular and simplest method of CSP power production uses “sensible heat” storage, and for this, molten salts are mostly used e.g. nitrate salt (60% NaNO₃ + 40% KNO₃) [18]. By heating these materials, thermal energy is stored as a function of its specific heat capacity. In this case oil or molten salts are used as heat transfer fluid to produce electricity in CSP plants, similar process that was described previously for solar thermal. The current state-of-the-art method used in commercial plants is during sunny periods, sun rays are focussed on to a receiver, molten salt collects the heat and flows towards the equipment to be heated (Fig. 1.2). Once warmed, the salt is stored in an insulated tank. As the energy is needed, this hot salt is moved from the storage tank to a heat exchanger, where the heat released generates steam to drive a turbine. The cooled salt is then stored in another tank, and it is sent once again to the receiver.

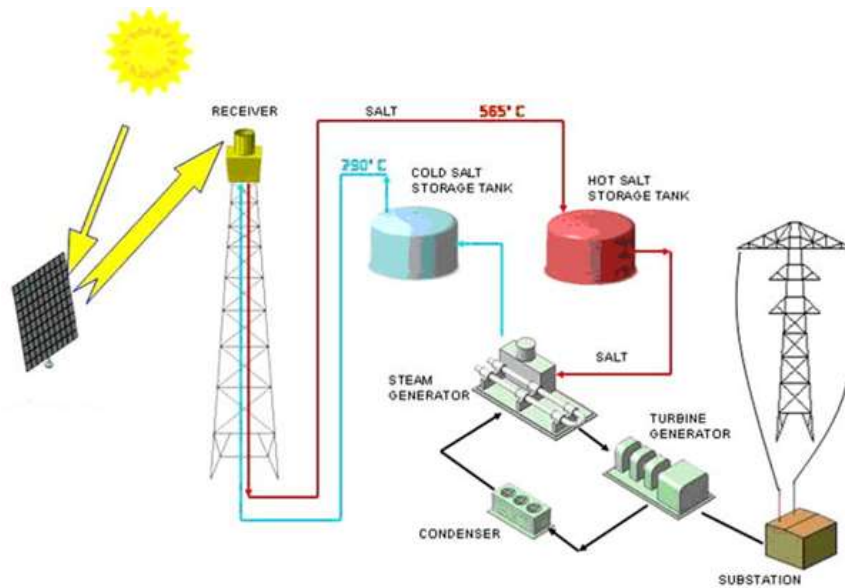


Figure 1.2. Schematic of a CSP plant using molten salts for thermal energy storage [19].

Molten salts used in CSP technology also have some drawbacks, as the molten salts (60% NaNO_3 and 40% KNO_3 , for example) have low thermal and electric efficiency due to their low mass energy density 413 kJ/kg [18], are corrosive, and tend to freeze below 200 °C [9]. In addition, massive volumes are required to store energy for several hours, and the operating temperature is limited to 565 °C [8, 19]. In all, these factors result in high costs. For example, the construction of the Astexol 2 plant sited in Spain, which represents an investment of over 300 million euros [20, 21], has two vertical indirect tanks, with 60% NaNO_3 and 40% KNO_3 as the molten salt mixture. The volume for the cold tanks is 15,246 m³ and the hot tank is 15,741 m³. This plant has a nominal capacity of 50 MW of electrical power and has a storage capacity of 8 hours.

The second method for thermal energy storage is the utilisation of latent heat materials. The principle behind this method consists of the utilisation of the energy required to change the phase of a material, e.g. melting and freezing. These materials are often called phase change materials (PCM). Nitrate salts (e.g. KNO_3), table 1.1, are often used due to their high gravimetric energy density (0.074 kWh.kg⁻¹) and their volumetric energy density (155 kWh.m⁻³) [12].

One strategy to implement these materials could be to use various latent heat materials to develop a cascading energy storage system, Figure 1.3. [9, 22, 23]. Although this configuration has advantages, including that the heat stored is the sum of the heat of fusion plus the specific heat, the thermal conductivity in the solid phase is too low, as a consequence the heat exchangers required are very large. For instance, a US patent for power plants using PCM method mentions that a rotary heat exchanger must have a 20 m diameter and be 15 m in height [24]. However, a new class of thermal energy storage material based on Miscibility Gap Alloys (MGA) was recently introduced by Sugo and Kisi et al. [14], they used an Al-Sn and Fe-Cu system in which the heat of fusion are 59 kJ.kg⁻¹ and 205 kJ.kg⁻¹, respectively (Table1.1), and this material

has potentially solved the problem of low thermal conductivity (paraffin wax $\sim 0.2 \text{ W/m } ^\circ\text{C}$ [13]), which limits their applications.

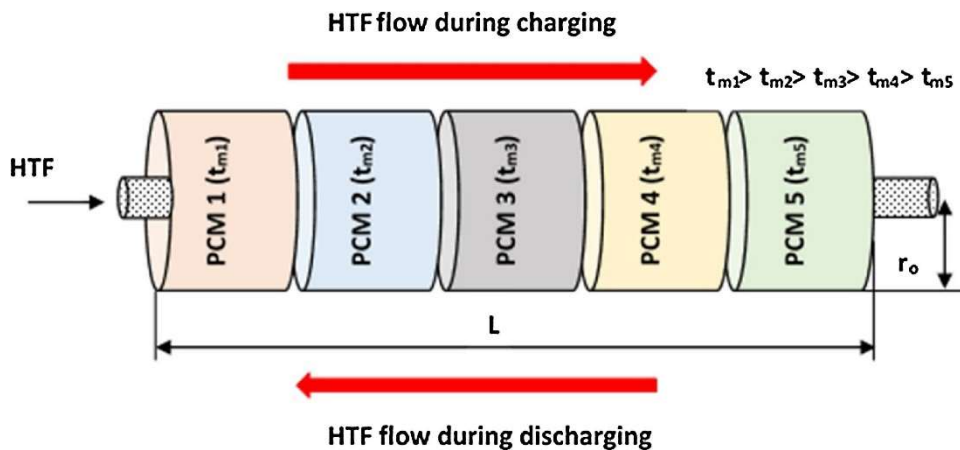


Figure 1.3. Schematic diagram of multiple PCM LHTES system [24].

MGA's are formed between metallic (or semi-metallic) elements that are immiscible. To make a miscibility gap alloy that is useful for thermal storage, the lower melting temperature metal is the active phase that is dispersed as discrete particles in a thermodynamically stable matrix phase, i.e. the higher melting temperature metal [14]. When a MGA is heated, it begins to absorb thermal energy until the melting point of the active phase is reached. At this point, it begins to melt, and the temperature remains stable utilising latent heat. Once this dispersed phase is completely liquid, the temperature increases again, but is kept below the melting point of the matrix phase. The matrix phase remains solid throughout the process ensuring the MGA storage material maintains its structure and general physical properties. The operating temperature of the MGA is the melting temperature of the active phase and the stored energy is the latent heat plus sensible heat. There are many systems studies, in Table 1.1 there are some examples including Fe-Cu which has a working temperature of $1414 \text{ }^\circ\text{C}$ and latent heat of fusion of 1926 kJ/kg .

Thermochemical energy storage (TCES) is the third method of thermal energy storage. TCES is the storage of heat by an endothermic reaction of break bonds within a substance at given conditions of pressure and temperature into two (or more) compounds. This reaction must be reversible, so that the stored thermal energy can be recovered through the reverse exothermic reaction. The energy storage density is determined by the enthalpy of reaction (ΔH) of the system. In general, this method possesses the highest energy per mass of material, examples of TCES are CaH_2 , SrH_2 , MgH_2 , CaCO_3 . For example CaH_2 reversibly reacts with H_2 at 1.2 bar back pressure at $1000 \text{ }^\circ\text{C}$ with an associated reaction enthalpy of $207.9 \text{ kJ.mol}^{-1} \text{ H}_2$, and SrH_2 reacts at 1 bar H_2 backpressure at $1070 \text{ }^\circ\text{C}$ and $183 \text{ kJ.mol}^{-1} \text{ H}_2$, respectively (Table 1.1) [12]. Reversible thermochemical reactions are possible in materials including the oxidation of metals, the calcination of metal carbonates, the dehydration of metal hydroxides, and hydrogen storage in metal hydrides (MH) [25]. The advantages of TCES materials over molten salts such as nitrate salts ($60\% \text{ NaNO}_3 + 40\% \text{ KNO}_3$) are high energy density 1657 kJ/kg

for CaCO_3 (413 kJ/kg for nitrate salts), a more extensive range of working temperature for example 890 °C for CaCO_3 and for nitrate salts it is limited at <565°C due to chemical instability (Table 1.1) [10, 11, 26]. Of these, MHs could become a promising system as they have a high energy density and can store energy and release it reversibly when it is required [25]. The main objective is to develop TCES materials with improved efficiency and reduced cost for use in a CSP system.

1.5. *Metal Hydrides*

Hydrogen is considered to be the most promising material for energy storage, and even more so for long term energy storage [27]. Table 1.2 details the various alternatives to store hydrogen, it compares the energy densities and operating temperatures among different storage materials. It also details the properties of hydrogen storage in hydrides (solid state), which is a great alternative to compressed hydrogen storage as the density of stored hydrogen increases significantly e.g. (hydrogen storage capacity of compressed gas is 7 – 39.1 kg.m^{-3} at 20 °C, between 100 to 700 bar, and for MH between 40 to 150 kg.m^{-3} [28]) and in turn allows hydrogen to be supplied under lower pressure conditions.

Table 1.2. Methods of storing hydrogen and their relevant properties [20, 22, 23, 24, 25, 26, 27].

Phase	Method	Hydrogen content regardless of system weight (reservoir and accessories for loading and unloading) (% w/w H ₂)	Energy density per unit mass taking into account the weight of the system (kWh/kg)	Energy density per unit volume considering the weight of the system (kWh/l)	Operating Temperature (°C)	Operating Pressure (bar)	Energy needed to release hydrogen (MJ/kgH ₂)
Gas	1 High Pressure Tank ^a	100 (5.4)	1.5	0.8	25	800	-
Liquid	2 Cryogenic Tank ^b	100 (18)	1.7	1.2	-252	1-6	0.45
	3 Metals and complexes with water (ex.H ₂ O _(l)) with Na _x to produce H _{2(g)}	<40 (-)	1.4	1.0	25	0.1	-
Solid	4 Cryogenic adsorption (zeolites or carbon nanotubes)	6.5 (-)	-	-	-196	1	3.5
	5 Hydrides						
	5.1 Absorption in interstitial material hydrides (e.g. FeTiH ₂ /LaNi ₅ H ₆) ^c	2 (1)	0.4	0.8	0-30	1-2	15
	5.2 Binary hydrides (MgH ₂ + Additives) ^d .	7.6 (2.8) ^e	-	-	300 - 350	1 – 8	37
	5.3 Complex hydrides (NaAlH ₄) ^f	5.5 (0.9)	0.3	0.7	70 - 170	1	23
	6 Petroleum Tanks ^g	- (-)	8	7	25	1	-

^a[29] Tank built with a structure of composite materials based on polyamide polymers. ^b[29] Tank built with reinforced fibers and metallic coatings to prevent permeation. ^c[29] Daimler company data. ^d[30-32] Data obtained from publications. ^e[31] Capacity achieved with an experimental tank of 500 g after 20 cycles of absorption. ^f[29] Experimental data; extrapolation to 5 kg of H₂ stored in sodium alanate. ^g[29] BMW data. Fuel tank plus accessories (activated carbon filter, pumps).

MHs have taken the lead from the other hydrogen storage methods as they can store large amounts of hydrogen in a smaller volume, at low pressures (less than 1 bar), and in a safe manner but they are more expensive. The main reason to use these materials for solar thermal storage is the high volumetric heat capacity of the MH reaction (formation and dissociation), as such the volume of the storage tanks and the storage material will be reduced and by consequence, the overall cost of the system will decrease.

The energy storage method of a MH for a TCES is based on a thermochemical reaction (eq. 1.1). Many metals can react with hydrogen to form strong ionic and covalent bonds and hence form very stable MHs. Materials that form hydrides and the different types of hydrides that are formed include: metallic materials (alkaline, alkaline earth, transition, and rare earth), intermetallic (Mg₂Ni, CaH₂, etc.) and non-intermetallic compounds (Mg-Fe, Mg-Co) and combinations of B or Al with an alkaline or alkaline earth metals [33]. These compounds are the indicated materials to be used as hydrogen storage as they react with gaseous hydrogen forming metal hydrides, in most of the cases through an exothermic reaction releasing heat. Moreover, the reaction

of metal hydrides involves high formation energy, (for example, MgH_2 has a $\Delta H = 74.06 \text{ kJ/mol H}_2$ [16]) this characteristic allows hydrides to store heat [34]. MH's can be considered a source of heat (by dissociation) as they often reversibly absorb and desorb hydrogen gas from their crystal structure, and as a consequence, the heat is reversibly stored in a chemical reaction [35, 36].



The operating principle of TCES is to use heat (from solar energy) which is to be consumed in an endothermic dissociation reaction, where the MH will dissociate into metal and hydrogen gas (Equation 1.1). The reaction can be carried out in a solar reactor or could also use a HTF to transfer heat from receiver to vessel. When the MH is desorbing hydrogen, chemical energy is absorbed when the bonds are broken (endothermic), so it absorbs heat [35]. When the MH is reformed, due to the metal reacting with hydrogen gas, heat energy is released (exothermic). The total heat released during this process is equal to that previously stored during the daytime. If the heat can be removed as fast as possible during the reabsorption of hydrogen, self-heating can be avoided allowing heat to be released at a constant temperature and avoiding engineering problems. This can readily be controlled with pressure. If the H_2 pressure is limited to 1 bar (for example) then the material will only heat up until it reaches its 1 bar equilibrium temperature and cannot absorb more gas, so therefore it cannot increase in temperature. Materials such as magnesium, calcium and titanium meet the requirements for TCES, and for this reason, they are widely investigated and much research has been conducted into implementing them into technology [25, 37-44]. The attractive and most exploited property of these materials is that they can absorb and desorb hydrogen at a constant pressure. This can be done by changing the applied hydrogen pressure (or the temperature) because a MH absorbs H_2 while releasing heat (exothermic reaction) or desorbs H_2 while absorbing heat (endothermic reaction) [9].

As mentioned previously, MHs possess some of the highest theoretical heat storage capacities through the reaction with hydrogen gas, which can occur at a large range of temperatures depending on the MH employed. As illustrated in Table 1.1, many MHs have a theoretical heat storage capacity of a magnitude higher than molten salt and PCMs. Also, these materials (molten salts, some PCM) have either high cost and/or low reversibility.

An interesting aspect of MH materials that are to be used as TCES is their versatility, as their properties can be tailored to suit application by either tuning by destabilization (like CaH_2 with Si [15]) or by stabilization (MgH_2 with MgF_2 to form $\text{Mg}(\text{H}_x\text{F}_{1-x})_2$ [45], NaMgH_3 with NaMgF_3 to synthesize $\text{NaMg}(\text{H}_{1-x}\text{F}_x)_3$ [39], NaH with NaF to produce $\text{NaH}_x\text{F}_{1-x}$ [46, 47]).

For MH materials to be considered for TCES they need to have some preferential characteristics. Ideally, the MH needs to be environmentally friendly, reversible, low cost, high availability, and most importantly they must have a high dissociation temperature to have a high conversion energy efficiency.

The preferred parameters for materials to be applied to MH TCES systems should have low corrosivity, good cyclic longevity, high metallic thermal conductivity (efficient heat transfer), and safe to store [9]. In addition some systems can work at sufficiently high temperatures (e.g. Mg_2FeH_6 500 °C at 66 bar [36]), and as a consequence of this, the efficiency to pass from thermal to electrical energy increases (e.g. Table 1.1. the thermal energy density for nitrates salts is 250 kWh.m⁻³ and for MgH_2 it is 1110 kWh.m⁻³). However, as a drawback, in general they have slow sorption kinetics and oxidise easily [34]. As a consequence of these disadvantages, sorption kinetics and cyclic capacity need to be improved and are partially the purpose of the work done in this thesis. A more detailed explanation of these types of MH materials will be described in the following sections.

1.5.1. Classification of hydride forming materials

A classification of hydrides is made based on the class of element that makes up the hydride-forming material, the type of interaction between hydrogen and the material, and the crystal structure of the hydride. This classification aims to describe concisely the different varieties of hydrides that exist and also detail those that are considered in this thesis [37, 48-54].

1.5.1.1. Metal or interstitial metal hydrides

Hydrogen reacts with many metals (transition and rare earths) and their alloys to form hydrides. They are called metallic hydrides because the interaction between the transition metal or intermetallic metal is of a metallic nature; so they are also good conductors of electricity. The crystalline structure of metallic hydrides is constituted by the metal network with hydrogen atoms chemically bound to the metal and found in octahedral or tetrahedral interstitial sites of the metal network. Because of the location of the hydrogen in these interstitial sites, these hydrides are also called "interstitial" [54]. These hydrides can be subclassified into two types:

Binary metal hydrides of transition metals and rare earths:

These are composed of metals of groups 1B to 4B and 8B of the periodic table and lanthanides and actinides, e.g. VH_2 , ZrH_2 , TiH_2 , ScH_2 , TaH , GdH_2 and CeH_3 . On many occasions they present large deviations of stoichiometry (MH_n , $n = 1, 2, 3$) and can exist as multiphase systems, that is hydrides of different stoichiometric proportions [49].

Hydrides of intermetallic compounds

These are composed of intermetallics formulated by AB_xH_n , where A is a transition metal or a rare earth and tends to form metallic hydrides. Element B is a transition metal that does not form hydrides or forms unstable hydrides ($x = 0.5; 1; 2; 5$). Examples of these are LaNi_5H_6 and TiFeH_2 [55].

1.5.1.2. Binary hydrides of group 1A and 2A metals

These are composed of alkaline and alkaline earth metals (groups 1A and 2A of the periodic table). Examples of these hydrides are NaH (4.2 theoretical H_2 wt.%), CaH_2 (4.8 theoretical H_2 wt.%), LiH (12.7 theoretical H_2 wt.%) and MgH_2 (7.66 theoretical H_2 wt.%). The crystalline network of these hydrides tends to be composed of metal cations and hydrogens in the form of anions and therefore they are considered "salt" type hydrides. In general, the metal-hydrogen bond presents characteristics of ionic bonding (e.g. LiH) or a mixture between ionic and covalent (e.g. MgH_2). These types of hydrides are analysed and studied in this thesis [53].

1.5.1.3. Complex transition metal hydrides

The name complex hydride (general composition: $M_m^{+\delta} [TH_n]^{-\delta}$, where m, n and $\delta = 1, 2, 3, \dots$, M : alkaline or alkaline earth metal, T : transition metal and δ : charge), derives from the existence of "discrete complexes" composed of a transition metal and hydrogen ($[TH_n]^{-\delta}$) within the structure of the hydride (anions). For the most part, these complex hydrides are mononuclear, i.e., they contain centred transition metal atoms surrounded by hydrogens that act as ligands. The interaction between hydrogen and metals occurs in the form of $T\text{-H}$ within the discrete complex, as well as $M^{+\delta} - \text{H}^-$. These interactions are based on the partial or total transfer of electrons through which the complex hydride is stabilized [52].

Mg_2NiH_4 (the unit of the discrete complex is $[\text{NiH}_4]^{-4}$) and Mg_2FeH_6 , (the unit of the discrete complex is $[\text{FeH}_6]^{-4}$) [52] are examples of complex hydrides.

1.5.1.4. Complex non-transition metal hydrides

These are composed of light metals of the groups 1A, 2A, and 3A of the periodic table. Hydrogen forms tetrahedral units with boron or aluminium, $[\text{BH}_4]^-$ and $[\text{AlH}_4]^-$, where the interactions of B-H or Al-H are of covalent nature. Therefore, this class of complex hydrides is composed of the combination between such tetrahedral units and a metal (M : alkaline or alkaline earth metal, group 1A and 2A). The character of the link between $[\text{BH}_4]^-$ or $[\text{AlH}_4]^-$ and the metal M^+ is given by the difference in electronegativities between them [49, 52].

Hydrides of the type $M^+[\text{BH}_4]^-$ and $M^+[\text{AlH}_4]^-$ are also called tetrahydroborates and tetrahydroaluminates, respectively. Examples of these are: LiBH_4 , $\text{Mg}(\text{BH}_4)_2$, NaAlH_4 , and LiAlH_4 .

There are also rare earth tetrahydroborates and tetrahydroaluminates such as $\text{Ce}(\text{BH}_4)_3$. However, they cannot operate at the temperatures required for TCES (greater than 650°C).

1.6. Medium range temperature metal hydrides – TCES metal hydrides pair

One method to permit a MH to function as a thermochemical energy storage system is to use a pair of metal hydrides, one high temperature MH (HTMH) and the other low temperature MH (LTMH) [25]. The main function of the HTMH is as a heat storage component, while the LTMH is a hydrogen storage component. The general idea is that the HTMH releases hydrogen during the day, which is then absorbed by the LTMH (Fig. 1.3). At night, the LTMH releases the H_2 gas to the HTMH, which is then absorbed and releases the heat stored. In this process, the HTMH and the LTMH are stored separately in different vessels to avoid any reaction occurring between them [9].

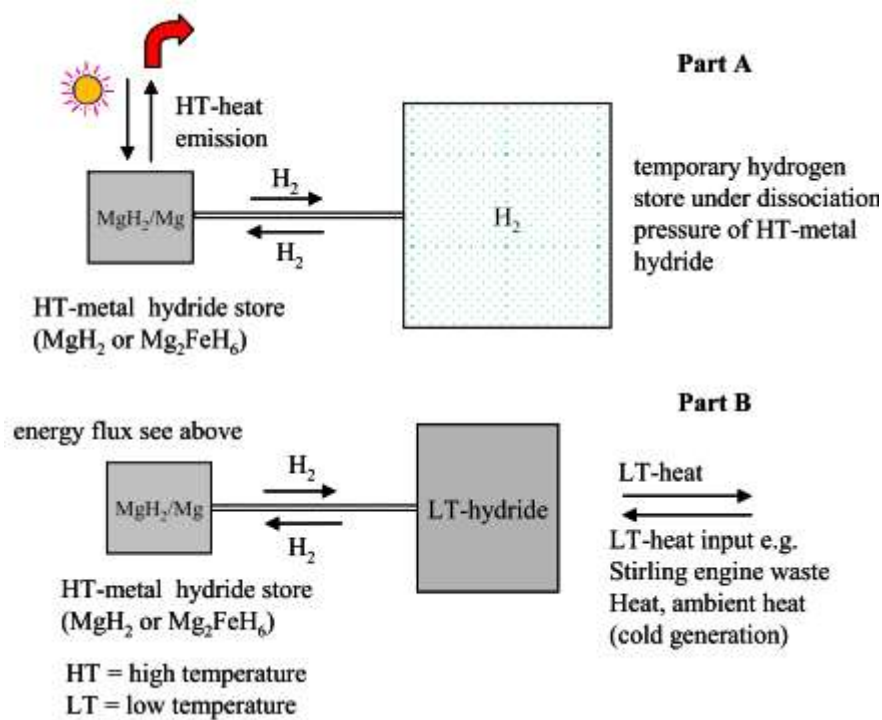


Figure 1.4. Schematic representation of the construction of MgH_2/Mg heat stores. Part A: temporary storage of hydrogen in a pressure container; part B: temporary storage of hydrogen in a low-temperature metal hydride [12].

The system will operate as follows: during the daytime, the temperature of the HTMH reactor will increase (due to CSP), and the endothermic chemical dissociation reaction starts. Hydrogen is released which in turn increases the pressure of the system. Then, the gas flows to the LTMH reactor, and when the H_2 pressure is above the equilibrium pressure of the LTMH, it starts to absorb the hydrogen. This is an exothermic reaction, so heat is released, which maintains the temperature of the vessel (this heat is of a smaller quantity than the heat required in the HTMH), for example a HTMH such as MgH_2 has an enthalpy of desorption of $74 \text{ kJ}\cdot\text{mol}^{-1} \text{ H}_2$ and a LTMH such as $\text{Ti}_{1.2}\text{Mn}_{1.8}\text{H}_{3.0}$ has an enthalpy of desorption of $28 \text{ kJ}\cdot\text{mol}^{-1} \text{ H}_2$ [56]. At night, when the

temperature of the HTMH decreases, desorption stops and the HTMH begins to reabsorb the hydrogen. At the same time, the decrease in pressure causes the LTMH to release hydrogen and the gas moves towards the HTMH reactor.

As absorption of hydrogen is an exothermic reaction, the heat released is used to produce electricity, when CSP is not available, thus allowing 24/7 heat production. The ideal pair of materials is a combination in which the LTMH releases hydrogen at a similar pressure to the operating pressure of the HTMH. Achieving this allows the efficiency of the system to be maximised since the gas will flow permanently [35]. Moreover, another issue that will increase the system efficiency is if the products of the endothermic reaction of the LTMH and HTMH are stored at ambient temperature. This results in the LTMH and HTMH) operating indefinitely without energy (thermal) losses and by consequence, the efficiency will be higher.

For a conventional CSP power plant, the operating temperature is approximately 500 °C due to decomposition of molten salt at 565 °C [57]. However, operating temperatures between 600 °C to 800 °C are optimal as this is the target set by the U.S. Department of Energy's Sunshot Initiative for the next generation CSP plants, although there are relatively few metal hydrides that can operate in this range of temperatures [19]. Considering the most abundant and low-cost materials only, Mg-based hydrides are ideal. Magnesium (Mg) and its hydride MgH₂ have been extensively studied [32, 41, 58, 59] for several years due to their extraordinary properties and characteristics. These studies have led to its interest as a potential candidate as a hydrogen storage material and possible implementation into CSP plants as a High Temperature Metal Hydride (HTMH) for thermal energy storage [41, 60]. The attraction of MgH₂ lies in the fact that it is a low cost, magnesium is abundant, and has a low environmental impact [25]. MgH₂ has a theoretical gravimetric storage capacity of 7.6 wt% of H₂ and a volumetric storage density of 111 kg m⁻³ H₂ [25]. Upon thermal treatment, MgH₂ decomposes into Mg and H₂ with $\Delta H_{abs} = -74.06 \pm 0.42 \text{ kJ.mol}^{-1} \text{ H}_2$ and $\Delta S_{abs} = -133.4 \pm 0.7 \text{ J.K}^{-1}.\text{mol}^{-1} \text{ H}_2$ [16]. There is little to no hysteresis at which the onset of hydrogen absorption lags causing the equilibrium plateau to shift. This is exemplified in Fig. 1.4.

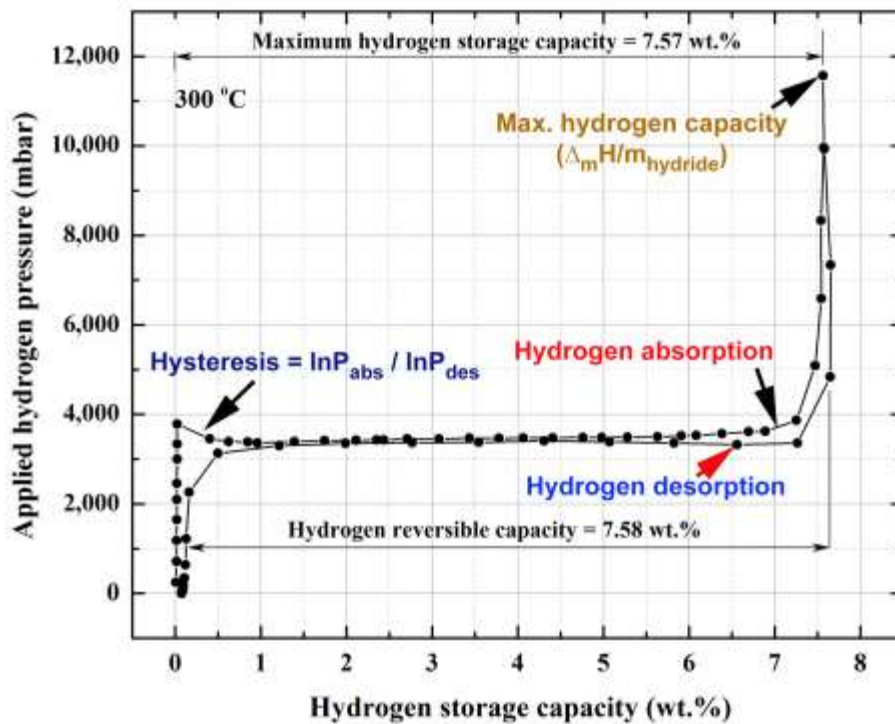


Figure 1.5. PCT curves of 1-cycle at 300 °C for MgH₂ powders obtained after reactive ball milling for 200 h [62].

Thermodynamic properties confirm that MgH₂ is a good candidate for a HTMH for thermal energy storage. However, several drawbacks limit the widespread use of this material, such as the operating temperatures are limited to work below 500 °C because of the high hydrogen equilibrium pressure at that temperature e.g MgH₂ at 500 °C has an equilibrium pressure of 92.15 bar [16, 61], and slow hydriding and dehydriding kinetics are a negative aspect for practical applications [41, 60, 62]. Moreover, pure MgH₂ presents very poor cycling stability where a significant reduction in the H₂ storage capacity is observed over multiple cycles (absorption/desorption) [36]. This is due to the fact that structural and morphological changes occur to magnesium/magnesium hydride during hydrogen cycling at higher temperatures, a phenomenon called sintering [63]. The use of particle refinement agents such as TiB₂ reduces sintering and improves MgH₂ cycling performance [64, 65]. Other studies with graphene also contribute to the prevention of MgH₂ sintering by forming more edge sites and diffusion channels promoting an improvement in hydrogen sorption properties [66].

Moreover, the Mg₂FeH₆ is another compound that can be used as a TCES material, Khan *et al.* [67] demonstrated on a compressed Mg₂FeH₆ pellet a 24% improvement in the yield of the generated Mg₂FeH₆, and the hydrogen sorption properties have been thoroughly investigated. Thermal analysis showed that the decomposition of Mg₂FeH₆ occurs in a single step and the onset decomposition temperature is 240 °C. PCI analysis of Mg₂FeH₆ showed that the enthalpy of formation is 68.3 and the decomposition enthalpy is 75.6 kJ/mol H₂, respectively. The hydrogen sorption kinetics of Mg₂FeH₆ occurs quite fast showing an

absorption/release of 5 wt% H in less than 2.5 min at 400 °C. Another study carried out by Bogdanovic *et al.* [68] indicates that Mg_2FeH_6 is a highly suitable compound for TCES at ≈ 500 °C, due to its high cyclability (600 cycles) with 5% H_2 , over a theoretical value of 5.47% H_2 , showing negligible hysteresis pointing out a high reversibility. The material is characterized by a high gravimetric (1921 kJ/kg) and volumetric (2344 kJ/dm³) thermal energy density in comparison to sensible or latent heat storage materials. Mg_2FeH_6 has a lower hydrogen dissociation pressure compared to MgH_2 , for instance, at 500 °C the dissociation pressure for Mg_2HF_6 is 65 bar and for MgH_2 is 100 bars. This lower pressure is quite favourable from a technical as well as economical point of view, making this material a potential candidate for hydrogen storage as a HTMH. However, large scale prototypes are required to understand and overcome thermal/gas management issues and ensure that a material can cycle 10,000 times to enable a 30-year lifetime. To find application as an HTMH for thermal energy storage in second generation CSP plants [35], it is necessary to increase the operating temperature of MgH_2 to above 600 °C, increase the reaction kinetics and also the cyclic stability. To address the development and production of a new MH, the challenge is to generate a stable component (one phase). This issue could possibly be achieved by using the concept that fluorine substitution into metal hydrides has the potential to increase the thermal stability of the MH and also raise the operating temperature. This will be obtained by combining metal fluorides and metal hydrides, such as $\text{Mg}(\text{H}_x\text{F}_{1-x})_2$ based on MgH_2 and MgF_2 , to store hydrogen.

1.7. Fluorine Substitution

Many MH and metal fluoride compounds are analogous in structure due to their anions sharing the same electronic structure as Helium (1S)². Indeed, due to the fact that the ionic radii of both anions are close ($\text{F}^- = 1.33$ Å or 1.3 Å for coordination number 6 or 3, respectively [67] and $\text{H}^- =$ varies from 1.27 to 1.52 Å, being sensitive to the particular cation [33]), their structural properties are also similar between their compounds [68]. This similarity is true for alkali and alkaline earth metals and aluminium [33].

For instance, some binary metal hydrides and its related metal fluoride are isotopic compounds (they present the same crystal structure but not necessary the same crystal lattice dimensions nor the same chemical composition) such as alkaline and alkaline earth metal hydrides and the corresponding metal fluoride. In the case of the alkaline metal hydrides (LiH, KH, CsH, NaH, RbH) they have a face centred cubic structure of the NaCl type ($P\bar{m}\bar{3}m$). Although among the alkaline earth metals the hydride of Mg and fluoride present the same tetragonal rutile structure ($P42/mnm$) [71-73], the hydrides of Ca, Ba, Sr do not share the same crystal structure with their corresponding fluorides, however they have analogous saline character. Another example of isostructural materials are the two polymorphs of AlH_3 and AlF_3 , as both compounds reside in the same crystal structure (rhombohedral space group $R\bar{3}c$, or orthorhombic, space group $Cmcm$) [74, 75].

In these compounds the comparable ionic sizes of both anions allows for partial substitution in hydrides of H⁻ for F⁻, or vice versa in fluorides. For example, NaH – NaF and LiH – LiF present total solubility forming solid solutions in the whole range of compositions [46, 71]. In the case of partial substitution, the CaH₂-CaF₂, SrH₂-SrF₂ and BaH₂-BaF₂ systems can be mentioned as examples, the maximum substitution achieved for these mixed hydrides fluoride compounds are CaH_{1.24}F_{0.76}, SrH_{0.93}F_{1.07} and BaH_{0.45}F_{1.5} [76, 77]. It is noted that while the atomic number increases the solubility decreases.

This analogy was first recognised before the 1960s, while recent studies have determined that this partial substitution of hydrogen for fluorine is economically beneficial for heat storage applications [39]. Firstly, metal fluorides are more stable than their equivalent metal hydrides, thus this characteristic can be used to raise the thermal stability of the complex, its operating temperature and efficiency to produce electricity from metal hydrides partially substituted for fluorine. Secondly, an increase in thermal stability means that as the operating temperature of metal hydrides depends on the enthalpy of H₂ absorption, a metal hydride with a higher ΔH can operate at higher temperatures and lower pressures. As a consequence, less quantity of metal hydride will be required (and therefore less hydrogen) to produce the same quantity of heat energy. As a result, the cost to store hydrogen (until it is required to generate heat) will be decreased [25]. Thirdly, the overall cost of the MH system is reduced as the metal fluoride raw material is cheaper and so dilution with the more expensive MH means that less MH is needed in terms of KJ of energy stored [35].

Maeland and Lahar used this analogy as a guide to synthesise new MH-ABH₃ type materials based on their known fluoride structure [68]. They also investigated the solid solution behaviour of the halide-fluoride system. Examples of these are BaLiH₃/BaLiF₃, SrLiH₃/SrLiF₃, and KMgH₃/KMgF₃. As such, Sheppard *et al.* [35] have shown that one method to increase the operating temperature of a MH is replacing hydrogen by fluorine, as this stabilises the corresponding metal hydrides. For this reason, these materials have been proposed for high-temperature thermal storage applications.

Humphries *et al.* and Sheppard *et al.* also used this analogy to synthesise the NaH/NaF system [46] and the NaMgH₂F system [39], respectively.

For the NaH/NaF system Humphries *et al.* investigated the solid-state solutions of NaH_xF_{1-x} ($x = 1, 0.95, 0.85, 0.5$), and the results were that fluorine substitution increases the NaH desorption temperature. For example the maximum H₂ release rate for NaH_{0.5}F_{0.5} was 443 °C versus 408 °C for pure NaH. Another discovery is that NaH_{0.5}F_{0.5} has a lower enthalpy and entropy than the pure NaH ($\Delta H_{des} = 106 \pm 5 \text{ kJ mol}^{-1} \text{ H}_2$ and $\Delta S_{des} = 143 \pm 5 \text{ JK}^{-1} \text{ mol}^{-1} \text{ H}_2$, while for pure NaH, $\Delta H_{des} = 117 \text{ kJ mol}^{-1} \text{ H}_2$, and $\Delta S_{des} = 167 \text{ JK}^{-1} \text{ mol}^{-1} \text{ H}_2$) meaning that the equilibrium temperature at which decomposition of the sample occurs is higher than NaH. Indeed, fluorine substitution into NaH makes these materials more reversible [46]. In the case of the NaMgH₂F system, it was proven that a more stable structure was formed with partial fluorine substitution into NaMgH₃ obtaining NaMgH₂F due to its high enthalpy ($\Delta H_{des} = 96.8 \text{ kJ mol}^{-1} \text{ H}_2$ vs NaMgH₃ $\Delta H_{des} = 86.6 \text{ kJ mol}^{-1} \text{ H}_2$) of hydrogen

absorption/desorption, as such it can be potentially used as HTMH for hydrogen thermal storage. The fluorine substitution increases the minimum operating temperature and as a consequence the amount of hydrogen that needs to be stored in the LTMH decreases [39].

Due to the fluorine substitution of hydrogen in a material, it has been found to generate changes in the kinetics of hydrogen absorption/desorption of the compounds by changing the operating temperature of the compounds. These changes make these materials to be considered capable of being used in technological applications because of their heat storage property. Also, because these materials can react reversibly with hydrogen, absorbing heat to release hydrogen (endothermic) and releasing heat (exothermic) when they absorb hydrogen gas, this cyclic property makes these materials interesting energy storages.

1.8. Thesis outline

One of the objectives for developing thermal energy storage (TES) materials is to improve efficiency and reduce the cost of current concentrating solar power plants. For this reason, the aim of this thesis is to develop and produce a stable single-phase material based on the concept of fluorine substitution into metal hydrides for thermal energy storage applications. This will be conducted by combining metal fluorides and metal hydrides, such as $Mg(H_xF_{1-x})_2$, synthesised from MgH_2 and MgF_2 , in order to study their hydrogen storage characteristics.

Thermodynamic properties for the system, plus gravimetric energy storage capacity and cost of the raw material of the HTMH are important to use the material as a storage system. It has been shown that the hydrogen absorption/desorption in a reversible reaction has a significant impact on cost [39]. However, the larger cost for an HTMH/LTMH system is mainly due to the LTMH, equating to more than 50% of the total TES system cost.

A summary introduction to the chapters and their contents are presented below. This thesis project is divided into the following steps and will be presented in this document as:

- Chapter 1: Introduction
- Chapter 2: Experimentation - Characterisation techniques

A summary of the techniques and methodologies applied to the synthesis and characterisation of the fluorine substitution into metal hydrides.

The different techniques include ball-milling of reagents, *in situ* and *ex situ* X-ray diffraction (XRD) analysis of each sample to determine the phases and obtain their proportions. For each candidate mixture, measurement of their hydrogen sorption properties such as thermodynamics, pressure-composition-isotherms (PCI), temperature programmed desorption (TPD), differential scanning calorimetry (DSC), and thermal gravimetric analysis (TGA) are presented.

- Chapter 3: The $Mg(H_{0.85}F_{0.15})_2$ system

This chapter is a peer reviewed article that studied the $\text{Mg}(\text{H}_{0.85}\text{F}_{0.15})_2$ system. It has the potential for sustainability, reversible and low-cost, and its cycling capacity makes this system interesting for HTMH applications.

- Chapter 4: Fluorine Substitution in Magnesium Hydride as a Tool for Thermodynamic Control

This chapter is based on a peer reviewed article in which it is demonstrated that the substitution of hydrogen by fluorine in MgH_2 permits a relationship between the amount of F substituted with an increment in Mg–H bond strength and thermal stability, improving the viability of Mg–H–F as potential TES materials. This is validated with inelastic neutron spectroscopy, powder X-ray diffraction, and thermal conductivity measurements, with the results being verified by density functional theory calculations.

- Chapter 5: The NaMgHF_2 system

In this chapter, the crystallographic studies and thermodynamics properties are measured for $\text{NaMg}(\text{H}_{1-x}\text{F}_x)_3$ system and it is found that NaMgHF_2 has attractive thermodynamics properties, making it a potential candidate as a HTMH.

1.9. References

- [1] D. Abbott. Hydrogen Without Tears: Addressing the Global Energy Crisis via a Solar to Hydrogen Pathway. Proceedings of the IEEE 97 (2009) 1931 - 4.
- [2] D. Abbott. Keeping the Energy Debate Clean: How Do We Supply the World's Energy Needs? Proceedings of the IEEE. 98 (2010) 42-66.
- [3] International Energy Agency, Global Energy & CO₂ Status Report 2017, <https://www.connaissancedesenergies.org/sites/default/files/pdf-actualites/geco2017.pdf>; 2017 [accessed 04-10-2023].
- [4] I.E. Agency. International Energy Agency, <https://www.iea.org>; 2020 [accessed 04-10-2023].
- [5] I.E. Agency. Short-term Energy Outlook, <https://www.eia.gov/outlooks/steo/> Short-term Energy Outlook, May 2020.; 2020 [accessed 4-10-2023].
- [6] Y. Chu, P. Meisen. Review and comparison of different solar energy technologies. Global Energy Network Institute (GENI), San Diego, CA. (2011).
- [7] physics world, Sunny superpower: solar cells close in on 50% efficiency, <https://physicsworld.com/a/sunny-superpower-solar-cells-close-in-on-50-efficiency/>; 2021 [accessed 04/10/2023].
- [8] M. Fellet, C.E. Buckley, M. Paskevicius, D.A. Sheppard. Research on metal hydrides revived for next-generation solutions to renewable energy storage. Mrs Bulletin. 38 (2013) 1012-3.
- [9] D.N. Harries, M. Paskevicius, D.A. Sheppard, T.E.C. Price, C.E. Buckley. Concentrating Solar Thermal Heat Storage Using Metal Hydrides. Proceedings of the IEEE. 100 (2012) 539-49.
- [10] T.D. Humphries, M. Paskevicius, A. Alamri, C.E. Buckley. Thermodynamic destabilization of SrH₂ using Al for the next generation of high temperature thermal batteries. Journal of Alloys and Compounds. 894 (2022) 162404.
- [11] K.T. Møller, A. Ibrahim, C.E. Buckley, M. Paskevicius. Inexpensive thermochemical energy storage utilising additive enhanced limestone. Journal of Materials Chemistry A. 8 (2020) 9646-53.
- [12] M. Felderhoff, R. Urbanczyk, S. Peil. Thermochemical heat storage for high temperature applications—a review. Green. 3 (2013) 113-23.
- [13] M.M. Farid, A.M. Khudhair, S.A.K. Razack, S. Al-Hallaj. A review on phase change energy storage: materials and applications. Energy Conversion and Management. 45 (2004) 1597-615.
- [14] H. Sugo, E. Kisi, D. Cuskelly. Miscibility gap alloys with inverse microstructures and high thermal conductivity for high energy density thermal storage applications. Applied Thermal Engineering. 51 (2013) 1345-50.
- [15] A.C. Griffond, M.V. Sofianos, D.A. Sheppard, T.D. Humphries, A.-L. Sargent, M. Dornheim, K.-F. Aguey-Zinsou, C.E. Buckley. High-temperature thermochemical energy storage using metal hydrides: Destabilisation of calcium hydride with silicon. Journal of Alloys and Compounds. 858 (2021) 158229.
- [16] M. Paskevicius, D.A. Sheppard, C.E. Buckley. Thermodynamic Changes in Mechanochemically Synthesized Magnesium Hydride Nanoparticles. Journal of the American Chemical Society. 132 (2010) 5077-83.
- [17] S. Balakrishnan, M.V. Sofianos, T.D. Humphries, M. Paskevicius, C.E. Buckley. Thermochemical energy storage performance of zinc destabilized calcium hydride at high-temperatures. Physical Chemistry Chemical Physics. 22 (2020) 25780-8.
- [18] T.D. Humphries, K.T. Møller, W.D. Rickard, M.V. Sofianos, S. Liu, C.E. Buckley, M. Paskevicius. Dolomite: A low cost thermochemical energy storage material. Journal of Materials Chemistry A. 7 (2019) 1206-15.
- [19] SunShot Vision Study, Chapter 5: Concentrating Solar Power Technologies, Cost, and Performance. US Department of Energy 2012.
- [20] H. Noticias. La central termosolar Astexol-2 de Dioxipe Solar funcionará en 2012, <http://helionoticias.es/la-central-termsolar-astexol-2-de-dioxipe-solar-funcionara-en-2012/>; 2012 [accessed 4-10-2023].
- [21] solar plant <https://www.reutersevents.com/renewables/csp-today/construction-begins-solar-thermoelectric-plant-astexol-2-developed-dioxipe-solar-badajoz>; 2021 [accessed 04-10-2023].

- [22] I.E. Agency. Technology Roadmap Concentrating Solar Power. (2010).
- [23] K. Reddy, V. Mudgal, T. Mallick. Review of latent heat thermal energy storage for improved material stability and effective load management. *Journal of Energy Storage*. 15 (2018) 205-27.
- [24] Y. Sun, M. McCarthy, Y.I. Cho, P. Boettcher, H. Hu, B. Shi, Q. Xie. Systems and methods of using phase change material in power plants. Google Patents 2016.
- [25] D.A. Sheppard, M. Paskevicius, T.D. Humphries, M. Felderhoff, G. Capurso, J. Bellosta von Colbe, M. Dornheim, T. Klassen, P.A. Ward, J.A. Teprovich, C. Corgnale, R. Zidan, D.M. Grant, C.E. Buckley. Metal hydrides for concentrating solar thermal power energy storage. *Applied Physics A*. 122 (2016).
- [26] K. Manickam, P. Mistry, G. Walker, D. Grant, C.E. Buckley, T.D. Humphries, M. Paskevicius, T. Jensen, R. Albert, K. Peinecke. Future perspectives of thermal energy storage with metal hydrides. *International Journal of Hydrogen Energy*. 44 (2019) 7738-45.
- [27] K. Kubo, Y. Kawaharazaki, H. Itoh. Development of large MH tank system for renewable energy storage. *International Journal of Hydrogen Energy*. 42 (2017) 22475-9.
- [28] J. Andersson, S. Grönkvist. Large-scale storage of hydrogen. *International Journal of Hydrogen Energy*. 44 (2019) 11901-19.
- [29] A. Zuttel. Hydrogen storage methods. *Naturwissenschaften*. 91 (2004) 157-72.
- [30] A. Chaise, P. De Rango, P. Marty, D. Fruchart. Experimental and numerical study of a magnesium hydride tank. *International Journal of Hydrogen Energy*. 35 (2010) 6311-22.
- [31] A. Maddalena, M. Petris, P. Palade, S. Sartori, G. Principi, E. Settimo, B. Molinas, S.L. Russo. Study of Mg-based materials to be used in a functional solid state hydrogen reservoir for vehicular applications. *International Journal of Hydrogen Energy*. 31 (2006) 2097-103.
- [32] M. Verga, F. Armanasco, C. Guardamagna, C. Valli, A. Bianchin, F. Agresti, S.L. Russo, A. Maddalena, G. Principi. Scaling up effects of Mg hydride in a temperature and pressure-controlled hydrogen storage device. *International Journal of Hydrogen Energy*. 34 (2009) 4602-10.
- [33] C.E. Messer. Hydrides versus Fluorides : Structural Comparisons. *Journal of Solid State Chemistry*. 2 (1970) 144-55.
- [34] X. Qu, Y. Li, P. Li, Q. Wan, F. Zhai. The development of metal hydrides using as concentrating solar thermal storage materials. *Frontiers of Materials Science*. 9 (2015) 317-31.
- [35] D.A. Sheppard, T.D. Humphries, C.E. Buckley. What is old is new again. *Materials Today*. 18 (2015) 414-5.
- [36] M. Felderhoff, B. Bogdanovic. High temperature metal hydrides as heat storage materials for solar and related applications. *Int J Mol Sci*. 10 (2009) 325-44.
- [37] K. Yvon, B. Berthelville. Magnesium based ternary metal hydrides containing alkali and alkaline-earth elements. *Journal of Alloys and Compounds*. 425 (2006) 101-8.
- [38] B. Bogdanovic, B. Spliethoff, A. Ritter. The Magnesium Hydride System for Heat-Storage and Cooling. *ZEITSCHRIFT FÜR PHYSIKALISCHE CHEMIE NEUE FOLGE*. 164 (1989) 1497-508.
- [39] D.A. Sheppard, C. Corgnale, B. Hardy, T. Motyka, R. Zidan, M. Paskevicius, C.E. Buckley. Hydriding characteristics of NaMgH₂F with preliminary technical and cost evaluation of magnesium-based metal hydride materials for concentrating solar power thermal storage. *RSC Advances*. 4 (2014) 26552-62.
- [40] S. Deledda, A. Borissova, C. Poinson, W.J. Botta, M. Dornheim, T. Klassen. H-sorption in MgH₂ nanocomposites containing Fe or Ni with fluorine. *Journal of Alloys and Compounds*. 404 (2005) 409-12.
- [41] S.A. Pighin, G. Urretavizcaya, F.J. Castro. Study of MgH₂ + NbF₅ mixtures: Formation of MgH₂-xFx solid solutions and interaction with hydrogen. *International Journal of Hydrogen Energy*. 40 (2015) 4585-96.
- [42] Q. Lai, M. Paskevicius, D.A. Sheppard, C.E. Buckley, A.W. Thornton, M.R. Hill, Q. Gu, J. Mao, Z. Huang, H.K. Liu. Hydrogen storage materials for mobile and stationary applications: current state of the art. *Chemsuschem*. 8 (2015) 2789-825.
- [43] T. Gamo, Y. Moriwaki, N. Yanagihara, T. Yamashita, T. Iwaki. Formation and properties of titanium-manganese alloy hydrides. *International Journal of Hydrogen Energy*. 10 (1985) 39-47.
- [44] L.-P. Ma, P. Wang, H.-M. Cheng. Hydrogen sorption kinetics of MgH₂ catalyzed with titanium compounds. *International Journal of Hydrogen Energy*. 35 (2010) 3046-50.

- [45] M.S. Tortoza, T.D. Humphries, D.A. Sheppard, M. Paskevicius, M.R. Rowles, M.V. Sofianos, K.F. Aguey-Zinsou, C.E. Buckley. Thermodynamics and performance of the Mg-H-F system for thermochemical energy storage applications. *Physical Chemistry Chemical Physics*. 20 (2018) 2274-83.
- [46] T.D. Humphries, D.A. Sheppard, M.R. Rowles, M.V. Sofianos, C.E. Buckley. Fluoride substitution in sodium hydride for thermal energy storage applications. *Journal of Materials Chemistry A*. 4 (2016) 12170-8.
- [47] M. Adams, C.E. Buckley, M. Busch, R. Bunzel, M. Felderhoff, T.W. Heo, T. Humphries, T.R. Jensen, J. Klug, K.-H. Klug. Hydride-based thermal energy storage. *Progress in Energy*. 4 (2022) 032008.
- [48] A. Borgschulte, L. Schlapbach, A. Züttel. *Hydrogen as a future energy carrier*. Wiley-VCH Verlag 2008.
- [49] G. Walker. *Multicomponent hydrogen storage systems*. *Solid-State Hydrogen Storage*. Elsevier 2008. pp. 478-99.
- [50] M. Dornheim, N. Eigen, G. Barkhordarian, T. Klassen, R. Bormann. Tailoring hydrogen storage materials towards application. *Advanced Engineering Materials*. 8 (2006) 377-85.
- [51] W. Grochala, P.P. Edwards. Thermal decomposition of the non-interstitial hydrides for the storage and production of hydrogen. *Chemical Reviews*. 104 (2004) 1283-316.
- [52] S.-i. Orimo, Y. Nakamori, J.R. Eliseo, A. Züttel, C.M. Jensen. Complex hydrides for hydrogen storage. *Chemical Reviews*. 107 (2007) 4111-32.
- [53] B. Sakintuna, F. Lamari-Darkrim, M. Hirscher. Metal hydride materials for solid hydrogen storage: a review. *International Journal of Hydrogen Energy*. 32 (2007) 1121-40.
- [54] A. Züttel. Materials for hydrogen storage. *Materials Today*. 6 (2003) 24-33.
- [55] S. Ono, K. Nomura, E. Akiba, H. Uruno. Phase transformations of the LaNi₅-H₂ system. *Journal of the Less Common Metals*. 113 (1985) 113-7.
- [56] McPhy Energy, <https://mcphy.com/en/>; [accessed 04/10/2023].
- [57] W.E. Wentworth, E. Chen. Simple thermal decomposition reactions for storage of solar thermal energy. *Solar Energy*. 18 (1976) 205-14.
- [58] A.-L. Chaudhary, G. Li, M. Matsuo, S.-i. Orimo, S. Deledda, M.H. Sørby, B.C. Hauback, C. Pistidda, T. Klassen, M. Dornheim. Simultaneous desorption behavior of M borohydrides and Mg₂FeH₆ reactive hydride composites (M= Mg, then Li, Na, K, Ca). *Applied Physics Letters*. 107 (2015) 073905.
- [59] S.A. Pighin, G. Urretavizcaya, F.J. Castro. Reversible hydrogen storage in Mg(H_xF_{1-x})₂ solid solutions. *Journal of Alloys and Compounds*. 708 (2017) 108-14.
- [60] I.P. Jain, C. Lal, A. Jain. Hydrogen storage in Mg: A most promising material. *International Journal of Hydrogen Energy*. 35 (2010) 5133-44.
- [61] D.A. Sheppard, T.D. Humphries, C.E. Buckley. Sodium-based hydrides for thermal energy applications. *Applied Physics A*. 122 (2016) 406.
- [62] P. Jain, V. Dixit, A. Jain, O. Srivastava, J. Huot. Effect of Magnesium Fluoride on Hydrogenation Properties of Magnesium Hydride. *ENERGIES*. 8 (2015) 12546-56.
- [63] B. Bogdanovic, H. Hofmann, A. Neuy, A. Reiser, K. Schlichte, B. Spliethoff, S. Wessel. Ni-doped versus undoped Mg-MgH₂ materials for high temperature heat or hydrogen storage. *Journal of Alloys and Compounds*. 292 (1999) 57-71.
- [64] V. Yartys, M. Lototskyy, E. Akiba, R. Albert, V. Antonov, J. Ares, M. Baricco, N. Bourgeois, C. Buckley, J.B. von Colbe. Magnesium based materials for hydrogen based energy storage: Past, present and future. *International Journal of Hydrogen Energy*. 44 (2019) 7809-59.
- [65] M. Pitt, M. Paskevicius, C. Webb, D. Sheppard, C. Buckley, E.M. Gray. The synthesis of nanoscopic Ti based alloys and their effects on the MgH₂ system compared with the MgH₂+ 0.01 Nb₂O₅ benchmark. *International Journal of Hydrogen Energy*. 37 (2012) 4227-37.
- [66] G. Liu, Y. Wang, C. Xu, F. Qiu, C. An, L. Li, L. Jiao, H. Yuan. Excellent catalytic effects of highly crumpled graphene nanosheets on hydrogenation/dehydrogenation of magnesium hydride. *Nanoscale*. 5 (2013) 1074-81.
- [67] D. Khan, S. Panda, Z. Ma, W. Ding, J. Zou. Formation and hydrogen storage behavior of nanostructured Mg₂FeH₆ in a compressed 2MgH₂-Fe composite. *International Journal of Hydrogen Energy*. 45 (2020) 21676-86.

- [68] B. Bogdanović, A. Reiser, K. Schlichte, B. Spliethoff, B. Tesche. Thermodynamics and dynamics of the Mg–Fe–H system and its potential for thermochemical thermal energy storage. *Journal of Alloys and Compounds*. 345 (2002) 77-89.
- [69] R.D. Shannon. Revised effective ionic radii and systematic studies of interatomic distances in halides and chalcogenides. *Acta crystallographica section A: crystal physics, diffraction, theoretical and general crystallography*. 32 (1976) 751-67.
- [70] A.J. Maeland, W.D. Lahar. The Hydride-Fluoride Analogy. *ZEITSCHRIFT FUR PHYSIKALISCHE CHEMIE-INTERNATIONAL JOURNAL OF RESEARCH IN PHYSICAL CHEMISTRY & CHEMICAL PHYSICS*. 179 (1993) 181-5.
- [71] C.E. Messer, J. Mellor. The system lithium hydride—Lithium fluoride. *The Journal of Physical Chemistry*. 64 (1960) 503-5.
- [72] E. Majzoub, J. Herberg, R. Stumpf, S. Spangler, R. Maxwell. XRD and NMR investigation of Ti-compound formation in solution-doping of sodium aluminum hydrides: Solubility of Ti in NaAlH₄ crystals grown in THF. *Journal of Alloys and Compounds*. 394 (2005) 265-70.
- [73] N.N. Greenwood, A. Earnshaw. *Chemistry of the Elements*. Elsevier 2012.
- [74] J. Graetz, J. Reilly, V. Yartys, J. Maehlen, B. Bulychev, V. Antonov, B. Tarasov, I. Gabis. Aluminum hydride as a hydrogen and energy storage material: past, present and future. *Journal of Alloys and Compounds*. 509 (2011) S517-S28.
- [75] D. Chateigner, X. Chen, M. Ciriotti, R. Downs, S. Gražulis, W. Kaminsky, A. Le Bail, L. Lutterotti, Y. Matsushita, A. Merkys. *Crystallography open database*, 2007 [accessed 20/06/24].
- [76] J.-F. Brice, M. Perrin, R. Leveque. Hydrurofluorures ioniques MF₂– xH_x (M= Sr, Ba): Synthèse et étude structurale par diffraction des neutrons. *Journal of Solid State Chemistry*. 30 (1979) 183-8.
- [77] J.-F. Brice, A. Courtois, J. Aubry. Preparation de la solution solide hydrurofluoree CaF₂– xH_x (0 < x ≤ 1, 24) etude structurale par diffraction des rayons X et par diffraction des neutrons. *Journal of Solid State Chemistry*. 24 (1978) 381-7.

2. Experimental and Characterisation Techniques

This chapter provides an introduction to the experimental techniques used in this thesis. It also includes the equipment and devices used in the laboratory of the Hydrogen Storage Research Group (HSRG) at Curtin University.

- 2 Argon Gloveboxes MBraun, Germany (less than 1 ppm H₂O and O₂) with vacuum pumps and Argon gas with 99.997% purity in order to maintain an inert atmosphere for manipulation of air sensitive materials.
- 3 manual Hydrogen rigs with 99.999% purity each one connected by a computer. They contain a reference volume that is connected to a manifold with multiple valves, forming a closed system, named a Sieverts' apparatus. This system is connected to a supply of hydrogen gas and at the other end to a reactor containing the sample cell. One of the rigs is for high pressure (600 bar) rig. The main purpose of this equipment is to measure the hydrogen uptake and release from a material.
- 6 tube furnaces with operating temperatures of up to 1100 °C.
- 2 ball milling machines: a Turbula T2C shaker-mixer machine with stainless-steel milling media, up to 500 rpm, and an Across International Planetary ball mill (PQ-N04) with canisters and balls of 304 and 316 stainless steel, respectively. The volume of the canisters were 50 ml and ball diameter size 8 and 6 mm.

2.1. Synthesis

All manipulations of chemicals were undertaken in an argon atmosphere using a Mbraun Unilab glovebox to prevent air exposure and to minimise oxygen (O₂ < 1 ppm) and water (H₂O < 1 ppm) contamination.

2.1.1. Sample Preparation

The reagents used for sample preparation were either obtained commercially or synthesised at Curtin University. Details on the chemical suppliers, purity, and synthesis method of each system are described below:

- MgH₂ and MgF₂ (Sigma-Aldrich, > 99.99 %).
- MgH₂ powder (95 wt% purity from Rietveld refinement) was first synthesised by annealing Mg powder (Aldrich, > 99 %) at 400 °C under 30 bar hydrogen pressure for 18 hours. The partially hydrogenated Mg was then ball-milled (BM) for 3 hours with a ball-to-powder mass ratio of 10:1 in a Shaker Mill (Turbula T2C shaker-mixer) and annealed once again under identical conditions (400 °C, 30 bar H₂, 18 h).
- NaH (95%, Sigma-Aldrich) and NaF (99.99%, Sigma-Aldrich).

For chapters 3 and 4, MgH₂ and MgF₂ were used as reagent materials. In the case of chapter 5, the reagent materials used were NaH and MgF₂.

2.1.2. Planetary Ball Milling

Ball milling or mechanochemical milling is a technique that allows the synthesis of materials without the use of solvents or additional heat. Canisters (typically stainless steel) are filled with reagents and balls (typically stainless steel), then the machine, through centrifugal forces (circular movements), provokes friction between the powder and balls, stressing the powders. This allows the powders to react chemically forming new compounds and also to form solid solutions [1] or in other cases there is no reaction and the powder is just ground into smaller particles and/or mixed homogeneously. In this thesis, mechanochemical synthesis of materials was achieved by mixing the starting materials in a PQ-N04 planetary ball mill (Across International). Ball milling times were 3, 10, or 40 hours in a 316 stainless-steel canister sealed in an argon atmosphere with 316 stainless-steel balls 8 mm and 6 mm in diameter. Rotational settings could be set to either uni-directional or bi-directional. Materials synthesized in this thesis used the following methods:

Chapter 3 and 4: The materials used in these chapters were MgH_2 and MgF_2 powders. The samples were ball milled unidirectionally for 10 hours, the machine was operated at 33 Hz, 450 rpm and the ball to powder ratio (BTP) was 50:1. Between 1 and 2 grams of material were typically ball milled in each 50 mL canister.

Chapter 5: Samples powders of NaH and MgF_2 were ball milled for 3 hours in bi-directional mode with fifteen-minute intervals (5 minutes' pause, zero delays between directions) and were operated at 33 Hz (450 rpm with a BTP ratio of 30:1) with 1 g of material in each 50 mL canister.

2.2 X-ray Diffraction

This is a non-destructive analytical technique that reveals information about the crystal structure, chemical composition, and physical properties of materials and allows phase identification of unknown samples.

The data collected by powder X-ray Diffraction (XRD) can be illustrated as Bragg peaks (reflections) that have a particular intensity at specific angles (2θ) and are characteristic for every individual material. In other words, the XRD pattern for each crystalline material is unique, and therefore the position and the intensity of the reflections can be used to identify unknown crystalline samples. As a consequence, identification of phases can be achieved by comparing the XRD pattern with the patterns from a reference database. In practice, peaks were initially identified using Diffract EVA[®] which uses the database from the International Centre for Diffraction Data (ICDD) (PDF4+[®] 2016 and 2018 edition) by comparing the measured diffraction peaks with the diffraction pattern in the database. The position of the diffraction peaks directly depends on the atomic structure of a compound and the wavelength of X-rays used [2].

The scattering of X-rays by atoms results in constructive interference at specific angles depending on the arrangement of atoms in the sample. Bragg's Law (Equation 2.1) describes the reflections of the atomic planes of the crystal lattice from the diffraction and interference of X-rays.

$$2d \sin \theta = n\lambda \quad (2.1)$$

where d = interplanar spacing hkl (hkl = miller indices), 2θ = angle between the incident (A and A') and reflected (C and C') beam, n = an integer (normally $n = 1$) and λ = wavelength of the incident X-ray beam. Figure 2.1 shows a graphical representation of Bragg's Law.

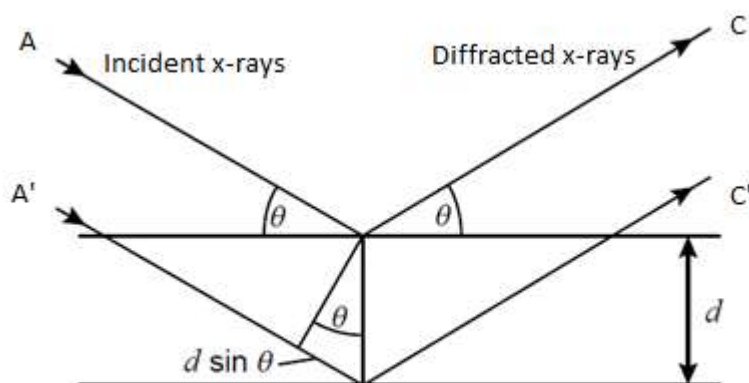


Figure 2.1. X-ray diffraction as described by Bragg's Law [3].

2.2.1 Ex situ X-Ray Diffraction (XRD)

Most of the samples and starting materials were initially investigated by lab based (*ex situ*) powder XRD to undertake quantitative phase analysis, identify reaction products, estimate the crystallinity of the samples and test purity of reagents. These measurements were performed using a Bruker® D8 Advance diffractometer (Curtin University, Australia) using Cu-K α_{1+2} radiation ($\lambda = 1.5418 \text{ \AA}$) equipped with a LynxEye detector. The diffractometer was configured in Bragg-Brentano geometry with a primary and secondary goniometer circle radius at 250 mm. The 2θ angular range of the LynxEye detector window size was 3 mm with a fixed divergence slit of 0.3° . The tube focal length was 12 mm that scans a 25 mm diameter of irradiated sample. The receiving slit length was 17 mm with primary and secondary Soller slit angles of 2.5° . Acquisition of data was subsequently restricted to $2\theta = 20 - 80^\circ$ (2θ), with a $\Delta 2\theta = 0.02^\circ$ and 2 s/step scanning rate with a sample rotation of 60 rpm and a total collection time of 60 minutes. The sample holders were made of polymethyl methacrylate (PMMA) and were sealed to prevent any oxygen/moisture contamination during data collection. The PMMA resulted in a broad hump in XRD patterns centred at $2\theta \approx 20^\circ$. Diffraction patterns were quantitatively analysed using the Rietveld method with TOPAS software (Bruker-AXS).

2.2.2 *In situ* synchrotron X-ray Diffraction (SR-XRD)

In situ synchrotron powder X-ray diffraction (SR-XRD) was performed at the Australian Synchrotron in Melbourne, Australia [4][4][4][75] [3, 4, 6]. Synchrotron X-ray diffraction is used to determine and quantify phase analysis of samples. SR-XRD data can be collected in 'real' time allowing the possibility to observe and measure chemical processes at high temperatures as a function of time. Indeed, it can be used for fast and high-resolution data collection on small amounts of powder samples, surfaces, or thin sections. Some samples could suffer a phase change before the hydrogen desorption reaction occurs, resulting in valuable information. Furthermore, these phase change events can cause difficulties when using *ex situ* XRD due to phase segregation and inconsistent reaction products.

In preparation for SR-XRD, powders were densely packed into borosilicate capillaries (outer diameter 0.5 or 0.7 mm, wall thickness 0.01 mm (Charles Supper Company, Massachusetts, USA) with polyamide/graphite ferrules (Chromalytic Technology, Victoria, Australia) and connected to a gas manifold without exposure to air. The samples were kept under dynamic vacuum and heated with a hot air blower (Cyberstar, France) at a rate of 5 °C min⁻¹. One-dimensional SR-XRD patterns (monochromatic X-rays) were collected using a Mythen microstrip detector with an exposure time of 57 s. The capillary was oscillated 120° during exposure to improve powder averaging. The wavelength for each experiment undertaken in this thesis will be provided in the respective chapter. An initial heat ramp was performed on a temperature standard (sodium chloride/silver). To calibrate the actual temperature at each frame, the change in lattice parameter was measured in correlation to the temperature (thermal expansion) recorded from SR-XRD data [5]. The temperature was recorded in 40 second intervals using a script command that was manually matched with each SR-XRD scan frame (using the recorded time stamps). Diffraction patterns were quantitatively analysed using the Rietveld method with TOPAS software (Bruker-AXS).

2.3 *Thermal Analysis*

In this thesis three thermal analysis techniques were used, Differential Scanning Calorimetry – Thermal Gravimetric Analysis and Temperature Program Desorption Mass Spectrometry each of which are described below.

Differential Scanning Calorimetry (DSC) is a thermal analysis technique used to investigate the thermodynamic properties of a material such as specific heat and enthalpy by measuring the heat flow to the sample material as a function of temperature [6].

Temperature variation in DSC is controlled by a computer and is typically linear. In this way, the specific heat as a function of temperature can be determined. Furthermore, the enthalpies of reactions and phase changes can be determined from the measurement.

In the context of hydrogen storage, DSC is primarily used to measure the desorption of hydrogen as the DSC equipment is not typically designed to handle the high pressures required for hydrogen absorption. The advantage of this technique is that other thermal events such as melting or crystal structure changes may be observed. A significant limitation for testing hydrogen storage using DSC is that there is no way to determine the amount of hydrogen desorbed by a sample, only the total enthalpy of a given reaction.

As with DSC measurements, the sample (solid or liquid) is weighed on a small crucible/sample pan. Typical sample pans are made of graphite, aluminium, alumina, silica, platinum, stainless steel, or inconel. The sample pan is selected based on material compatibility with the sample and products. Sample size (≈ 10 mg) should be kept to a minimum, but large enough to observe the necessary heat flows.

Thermal Gravimetric Analysis (TGA) instruments typically operate under vacuum or low-pressure flowing gas conditions. Mass loss (or gain) from a sample is then measured as a function of temperature. It is a gravimetric method, but it is necessary to point out a distinction, most gravimetric instruments generally operate under isothermal conditions with a controlled overpressure of gas. TGA is a thermal analysis technique often used in conjunction with DSC to determine the hydrogen storage properties of a sample. For the measurements conducted in this thesis, DSC-TGA were measured simultaneously on the same instrument. TGA is now traditionally used for the quantitative investigation of decomposition reactions. Samples are measured by placing the sample in an environment that is heated or cooled at a controlled rate and monitoring the weight change. The equipment necessary to perform TGA consists of an accurate balance, a programmable furnace, a reaction chamber and a data collection system. As the temperature inside the furnace and reaction chamber changes, the balance measures the variation in weight due to various chemical reactions including dehydrogenation. The microbalance used in a TGA is extremely accurate (± 20 μg). For this reason, TGA is one of the best methods to determine hydrogen capacity in a material and can be measured from room temperature up to 1200 °C. A means to reduce the temperature gradients present within the sample is to impose slower heating rates (typical heating rates rarely exceed 10 K/min).

In this thesis, the TGA experiments were performed under an inert carrier gas, Argon (99.997% purity). The flow rates and type of gas will affect the apparent mass change. Consequently, buoyancy calibration needs to be conducted with an empty pan for a given gas composition, heating rate, and purge/sweep gas flow rate. Buoyancy calibrations need to be performed on a regular basis, ideally every time a sample is performed. The corrected mass change is constructed by subtracting the apparent mass change as a function of temperature from the sample under study. The experimentally corrected mass loss should be confirmed and be in good agreement with the calculated mass loss from the reaction stoichiometry.

Temperature-Programmed Desorption Mass Spectrometry (TPD-MS) is a technique that allows the detection of any gaseous species released from a material as a function of time and temperature. The sample

is kept under dynamic vacuum for the duration of the measurement. As the temperature increases, the material releases gas which is detected using a quadruple mass spectrometer (MS). The mass spectrometer is set to detect selected gases with different atomic mass, e.g. hydrogen, water, methane, etc., that are desorbed in each temperature range.

TPD measurements can be used to determine the kinetics and thermodynamic properties of a material, such as the onset temperature T_{onset} which is the temperature at which hydrogen desorption is first detected, and T_{max} which is the temperature at which the hydrogen desorption rate reaches its maximum. From these parameters, it is possible to quantitatively compare the hydrogen desorption kinetics between samples. Quantitative analysis requires accurate calibration of the MS against known flow rates. It is also important to understand that TPD or any dynamic type of measurement provides results that are a convolution of both thermodynamic and kinetic properties of the hydrogen storage material. The sorption profile reveals indirect information about the number of various desorption events. Furthermore, the peak shape can be used to determine the order of the desorption reaction.

Typically, the sample is loaded into a temperature-programmed heater contained in a vacuum chamber, as the temperature increase the gases start to be released and are evacuated through the vacuum line. A MS is connected to the evacuation line and analyses the relative composition of the desorbed gases and quantifies the amount of hydrogen desorbed by the sample. TPD systems can distinguish between hydrogen and other constituents in the gas stream.

The HSRG collaborates with Prof. Kondo-Francois Aguey-Zinsou at the University of New South Wales, Australia (UNSW). The collaboration allows for measurement of samples using simultaneous DSC, TGA and MS (DSC-TGA-MS, Mettler Toledo TGA/DSC 1 coupled with an Omnistar MS ($m/e = 2 - 100$)) inside an inert atmosphere Glovebox (argon gas). These measurements are included in Chapters 3 and 5 and were conducted using sample masses of ~ 10 mg at a heating rate of 10 °C/min up to 850 °C under an argon flow of 20 mL/min.

2.4 Sorption Analysis

2.4.1 The Sieverts' Method

The volumetric method of hydrogen storage measurement, also known as the manometric method, or the Sievert's method in honour of the German chemist of the same name [7], uses temperature-pressure-volume correlations to determine the hydrogen capacity and thermodynamic properties of a material. At Curtin University the HSRG have rigs as represented by the following image (Fig 2.2).

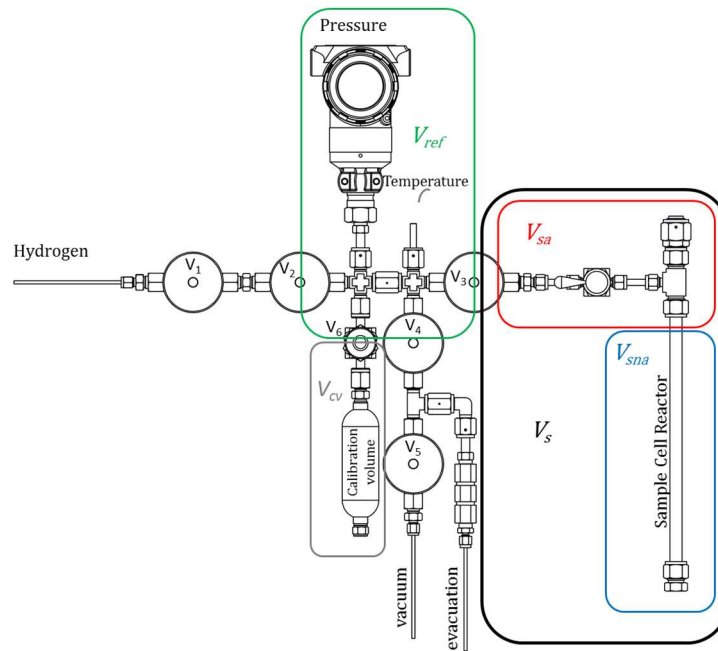


Figure 2.2. Schematic of the Sievert's apparatus rig at Curtin University [8]. V_1, V_2, V_3, V_4, V_5 and V_6 are valves : V_{ref} : reference volume: V_{sa} : ambient sample volume : V_{sna} : non-ambient sample volume, Sample Volume: V_s and calibration volume: V_{cv} .

The apparatus consists of a gas reservoir connected to a reactor (sample holder). The reference volume (reservoir) is calibrated and filled with a gas at a measured pressure. Because the volumetric method measures the number of moles of gas absorbed or desorbed during a reaction indirectly through temperature-pressure-volume correlations, the volumes of the reservoirs and sample holder (system) must be known in advance, therefore all the volumes are calibrated before an experiment. Once the reference volume is opened to the reactor side, the gas that is absorbed by the sample placed inside the reactor is calculated due to the pressure changes in the system, which allow for the calculation of the number of moles of gas in the system [7]. The thermocouple should always be positioned within close contact to the sample to measure an accurate value. The system volumes are carefully pre-calibrated, and the reservoir and sample holder are maintained at constant temperature (but not necessarily equal). By fixing volume and sample temperature, reservoir and sample holder pressures can be measured using pressure transducers to provide the number of moles of gas.

The ideal gas law is altered by a compressibility hydrogen factor (Z) to be used to calculate the pressure change [9]. (Equation 2.2).

$$n = \frac{P \cdot V}{Z \cdot R \cdot T} \quad (2.2)$$

Where n is the number of moles of gas, P is the pressure of the gas in a specific volume (Pa), V is the volume that the gas occupies (m^3), T is the temperature of the gas in Kelvin, R is the universal gas constant ($8.3145 \text{ J}\cdot\text{K}^{-1}\cdot\text{mol}^{-1}$) and Z is the compressibility factor.

The quantity of moles desorbed or absorbed during a step i is determined from the following equation (Equation 2.3):

$$n_{sor}^i = \frac{P_{ref}^i \cdot V_{ref}}{Z_{ref}^i \cdot R \cdot T_{ref}^i} + \frac{P_{sa}^i \cdot V_{sa}}{Z_{sa}^i \cdot R \cdot T_{sa}^i} + \frac{P_{sna}^i \cdot V_{sna}}{Z_{sna}^i \cdot R \cdot T_{sna}^i} \quad (2.3)$$

Where n_{sor}^i is the number of moles of gas desorbed or absorbed during each step, i , the subscript *ref* means reference, *sa* means sample ambient and *sna* means sample non-ambient.

The volume of the sample cell is measured empty and then the density and mass of the sample are used to calculate the sample volume and subtract that from the volume of the sample cell once this is heated (hot volume).

In Figure 2.2 the rig used for the measurements conducted in this thesis is represented. The rig consists of a reference volume (green frame), a digital pressure gauge (Rosemount 3051S) with a precision and accuracy of 14 mbar and a sample volume (black frame). The valves V_2 , V_3 , V_4 and V_6 (green frame) of the rig comprise the reference volume V_{ref} . The sample volume has 2 parts: one at ambient temperature named ambient sample volume V_{sa} (red frame) and the other part is the non-ambient sample volume V_{sna} , the reactor which contains the sample, which is heated by a furnace (blue frame). To measure, control and collect the temperature, a K type thermocouple is attached as close as possible to the reactor. The temperatures at V_{sa} and V_{ref} are measured by two 4 wire platinum resistance temperature detectors (RTD).

2.4.2 Pressure Composition Temperature Isotherms

Pressure-composition-temperature measurements (PCTs) together with Thermal Gravimetric Analysis (TGA) are one of the most used hydrogen storage measurement types (composition in this context is synonymous with the concentration of hydrogen in a sample) and allows the determination of thermodynamic properties of hydrogen absorption and desorption. A PCT measurement is a collection of data points that represents the pressure, concentration and temperature of a sample in thermodynamic equilibrium with its hydrogen atmosphere and relates the influence of the thermodynamic variables on concentration [7]. PCTs are also known as PCI (Pressure-Composition Isotherms) because they are taken at isothermal conditions, in order to minimize the number of free variables and to allow the relationship between concentration and pressure because it will be represented in a two-dimensional graphic named a van't Hoff plot.

For the PCT technique, the reactor which contains the sample, is positioned inside the furnace together with the thermocouple. Once the furnace is at the correct temperature it is maintained isothermal. The pressure gauge measures the pressure developed to measure any gas sorption. It is a step-by-step method for establishing the thermodynamic pressure conditions at a constant temperature of a sorption reaction [7]. If the sample releases hydrogen (desorb) the gas pressure should increase and when hydrogen absorption occurs the system pressure should decrease.

In the case of desorption measurements, the measurement starts at an overpressure to prevent premature hydrogen release. Once the sample is heated up and reaches isothermal temperature conditions, valve V_3 is opened and then the change in gas pressure is measured. After a pre-set time step that takes into account the sorption behaviour, V_3 is closed by a pre-set pressure step and then the pressure in the reference volume is decreased. While waiting for the pressure to reach equilibrium, V_3 is opened again to measure the pressure change. This process is repeated until the pressure drops below the equilibrium pressure, moment in which the metal hydride (sample) releases hydrogen. Since the step size of time and the pressure step rise have been properly established, this means that it is necessary to wait long enough so that kinetics are not a limiting factor, in other words achieving true equilibrium pressures is what removes any kinetics effects from the pressure measurements. The effect of temperature on hydrogen storage properties can be determined by comparing PCT isotherms at various temperatures. Because PCTs represent a sample in equilibrium, they can also be used to determine the thermodynamic properties of a hydrogen storage material by conducting various PCT measurements at different isothermal conditions, after which a van't Hoff plot can be created and, ultimately, determine reaction enthalpies and entropies. From eq. 2.4 and 2.5 (van't Hoff equation) the enthalpy $\Delta H_{reaction}$ and entropy $\Delta S_{reaction}$ of the chemical reaction can be computed [10].

$$\ln\left(\frac{P_{H_2}}{P_0}\right) = -\frac{\Delta H_{reaction}(P,T)}{R \cdot T} + \frac{\Delta S_{reaction}(P,T)}{R} \quad \text{Desorption} \quad (2.4)$$

$$\ln\left(\frac{P_{H_2}}{P_0}\right) = \frac{\Delta H_{reaction}(P,T)}{R \cdot T} - \frac{\Delta S_{reaction}(P,T)}{R} \quad \text{Absorption} \quad (2.5)$$

where $P_0 = 1 \text{ bar}$

To achieve accurate results, it is important to collect enough data points in each PCT isotherm, which will allow the construction of precise van't Hoff plots. Moreover, it is also necessary to identify plateau pressures and distinguish phase transitions. The van't Hoff plot shows the relationship between pressure and temperature and is often used as a simple way to compare the stability of hydrides.

2.4.2.1 Full Isotherm van't Hoff Measurements

As it was mentioned before (2.4.2), the classical method for determining the thermodynamics of hydride formation and decomposition is to make a series of PCT isotherm measurements at different temperatures (e.g. fig. 2.3). Then by plotting the natural log of the plateau pressures vs. $1/\text{sample temperature}$ to create a van't Hoff diagram (e.g. Fig. 2.4). A good example of this method is exemplified *Sheppard et al.*, who measured the PCT curves for sodium magnesium hydride and by using the measured equilibrium pressures and temperatures constructed a van't Hoff plot [11].

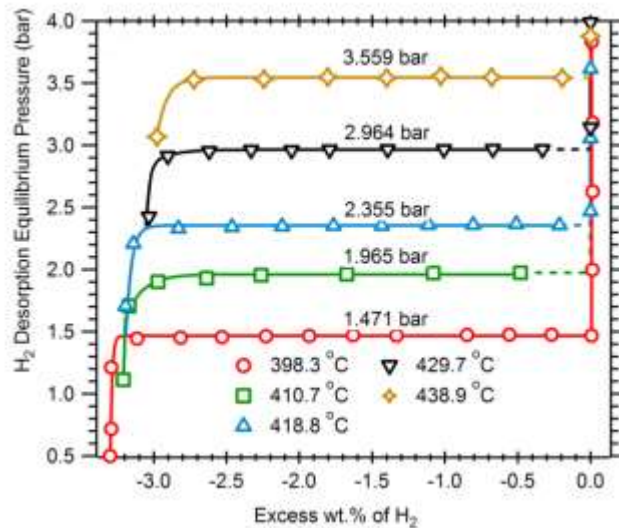


Figure 2.3. Hydrogen desorption pressure composition isotherms (PCT) for NaMgH_3 performed at temperatures between 398 and 439 °C [11].

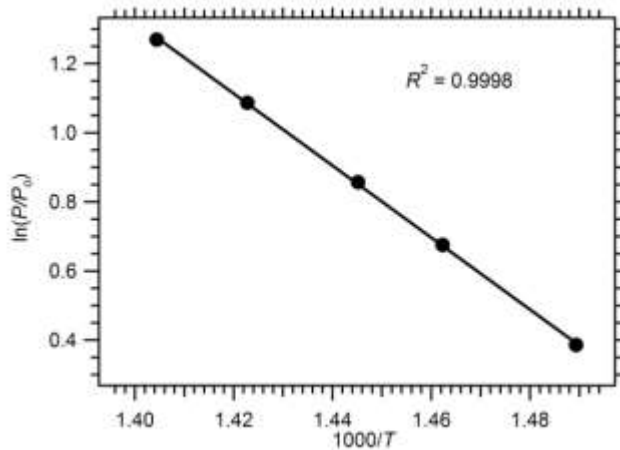


Figure 2.4. Van't Hoff diagram of hydrogen desorption equilibrium pressures and linear fit to the data [11, 12]. The data points plotted come from the centre point of the plateaus from Fig 2.3.

From the graph of figure 2.4 ΔH and ΔS can be determined by:

$$-\Delta H/R = \text{slope and } \Delta S/R = \text{intercept of linear fit}$$

Where R is the gas constant = 8.314 kJ/(mol H₂); $\Delta H = -(1.27-0.38)/(1.405-1.49) \times 8.314 = 86.6$ kJ/(mol H₂) and $\Delta S = 15.9 \times 8.314 = 132.2$ kJ/(mol H₂).

There are two factors that need to be taken into account when these measurements are carried out, one is the permeability of hydrogen through the stainless-steel walls of the reactor. At temperatures above 400 °C corrections in the weight percent of hydrogen release are required according to the permeability Φ of the reactor since a quantity of hydrogen may diffuse during the measurement. This problem is exacerbated as a function of temperature. The number of moles lost at each step can be calculated [13] as in (equation 2.6):

$$n(\text{H}_2)_{\Phi}^{\text{reactor calc.}} = \left(\frac{SA}{t}\right)_{\text{eff}} \cdot \Phi_0 \cdot e^{\left(\frac{-H_{\Phi}}{R \cdot T}\right)} \cdot f^{\frac{1}{2}} \cdot s \quad (2.6)$$

Where $n(\text{H}_2)_{\Phi}^{\text{reactor calc.}}$ = calculated moles of hydrogen that has permeated through the stainless steel reactor (mol of H₂), SA is the internal surface area of stainless steel exposed to gaseous hydrogen (m²), s is the measurement duration (s), Φ_0 is the temperature dependent permeability of hydrogen (mol H₂·m⁻¹·s⁻¹·MPa^{-1/2}), t is the thickness of stainless steel (m), f is the fugacity of hydrogen (MPa), H_{Φ} is the permeability activation energy (kJ·mol⁻¹), $\left(\frac{SA}{t}\right)_{\text{eff}}$ is a variable dependent on the geometry of the reactor. Due to the form of the reactor, it can be complicated to calculate this value, although this can be done experimentally by measuring the pressure drop of an empty reactor over a long period of time (Eq. 2.7):

$$\left(\frac{SA}{t}\right)_{\text{eff}} = \frac{n(\text{H}_2)_{\Phi}^{\text{SCR.}}}{\Phi \cdot f^{\frac{1}{2}} \cdot s} \quad (2.7)$$

The other factor is the solubility of hydrogen in the stainless steel. H₂ is absorbed into the reactor walls at each pressure and when the pressure is reduced part of the hydrogen is released through the walls and needs to be corrected for using the following equations, 2.8 and 2.9 [13].

$$C_l = K \cdot f^{1/2} \quad (2.8)$$

$$K = K^0 \cdot e^{\left(\frac{-\Delta H_S}{R \cdot T}\right)} \quad (2.9)$$

Where C_l is the equilibrium concentration of hydrogen dissolved in the metal lattice (mol·m⁻³), depending on the operating temperature and pressure (or fugacity), K is the solubility, which is independent of pressure, but dependent on temperature (mol H₂·m⁻³·MPa^{-1/2}), K^0 is the standard state solubility coefficient (mol H₂·m⁻³·MPa^{-1/2}).

$^3 \cdot \text{MPa}^{-1/2}$) and ΔH_s = enthalpy of formation of H-atoms bound in the metal ($\text{kJ} \cdot \text{mol}^{-1}$). To calculate the moles of H_2 released at each step due to the solubility from the reactor equation 2.10 is used:

$$n(\text{H}_2)_K^{SCR} = C_l^{final} \cdot V^{SCR} - C_l^{beginning} \cdot V^{reactor} \quad (2.10)$$

Unfortunately, the absolute interpretation of PCT data must be kept in perspective because it is difficult to make true equilibrium measurements due to long measurement times and permeation of hydrogen through stainless steel [14]. This is because as the pressure approaches true equilibrium, the driving force (or potential) becomes diminishingly small and therefore, kinetics become increasingly slower. In other words, it would take an infinitely long time to reach equilibrium. This is the reason why it is necessary to program these measurements with long step sizes, such as 3 hr or more.

A vital parameter for a hydrogen storage material is reversibility. The reversibility is the capacity of the hydrogen to be absorbed and desorbed from the sample several times. This capacity can be measured by cycling the sample in a Sieverts device. There are multiple ways to cycle the material, most commonly, by either cycling the pressure or by cycling the temperature. In this thesis the latter was used [15]. During this study the sample was cycled between two temperatures and then repeated several times, the lower temperature is the minimum operating temperature at the hydrogen equilibrium pressure of the material, and the maximum temperature is normally some tens degrees higher than the minimum operating temperature. With the increment in temperature, hydrogen starts to be desorbed from the sample until the maximum temperature is reached as long as the equilibrium pressure corresponding to the high temperature level is not reached. Once fully dehydrogenation is achieved the temperature is decreased and the sample starts to absorb the hydrogen that was released previously. The repetition of this process through the stages of hydrogen absorption and desorption several times is called cycling.

All hydrogen sorption measurements were performed by using computer-controlled Sieverts/volumetric apparatus. The digital pressure transducer (Rosemount 3051S) had a precision and accuracy of 14 mbar, whilst room temperature measurements were recorded using a 4-wire platinum resistance temperature detector (RTD). PCT measurements were monitored by a K-type thermocouple ($\pm 1.5 \text{ }^\circ\text{C}$). PCT curves were performed for: [Chapter 3](#) at 437, 444, 450, and 461 $^\circ\text{C}$. In addition, hydrogen absorption PCT measurements were carried out at $\approx 448.5 \text{ }^\circ\text{C}$ on the same apparatus. Hydrogen sorption cycles were conducted by heating a sample of $\text{Mg}(\text{H}_{0.85}\text{F}_{0.15})_2$ at $4 \text{ }^\circ\text{C}/\text{min}$ from room temperature to $425 \text{ }^\circ\text{C}$ followed by a 6 h isothermal period. The temperature was then ramped at $2 \text{ }^\circ\text{C}/\text{min}$ to $480 \text{ }^\circ\text{C}$ followed by another 6 h isothermal step; it is during this stage the first decomposition begins. The temperature was then cycled between $425 \text{ }^\circ\text{C}$ (hydrogen absorption) and $480 \text{ }^\circ\text{C}$ (hydrogen desorption) 6 times under a closed gas system pressure varying between 30 to 42 bar.

For [Chapter 5](#): PCT isotherm curves were measured at 514, 533, 543, and 554 °C. Hydrogen PCT sorption cycles (pressure cycling) were conducted by heating a dehydrogenated sample from room temperature to isothermal temperature with a heating ramp of 4 °C/min and kept isothermal during the entire measurement. The pressure was changed in ≈ 3 bar steps every 3 h from 17 to 0.2 bar during the desorption phase and doing the opposite in the absorption stage. The sample was cycled 4 times.

2.5 *Inelastic neutron scattering (INS)*

Inelastic neutron scattering (INS) is a potent method for studying the vibrational properties of materials and provides information on bonding and other properties [16]. INS is a spectroscopy method based on the energy analysis of neutrons after they have been scattered by a sample. A perceived energy exchange can be related to physical interaction of the respective atoms with their surroundings. An energy transfers of some millielectronvolts (meVs) typically arises from the vibrations of the atoms. Hence, the INS spectrum provides a density of phonon states weighted by the amplitude of movement and the incoherent neutron cross section. Since the incoherent scattering cross section of hydrogen is much larger than that of all other elements, INS is especially sensitive to hydrogen-based vibrations. The method is used extensively in condensed matter physics and solid-state chemistry, because the vibrational properties of matter define various physical properties, such as heat capacity [17]. INS can be used to classify chemical bonds both in the bulk and at the surface. The technique takes advantage of the slightly different behaviour between bound and free atoms during the scattering process and uses the discrepancy in energy and momentum transfer to calculate the vibrational states of the system. The advantage of INS is its independence from optical selection rules [18]. In addition, the advantage of INS compared to the related Raman scattering (i.e., inelastic photon scattering) and infrared spectroscopies (IR absorption and reflectivity) is its independence on optical selection rules. Moreover, phonons (lattice vibrations) in metals cannot readily be detected by IR techniques, and Raman scattering from metals is weak due to the screening of electromagnetic radiation by quasi-free electrons [19]. In contrast, neutrons do not interact with electrons and sample the entire Brillouin zone (different k-vector and momentum transfer), while Raman and IR are restricted to the zone centre (Γ -point), therefore, with INS one can exclusively obtain the full vibrational spectra of many metal hydrides [20, 21]. Inelastic neutron scattering (INS) data were collected using the Pelican cold-neutron time of-flight spectrometer located at the OPAL reactor Lucas Heights, Australia. This technique was applied in Chapter 5, samples were placed in a rectangular, flat plate, with aluminium sample cans. The sample cans were placed at an angle of 45° to the beam in a vacuum chamber at room temperature. The instrument was aligned for neutrons with a wavelength of 4.69 Å with a resolution at the elastic line of 135 μ eV. Vanadium was used as the standard (having the same geometry as the sample can).

2.6 References

- [1] S. Rosenkranz, S. Breitung-Faes, A. Kwade. Experimental investigations and modelling of the ball motion in planetary ball mills. *Powder Technology*. 212 (2011) 224-30.
- [2] M. Ermrich, D. Opper. XRD for the analyst. Getting acquainted with the principles Second Panalytical. (2013).
- [3] M. Ermrich, D. Opper. XRD for the analyst. PANalytical. (2013).
- [4] K.S. Wallwork, B.J. Kennedy, D. Wang. The high resolution powder diffraction beamline for the Australian Synchrotron. *Synchrotron Radiation Instrumentation: Ninth International Conference on Synchrotron Radiation Instrumentation*. AIP Publishing 2007. pp. 879-82.
- [5] B.R. Hansen, K.T. Møller, M. Paskevicius, A.-C. Dippel, P. Walter, C.J. Webb, et al. In situ X-ray diffraction environments for high-pressure reactions. *Journal of Applied Crystallography*. 48 (2015) 1234-41.
- [6] H. Bhadeshia. *Differential scanning calorimetry*. Materials Science & Metallurgy, University of Cambridge, London. (2002).
- [7] T. Blach, E.M. Gray. Sieverts apparatus and methodology for accurate determination of hydrogen uptake by light-atom hosts. *Journal of Alloys and Compounds*. 446 (2007) 692-7.
- [8] M. Paskevicius, D.A. Sheppard, C.E. Buckley. Thermodynamic Changes in Mechanochemically Synthesized Magnesium Hydride Nanoparticles. *Journal of the American Chemical Society*. 132 (2010) 5077-83.
- [9] L. Zhou, Y. Zhou. Determination of compressibility factor and fugacity coefficient of hydrogen in studies of adsorptive storage. *International Journal of Hydrogen Energy*. 26 (2001) 597-601.
- [10] T.G. Manivasagam, K. Kiraz, P.H. Notten. Electrochemical and optical properties of magnesium-alloy hydrides reviewed. *Crystals*. 2 (2012) 1410-33.
- [11] D.A. Sheppard, M. Paskevicius, C.E. Buckley. Thermodynamics of Hydrogen Desorption from NaMgH₃ and Its Application As a Solar Heat Storage Medium. *Chemistry of Materials*. 23 (2011) 4298-300.
- [12] M. Sharpe, W. Shmayda, K. Glance. Measurement of Palladium Hydride and Palladium Deuteride Isotherms Between 130 K and 393 K. *Fusion Science and Technology*. 76 (2020) 642-8.
- [13] C. San Marchi, B.P. Somerday, S.L. Robinson. Permeability, solubility and diffusivity of hydrogen isotopes in stainless steels at high gas pressures. *International Journal of Hydrogen Energy*. 32 (2007) 100-16.
- [14] D.A. Sheppard, M. Paskevicius, P. Javadian, I.J. Davies, C.E. Buckley. Methods for accurate high-temperature Sieverts-type hydrogen measurements of metal hydrides. *Journal of Alloys and Compounds*. 787 (2019) 1225-37.
- [15] T. Gamo, Y. Moriwaki, N. Yanagihara, T. Yamashita, T. Iwaki. Formation and properties of titanium-manganese alloy hydrides. *International Journal of Hydrogen Energy*. 10 (1985) 39-47.
- [16] P.C.H. Mitchell. *Vibrational spectroscopy with neutrons: with applications in chemistry, biology, materials science and catalysis*. World Scientific 2005.
- [17] R. Dovesi, A. Erba, R. Orlando, C.M. Zicovich-Wilson, B. Civalleri, L. Maschio, et al. Quantum-mechanical condensed matter simulations with CRYSTAL. *Wiley Interdisciplinary Reviews: Computational Molecular Science*. 8 (2018) e1360.
- [18] P. Brüesch. *Phonons: Theory and Experiments II: Experiments and Interpretation of Experimental Results*. Springer Science & Business Media 2012.
- [19] A. Borgschulte, J. Terreni, E. Billeter, L. Daemen, Y. Cheng, A. Pandey, et al. Inelastic neutron scattering evidence for anomalous H–H distances in metal hydrides. *Proceedings of the National Academy of Sciences*. 117 (2020) 4021-6.
- [20] A. Kolesnikov, V. Antonov, V. Fedotov, G. Grosse, A. Ivanov, F. Wagner. Lattice dynamics of high-pressure hydrides of the group VI–VIII transition metals. *Physica B: Condensed Matter*. 316 (2002) 158-61.
- [21] J. Terreni, O. Sambalova, A. Borgschulte, S. Rudić, S.F. Parker, A.J. Ramirez-Cuesta. Volatile Hydrogen Intermediates of CO₂ Methanation by Inelastic Neutron Scattering. *Catalysts*. 10 (2020) 433.

3. Thermodynamics and performance of the Mg-H-F system for thermochemical energy storage applications

M.S. Tortoza, T.D. Humphries, D.A. Sheppard, M. Paskevicius, M.R. Rowles, M.V. Sofianos, K-F. Aguey-Zinsou, C.E. Buckley Thermodynamics and performance of the Mg-H-F system for thermochemical energy storage applications. *Physical Chemistry Chemical Physics*. 20 (2018) 2274 - 83. <https://doi.org/10.1039/C7CP07433F>

This chapter consists of a published article which describes the synthesis and thermal analysis of $\text{Mg}(\text{H}_x\text{F}_{1-x})_2$ and its interaction with hydrogen. This material has been explored as a potential high temperature metal hydride. The fluorine substitution stabilises the MgH_2 and improves the hydrogen absorption and desorption properties. This hydride can release and uptake hydrogen, improving kinetics and reversibility with little to no hysteresis. The thermodynamic analysis has been undertaken and the enthalpy and entropy determined for a range of compositions. Furthermore, hydrogen sorption cycling was measured and analysed for $\text{Mg}(\text{H}_{0.85}\text{F}_{0.15})_2$.

Hence the motivation for testing this hydride is the potential for improvement in kinetics and thermal stabilisation as well as reversibility which means that it may potentially act as a HTMH.

Abstract

Magnesium hydride (MgH_2) is a hydrogen storage material that operates at temperatures above 300 °C. Unfortunately, magnesium sintering occurs above 420 °C, inhibiting its application as a thermal energy storage material. In this study, the substitution of fluorine for hydrogen in MgH_2 to form a range of $\text{Mg}(\text{H}_x\text{F}_{1-x})_2$ ($x = 1, 0.95, 0.85, 0.70, 0.50, 0$) composites has been utilised to thermodynamically stabilise the material, so it can be used as a thermochemical energy storage material that can replace molten salts in concentrating solar thermal plants. These materials have been studied by *in situ* synchrotron X-ray diffraction, differential scanning calorimetry, thermogravimetric analysis, temperature-programmed-desorption mass spectrometry and Pressure-Composition-Isothermal (PCI) analysis. Thermal analysis has determined that the thermal stability of Mg–H–F solid solutions increases proportionally with fluorine content, with $\text{Mg}(\text{H}_{0.85}\text{F}_{0.15})_2$ having a maximum rate of H_2 desorption at 434 °C, with a practical hydrogen capacity of $4.6 \pm 0.19 \text{ H}_2 \text{ wt\%}$ (theoretical 5.4 wt% H_2). An extremely stable $\text{Mg}(\text{H}_{0.43}\text{F}_{0.57})_2$ phase is formed upon the decomposition of each Mg–H–F composition of which the remaining H_2 is not released until above 505 °C. PCI measurements of $\text{Mg}(\text{H}_{0.85}\text{F}_{0.15})_2$ have determined the enthalpy (ΔH_{des}) to be $73.6 \pm 0.2 \text{ kJ/mol H}_2$ and entropy (ΔS_{des}) to be $131.2 \pm 0.2 \text{ J/K/mol H}_2$, which is slightly lower than MgH_2 with ΔH_{des} of 74.06 kJ/mol H_2 and $\Delta S_{\text{des}} = 133.4 \text{ J/K/mol H}_2$. Cycling studies of $\text{Mg}(\text{H}_{0.85}\text{F}_{0.15})_2$ over six absorption/desorption cycles between 425 and 480 °C show an increased usable cycling temperature of $\sim 80 \text{ °C}$ compared to bulk MgH_2 , increasing the thermal operating temperatures for technological applications.

3.1. Introduction

Metal hydrides have been identified as next generation storage materials for multiple applications including hydrogen and thermal energy storage as well as solid state electrolytes [1-5]. Magnesium hydride was first identified as a hydrogen storage material in the early 1950s with one of the first thermal decomposition studies published in 1960 [6, 7]. Due to its high gravimetric hydrogen content (7.6 wt% H_2), its high volumetric storage density of $111 \text{ kg m}^{-3} \text{ H}_2$, and the relatively low cost of magnesium, this material, and many other magnesium based metal hydrides have been identified as having potential for a variety of technologies [8-12]. To date, MgH_2 has been targeted as a stationary hydrogen storage material and thermochemical energy storage (TES) material due to its relatively high thermal stability. Upon thermal treatment at 330°C, MgH_2 decomposes into Mg and H_2 with $\Delta H_{\text{des}} = 74.06 \text{ kJ.mol}^{-1} \text{ H}_2$ and $\Delta S_{\text{des}} = 133.4 \text{ J. K}^{-1}.\text{mol}^{-1} \text{ H}_2$ [13].

The implementation of MgH_2 as a TES material was discussed as early as 1987 and since this time, a number of MgH_2 -based hydrogen storage tanks have been developed and prototype systems manufactured [14-20]. One of the most promising applications for MgH_2 is as a TES material in concentrating solar (CSP) plants [5, 19]. The current operating temperature for a conventional CSP power plant with TES is approximately 565 °C [21], while for next-generation CSP plants, operating temperatures between 600 °C to 800 °C are proposed

[5, 22, 23]. Although the thermal properties of MgH_2 confirm that it is a good candidate as a high-temperature metal hydride (HTMH) coupled with a low-cost metal hydride pair for energy storage, the typical operating temperature ($\sim 400^\circ\text{C}$) is not high enough to meet the targets set by industry. In addition, other contributing factors inhibit the use of pure MgH_2 as TES material due to poor cycling stability above 400°C with a significant reduction in the H_2 storage capacity over tens to hundreds of absorption/desorption cycles due to sintering of the Mg particles [24]. Furthermore, the high H_2 equilibrium pressure of MgH_2 at 550°C , ~ 210 bar, makes its use impractical from an engineering perspective [13].

The focus of the current study is to enhance the cyclic stability and to decrease the H_2 equilibrium pressure of MgH_2 by forming a solid solution between MgH_2 and MgF_2 . *Sheppard et al.* recently reported that one method to increase the operating temperature of a metal hydride (MH) is to partially replace hydrogen by fluorine, as this thermodynamically stabilises the corresponding solid-solution metal hydride-fluoride [25-27]. As such, many materials that operate below the target temperature of $\sim 500^\circ\text{C}$ may become feasible for higher temperature applications. Furthermore, the addition of fluorine can reduce the cost of a TES system and improve metal hydride reversibility, which is a key factor given the typical 30-year lifetime of a CSP plant [26, 28].

To increase the operating temperature of the Mg-H system, fluorine substitution to form $\text{Mg}(\text{H}_x\text{F}_{1-x})_2$ solid solutions have been studied herein. Previous studies on mixtures of $\text{MgH}_2 + x\text{MF}_y$ ($M = \text{Mg, Zr, Ti, Fe, Ta, Ni, Nb}$; $x = 5 - 7$ mol%; $y = 2 - 5$) have concentrated on improving the kinetics of MgH_2 for operation at lower temperatures [29-34]. The kinetics of decomposition were determined to be considerably faster than pure MgH_2 with full H_2 release within 600 s [29], with negligible loss in H_2 cycling capacity at 310°C . The reason for the improved kinetics has been explored by a variety of techniques including X-ray photoemission spectroscopy (XPS) and powder X-ray diffraction (XRD) [32, 33], although there are mixed reports on whether the transition metal or MgF_2 species formed is responsible for the enhanced performance [29, 32, 33]. Recently a preliminary study has shown that MgH_2 and MgF_2 forms solid solutions with $\text{Mg}(\text{H}_{0.9}\text{F}_{0.1})_2$ reversibly absorbing 5.5 wt % H_2 in less than 3 min at 440°C [35]. Thermal analysis by differential scanning calorimetry (DSC) indicates that ΔH_{des} for $\text{Mg}(\text{H}_{0.9}\text{F}_{0.1})_2$ is close to that of MgH_2 ($74.0 \text{ kJ}\cdot\text{mol}^{-1} \text{H}_2$) [13], and decreases with decreasing H content. However, without the determination of ΔS_{des} the stability of the material can't be truly assessed. Previous studies have shown that incremental substitution of F causes a decrease in ΔH_{des} although a concomitant decrease in ΔS_{des} causes an overall stabilisation of the material [26]. Further analysis of this system by pressure-composition-isotherm (PCI) analysis is required to precisely determine the decomposition pathway and the associated thermodynamics. These properties are required to assess the viability of $\text{Mg}(\text{H}_x\text{F}_{1-x})_2$ as a TES material, especially at temperatures $> 400^\circ\text{C}$.

In this study, MgH_2 has been ball-milled with MgF_2 followed by annealing to successfully form solid solutions of $\text{Mg}(\text{H}_x\text{F}_{1-x})_2$ ($x = 1, 0.95, 0.85, 0.70, 0.50, 0$) to determine differences in their structural and thermodynamic

properties. Time resolved synchrotron radiation powder X-ray diffraction (SR-XRD) studies have been carried out on a range of $\text{Mg}(\text{H}_x\text{F}_{1-x})_2$ compositions to ascertain the differences in thermal decomposition pathways of these compounds. The thermodynamic and kinetic properties of these solid solutions have been determined by PCI analysis using the van't Hoff method, differential scanning calorimetry (DSC), thermogravimetric analysis (TGA), temperature-programmed-desorption mass spectrometry (TPD-MS). Cycling studies have also been carried out to determine the feasibility of the Mg–H–F system for CSP application.

3.2. Experimental

All manipulations of chemicals were undertaken in an argon atmosphere using an Mbraun Unilab glovebox to prevent air exposure and to minimise oxygen ($\text{O}_2 < 1$ ppm) and water ($\text{H}_2\text{O} < 1$ ppm) contamination. $\text{Mg}(\text{H}_x\text{F}_{1-x})_2$ ($x = 1, 0.95, 0.85, 0.70, 0.50, 0$) samples were prepared by ball milling (BM) various ratios (Table 3.1) of MgH_2 and MgF_2 (Sigma-Aldrich, >99.99 %) at room temperature. MgH_2 powder (95 wt% purity from Rietveld refinement) was first synthesised by annealing Mg powder (Aldrich, >99 %) at 400 °C under 30 bar hydrogen pressure for 18 hours. The partially hydrogenated Mg was then BM for 3 hours with a ball-to-powder mass ratio of 10:1 in a Shaker Mill (Turbula T2C shaker-mixer) and annealed once again under identical conditions (400 °C, 30 bar H_2 , 18 h). BM of MgH_2 and MgF_2 was undertaken at 400 rpm for 10 hours (labelled S) or 40 hours (labelled L) in an Across International Planetary Ball Mill (PQ-N04) with a ball-to-powder mass ratio of 50:1 using stainless steel vials and balls (6 and 8 mm in diameter) under an Ar atmosphere. After milling, samples were annealed under a hydrogen atmosphere of 60 bar at 450 °C for a period of 90 hours to form uniform solid solutions. Annealing samples under H_2 prevents hydrogen release from the material [26].

Before and after annealing the $\text{Mg}(\text{H}_x\text{F}_{1-x})_2$ powders, quantitative phase analysis was undertaken by conducting *ex-situ* XRD analysis on each sample. The powders were mixed with ~10 wt% Si (–325 mesh, Aldrich) as an internal standard ($a = 5.42960(4)$ Å), used to extract reliable lattice parameters for the solid solutions. *Ex-situ* XRD was performed using a Bruker D8 Advance diffractometer (Cu- $\text{K}_{\alpha 1+2}$ radiation, $\lambda = 1.5418$ Å) with flat-plate sample holders sealed by a polymethylmethacrylate (PMMA) dome in order to prevent oxygen/moisture contamination during data collection. The PMMA dome resulted in a broad hump in XRD patterns centred at $\sim 20^\circ 2\theta$. Acquisition of data was subsequently restricted to $2\theta = 20 - 80^\circ$, with a $\Delta 2\theta = 0.02^\circ$ and 2 s/step scanning rate with a sample rotation rate of 60 rpm.

In-situ synchrotron radiation SR-XRD was performed at the Australian Synchrotron in Melbourne, Australia.[36] Without exposure to air, the $\text{Mg}(\text{H}_x\text{F}_{1-x})_2$ powders (ball milled for 40 h) were loaded into borosilicate or quartz capillaries (outer diameter 0.7 mm, wall thickness 0.01 mm) that were then, using graphite ferrules, mounted in 1/16" tube fittings connected to a gas manifold. The samples were kept under

dynamic vacuum while heated with a hot air blower up to 615 °C (Room Temperature (RT) → 200 °C at 10 °C/min, 200 → 615 °C at 5 °C/min). Mg(H_{0.50}F_{0.50})₂ was measured with a temperature heating rate of 8 °C/min from 150 to 785 °C. One-dimensional SR-XRD patterns (monochromatic X-rays with $\lambda = 1.000389(1)$, 0.826307(1) or 0.774541(1) Å) were collected using a Mythen microstrip detector with an exposure time of 54 s per pattern. The capillaries were continuously oscillated through 120° during exposure to improve powder averaging. Diffraction patterns were quantitatively analysed using the Rietveld refinement method with TOPAS software (Bruker-AXS). The temperature of the hot-air blower was calibrated against the known thermal expansion coefficients for NaCl and Ag [37, 38].

TGA and DSC in conjunction with MS (DSC-TGA-MS) analyses were conducted using sample masses of ~10 mg at a heating rate of 10 °C/min under an argon flow of 20 mL/min using a Mettler Toledo TGA/DSC 1 coupled with an Omnistar MS. Masses ($m/e = 2 - 100$) were monitored up to 550 °C, however the Mg(H_{0.50}F_{0.50})₂ was measured up to 850 °C. The instrument was installed in an Ar filled glovebox to avoid air contamination during sample handling. The temperature accuracy of this instrument is ±0.2 °C, while the balance has an accuracy of ±20 µg.

All hydrogen absorption/desorption measurements were performed by using a computer controlled Sieverts/volumetric apparatus previously described elsewhere [13]. The digital pressure.

Table 3.1. Structural properties of Mg(H_xF_{1-x})₂-L mixtures (P42/mnm) at room temperature. Estimated standard deviations (esd's) of lattice parameters and H occupancies in the 4f site are in parentheses

Sample Name	MgH ₂ :MgF ₂ Molar ratio (target)	Lattice Parameter (Å)		H Occupancy	Unit cell volume (Å ³)	Mg ₂ FeH ₆ impurity (wt%)	Theoretical H ₂ capacity excluding Mg ₂ FeH ₆ content (wt%)
		a	c				
MgH ₂	1:0	4.51746(5)	3.02215(6)	1(0)	61.674(2)	0	7.66
Mg(H _{0.95} F _{0.05}) ₂	0.95:0.05	4.52109(4)	3.02306(4)	0.919(9)	61.792(1)	0	6.81
Mg(H _{0.85} F _{0.15}) ₂	0.85:0.15	4.54238(6)	3.029517(7)	0.801(2)	62.509(0)	3	5.40
Mg(H _{0.70} F _{0.30}) ₂	0.7:0.3	4.55932(3)	3.03417(3)	0.727(5)	63.072(1)	7	3.80
Mg(H _{0.50} F _{0.50}) ₂	0.5:0.5	4.59133(2)	3.04372(2)	0.393(4)	64.162(1)	12	2.27
MgF ₂	0:1	4.62312(2)	3.05195(2)	0(0)	65.230(1)	0	---

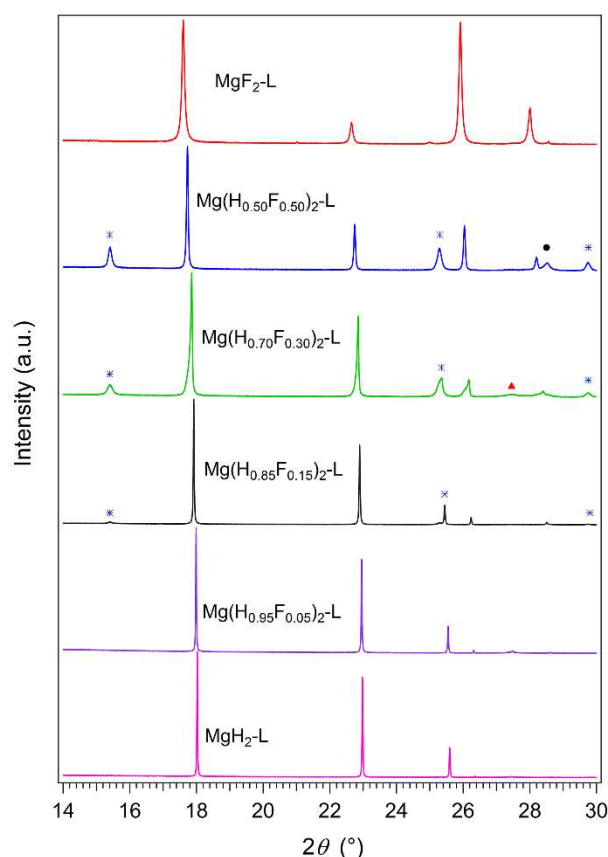


Figure 3.1. In-situ SR-XRD at room temperature of $Mg(H_xF_{1-x})_2$ samples ball milled for 40 hours and annealed. * signifies Mg_2FeH_6 , • signifies Fe and ▲ signifies MgO. All other Bragg peaks are associated with the $Mg(H_xF_{1-x})_2$ mixtures. $\lambda = 1.000389(1) \text{ \AA}$.

transducer (Rosemount 3051S) had a precision and accuracy of 14 mbar, whilst room temperature measurements were recorded using a 4-wire platinum resistance temperature detector (RTD). Isothermal PCI curves were performed at 437, 444, 450 and 461 °C and monitored by a K-type thermocouple ($\pm 4 \text{ }^\circ\text{C}$). Above $\sim 420 \text{ }^\circ\text{C}$, the permeation of hydrogen directly through the walls of the stainless steel sample cell becomes an issue and the measured hydrogen content at each PCI data point has to be corrected for this loss, as previously explained [27]. In addition, hydrogen absorption PCI measurements were carried out at $\sim 450 \text{ }^\circ\text{C}$ on the same apparatus.

Hydrogen absorption/desorption cycles were conducted by heating a sample of $Mg(H_{0.85}F_{0.15})_2$ at $4 \text{ }^\circ\text{C}/\text{min}$ from room temperature to $425 \text{ }^\circ\text{C}$ followed by a 6 h isothermal period. The temperature was then heated at $2 \text{ }^\circ\text{C}/\text{min}$ to $480 \text{ }^\circ\text{C}$ followed by another 6 h isothermal step; it is during this stage the first decomposition begins. The temperature was then cycled between $425 \text{ }^\circ\text{C}$ (hydrogen absorption) and $480 \text{ }^\circ\text{C}$ (hydrogen desorption) 6 times under a closed gas system pressure varying between 30 - 42 bar.

3.3. Results and Discussion

3.3.1. Structure and Composition.

The BM powders were analysed by *ex-situ* XRD before and after annealing to confirm that a $\text{Mg}(\text{H}_x\text{F}_{1-x})_2$ solid solution was formed and that neither of the MgH_2 and MgF_2 starting materials were present (Fig. I.1). Due to the fact that MgH_2 and MgF_2 both exist in a tetragonal rutile crystal structure ($P42/mnm$) [39, 40], the solid solutions of $\text{Mg}(\text{H}_x\text{F}_{1-x})_2$ also possess identical structures, as predicted by Messer [41]. The annealing process, while also enhancing the crystallinity of the samples, was necessary to allow the H and F atoms to substitute in to the $4f$ sites and form a uniform solid solution (Table 3.1). Milling alone is not enough to facilitate the formation of a uniform single phase, although extended milling time aids in attaining a uniform sample composition. However, extended milling may lead to the introduction of iron impurities from the stainless-steel canisters and balls, resulting in the formation of small amounts of Mg_2FeH_6 being evident after annealing (Fig. 3.1, Table 3.1) [42, 43]. Therefore, it is important to restrict long milling times in order to reduce the quantity of impurities. After BM for 40 h the samples were analysed by XRD and it can be seen that the samples exhibit broad diffraction peaks suggestive of a single tetragonal phase or an extended range of $\text{Mg}(\text{H}_x\text{F}_{1-x})_2$ compositions (Fig. I.1), but annealing promotes crystallisation into single phase compositions (Fig. 3.1). Quantitative phase analysis of each the mixtures identifies that $\text{Mg}(\text{H}_{0.50}\text{F}_{0.50})_2\text{-L}$ contains the largest quantity of Mg_2FeH_6 [42, 43] (Table 3.1) and it is deemed that the greater hardness of MgF_2 compared to stainless-steel is responsible (MgF_2 has a hardness of 415 kg/mm^2 Knoop [44], whereas stainless steel has a hardness of 166 kg/mm^2 Knoop) [45]. Therefore, increased MgF_2 content in the sample promotes erosion of the stainless steel and, by consequence, incremental quantities of Mg_2FeH_6 are observed. In addition, Fe metal is observed in only the $\text{Mg}(\text{H}_{0.50}\text{F}_{0.50})_2\text{-L}$ materials. Some MgO is observed in sample $\text{Mg}(\text{H}_{0.70}\text{F}_{0.30})_2\text{-L}$ due to an inadvertent exposure of the sample to air during mounting of the capillary before XRD. MgO and other impurities may also be formed due to reaction with the borosilicate or quartz capillaries. In this study, no additional impurity phases were identified to form during the in situ heating experiment.

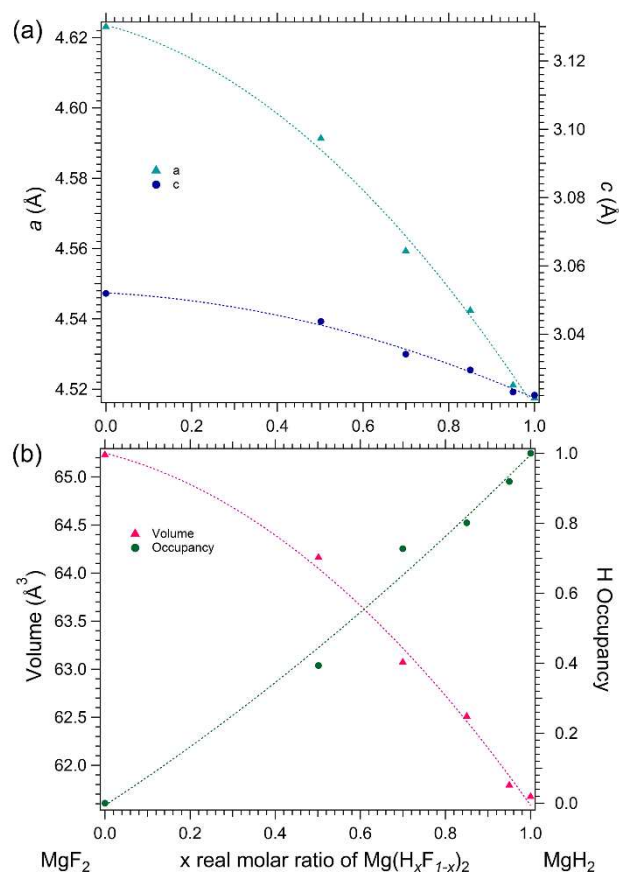


Figure 3.2. Refined lattice parameters of Mg(H_xF_{1-x})₂-L mixtures from room temperature in-situ SR-XRD. (a) Quadratic fit for lattice parameters *a* and *c* versus composition. $a = -0.0762x^2 - 0.0326x + 4.6236$. $c = -0.0239x^2 - 0.0069x + 3.0521$ (b) quadratic fit for unit cell volume and H occupancy versus composition. Unit cell volume $V = -2.5527x^2 - 1.1113x + 65.246$. H Occupancy = $0.2073x^2 + 0.7952x - 0.0064$.

Fig. 3.1 illustrates the SR-XRD patterns for each of the L-solid solutions at room temperature. It is noted that the peaks for Mg(H_xF_{1-x})₂ move to lower angles (higher *d*-spacing) with increased F content. This is emphasised in Fig. I.2. This shift causes a concomitant increase in unit cell volume from 61.674(2) Å³ for MgH₂ to 65.230(1) Å³ for MgF₂ (Table 3.1). This is expected due to the longer Mg–F bond distances of 1.9968 Å [46] in MgF₂ compared to the apical Mg–H distance of 1.94(2) Å and the equatorial Mg–H distance of 1.97(2) Å in MgH₂ [47]. The lattice parameters for the Mg–H–F solid solution are illustrated in Fig. 3.2a and clearly show that the *a* and *c* parameters increase with increasing fluorine content, with *a* having a dominant influence on the unit cell expansion. Previous studies have used the lattice parameters to predict the H/F compositions of the materials after hydrogen absorption/desorption cycles [26], while the unit cell volume can also be utilised (Fig. 3.2b). The H occupancy factor may also be employed as a measure of substitution between H and F (Fig. 3.2b). Despite H having a negligible scattering factor, the X-ray cross section of F allows for appreciable determination of the occupancy of the 4*f* site of which the F and H share.

To avoid Fe impurities the milling time of the samples were reduced to 10 h while maintaining the annealing conditions (90 h at 450 °C at 60 bar H₂). These samples are labelled as Mg(H_xF_{1-x})₂-S. The annealed S samples

were analysed by XRD and show no presence of Mg_2FeH_6 although the shape of the $\text{Mg}(\text{H}_x\text{F}_{1-x})_2$ solid solution Bragg peaks were asymmetric (Fig. I.3).

3.3.2. Thermal analysis.

In-situ SR-XRD was carried out up to 615 °C on all sample compositions with Fig. 3.3a illustrating $\text{Mg}(\text{H}_{0.85}\text{F}_{0.15})_2$ and exemplifying the decomposition process (also see Fig. I.4-I.6). As temperature increases, thermal expansion causes the lattice parameters of $\text{Mg}(\text{H}_{0.85}\text{F}_{0.15})_2$ (and the minor Mg_2FeH_6 phase) to expand (2θ decreases) before both materials decompose simultaneously at an onset temperature of 433 °C with total decomposition occurring by 440 °C. The decomposition observed in XRD data is also mirrored in the TGA-DSC-MS data (Fig. 3.3b - d). The DSC data show a single endothermic event between 350 - 450 °C for all hydrogen containing samples (Fig. 3.3b, Table 3.2). The onset temperature for the decomposition of pure MgH_2 -S is ~394 °C with a maximum H_2 release at ~413 °C. The decomposition temperature of the pure hydride is greater than that of $\text{Mg}(\text{H}_{0.95}\text{F}_{0.05})_2$ -S, which has an onset temperature of 360 °C and a maximum H_2 release temperature of 405 °C. From this it can be inferred that $\text{Mg}(\text{H}_{0.95}\text{F}_{0.05})_2$ -S has faster kinetics of desorption than pure MgH_2 -S, a result that has also been noted previously [31]. Further substitution of H by F appears to kinetically and/or thermodynamically stabilise MgH_2 with $\text{Mg}(\text{H}_{0.85}\text{F}_{0.15})_2$ -S having a decomposition onset of

405 °C (peak maximum of 434 °C), while $\text{Mg}(\text{H}_{0.70}\text{F}_{0.30})_2\text{-S}$ has an onset of ~ 415 °C (peak maximum of 437 °C). One of the most intriguing results is that $\text{Mg}(\text{H}_{0.50}\text{F}_{0.50})_2\text{-S}$ shows no obvious

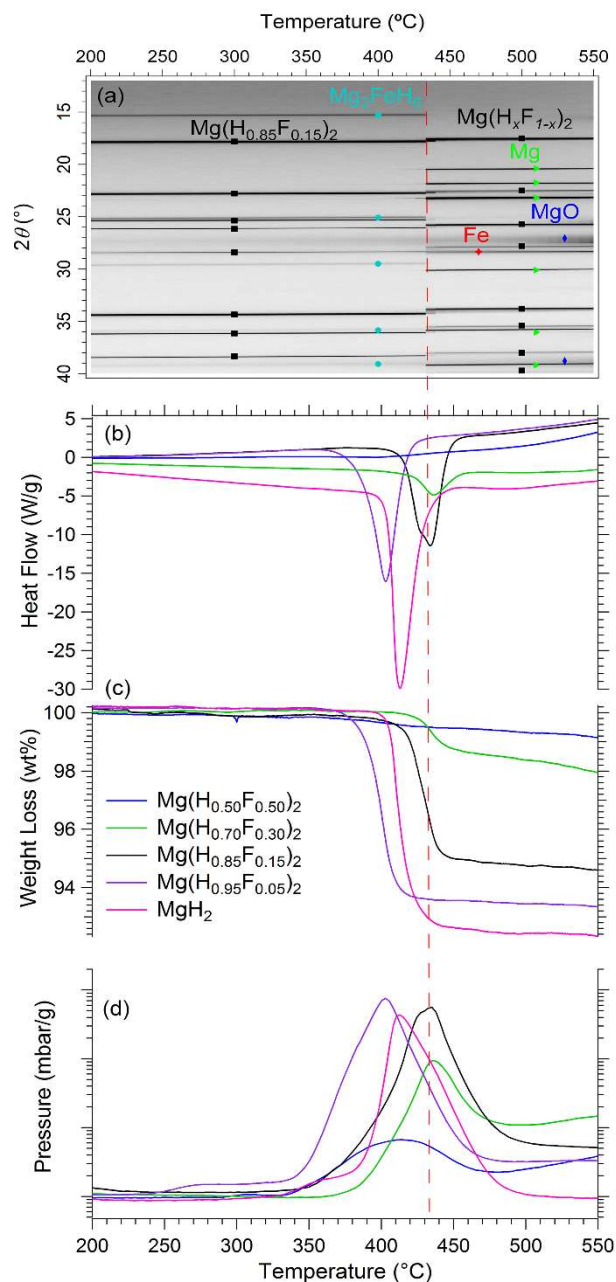


Figure 3.3. (a) *In-situ* XRD for $\text{Mg}(\text{H}_{0.85}\text{F}_{0.15})_2$. $\lambda = 1.000389(1)$ Å. Simultaneous thermal analysis of $\text{Mg}(\text{H}_x\text{F}_{1-x})_2$ samples by (b) DSC, (c) TGA and (d) MS. $\Delta T/\Delta t = 10$ °C/min. DSC and MS data are normalised to the mass of the sample.

decomposition event during DSC measurement up to 550 °C (Fig. 3.3b). This is in agreement with the *in-situ* SR-XRD measurement of $\text{Mg}(\text{H}_{0.5}\text{F}_{0.50})_2\text{-L}$ up to 615 °C, Fig. I.5. This particular *in-situ* SR-XRD pattern also shows the presence of Mg_2FeH_6 , which disappears at ~ 450 °C in conjunction with the appearance of Mg at the same temperature. The disappearance of the Mg at ~ 530 °C is due to the migration of Mg vapour from the hot-zone during measurement. The decomposition onset for the Mg_2FeH_6 impurity phase

determined in each of the $\text{Mg}(\text{H}_x\text{F}_{1-x})_2$ ($x = 0.85, 0.70, 0.50$) samples measured by *in-situ* XRD occurs at ~ 430 °C. A previous *in-situ* XRD decomposition study of Mg_2FeH_6 shows the onset of decomposition to occur at ~ 340 °C under 1 bar Ar [48]. To ascertain if F substitution had occurred within Mg_2FeH_6 during annealing, refinement of the lattice parameter and H/F occupancy factors on the 24e site in the $\text{Fm}\bar{3}\text{m}$ unit cell was undertaken. At room temperature the unit cell dimension was determined as 6.46277(8) Å, which is only 0.25% larger than 6.44686(2) Å determined in a previous study [49], while the hydrogen occupancy was refined to be 100%. At ~ 380 °C the hydrogen occupancy was determined to be 96.8(9) %, which indicates that some F substitution may have occurred at higher temperatures, and in turn may have increased the thermal stability of the Mg_2FeH_6 material.

DSC and TPD-MS data were also collected for the samples milled for 40 h (L, Fig. I.7). Upon comparing the L and S samples measured by DSC, it appears that extended milling times reduce the observed temperature of the endothermic peak compared to the corresponding compositions milled for 10 h. For instance, the maximum rate of H_2 release for $\text{Mg}(\text{H}_{0.70}\text{F}_{0.30})_2$ -S is 437 °C, whereas it is 367 °C for $\text{Mg}(\text{H}_{0.70}\text{F}_{0.30})_2$ -L. Extended milling decreases the crystallite and particle size, decreases diffusion pathways, increases the specific surface area and introduces defects. All of these factors contribute to faster kinetics that allow the hydride to decompose at a lower temperature [13].

TPD-MS was used to analyse the gases released by materials upon thermal treatment. In this study, the gases released during DSC-TGA were analysed for all m/e up to 100 showing that only H_2 was released during thermal treatment (Fig. 3.3d, log scale). The most striking result is that for $\text{Mg}(\text{H}_{0.50}\text{F}_{0.50})_2$ -S only minor H_2 evolution is observed between 290 and 475 °C. In fact, all samples apart from $\text{Mg}(\text{H}_{0.70}\text{F}_{0.30})_2$ -S start to desorb hydrogen between 290 and 340 °C, while it is only the peak rate of release that differs between the samples.

Considering that the thermal analysis experiments have indicated that increasing the F content in the samples increases thermal stability compared to pure MgH_2 , it would be assumed that the $\text{Mg}(\text{H}_{0.50}\text{F}_{0.50})_2$ sample would be the ideal candidate for further studies as a HTMH for TES applications. However, the larger practical hydrogen capacity of $\text{Mg}(\text{H}_{0.85}\text{F}_{0.15})_2$ is far greater than $\text{Mg}(\text{H}_{0.50}\text{F}_{0.50})_2$ below 550 °C (5.06 ± 0.02 wt% H_2 and 0.77 ± 0.01 wt% H_2 , respectively). As such, $\text{Mg}(\text{H}_{0.85}\text{F}_{0.15})_2$ -S was deemed an ideal candidate to be studied by PCI between 437 and 461 °C to determine its thermodynamics of decomposition (Fig. 3.4a). The PCI curves in Fig. 3.4a show that decomposition follows a single step process that releases an average total of 4.6 ± 0.2 wt% H_2 for the four temperatures measured, with equilibrium pressures between 32 and 38 bar. Each of the curves exhibits a sloping plateau that is highly characteristic of a solid solution of this type, albeit not as sloped as those observed in the $\text{NaH}_{0.50}\text{F}_{0.50}$ or NaMgH_2F systems [26, 27]. Sloping plateaus are not ideal in practical applications due to the fact that hydrogen absorption and desorption does not occur in an isobaric process [27], and the range of operational process [27], and the range of operational system pressures over

the equilibrium transition becomes larger. Generally, the thermodynamics of absorption/desorption are determined by measuring the pressure at the midpoint of the equilibrium plateau and plotting this as a

Table 3.1. Decomposition temperatures and hydrogen capacities and values of $Mg(H_xF_{1-x})_2$ -S mixtures measured by DSC-TGA up to 550 °C. $\Delta T/\Delta t = 10$ °C/min.

Sample	Practical / theoretical H ₂ capacity (TGA, wt %)	Hydrogen yield (%)	Onset/Peak Temperature of H ₂ desorption (DSC, °C) *	Temperature in middle point of step (TGA, °C) *	Peak Temperature of H ₂ desorption (MS, °C) *
MgH ₂	7.50 ± 0.03 / 7.66	97.9	394/413	413	412
Mg(H _{0.95} F _{0.05}) ₂	6.60 ± 0.03 / 6.81	96.9	360/405	400	403
Mg(H _{0.85} F _{0.15}) ₂	5.06 ± 0.02 / 5.4	93.7	405/434	430	435
Mg(H _{0.70} F _{0.30}) ₂	1.60 ± 0.01 / 3.8	42.1	415/437	433	436
Mg(H _{0.50} F _{0.50}) ₂	0.77 ± 0.01 / 2.27	33.9	---	---	~414

* Temperature reported as integers although accurate to 0.02 °C.

function of temperature in a van't Hoff plot. In this study, due to the sloping plateau, each of the four curves were numerically fitted throughout the plateau region so that the enthalpy and entropy could be determined at any hydrogen content (Fig. 3.4) [27]. All of the information obtained from the PCI measurements presented in Fig. 3.4, are summarised in Table 3.3. The enthalpy (ΔH_{des}) and entropy (ΔS_{des}) of hydrogen desorption are also presented in Table 3.3. The uncertainties for the data were calculated using the weighted least squares method with a 95% confidence interval as described in previous work [13]. The enthalpy, ΔH_{des} , decreases from 74.7 to 72.2 kJ/mol H₂ between -1 wt% to -3 wt% H₂ desorption. With regards to entropy, these values also show the same trend, decreasing in value from 133.0 to 129.1 J/K/mol H₂. This means that at -2 wt% H₂ (middle point of the plateau), $\Delta H_{des} = 73.6 \pm 1.2$ kJ/mol H₂ and $\Delta S_{des} = 131.2 \pm 2$ J/K/mol H₂, are 0.66% and 1.65% lower than that of pure MgH₂, respectively. This indicates that the equilibrium pressure at which decomposition will occur is insignificantly lower than that for MgH₂ at the same temperature. However, along the plateau the equilibrium pressures change (due to the sloping plateau) resulting in $\Delta H_{des} (Mg(H_{0.85}F_{0.15})_2-S) > \Delta H_{des} MgH_2$ while < -1.58 wt%, and after this point (> -1.58 wt%) $\Delta H (Mg(H_{0.85}F_{0.15})_2-S) < \Delta H MgH_2$. However, $\Delta S_{des} (Mg(H_{0.85}F_{0.15})_2-S) < \Delta S_{des} MgH_2$ all along the plateau. Although these are only small changes in ΔH and ΔS , it is still significant and are linked with the sloping nature of the plateau. Frequently, a flat equilibrium plateau is observed when a material decomposes into another with a different crystal structure. In this particular case, the same space group, $P42/mnm$, is shared for both the starting and final products. As a consequence, it is observed that during PCI experiments, H₂ is progressively desorbed allowing an F rich phase to emerge.

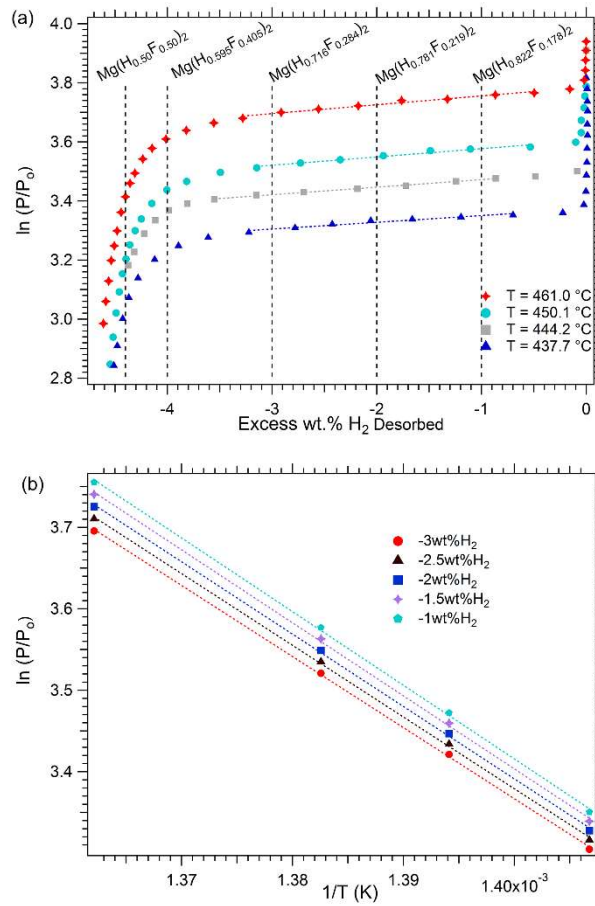


Figure 3.4. (a) Pressure–Composition–Isotherms (PCI) for $\text{Mg}(\text{H}_{0.85}\text{F}_{0.15})_2\text{-S}$ performed between 437 °C and 461°C. $\blacklozenge \ln(P/P_0)_{461^\circ\text{C}} = 0.02978x + 3.7850$, $\bullet \ln(P/P_0)_{450.1^\circ\text{C}} = 0.0279x + 3.6048$, $\blacksquare \ln(P/P_0)_{444.2^\circ\text{C}} = 0.0256x + 3.4978$, $\blacktriangle \ln(P/P_0)_{436^\circ\text{C}} = 0.0227x + 3.3731$, where $x = \text{wt}\% \text{H}_2$ desorbed. (b) van't Hoff plot of respective H_2 desorption equilibrium pressures, where T is temperature (K). $P_0 = 1$ bar.

Table 3.2. Thermodynamic properties at 5 different hydrogen contents for $\text{Mg}(\text{H}_{0.85}\text{F}_{0.15})_2\text{-S}$

At H_2 wt%	ΔH_{des} (kJ/mol H_2)	ΔS_{des} (J/K/mol H_2)	van't Hoff plot $\ln(P/P_0)$
-1	74.7 ± 1.2	133.0 ± 2	$-8981.84/T + 15.99$
-1.5	74.1 ± 1.2	132.1 ± 2	$-8915.58/T + 15.87$
-2	73.6 ± 1.2	131.2 ± 2	$-8848.59/T + 15.78$
-2.5	72.9 ± 1.2	130.2 ± 2	$-8771.91/T + 15.66$
-3	72.2 ± 1.2	129.1 ± 2	$-8685.35/T + 15.53$
Pure MgH_2^*	74.06	133.4	---

*ref [13]

This F-rich phase also possesses the same crystal structure, allowing for changes to occur gradually, which explains the nature of the sloping plateau. For this reason, the thermodynamics of decomposition change gradually during the measurement.

Figure 3.5b also shows that the H₂ equilibrium pressures of the Mg(H_xF_{1-x})₂ decreases and moves closer to that of Mg₂FeH₆ as the temperature increases. It should be noted that during PCI measurements the quantity of desorbed H₂ for Mg(H_{0.85}F_{0.15})₂ (4.6 wt% H₂, Table I.1) did not reached the theoretical hydrogen capacity of 5.4 wt%. This can be attributed to the formation of a stable Mg–H–F phase. An XRD pattern of desorption at 450 °C XRD capacity of 5.4 wt%.

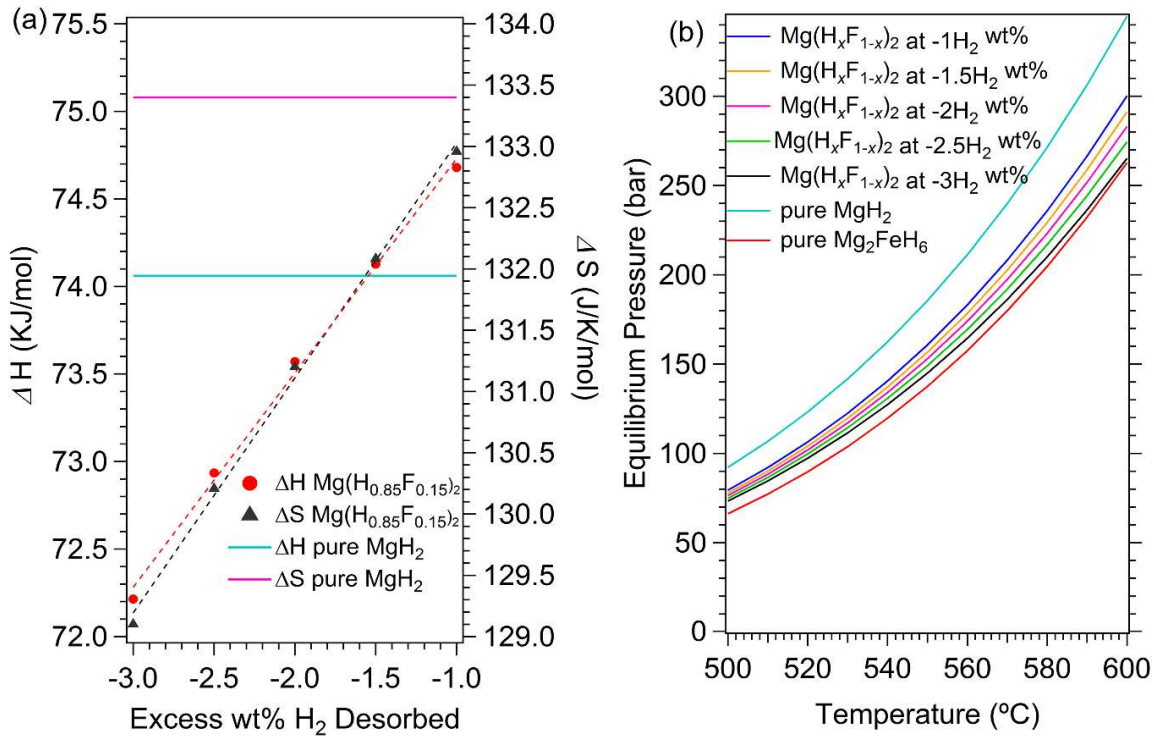


Figure 3.5. (a) Reaction enthalpy and entropy for Mg(H_{0.85}F_{0.15})₂. $\Delta S_{des} = 1.9181 \times (\text{wt}\% \text{H}_2) + 134.95$, $\Delta H_{des} = 1.225 \times (\text{wt}\% \text{H}_2) + 75.995$ (b) Predicted equilibrium pressures of MgH₂ and Mg(H_{0.85}F_{0.15})₂ at 5 different values of H₂ wt% along the equilibrium plateau. For Fig 5b: pure MgH₂[13] and Mg₂FeH₆ [43].

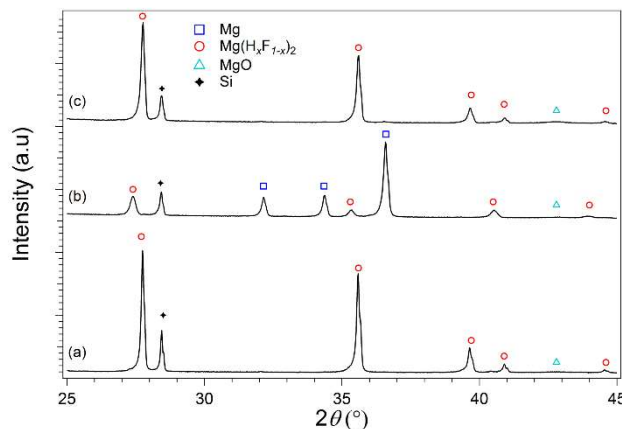


Figure 3.5. a) Ex-situ XRD of Mg(H_{0.85}F_{0.15})₂; (b) after PCI desorption at 450 °C; (c) after PCI absorption at 450 °C. $\lambda = 1.5418 \text{ \AA}$, at room temperature.

This can be attributed to the formation of a stable Mg–H–F phase. An XRD pattern of Mg(H_{0.85}F_{0.15})₂-S was measured before and after the PCI test (Fig. 3. 6 a and b), after PCI confirmed that Mg(H_xF_{1-x})₂

was present, supporting the hypothesis of a stable Mg–H–F phase. This finding correlates well with the high stability observed for $\text{Mg}(\text{H}_{0.50}\text{F}_{0.50})_2$ during thermal analysis by *in-situ* SR-XRD and DSC-TGA-MS. Rietveld refinement of the XRD pattern to determine the unit cell volume provides a composition of $\text{Mg}(\text{H}_{0.43}\text{F}_{0.57})_2$, also corresponding to the fact that ~ 0.8 wt% H_2 remains within the sample (Table I.1).

The thermal stability of the $\text{Mg}(\text{H}_{0.50}\text{F}_{0.50})_2$ -L composition was subsequently investigated by TGA-MS and *in-situ* SR-XRD up to 850 °C to determine the temperature at which the remaining H_2 could be desorbed (Fig. I.8 and I.9). As noted previously, during TGA measurement (Fig. 3.3c) of $\text{Mg}(\text{H}_{0.50}\text{F}_{0.50})_2$, before 480 °C only 0.77 wt% H_2 is desorbed, but after 505 °C a major desorption event occurs (Fig. I.8) releasing a total mass loss of 2.3 wt% before 830 °C. This value is slightly greater than the theoretical quantity of 2.27 wt % H_2 as Mg evaporates at this temperature due to its low vapour pressure. The first step of decomposition, observed at ~ 400 °C during TGA-MS, Fig. I.8, is not clearly witnessed by *in-situ* SR-XRD but at ~ 545 °C a significant expansion of the unit cell is observed, beyond that expected from thermal expansion alone (Fig. I.9). At the same time, the peaks become broader and asymmetric in shape. This is most likely a consequence of a variety of solid-solution compositions being present during decomposition. At ~ 755 °C the hydrogen occupancy factor is 2.9(5) % indicating that full decomposition has almost been achieved under vacuum conditions.

The high thermal stability of the $\text{Mg}(\text{H}_{0.43}\text{F}_{0.57})_2$ composition may permit this material to be implemented as a TES material as it will operate at above 600 °C, which is above the operating temperature currently achievable using molten salts of 565 °C [22]. The evaporation of Mg at high temperatures is a major concern as upon decomposition, 22.7 wt% of Mg metal is formed. Over time, this will lead to a major decrease in capacity unless a method of inhibiting segregation is utilised. One such method, previously used in studies of Na/NaH at temperatures of up to 900 °C and H_2 pressures of 650 bar, is to enclose the sample in thin Fe tubing or foil [50]. The extreme thermal stability of this material should be investigated by theoretical methods to understand the unexpected thermodynamic stability, while the thermodynamic properties should also be determined experimentally.

Overall, each method of thermal analysis used in this study illustrates that the thermal stability of the Mg–H–F systems increases with addition of F. A previous report on this system mentions that data measured by DSC indicates a destabilisation due to a decrease in ΔH_{des} [35]. As stated above, ΔS_{des} is required to ultimately determine the overall stability of the system. This study shows that for $\text{Mg}(\text{H}_{0.85}\text{F}_{0.15})_2$, a concomitant decrease in ΔS_{des} is observed during addition of F to the mixture, which causes an overall increase in stability. This pattern has been established previously during the study of Na–H–F in which PCI measurements determined a ΔH_{des} of $106 \pm 5 \text{ kJ}\cdot\text{mol}^{-1} \text{H}_2$ and ΔS_{des} of $143 \pm 5 \text{ J}\cdot\text{K}^{-1}\cdot\text{mol}^{-1} \text{H}_2$ for $\text{NaH}_{0.50}\text{F}_{0.50}$ compared to $117 \text{ kJ}\cdot\text{mol}^{-1} \text{H}_2$ and $167 \text{ J}\cdot\text{K}^{-1}\cdot\text{mol}^{-1} \text{H}_2$ for pure NaH [26].

3.3.3. Rehydrogenation studies

In order for $\text{Mg}(\text{H}_{0.85}\text{F}_{0.15})_2$ to be considered as potential material for hydrogen storage or thermal energy storage applications, characteristics such as hysteresis (absorption/desorption pressure),

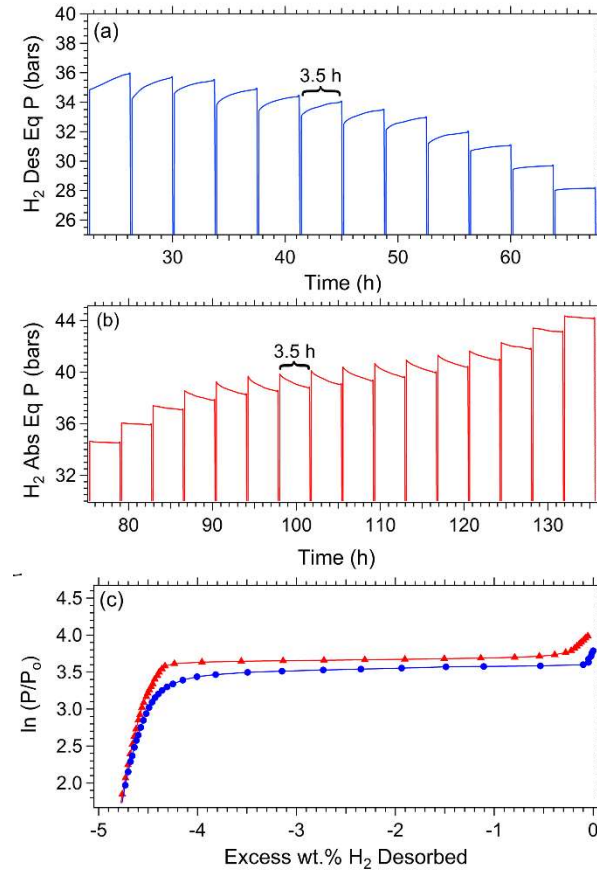


Figure 3.6. Figure 3.7. (a) Hydrogen desorption kinetic data for the PCI of $\text{Mg}(\text{H}_{0.85}\text{F}_{0.15})_2$ performed at 450 °C, (b) Hydrogen absorption kinetic data for the PCI of $\text{Mg}(\text{H}_{0.85}\text{F}_{0.15})_2$ performed at 450 °C; (c) Hydrogen desorption and absorption PCIs performed at 450 °C.

cyclic stability and reversibility need to be assessed [13, 20]. After the PCI measurement at 450 °C (Fig. 3.7a), a hydrogen absorption experiment was performed on the sample at the same

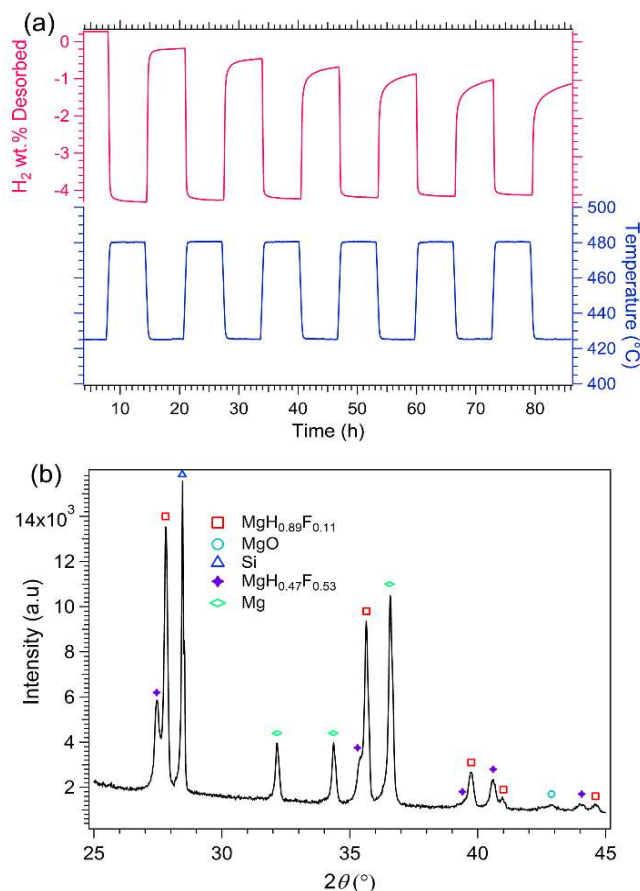


Figure 3.7. (a) Cycling studies of $\text{Mg}(\text{H}_{0.85}\text{F}_{0.15})_2$; (b) XRD after cycling in the hydrogenated state. $\lambda = 1.5418 \text{ \AA}$, at room temperature.

temperature (450 °C) (Fig. 3.7b). An initial pressure of 3 bar was increased to 55 bar in a step-wise fashion, with 3.5 h equilibrium step times (identical to desorption measurements). According to the ΔH_{des} and ΔS_{des} for $\text{Mg}(\text{H}_{0.85}\text{F}_{0.15})_2$ determined by PCI, the sample is predicted to start absorbing H₂ at an equilibrium pressure of ~34 bar (Fig. 3.7b). As observed in Fig. 3.7c, the sample starts to absorb a significant amount of H₂ above ~36 bar. Figures 3.7a and 3.7b represent the kinetic data for desorption and absorption, respectively. These graphs show that $\text{Mg}(\text{H}_{0.85}\text{F}_{0.15})_2$ does not reach true equilibrium after 3.5 h, indicating that reaction kinetics during absorption are appreciably slower than observed during dehydrogenation. If a longer equilibration step time was afforded for each step then hysteresis may not be observed. Despite the kinetics of absorption being slow, the sample absorbed ~98% of the hydrogen that was previously desorbed and equates to ~88% of the theoretical value. At the end of the absorption PCI, quantitative Rietveld refinement of the XRD data shows that two compositions of $\text{Mg}(\text{H}_x\text{F}_{1-x})_2$ are identified, although due to the asymmetry of the peaks there are maybe a larger distribution of compositions (Fig. 3.6c). The compositions are determined, based on the unit cell volume method (Fig. 3.2b), to be approximately 90 wt% $\text{Mg}(\text{H}_{0.86}\text{F}_{0.14})_2$ and 10 wt% $\text{Mg}(\text{H}_{0.56}\text{F}_{0.44})_2$. Macroscopic flakes are evident in the rehydrogenated sample when visually

inspected, which are attributed to the sintering of the material at high temperature. This was previously reported by Bogdanovic *et al.* [51] by observing that Mg metal agglomerates during and is likely to be responsible for the reduced kinetics [13].

3.3.4. Cycling studies

The cyclability of $\text{Mg}(\text{H}_{0.85}\text{F}_{0.15})_2$ -S was investigated to characterise its long-term reversibility and its potential use in technological applications. Cycling studies were conducted over six absorption/desorption cycles between 480 °C (desorption) and 425 °C (absorption) (Fig.3.8a). A system pressure of ~27 bar was utilised to ensure full absorption and desorption could occur during the cycling studies. Over the course of the 6 consecutive absorption/desorption cycles, the hydrogen capacity of the sample decreased gradually, as seen in Fig. 3.8a. For these conditions, the hydride desorbed 4.6 wt% H_2 for the first desorption with ~92% of hydrogen being desorbed after ~35 min. The sample then absorbed 4.08 wt% H_2 with 97 % being absorbed in less than 30 min. After the first cycle, the capacity of $\text{Mg}(\text{H}_{0.85}\text{F}_{0.15})_2$ was reduced by 19 % and over the 6 cycles the sample lost a total of ~27 % capacity. Sintering of the Mg in the sample is responsible for the decrease in capacity (clearly impacting kinetics) and was confirmed by visual observation of flakes inside the sample after cycling. The cycling measurement was stopped after absorption, at which point XRD was undertaken (Fig. 3.8b). Quantitative analysis shows that two $\text{Mg}(\text{H}_x\text{F}_{1-x})_2$ phases were present, both of which are H-rich, along with Mg metal, confirming what was previously observed in the absorption stage of the PCI experiment. The main phase is $\text{Mg}(\text{H}_{0.89}\text{F}_{0.11})_2$ and the other is $\text{Mg}(\text{H}_{0.47}\text{F}_{0.53})_2$.

3.4. Conclusions

A range of $\text{Mg}(\text{H}_x\text{F}_{1-x})_2$ ($x = 1, 0.95, 0.85, 0.70, 0.50, 0$) solid solutions have been synthesised by ball milling quantitative ratios of MgH_2 and MgF_2 followed by annealing under a hydrogen backpressure. Their potential use as hydrogen storage or thermal energy storage materials has been examined by *in-situ* synchrotron XRD, DSC-TGA-MS and PCI analysis. Thermal studies were carried out on all $\text{Mg}(\text{H}_x\text{F}_{1-x})_2$ mixtures concluding that increased F content increases the thermal stability and decreases the absorption/desorption kinetics compared to pure MgH_2 . As such, decomposition occurs in a single step with DSC data showing a maximum rate of H_2 desorption at 434 °C for $\text{Mg}(\text{H}_{0.85}\text{F}_{0.15})_2$, with a practical hydrogen capacity of $4.6 \pm 0.2 \text{ H}_2 \text{ wt\%}$ (theoretical 5.4 wt% H_2). An extremely stable $\text{Mg}(\text{H}_{0.43}\text{F}_{0.57})_2$ phase is formed upon the decomposition of each Mg–H–F composition of which the remaining H_2 is not released until after 505 °C. PCI measurements of $\text{Mg}(\text{H}_{0.85}\text{F}_{0.15})_2$ determined an enthalpy of decomposition of $73.6 \pm 1.2 \text{ kJ/mol H}_2$ and an entropy of $131.2 \pm 2 \text{ J/K/mol H}_2$. In comparison with MgH_2 , these values are decreased from 74.06 kJ/mol H_2 and 133.4 J/K/mol H_2 , respectively [13]. Cycling of $\text{Mg}(\text{H}_{0.85}\text{F}_{0.15})_2$ has been investigated over six cycles between 420 and 480 °C, with a reduction of 27 % of the practical hydrogen capacity of 4.6 wt% H_2 . This represents an increased cycling

temperature of ~ 80 °C compared to bulk MgH_2 which increases the thermal operating temperatures for technological applications, thereby increasing efficiency.

3.5. *Acknowledgements*

CEB, DAS and MP acknowledge the financial support of the Australian Research Council (ARC) for ARC Linkage grants LP120101848 and LP150100730, and CEB acknowledges the financial support of the ARC LIEF grants LE0775551 and LE0989180, which enabled the XRD and gas absorption/desorption measurements to be undertaken. DAS acknowledges the financial support of a Curtin University Postdoctoral Research Fellowship and MP acknowledges his ARC Future Fellowship FT160100303. The authors also acknowledge funding from the Australian Synchrotron (ANSTO), which enabled the research at the powder diffraction beamline to be undertaken.

3.6. References

- [1] M. Paskevicius, L.H. Jepsen, P. Schouwink, R. Černý, D.B. Ravnsbæk, Y. Filinchuk, et al. Metal borohydrides and derivatives—synthesis, structure and properties. *Chemical Society Reviews*. 46 (2017) 1565-634.
- [2] R. Mohtadi, S.-i. Orimo. The renaissance of hydrides as energy materials. *Nature Reviews Materials*. 2 (2016) 16091.
- [3] S.-i. Orimo, Y. Nakamori, J.R. Eliseo, A. Züttel, C.M. Jensen. Complex hydrides for hydrogen storage. *Chemical Reviews*. 107 (2007) 4111-32.
- [4] K.T. Møller, D. Sheppard, D.B. Ravnsbæk, C.E. Buckley, E. Akiba, H.-W. Li, et al. Complex Metal Hydrides for Hydrogen, Thermal and Electrochemical Energy Storage. *ENERGIES*. 10 (2017) 1645.
- [5] D.A. Sheppard, M. Paskevicius, T.D. Humphries, M. Felderhoff, G. Capurso, J. Bellosta von Colbe, et al. Metal hydrides for concentrating solar thermal power energy storage. *Applied Physics A*. 122 (2016).
- [6] J.F. Stampfer, C.E. Holley, J.F. Suttle. The Magnesium-Hydrogen System1-3. *Journal of the American Chemical Society*. 82 (2002) 3504-8.
- [7] D.L. Douglass. The formation and dissociation of magnesium alloy hydrides and their use for fuel storage in the hydrogen car. *Metallurgical and Materials transactions A*. 6 (1975) 2179.
- [8] Q. Lai, M. Paskevicius, D.A. Sheppard, C.E. Buckley, A.W. Thornton, M.R. Hill, et al. Hydrogen Storage Materials for Mobile and Stationary Applications: Current State of the Art. *Chemsuschem*. 8 (2015) 2789-825.
- [9] J.C. Crivello, R.V. Denys, M. Dornheim, M. Felderhoff, D.M. Grant, J. Huot, et al. Mg-based compounds for hydrogen and energy storage. *Applied Physics A*. 122 (2016) 85.
- [10] T.D. Humphries, D.A. Sheppard, C.E. Buckley. Recent advances in the 18-electron complex transition metal hydrides of Ni, Fe, Co and Ru. *Coordination Chemistry Reviews*. 342 (2017) 19-33.
- [11] McPhy Energy, <https://mcphy.com/en/>; [accessed 04/10/2023].
- [12] D.A. Sheppard, T.D. Humphries, C.E. Buckley. Sodium-based hydrides for thermal energy applications. *Applied Physics A*. 122 (2016) 406.
- [13] M. Paskevicius, D.A. Sheppard, C.E. Buckley. Thermodynamic Changes in Mechanochemically Synthesized Magnesium Hydride Nanoparticles. *Journal of the American Chemical Society*. 132 (2010) 5077-83.
- [14] M. Wierse, R. Werner, M. Groll. Magnesium hydride for thermal energy storage in a small-scale solar-thermal power station. *Journal of the Less Common Metals*. 172-174 (1991) 1111-21.
- [15] B. Bogdanović, B. Spliethoff. Active $MgH_2 \cdot Mg$ -systems for hydrogen storage. *International Journal of Hydrogen Energy*. 12 (1987) 863-73.
- [16] B. Bogdanovic, B. Spliethoff, A. Ritter. The Magnesium Hydride System for Heat-Storage and Cooling. *ZEITSCHRIFT FÜR PHYSIKALISCHE CHEMIE NEUE FOLGE*. 164 (1989) 1497-508.
- [17] B. Bogdanović, T.H. Hartwig, B. Spliethoff. The development, testing and optimization of energy storage materials based on the MgH_2 -Mg system. *International Journal of Hydrogen Energy*. 18 (1993) 575-89.
- [18] B. Bogdanovic, A. Ritter, B. Spliethoff. A Process Steam-Generator Based on the High-Temperature Magnesium Hydride Magnesium Heat-Storage System. *International Journal of Hydrogen Energy*. 20 (1995) 811-22.
- [19] M. Paskevicius, D.A. Sheppard, K. Williamson, C.E. Buckley. Metal hydride thermal heat storage prototype for concentrating solar thermal power. *Energy*. 88 (2015) 469-77.
- [20] D. Dong, T.D. Humphries, D.A. Sheppard, B. Stansby, M. Paskevicius, M.V. Sofianos, et al. Thermal optimisation of metal hydride reactors for thermal energy storage applications. *Sustainable Energy and Fuels*. 1 (2017) 1820-9.
- [21] W.E. Wentworth, E. Chen. Simple thermal decomposition reactions for storage of solar thermal energy. *Solar Energy*. 18 (1976) 205-14.
- [22] SunShot Vision Study, Chapter 5: Concentrating Solar Power Technologies, Cost, and Performance. US Department of Energy2012.
- [23] P.A. Ward, C. Corgnale, J.A. Teprovich, T. Motyka, B. Hardy, D. Sheppard, et al. Technical challenges and future direction for high-efficiency metal hydride thermal energy storage systems. *Applied Physics A*. 122 (2016) 462.

- [24] M. Felderhoff, B. Bogdanovic. High temperature metal hydrides as heat storage materials for solar and related applications. *Int J Mol Sci.* 10 (2009) 325-44.
- [25] D.A. Sheppard, T.D. Humphries, C.E. Buckley. What is old is new again. *Materials Today.* 18 (2015) 414-5.
- [26] T.D. Humphries, D.A. Sheppard, M.R. Rowles, M.V. Sofianos, C.E. Buckley. Fluoride substitution in sodium hydride for thermal energy storage applications. *Journal of Materials Chemistry A.* 4 (2016) 12170-8.
- [27] D.A. Sheppard, C. Corgnale, B. Hardy, T. Motyka, R. Zidan, M. Paskevicius, et al. Hydriding characteristics of NaMgH₂F with preliminary technical and cost evaluation of magnesium-based metal hydride materials for concentrating solar power thermal storage. *RSC Advances.* 4 (2014) 26552-62.
- [28] P.A. Ward, C. Corgnale, J.A. Teprovich, T. Motyka, B. Hardy, B. Peters, et al. High performance metal hydride based thermal energy storage systems for concentrating solar power applications. *Journal of Alloys and Compounds.* 645 (2015) S374-S8.
- [29] S. Deledda, A. Borissova, C. Poinsignon, W.J. Botta, M. Dornheim, T. Klassen. H-sorption in MgH₂ nanocomposites containing Fe or Ni with fluorine. *Journal of Alloys and Compounds.* 404 (2005) 409-12.
- [30] A. Yavari, A. Lemoulec, F. Decastro, S. Deledda, O. Friedrichs, W. Botta, et al. Improvement in H-sorption kinetics of MgH powders by using Fe nanoparticles generated by reactive FeF addition. *Scripta Materialia.* 52 (2005) 719-24.
- [31] P. Jain, V. Dixit, A. Jain, O. Srivastava, J. Huot. Effect of Magnesium Fluoride on Hydrogenation Properties of Magnesium Hydride. *ENERGIES.* 8 (2015) 12330.
- [32] L.-P. Ma, P. Wang, H.-M. Cheng. Hydrogen sorption kinetics of MgH₂ catalyzed with titanium compounds. *International Journal of Hydrogen Energy.* 35 (2010) 3046-50.
- [33] I.E. Malka, M. Pisarek, T. Czujko, J. Bystrzycki. A study of the ZrF₄, NbF₅, TaF₅, and TiCl₃ influences on the MgH₂ sorption properties. *International Journal of Hydrogen Energy.* 36 (2011) 12909-17.
- [34] S.A. Pighin, G. Urretavizcaya, F.J. Castro. Study of MgH₂ + NbF₅ mixtures: Formation of MgH_{2-x}F_x solid solutions and interaction with hydrogen. *International Journal of Hydrogen Energy.* 40 (2015) 4585-96.
- [35] S.A. Pighin, G. Urretavizcaya, F.J. Castro. Reversible hydrogen storage in Mg(H_xF_{1-x})₂ solid solutions. *Journal of Alloys and Compounds.* 708 (2017) 108-14.
- [36] K.S. Wallwork, B.J. Kennedy, D. Wang. The high resolution powder diffraction beamline for the Australian Synchrotron. *Synchrotron Radiation Instrumentation: Ninth International Conference on Synchrotron Radiation Instrumentation.* AIP Publishing 2007. pp. 879-82.
- [37] P. Pathak, N. Vasavada. Thermal expansion of NaCl, KCl and CsBr by X-ray diffraction and the law of corresponding states. *Acta Crystallogr A.* 26 (1970) 655-8.
- [38] I.-K. Suh, H. Ohta, Y. Waseda. High-temperature thermal expansion of six metallic elements measured by dilatation method and X-ray diffraction. *Journal of Materials Science.* 23 (1988) 757-60.
- [39] G. Vidal-Valat, J.-P. Vidal, C.M. Zeyen, K. Kurki-Suonio. Neutron diffraction study of magnesium fluoride single crystals. *Acta Crystallographica Section B Structural Crystallography and Crystal Chemistry.* 35 (1979) 1584-90.
- [40] F.H. Ellinger, C.E. Holley, B.B. McInteer, D. Pavone, R.M. Potter, E. Staritzky, et al. The Preparation and Some Properties of Magnesium Hydride. *Journal of the American Chemical Society.* 77 (1955) 2647-8.
- [41] C.E. Messer. Hydrides versus fluorides: Structural comparisons. *Journal of Solid State Chemistry.* 2 (1970) 144-55.
- [42] M. Polanski, T. Płociński, I. Kunce, J. Bystrzycki. Dynamic synthesis of ternary Mg₂FeH₆. *International Journal of Hydrogen Energy.* 35 (2010) 1257-66.
- [43] B. Bogdanović, A. Reiser, K. Schlichte, B. Spliethoff, B. Tesche. Thermodynamics and dynamics of the Mg-Fe-H system and its potential for thermochemical thermal energy storage. *Journal of Alloys and Compounds.* 345 (2002) 77-89.
- [44] Astron optical material, https://www.astron-japan.co.jp/pdf/b01_Optical_Material_2010.pdf; 2017 [accessed 04/10/2023].
- [45] Ecreativeworks & CDS, 316 Stainless Steel Mechanical Properties, <https://www.ezlok.com/technical-info/mechanical-properties/316-stainless-steel>; 2016 [accessed 04/10/2023].

- [46] W.H. Baur. Rutile-type compounds. V. Refinement of MnO_2 and MgF_2 . *Acta Crystallographica Section B Structural Crystallography and Crystal Chemistry*. 32 (1976) 2200-4.
- [47] T. Noritake, M. Aoki, S. Towata, Y. Seno, Y. Hirose, E. Nishibori, et al. Chemical bonding of hydrogen in MgH_2 . *Applied Physics Letters*. 81 (2002) 2008-10.
- [48] M. Polanski, T.K. Nielsen, Y. Cerenius, J. Bystrzycki, T.R. Jensen. Synthesis and decomposition mechanisms of Mg_2FeH_6 studied by in-situ synchrotron X-ray diffraction and high-pressure DSC. *International Journal of Hydrogen Energy*. 35 (2010) 3578-82.
- [49] S.S.S. Raman, D.J. Davidson, J.L. Bobet, O.N. Srivastava. Investigations on the synthesis, structural and microstructural characterizations of Mg-based K_2PtCl_6 type (Mg_2FeH_6) hydrogen storage material prepared by mechanical alloying. *Journal of Alloys and Compounds*. 333 (2002) 282-90.
- [50] W. Klostermeier, E.U. Franck. Liquid-Mixtures of Sodium and Sodium Hydride at High-Pressures and Temperatures. *Berichte Der Bunsen-Gesellschaft-Physical Chemistry Chemical Physics*. 86 (1982) 606-12.
- [51] B. Bogdanovic, H. Hofmann, A. Neuy, A. Reiser, K. Schlichte, B. Spliethoff, et al. Ni-doped versus undoped Mg- MgH_2 materials for high temperature heat or hydrogen storage. *Journal of Alloys and Compounds*. 292 (1999) 57-71.

4. Fluorine Substitution in Magnesium Hydride as a Tool for Thermodynamic Control

T.D. Humphries, J. Yang, R.A. Mole, M. Paskevicius, J.E. Bird, M.R. Rowles, M.S. Tortoza, M.V. Sofianos, C.E. Buckley. Fluorine Substitution in Magnesium Hydride as a Tool for Thermodynamic Control. The Journal of Physical Chemistry C. 124 (2020) 9109 - 17. <https://doi.org/10.1021/acs.jpcc.9b11211>

This chapter consists of a published article which describes the physical properties of the $\text{Mg}(\text{H}_x\text{F}_{1-x})_2$ system, which was studied by XRD, inelastic neutron spectroscopy and thermal conductivity. Moreover, these measurements were verified by DFT calculations. This investigation is a progression on the previous Chapter, in which the focus is to analyse and discover other properties of this material to reach potential as a candidate for a TES system. Furthermore, the thermal transport properties for the $\text{Mg}(\text{H}_x\text{F}_{1-x})_2$ system, including thermal conductivity, diffusivity, and heat capacity, were determined.

Abstract

Metal hydrides continue to vie for attention as materials in multiple technological applications including hydrogen storage media, thermal energy storage (TES) materials and hydrogen compressors. These applications depend on the temperature at which the materials desorb and reabsorb hydrogen. Magnesium hydride is ideal as a TES, although its practical operating temperature is capped at ~ 450 °C due to material degradation and high operating pressure. Fluorine substitution for hydrogen in magnesium hydride has previously been shown to increase the operating temperature of the metal hydride whilst limiting degradation, although full characterisation is required before technological application can be ensured. The present study characterises $\text{Mg}(\text{H}_x\text{F}_{1-x})_2$ solid solutions ($x = 1, 0.95, 0.70, 0.85, 0.50, 0$) by inelastic neutron spectroscopy, powder X-ray diffraction and thermal conductivity measurements, with the results being verified by density functional theory. For each experiment, a clear trend is observed throughout the series of solid-solutions, showing the possibility of tuning the properties of MgH_2 . As F^- substitution increases, the average Mg–H(F) bond distance elongates along the axial positions of the Mg–H(F) octahedra. Overall this leads to an increase in Mg–H bond strength and thermal stability, improving the viability of Mg–H–F as potential TES materials.

4.1. Introduction

For the global energy network to convert to a green hydrogen economy, four challenges must be met: (i) hydrogen production must primarily be from a renewable source; (ii) utilisation must be optimised including refuelling station infrastructure and fuel cells; (iii) hydrogen distribution must be safe and cost effective; and (iv) storage media for the hydrogen must be developed. There are a number of ways that hydrogen can be stored, including as a gas, cryogenic liquid, or chemically, e.g. within a metal hydride or ammonia [1, 2]. Metal hydrides, and in particular magnesium-based hydrides, have received enormous attention over the last 60 years for their potential as hydrogen storage materials [3-6]. This has largely been due to the relatively high abundance of magnesium metal in the Earth's crust and its relatively low cost of extraction [5]. In addition, magnesium hydride has been shown to be highly reversible when used as a hydrogen storage material at a modest temperature. The binary hydride (MgH_2) has a theoretical hydrogen storage capacity of 7.7 wt% H_2 , but due to its relatively high enthalpy of hydrogen desorption of 74 kJ/mol H_2 and entropy of 133 J/K/mol. H_2 , its operational temperatures are limited to only 300 °C at 1 bar H_2 pressure [7], ensuring that MgH_2 will never find technological application as a reversible fuel store for vehicular applications, as temperatures of ~ 85 °C are preferred [8]. As such, MgH_2 has alternatively been considered as a material for thermal energy storage (TES) applications, such as storing heat from the sun to use at periods of weak solar irradiation, as a thermal battery. However, it cannot operate above ~ 450 °C due to the tendency for magnesium to agglomerate, thus reducing its long term hydrogen storage capacity and also reducing the reaction kinetics [9].

Many studies have been published in which issues with kinetics and agglomeration have been addressed by innovative approaches including nano-sizing, infiltration into porous scaffolds, and the incorporation of additives, including TiB₂ as a particle refinement agent [4, 5, 9, 10]. All of these methods have proven successful in some regard and combinations of methods seem to be ideal. Recently, fluoride substitution for hydrogen in the Mg–H system has been reported in which solid–solutions are synthesised by ball milling MgH₂ and MgF₂ in various ratios and also studied by density functional theory calculations [10-12]. Fluorine substituted magnesium hydride solid solutions, Mg(H_xF_{1-x})₂, were deemed to be stabilised compared to pure MgH₂ and attributed to the positive enthalpy of mixing ($\Delta H_{mix} > 0$) [11].

The decomposition temperature of Mg(H_xF_{1-x})₂ was determined *via* simultaneous differential scanning calorimetry – thermogravimetry (DSC-TGA) and powder X-ray diffraction (XRD) experiments. In addition, the thermodynamics of hydrogen release for Mg(H_{0.85}F_{0.15})₂ were determined to be 73.6 kJ/mol.H₂ and 131.2 J/K/mol.H₂ close to that of pure MgH₂. Interestingly, this material was shown to cycle at high temperatures, between 425 and 480 °C. Despite the determination of these physical properties, little else is known regarding the fluorine substituted materials, although a smattering of analysis techniques have been used to study the physical properties of pure MgH₂ (other than thermodynamics and kinetics) including powder neutron and X-ray diffraction [13], NMR spectroscopy [14, 15], vibrational spectroscopy [16-20] and thermal conductivity [21, 22].

With Mg(H_{0.85}F_{0.15})₂ showing favourable operating temperatures as a thermal energy storage material, additional exploration of the physical properties for Mg(H_xF_{1-x})₂ solid solutions have herein been undertaken by inelastic neutron spectroscopy, powder X-ray diffraction and thermal conductivity measurement. In addition, DFT calculations have been performed to corroborate the inelastic neutron spectroscopy and powder X-ray diffraction results. This has allowed a full comparison on the stability of fluorine substitution in magnesium hydride.

4.2. Experimental Section

4.2.1. Sample Preparation

All manipulations of chemicals were undertaken in an argon atmosphere using an Mbraun Unilab glovebox to prevent air exposure and to minimise oxygen (O₂ < 1 ppm) and water (H₂O < 1 ppm) contamination. Mg(H_xF_{1-x})₂ (x = 1, 0.95, 0.85, 0.70, 0.50, 0) samples were prepared by ball milling (BM) various ratios of MgH₂ and MgF₂ (Sigma-Aldrich, >99.99 %) at room temperature. MgH₂ powder (95 wt% purity from Rietveld refinement of X-ray diffraction data) was synthesised by annealing Mg powder (Aldrich, >99 %) at 400 °C under 30 bar hydrogen pressure for 18 hours. The full synthesis description is found in ref [10]. BM of MgH₂ and MgF₂ was undertaken at 400 rpm for 40 hours in an Across International Planetary Ball Mill (PQ-N04) with a ball-to-powder mass ratio of 50:1 using stainless steel vials and balls (6 and 8 mm in diameter) under

an Ar atmosphere. After milling, samples were annealed under a hydrogen atmosphere of 60 bar at 450 °C for a period of 90 hours to form solid solutions.

4.2.2 Synchrotron X-ray Characterisations

Synchrotron powder X-ray diffraction (SR-XRD) was performed on the Powder Diffraction beamline at the Australian Synchrotron in Melbourne, Australia [23]. Without exposure to air, the $\text{Mg}(\text{H}_x\text{F}_{1-x})_2$ powders were loaded into borosilicate or quartz capillaries (outer diameter 0.7 mm, wall thickness 0.01 mm) that were then, using graphite ferrules, mounted in 1/16" tube fittings connected to a gas manifold. One-dimensional SR-XRD patterns (monochromatic X-rays with $\lambda = 1.0003896$ or 0.8263076 Å) were collected using a Mythen microstrip detector [24] with an exposure time of 54 s per pattern. The wavelength and line shape parameters were calibrated against an external standard of LaB_6 (NIST SRM660c). The capillaries were continuously oscillated through 120° during exposure to improve powder averaging. Diffraction patterns were quantitatively analysed using the Rietveld refinement method [25, 26] with TOPAS software (Bruker-AXS) [27].

4.2.3 Inelastic Neutron Scattering Characterisations

Inelastic neutron scattering (INS) data were collected using the Pelican cold-neutron time-of-flight spectrometer located at the OPAL reactor Lucas Heights, Australia. Samples were mounted in rectangular, flat plate, aluminium sample cans, with the thickness optimised for a 10 % scatter, i.e. to minimise multiple scattering. The sample cans were mounted at 45° to the incident beam and placed in a vacuum chamber at room temperature. The instrument was aligned for 4.69 Å neutrons and the choppers were run in a time focusing configuration at either 100 or 200 Hz. The resolution at the elastic line was 135 µeV. An empty can was subtracted to determine the background contribution and the data was normalised using data collected with a vanadium standard that had the same geometry as the sample can. All data manipulations were performed using the freely available software Lamp [28]. Data were collected as $S(Q, \omega)$ [i.e. scattering cross-section as a function of scattering wavevectors (Q) and phonon frequency (ω)], and these were transformed to a generalised density of states using formula (4.1), where k_b is Boltzmann's constant, T is temperature and \hbar is the reduced Planck's constant [29].

$$g(\omega) = \int \frac{\omega}{Q^2} S(Q, \omega) (1 - e^{\frac{-\hbar\omega}{k_b T}}) dQ \quad (4.1)$$

4.2.2. Thermal Property Characterisation

The thermal conductivity (λ_{TC}), thermal diffusivity (k) and the heat capacity per unit volume (C) of 5 ratios of F^- and H^- in $Mg(H_xF_{1-x})_2$ were measured using a TPS 500S (Hot Disk, Thermtest). Measurements were undertaken in an argon atmosphere at a constant ambient temperature, measured by a K type thermocouple. 1.5 g of $Mg(H_xF_{1-x})_2$ ($x = 1, 0.95, 0.85, 0.70, 0.50, 0$) were pressed in a die (13 mm diameter) using a manual hydraulic press (370 MPa of pressure for 5 minutes). A nickel double-spiral sensor (2 mm radius), laminated by electrically insulating Kapton was firmly clamped co-centrally between the pellets. 10 measurements per sample were conducted, with 15 minutes in between each measurement to allow the sample and sensor to cool.

4.2.3. First-Principle Calculations

Density Functional Theory (DFT) based lattice dynamic calculations were performed to complement the INS measurements in order to better understand the stability and bonding in $Mg(H_xF_{1-x})_2$ systems. All DFT calculations were performed with VASP [30] under a generalised gradient approximation (GGA) using the Perdew-Burke-Ernzerhof (PBE) functionals together with the projector augmented wave (PAW) potentials [31, 32]. The energy cut-off for planewave expansion was set to 500 eV. The minimum-energy configurations for MgH_2 and MgF_2 were optimised with a dense ($15 \times 15 \times 15$) Monkhorst-Pack K -point mesh. For all subsequent phonon calculations, geometry optimisations were relaxed with an energy convergence of 10^{-7} eV and forces less than 10^{-6} eV/atom.

In order to account for the statistically disordered nature of F-substitution in MgH_2 , all unique configurations of F-substituted MgH_2 supercells were sampled for calculating the corresponding thermodynamic stabilities and phonon density of states (DOS). Here, $Mg(H_xF_{1-x})_2$ at different concentrations ($x = 0.95, 0.90, 0.85, 0.80, 0.75, 0.70$ and 0.50) were simulated, which led to a total number of configurations of 34, 33, 30, 27, 26, 2, 2, respectively, for each nominated F concentration. Supercells of sizes ($1 \times 1 \times 1$) [for $x = 0.50$], ($5 \times 1 \times 1$) and ($1 \times 1 \times 5$) [for all other fluoride concentrations] were used with corresponding Monkhorst-Pack K -point meshes of ($6 \times 6 \times 9$), ($2 \times 6 \times 6$) and ($6 \times 6 \times 2$), respectively. Because MgH_2 adopts an orthorhombic lattice, supercell expansions along both the a and c axis were considered, as well as several possible unique F^- positions at a given x and supercell size. Thermodynamic stabilities (formation energies ΔE_f) for the substituted structure were modelled according to the following reaction:



Such that:

$$\Delta E_f = E[Mg(H_xF_{1-x})_2] - E[Mg] - xE[H_2] - (1-x)E[F_2] \quad (4.3)$$

where E is the total energy from DFT calculations that contains both the ionic and electronic contributions. Phonon DOS were calculated using a finite-displacement method as implemented in PHONOPY interfaced with VASP [33]. For $Mg(H_xF_{1-x})_2$ systems simulated with different supercells, the corresponding supercells and K -point meshes used in phonon calculations are summarised in Table 4.1.

The theoretically calculated phonon DOS were subsequently re-scaled to consider the differences in the inelastic neutron scattering cross sections for different elements, as adopted by Bansal *et al.* [34], where the neutron weighted DOS was calculated according to the following formula:

$$G = \sum_i \frac{\sigma_i}{m_i} g_i / N_{tot} \quad (4.4)$$

Here σ_i is either the coherent and incoherent neutron scattering cross-section for the i -th element, m_i is the corresponding atomic mass, g_i is the partial phonon density-of-states for the i -th element and N_{tot} is the total number of atoms in the supercell [35]. To effectively compare the phonon DOS across systems with different F concentrations, the phonon DOS at any given F concentration was averaged across all supercell configurations (N_{config}) considered at that concentration according to:

$$\overline{DOS(E)} = \frac{1}{N_{config}} \sum_{i=1}^{N_{config}} DOS_i(E) \quad (4.5)$$

No additional weighting parameter, such as the relative stabilities of different configurations (at a fixed F concentration) was used, because the differences in the calculated formation energies were almost negligible [see the Results section].

Table 4.1. Supercells and K -point meshes chosen for finite-displacement phonon calculations in VASP. Also shown is the Γ -centred K -point grids used for phonon density-of-states integrations. Note that the supercell for phonon simulations were specified with respect to the supercells for calculating the substitution formation energies, not the primitive MgH_2 unit cell.

Defect supercell	Phonon supercell	Phonon meshes	K -point	DOS integration grid
$1 \times 1 \times 1$	$3 \times 3 \times 3$	$2 \times 2 \times 3$		$20 \times 20 \times 20$
$5 \times 1 \times 1$	$1 \times 2 \times 2$	$2 \times 3 \times 3$		$10 \times 10 \times 10$
$1 \times 1 \times 5$	$2 \times 2 \times 1$	$3 \times 3 \times 2$		$10 \times 10 \times 10$

4.3. Results and Discussion

4.3.1. Powder X-ray diffraction

MgH₂ and MgF₂ both exist in the aristotypic rutile-type structure in space group P4₂/mnm. The lattice parameters measured after ball milling and annealing in this study are provided in Tables 4.2, II.1 and II.2. These values agree with the literature values for MgH₂ and MgF₂, respectively [36, 37]. Despite the larger covalent character exhibited by MgH₂, the lattice parameters for MgH₂ are smaller than that observed for MgF₂ [12, 38, 39]. Along with the fact that MgF₂ is significantly more stable than MgH₂, it is expected that Mg–F bonds be shorter. In fact, the axial Mg–H bond distances are 1.935973(6) Å compared to 1.98114(2) Å for the equivalent Mg–F bonds. Since F[−] is highly electronegative, it will also form small covalent interactions between neighbouring F[−], which not only creates further stabilisation, but allows the Mg–F bond distance to increase [12]. This has been illustrated using electron density maps derived from theoretical calculations and X-ray diffraction measurements [12, 39, 40]. In MgF₂, electron density between the F[−] atoms is observed, while most of the electron density has been withdrawn from the Mg²⁺ by the F[−]. In MgH₂, some anisotropic charge distribution between the Mg and H and H atoms suggesting partial covalency [12].

From Table 4.2 it can be seen that the greatest difference in lattice parameters is experienced in the a-axis of the unit cell with a 2.3 % decrease from MgF₂ to MgH₂ compared to 1.0 % in the c axis. This manifests into an overall decrease in unit cell volume of 5.4 % for MgH₂. The anisotropic nature of the lattice parameters points to the stability of the octahedral chains that run in the direction of the c-axis (Figure 4.1) [36]. These chains, with four coplanar equatorial Mg–H(F) bonds, are connected via corner-sharing with four symmetrically equivalent chains, and are therefore quite stable. Thus there is only a 1.5 % change in the equatorial Mg–H(F) bonds compared to 2.3 % for the axial Mg–H(F) bonds.

Upon ball milling and annealing MgH₂ and MgF₂ in varying ratios (Table 4.2), Mg(H_xF_{1-x})₂ (x = 1, 0.95, 0.85, 0.70, 0.50, 0) was produced. No peak splitting was observed in the diffraction patterns, indicating that solid solutions were formed [10]. The lattice parameters, and by association, unit cell volume and bond distances increase with increasing F[−] content, with each following a quadratic trend. Analysis was undertaken by quantitative Rietveld refinement of the SR-XRD data using Topas (illustrated in Figure II.1 and Table II.1) [27]. Fifteen individual Mg(H_xF_{1-x})₂ structure phases (11 for MgH_{0.85}F_{0.15}) were refined allowing the lattice parameters to refine freely and H/F occupancy was calculated from the lattice parameters assuming Vegards Law [41]. The fractional atomic coordinate of H/F in the 4f position was fixed at 0.303 as it did not move significantly during refinement.

Table 4.2 details the weight averaged lattice parameters, while Figure 4.2 illustrates the data by focusing on the (110) Bragg peak. The lattice parameters of each phase are detailed in Table II.1) Phase segregation is apparently minimal for all samples, which is in contrast with a recent study on NaH_xF_{1-x} (x = 1, 0.95, 0.85, 0.70, 0.50, 0),

Table 4.2. Structural properties of $Mg(H_xF_{1-x})_2$ ($x = 1, 0.95, 0.85, 0.70, 0.50, 0$) materials measured by SR-XRD at room temperature. Estimated standard deviations (esd's) are in parentheses.

Sample name	Lattice parameter (Å)		Mg–H(F) (Å)	
	A	c	Axial	Equatorial
MgH ₂	4.51795(1) 4.516(8) ^a	3.02257(1) 3.020(5) ^a	1.935976(6) ---	1.966804(5) ---
Mg(H _{0.95} F _{0.05}) ₂	4.52458(1)	3.02345(1)	1.946(3)	1.964(2)
Mg(H _{0.85} F _{0.15}) ₂	4.54284(1)	3.02982(1)	1.946637(4)	1.974028(4)
Mg(H _{0.70} F _{0.30}) ₂	4.56514(4)	3.04023(3)	1.95619(2)	1.98201(1)
Mg(H _{0.50} F _{0.50}) ₂	4.59225(3)	3.04441(2)	1.9716(8)	1.9860(5)
MgF ₂	4.62337(5) 4.6249(1) ^b	3.05214(5) 3.0520(1) ^b	1.98114(2) ---	1.99700(2) ---

^a Ref [36], ^b Ref [37]

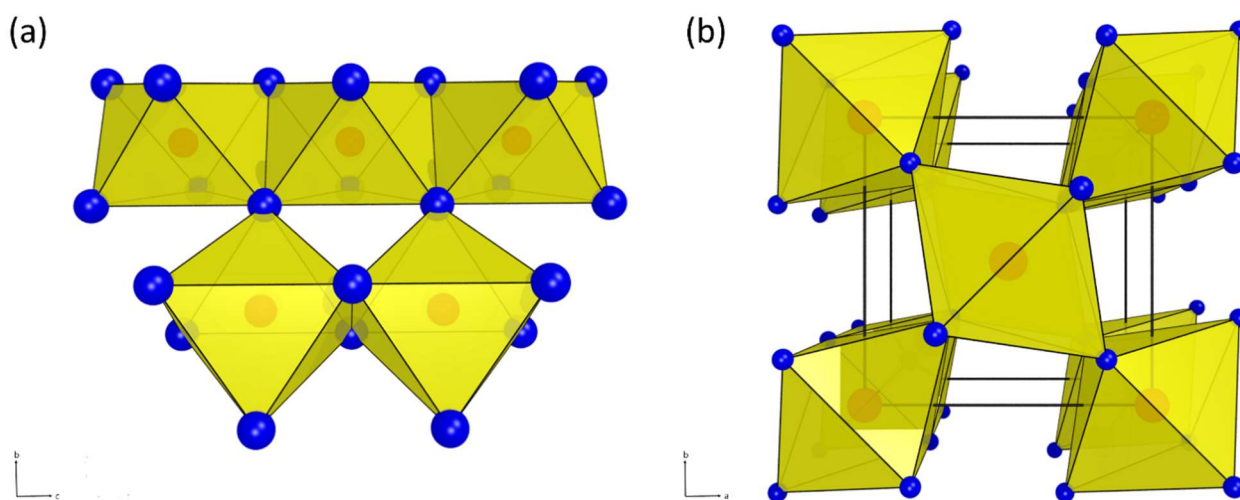


Figure 4.1. Representative views of $Mg(H_xF_{1-x})_2$; (a) $Mg-H(F)_6$ octahedral units viewed along the a -axis and (b) along the c axis. Mg atoms represented as red spheres, H(F) atoms as blue spheres and $Mg-H(F)_6$ octahedra represented with yellow faces.

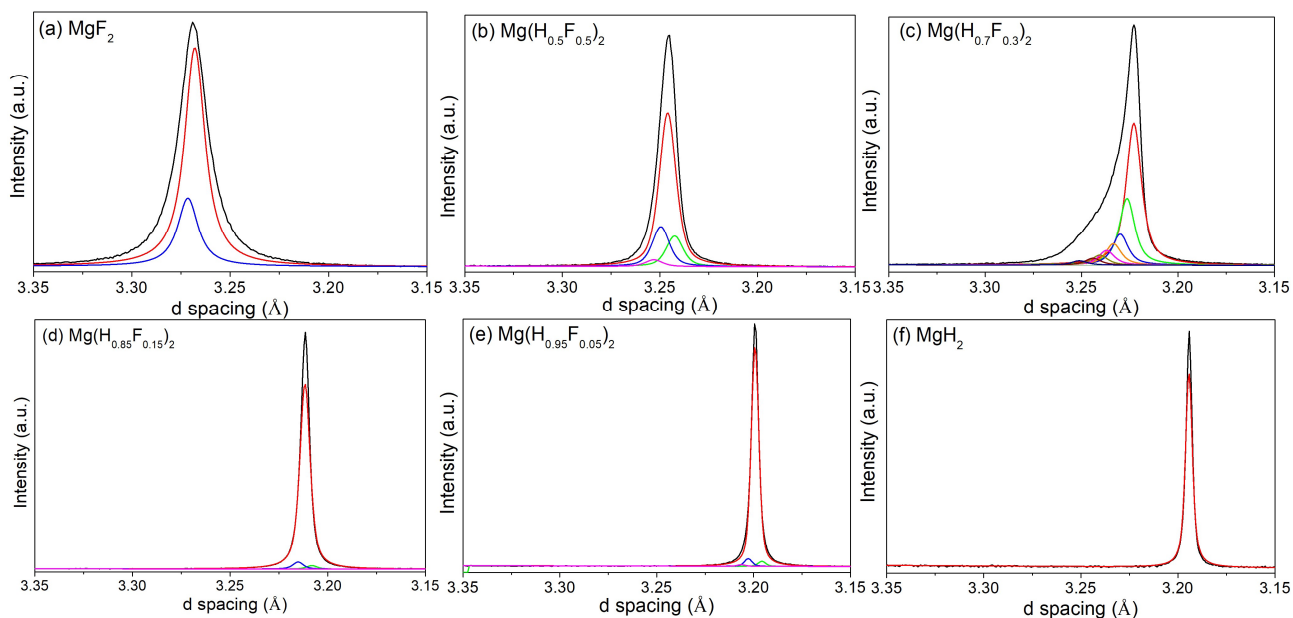


Figure 4.2. Phase distribution in $Mg(H_xF_{1-x})_2$ solid solutions determined by SR-XRD as observed at the (110) Bragg peak. $T = 27^\circ\text{C}$.

where a statistical distribution of phases was observed after annealing for 6 days [42]. The only sample exhibiting a large dispersion of phases was $\text{Mg}(\text{H}_{0.70}\text{F}_{0.3})_2$, which is most likely due to insufficient annealing during synthesis. The tail of the peak tends towards higher d spacing of which is indicative of a large spread of phases with increased F content.

Each of these solid solutions was modelled using DFT in order to complement the XRD and INS data. The optimised DFT supercells were first analysed to ensure that the unit cell parameters and bond distances agreed with the experimental data. Table II.3 details the unit cell volumes, lattice parameters and bond distances for the supercells and compares them to the experimental data. For each of the parameters a similar trend observed between the calculated and measured data sets. In addition, each of the respective experimental and theoretical data sets agree to within 3.1%, of which the largest deviation is for the MgF_2 unit cell volume. Overall, the significant agreement suggests that the calculated DFT data represents a quality model to fit against the INS data.

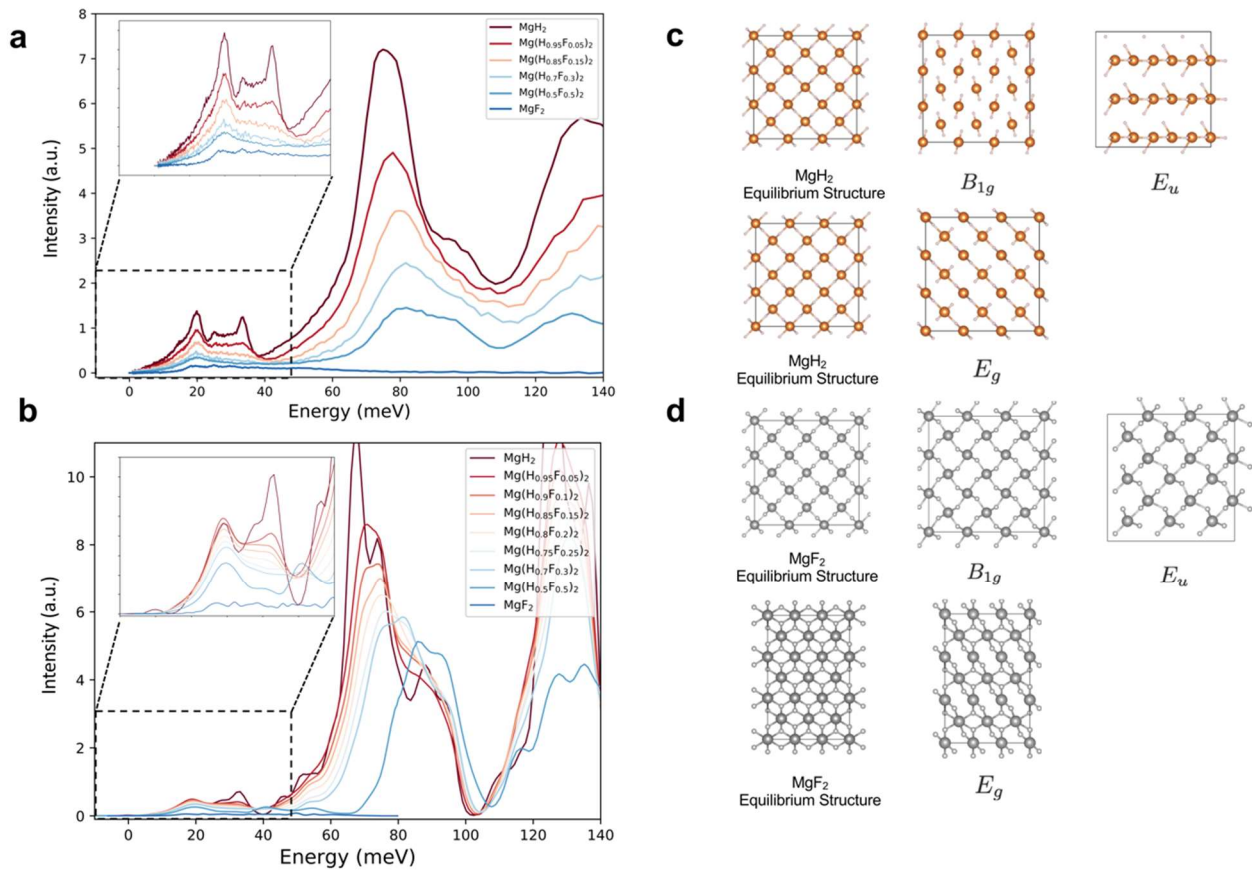


Figure 4.3. Phonon density-of-states of $\text{Mg}(\text{H}_x\text{F}_{1-x})_2$ solid solutions determined by (a) INS (intensity is normalised) and (b) DFT-based lattice dynamic calculations. For calculated data the contributions from different constituent atoms are weighted by their corresponding inelastic neutron scattering cross-sections. For MgF_2 , there are no phonon branches beyond 80 meV. Insets show the enlarged low-energy part of the phonon density-of-states. (c-d) show the pattern of atomic vibrations for the B_{1g} , E_u and E_g phonon modes for MgH_2 and MgF_2 .

4.3.2. Inelastic Neutron Spectroscopy

The INS spectra, for each of the Mg–H–F compositions, were measured to determine the similarities in the structural dynamics between the solid solutions and pure components (Figure 4.3). The spectrum for MgH₂ agrees with previously reported ones [17, 18]. There are three low intensity vibrations below 40 meV at 20, 25 and 33 (B_{1g}) meV, which have been previously ascribed primarily to in-phase vibrations of hydrogen atoms with in-phase vibrations of the Mg atoms (lattice vibrations) [17]. The broad mode between 60 – 105 meV is described as H-related E_u optic modes, which are three-fold degenerated, and the large widths suggest a large dispersion of the optic phonon branches and consequently strong H–H interactions [17]. Above 105 meV, a very broad region is observed that is attributed to the E_g mode, which is a two-fold degenerate mode that corresponds to the asymmetric bending of the H(F)–Mg–H(F) bond (equatorial) in the [001] plane parallel to the c -axis [43]. A schematic illustration of these three vibrational modes for MgH₂ and MgF₂ is shown in Figures 4.3(c) and 4.3(d). To complement the INS results, DFT-based lattice dynamics were applied to model the generalised phonon density-of-states (GDOS). Upon weighting the results with the inelastic neutron scattering cross-sections for different elements, Figure 4.3(b) shows an excellent agreement between theoretical GDOS and INS spectrum for MgH₂. This validates our theoretical calculations, which allows us to extract useful information for understanding the influence of F[−] doping on the lattice dynamics for the systems as probed by the INS experiments. Notice that under harmonic approximations, GDOS for MgH₂ shows a small non-vanishing GDOS at negative phonon energies, suggesting that MgH₂ is anharmonic and thus MgH₂ is thermally stabilised at 300 K. Such a feature is not observed in all F[−] doped structures. As F[−] content in the solid solution increases, a number of changes to the INS spectra are observed. The vibration at 33 meV becomes broader and almost vanishes along with the peak at 25 meV, while the vibration at 20 meV remains. This can be attributed to the fact that the B_{1g} mode for MgF₂ is much softer than that of MgH₂, which occurs at around 9.1 meV, as revealed by lattice dynamic calculations. The most intense peak at 75 meV gradually shifts to higher energy with higher F[−] content, to 83 meV for MgH_{0.50}F_{0.50}, which also agrees well with GDOS obtained from lattice dynamic calculations. Atomic vibrations within this energy range are typically dominated by the optical E_u modes Figure 4.3(c) arising from the vibrations of H sublattices, an upshift in the energy thus indicates this mode is significantly stiffened by the addition of fluorine in the system. Such a shift in the frequencies of optical phonon reflects the enhancement of ionicity in the Mg(H_{*x*}F_{*1-x*})₂ with increasing fluoride content, as F[−] is of larger electronegativity to hydrogen, which consequently draws more electrons from Mg compared to H[−].

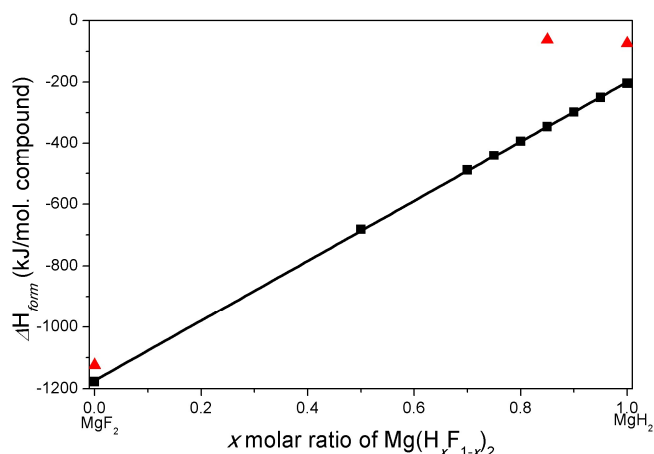


Figure 4.4. Formation energies for $Mg(H_xF_{1-x})_2$. Black squares correspond to DFT calculated formation energies, red triangles correspond to experimentally derived formation energies [7, 10, 44].

4.3.3. Thermodynamics of $Mg(H_xF_{1-x})_2$

DFT modelling enables the extraction of more information than just the phonon density-of-states, with formation energy (ΔH_{form}) of $Mg(H_xF_{1-x})_2$ solid solutions being an indicator for material stability. Figure 4.4 and Table II.4 illustrate a linear trend with ΔH_{form} becoming more negative as the concentration of F^- increases in $Mg(H_xF_{1-x})_2$. As such, the theoretical ΔH_{form} for MgH_2 and MgF_2 is -204 and -1178 kJ/mol of compound, respectively. This indicates that as F^- substitution increases so does the thermal stability of the compound. Experimental thermodynamic data do not mirror this trend. Although the experimental and DFT calculated ΔH_{form} for MgF_2 differs by only 4.5% (experimental $\Delta H_{form} = -1124$ kJ/mol of compound) [44], the DFT value for MgH_2 is 175% the magnitude of the experimentally determined value of -74.06 ± 0.42 kJ/mol [7]. These two data points do suggest that ΔH_{form} becomes more negative with F^- content, but the experimental value for $Mg(H_{0.85}F_{0.15})_2$ of -62.6 ± 0.2 kJ/mol does not follow a linear trend and actually becomes less negative compared to MgH_2 .

The experimental ΔH_{form} for MgH_2 and $Mg(H_{0.85}F_{0.15})_2$ is derived from the enthalpy of hydrogen desorption (ΔH_{des}) determined by PCI (Pressure–concentration isotherm) analysis. Therefore an assumption must be made in that there is no pressure hysteresis between the absorption and desorption process. For these particular materials, hysteresis has been shown not to occur and any artefact is likely due to the slow kinetics of the reaction process [7, 10]. As such these values can be expressed as ΔH_{form} . Pressure–concentration isotherm (PCI) analysis is the ideal method to determine the thermodynamics associated with the reaction of hydrogen release, in which the enthalpic and entropic contributions can be individually identified using a van't Hoff plot [45]. Unfortunately, PCI analysis has only been conducted on pure MgH_2 ($\Delta H_{des} = 74.06 \pm 0.42$ kJ/mol; $\Delta S_{des} = 133.4 \pm 0.7$ J/K/mol) [7] and $Mg(H_{0.85}F_{0.15})_2$ ($\Delta H_{des} = 62.6 \pm 0.2$ kJ/mol ; $\Delta S_{des} = 111.5 \pm 0.2$ J/K/mol) [10]. Although at first glance, the magnitude of ΔH_{des} and ΔS_{des} are both observed to decrease with increasing F^- content, which seems to be counterintuitive when claiming the system is becoming stabilised.

However, the magnitude of ΔS_{des} decreases to a larger extent than the magnitude of ΔH_{des} , resulting in ΔG_{des} becoming less negative as F^- content increased, implying that decomposition will occur at higher temperatures when under the same back pressure of H_2 . In short, ΔS_{des} has a larger impact on the temperature of decomposition than ΔH_{des} .

The difference between the DFT and experimentally determined enthalpy of formation may be attributed to the reaction pathways employed when determining ΔH_{form} . DFT calculations assume direct formation from the elements, whereas the measured values are determined based on the reversible reaction displayed in equation (4.2). The endothermic ΔH_{des} determined by PCI experiments includes the formation of pure MgF_2 of which is an exothermic reaction. Therefore, the exothermic formation of additional Mg-F bonds reduces the overall measured ΔH_{des} . During the formation of $Mg(H_xF_{1-x})_2$ from $MgF_2 + Mg$ the endothermic contribution encountered during the breaking of Mg-F bonds therefore decreases the ΔH_{form} compared to that expected if formed from the elements. As a result, ΔH_{form} determined by DFT calculations would be more negative than those determined experimentally.

The increased thermal stability with increasing F^- content has been demonstrated using DSC-TGA and as such the temperature of decomposition is a better measure of thermal stability than using ΔH_{form} calculated using DFT alone. In this study, ΔH_{form} was calculated at 0 K and therefore it is impossible to estimate the temperature of decomposition using these calculations, although it does provide a good qualitative estimate of stability. ΔS_{form} must be calculated in order to determine the temperature of formation/decomposition. The enthalpy and entropy determined by PCI analysis the temperature of formation under 1 bar H_2 to be 282 and 288 °C for MgH_2 and $MgH_{0.85}F_{0.15}$, respectively ($\Delta G = \Delta H - T\Delta S$, where $\Delta G = 0$).

4.3.4. Thermal Transport Properties of $Mg(H_xF_{1-x})_2$

If these $Mg(H_xF_{1-x})_2$ compounds are to be implemented as thermal energy storage materials, the thermal properties must be determined. The thermal transport properties of the $Mg(H_xF_{1-x})_2$ compounds are presented in Table 4.3. A non-linear relationship exists between the thermal transport properties and amount of H/F present (Figure 4.5). The data collected for MgF_2 of 0.676(6) W/m.K is lower than that measured in the literature of 11.6 W/m.K [46]. The measurement of thermal transport properties are highly susceptible towards sample preparation and measurement conditions, in this study the samples were measured as a pelletised powder (370 MPa), while a pre-melted MgF_2 pellet was used previously leading to an increased λ_{TC} . The results provided here are all self-consistent and comparable due to the identical sample preparation.

The thermal conductivity of MgH_2 was measured in this study as 2.08(3) W/m.K, where $k = 1.53(7)$ mm²/s and $C = 1.37(8)$ MJ/m³.K. λ_{TC} measured in this study is therefore reasonably close with literature values of 0.40 – 1.21 W/m.K [21, 47, 48]. The literature values were obtained from samples measured as a pellet

pressed at a pressure of 100 MPa with a $\lambda_{TC} = 0.70$ W/m·K being determined [21], while additional cold rolling enabled a measurement of 1.21 W/m.K [48]. The variation in results is therefore attributed to the effect of sample preparation conditions. Thermal properties are enhanced by phonon interactions,[49] hence smaller particle size, increased pressure and pre-melting enhance thermal transport properties. The sample measurements in this study were conducted under identical conditions under an Ar atmosphere. Thermal conductivity and diffusivity decrease with increasing F⁻ content, and is at a minima for MgH_{0.5}F_{0.5}, before a slight increase is observed for MgF₂. The heat capacity per unit volume of these materials appears to vary between 1.17(4) and 1.58(3) MJ/m³·K with a specific trend not being observed. In fact, the values for the F⁻ containing materials may be considered as being almost equivalent within error.

Overall, the λ_{TC} for these F-substituted materials are highly comparable to other metal hydride materials. For instance $\lambda_{TC} = 0.96$ W/m·K for NaBH₄ [50] and 0.06 – 4.5 W/m·K for NaAlH₄ depending on conditions [51, 52]. It was determined that an optimal value of ~5 W/m.K for a hydrogenated sample of LaNi_{4.9}Al_{0.3} allows for optimal hydrogen absorption kinetics, while a larger value only has a minor incremental influence [53]. Therefore, to gain technological application, it may be beneficial to enhance λ_{TC} by the addition a material such as exfoliated natural graphite [9, 21].

Table 4.3. Thermal Transport Properties of Mg(H_xF_{1-x})₂ measured at room temperature under Ar atmosphere. λ_{TC} is thermal conductivity (W/m.K), k is thermal diffusivity (mm²/s), and C is the heat capacity per unit volume (MJ/m³·K).

	λ_{TC} [W/m·K]	k [mm ² /s]	C [MJ/m ³ ·K]
MgH ₂	2.08(3)	1.53(7)	1.37(8)
MgH _{0.95} F _{0.05}	1.297(6)	0.98(4)	1.32(5)
MgH _{0.85} F _{0.15}	0.717(3)	0.49(1)	1.46(3)
MgH _{0.70} F _{0.30}	0.584(2)	0.42(1)	1.39(3)
MgH _{0.50} F _{0.50}	0.481(3)	0.41(2)	1.17(4)
MgF ₂	0.676(6)	0.43(1)	1.58(3)

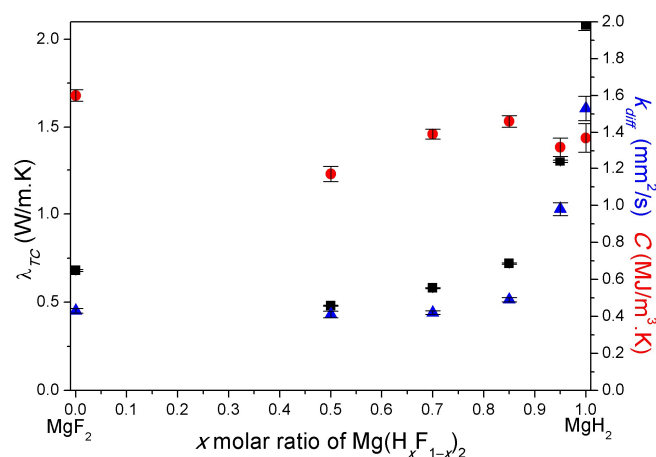


Figure 4.5. Thermal transport properties of Mg(H_xF_{1-x})₂. Thermal conductivity (black square), thermal diffusivity (blue triangle) and volumetric heat capacity (red circle) measured at RT under Ar atmosphere.

4.4. Conclusions

This study has detailed a thorough characterisation of fluorine substituted magnesium hydride ($\text{Mg}(\text{H}_x\text{F}_{1-x})_2$ where $x = 1, 0.95, 0.85, 0.70, 0.50, 0$), a class of materials that have potential application as hydrogen storage or thermal energy storage materials. The physical properties of these solid solutions have been studied by powder X-ray diffraction, inelastic neutron spectroscopy, and thermal conductivity. In addition, these measurements have been verified by density functional theory calculations.

Using these techniques, a number of trends have been identified that can be correlated to the random substitution of F^- into the crystal lattice. The tetragonal unit cell volume expands in a quadratic trend by 5.4 % from MgH_2 to MgF_2 . This expansion is isotropic in nature with a 2.3 % expansion in the a -axis compared to c -axis. This is mirrored with a preferred extension of the axial Mg-H(F) bond distances over the equatorial bond distances. Overall, the addition of F^- increases the average Mg-H(F) bond strength, which increases the thermal stability of the material, making fluorine rich Mg-H-F compounds efficient thermal energy storage materials. Despite the reduction in hydrogen-storage capacity, the increased thermal stability will permit hydrogen cycling at higher temperatures and therefore greater efficiency for thermal energy storage.

Inelastic neutron diffraction data has been collected for the first time for fluorine substituted magnesium hydride. Along with the simulated GDOS data from density functional theory calculations, these materials have exhibited a trend in vibrational frequencies and intensities from MgH_2 towards MgF_2 that is in line with the expansion in lattice parameters and bond distances.

The thermal transport properties, including thermal conductivity, diffusivity and heat capacity, for the range of $\text{Mg}(\text{H}_x\text{F}_{1-x})_2$ samples was also determined. This was the first time that MgH_2 and MgF_2 have been measured under the same conditions which has allowed a direct comparison with the fluorine substituted analogues.

4.4. References

- [1] A. Züttel, A. Remhof, A. Borgschulte, O. Friedrichs. Hydrogen: the future energy carrier. *Philosophical Transactions of the Royal Society, Series A: Physical Sciences and Engineering*. 368 (2010) 3329-42.
- [2] J.W. Makepeace, T. He, C. Weidenthaler, T.R. Jensen, F. Chang, T. Vegge, et al. Reversible ammonia-based and liquid organic hydrogen carriers for high-density hydrogen storage: Recent progress. *International Journal of Hydrogen Energy*. 44 (2019) 7746-67.
- [3] J.-C. Crivello, R.V. Denys, M. Dornheim, M. Felderhoff, D.M. Grant, J. Huot, et al. Mg-based compounds for hydrogen and energy storage. *Applied Physics A*. 122 (2016) 85.
- [4] C.J. Webb. A review of catalyst-enhanced magnesium hydride as a hydrogen storage material. *Journal of Physics and Chemistry of Solids*. 84 (2015) 96-106.
- [5] V.A. Yartys, M.V. Lototskyy, E. Akiba, R. Albert, V.E. Antonov, J.R. Ares, et al. Magnesium Based Materials for Hydrogen Based Energy Storage: Past, Present and Future. *International Journal of Hydrogen Energy*. 44 (2019) 7809-59.
- [6] T.D. Humphries, D.A. Sheppard, C.E. Buckley. Recent advances in the 18-electron complex transition metal hydrides of Ni, Fe, Co and Ru. *Coordination Chemistry Reviews*. 342 (2017) 19-33.
- [7] M. Paskevicius, D.A. Sheppard, C.E. Buckley. Thermodynamic changes in mechanochemically synthesized magnesium hydride nanoparticles. *Journal of the American Chemical Society*. 132 (2010) 5077-83.
- [8] DOE Technical targets for onboard hydrogen storage for light-duty vehicles, <https://www.energy.gov/eere/fuelcells/doe-technical-targets-onboard-hydrogen-storage-light-duty-vehicles>; [accessed 19/03/2019].
- [9] D. Dong, T.D. Humphries, D.A. Sheppard, B. Stansby, M. Paskevicius, M.V. Sofianos, et al. Thermal optimisation of metal hydride reactors for thermal energy storage applications. *Sustainable Energy & Fuels*. 1 (2017) 1820-9.
- [10] M.S. Tortoza, T.D. Humphries, D.A. Sheppard, M. Paskevicius, M.R. Rowles, M.V. Sofianos, et al. Thermodynamics and performance of the Mg-H-F system for thermochemical energy storage applications. *Physical Chemistry Chemical Physics*. 20 (2018) 2274-83.
- [11] E.R. Pinatel, M. Corno, P. Ugliengo, M. Baricco. Effects of metastability on hydrogen sorption in fluorine substituted hydrides. *Journal of Alloys and Compounds*. 615 (2014) S706-S10.
- [12] R. Varunaa, P. Ravindran. Phase stability, phase mixing, and phase separation in fluorinated alkaline earth hydrides. *The Journal of Physical Chemistry C*. 121 (2017) 21806-20.
- [13] M. Bortz, B. Bertheville, G. Böttger, K. Yvon. Structure of the high pressure phase γ -MgH₂ by neutron powder diffraction. *Journal of Alloys Compounds*. 287 (1999) L4-L6.
- [14] R.L. Corey, T.M. Ivancic, D.T. Shane, E.A. Carl, R.C. Bowman, J.M. Bellosta von Colbe, et al. Hydrogen motion in magnesium hydride by NMR. *The Journal of Physical Chemistry C*. 112 (2008) 19784-90.
- [15] J. Senegas, M. Pezat, J.P. Darnaudery, B. Darriet. Study by NMR on localization and movements of protons in MgH₂ and Mg₂NiH₄ hydrides. *Journal of Physics and Chemistry of Solids*. 42 (1981) 29-35.
- [16] J. Felsteiner, M. Heilper, I. Gertner, A.C. Tanner, R. Opher, K.F. Berggren. Compton scattering study of the electronic structure of magnesium hydride. *Physical Review B*. 23 (1981) 5156-62.
- [17] J.R. Santisteban, G.J. Cuello, J. Dawidowski, A. Fainstein, H.A. Peretti, A. Ivanov, et al. Vibrational spectrum of magnesium hydride. *Physical Review B*. 62 (2000) 37-40.
- [18] H.G. Schimmel, M.R. Johnson, G.J. Kearley, A.J. Ramirez-Cuesta, J. Huot, F.M. Mulder. The vibrational spectrum of magnesium hydride from inelastic neutron scattering and density functional theory. *Materials Science and Engineering: B*. 108 (2004) 38-41.
- [19] H.G. Schimmel, M.R. Johnson, G.J. Kearley, A.J. Ramirez-Cuesta, J. Huot, F.M. Mulder. Structural information on ball milled magnesium hydride from vibrational spectroscopy and ab-initio calculations. *Journal of Alloys and Compounds*. 393 (2005) 1-4.
- [20] N. Hanada, T. Ichikawa, S. Isobe, T. Nakagawa, K. Tokoyoda, T. Honma, et al. X-ray absorption spectroscopic study on valence state and local atomic structure of transition metal oxides doped in MgH₂. *The Journal of Physical Chemistry C*. 113 (2009) 13450-5.

- [21] A. Chaise, P. de Rango, P. Marty, D. Fruchart, S. Miraglia, R. Olivès, et al. Enhancement of hydrogen sorption in magnesium hydride using expanded natural graphite. *International Journal of Hydrogen Energy*. 34 (2009) 8589-96.
- [22] J.-H. Shim, M. Park, Y.H. Lee, S. Kim, Y.H. Im, J.-Y. Suh, et al. Effective thermal conductivity of MgH₂ compacts containing expanded natural graphite under a hydrogen atmosphere. *International Journal of Hydrogen Energy*. 39 (2014) 349-55.
- [23] K.S. Wallwork, B.J. Kennedy, D. Wang. The High Resolution Powder Diffraction Beamline for the Australian Synchrotron. *Synchrotron Radiation Instrumentation, Pts 1 and 2*. 879 (2007) 879-+.
- [24] B. Schmitt, C. Bronnimann, E.F. Eikenberry, F. Gozzo, C. Hormann, R. Horisberger, et al. Mythen Detector System. *Nuclear Instruments and Methods in Physics Research Section a-Accelerators Spectrometers Detectors and Associated Equipment*. 501 (2003) 267-72.
- [25] R.A. Young, R.A. Young. *The Rietveld Method*. Oxford University Press 1995.
- [26] B.O. Loopstra, H.M. Rietveld. The structure of some alkaline-earth metal uranates. *Acta Crystallographica Section B*. 25 (1969) 787-91.
- [27] A.A. Coelho. TOPAS and TOPAS-Academic: An optimization program integrating computer algebra and crystallographic objects written in C Plus. *Journal of Applied Crystallography*. 51 (2018) 210-8.
- [28] D. Richard, M. Ferrand, G.J. Kearley. Analysis and visualisation of neutron-scattering data. *Journal of Neutron Research*. 4 (1996) 33-9.
- [29] H. Mutka, M.M. Koza, M.R. Johnson, Z. Hiroi, J.-I. Yamaura, Y. Nagao. Generalized density-of-states and anharmonicity of the low-energy phonon bands from coherent inelastic neutron scattering response in the pyrochlore osmates AOs₂O₆ (A = K, Rb, Cs). *Physical Review B*. 78 (2008) 104307.
- [30] G. Kresse, J. Furthmuller. Efficient iterative schemes for ab initio total-energy calculations using a plane-wave basis set. *Physical Review B*. 54 (1996) 11169-86.
- [31] J.P. Perdew, K. Burke, M. Ernzerhof. Generalized gradient approximation made simple. *Physical Review Letters*. 77 (1996) 3865-8.
- [32] G. Kresse, D. Joubert. From ultrasoft pseudopotentials to the projector augmented-wave method. *Physical Review B*. 59 (1999) 1758-75.
- [33] A. Togo, I. Tanaka. First principles phonon calculations in materials science. *Scripta Materialia*. 108 (2015) 1-5.
- [34] D. Bansal, J. Hong, C.W. Li, A.F. May, W. Porter, M.Y. Hu, et al. Phonon anharmonicity and negative thermal expansion in SnSe. *Physical Review B*. 94 (2016) 054307.
- [35] NIST Center for Neutron Research, <https://www.ncnr.nist.gov/resources/n-lengths/list.html>; [accessed November 2, 2019].
- [36] W.H. Baur. The rutile type and its derivatives. *Crystallography Reviews*. 13 (2007) 65-113.
- [37] J. Haines, J.M. Léger, F. Gorelli, D.D. Klug, J.S. Tse, Z.Q. Li. X-ray diffraction and theoretical studies of the high-pressure structures and phase transitions in magnesium fluoride. *Physical Review B*. 64 (2001) 134110.
- [38] K. Ramesh Babu, C. Bheema Lingam, S. Auluck, S.P. Tewari, G. Vaitheeswaran. Structural, thermodynamic and optical properties of MgF₂ studied from first-principles theory. *Journal of Solid State Chemistry*. 184 (2011) 343-50.
- [39] T. Noritake, M. Aoki, S. Towata, Y. Seno, Y. Hirose, E. Nishibori, et al. Chemical bonding of hydrogen in MgH₂. *Applied Physics Letters*. 81 (2002) 2008-10.
- [40] J.P. Vidal, G. Vidal-Valat, M. Galtier, K. Kurki-Suonio. X-ray study of the charge distribution in MgF₂. *Acta Crystallographica Section A*. 37 (1981) 826-37.
- [41] A.R. Denton, N.W. Ashcroft. Vegard's law. *Physical Review A*. 43 (1991) 3161-4.
- [42] T.D. Humphries, D.A. Sheppard, M.R. Rowles, M.V. Sofianos, C.E. Buckley. Fluoride substitution in sodium hydride for thermal energy storage applications. *Journal of Materials Chemistry A*. 4 (2016) 12170-8.
- [43] A.S. Gangrade, A.A. Varma, N.K. Gor, S. Shrinivasan, S.S.V. Tatiparti. The dehydrogenation mechanism during the incubation period in nanocrystalline MgH₂. *Physical Chemistry Chemical Physics*. 19 (2017) 6677-87.
- [44] J.D. Cox, D.D. Wagman, V.A. Medvedev. *CODATA key values for thermodynamics*. Hemisphere Pub. Corp., New York, 1989.

- [45] D.A. Sheppard, M. Paskevicius, C.E. Buckley. Thermodynamics of hydrogen desorption from NaMgH₃ and its application as a solar heat storage medium. *Chemistry of Materials*. 23 (2011) 4298-300.
- [46] K. Koyama. Thermal conductivity of magnesium fluoride between 25° and 900°C. *Journal of the American Ceramic Society*. 52 (1969) 222-4.
- [47] C.P. Camirand. Measurement of thermal conductivity by differential scanning calorimetry. *Thermochimica Acta*. 417 (2004) 1-4.
- [48] J. Lang, M. Eagles, M.S. Conradi, J. Huot. Hydrogenation rate limiting step, diffusion and thermal conductivity in cold rolled magnesium hydride. *Journal of Alloys and Compounds*. 583 (2014) 116-20.
- [49] C. Kittel, P. McEuen, P. McEuen. *Introduction to solid state physics*. Wiley New York 1976.
- [50] B. Sundqvist, O. Andersson. Thermal conductivity and phase diagrams of some potential hydrogen storage materials under pressure. *International Journal of Thermophysics*. 30 (2009) 1118-29.
- [51] S.D. Beattie, A. Harris, A. Levchenko, J. Rudolph, C.D. Willson, G.S. McGrady. Thermal conductivity and specific heat measurements of metal hydrides. *ITCC Proceedings 2009*.
- [52] M. Sulic, M. Cai, S. Kumar. Cycling and engineering properties of highly compacted sodium alanate pellets. *International Journal of Hydrogen Energy*. 37 (2012) 15187-95.
- [53] H. Choi, A.F. Mills. Heat and mass transfer in metal hydride beds for heat pump applications. *International Journal of Heat and Mass Transfer*. 33 (1990) 1281-8.

5. Thermodynamics and performance of the Na-Mg-H-F system for thermochemical energy storage applications

This Chapter investigates the properties of NaMgHF₂ to be used as TCES material, and will be published post acceptance of this thesis. The NaMgH₂F system has been studied previously and its thermodynamic properties were measured, while a simultaneous cost assessment was conducted. NaMgH₃ has an enthalpy of hydrogen desorption (ΔH_{des}) = 86.6 ± 1.0 kJ/mol.H₂, while NaMgH₂F has a ΔH_{des} = 96.6 kJ/mol.H₂ implying its operating temperature is considerably higher and also reduce quantities of hydrogen gas need to be stored. To date, the NaMgHF₂ system has not been studied but is anticipated to have superior TES properties than its counterparts. In this study all materials in the NaMgH_{1-x}F_x (x = 0 to 3) system have been synthesised and their physical properties determined by thermal analysis, powder X-ray diffraction, and Sieverts analysis. As predicted, NaMgHF₂ is more thermodynamically stable with an enthalpy of 89 ± 12 kJ/mol H₂ and entropy of 121 ± 16 J/K/mol H₂. Hydrogen cycling of this material has also shown that this material has potential as a TES material for multiple applications, with only NaMgF₃ and H₂ being formed during the decomposition step with no unwanted by-products.

5.1 Introduction

One of the safest and most durable methods to store hydrogen is in the solid state, for example as a metal hydride. To store hydrogen in a gaseous or liquid state, high pressures and very low temperatures are required, respectively. Also, the storage tanks must be made of special materials to be insulated, to avoid leakage and fracture of the material, for example, to store 1 kg of hydrogen gas at 20°C, it is necessary to have pressures of 200 bar and a volume of 68.4 L [1]. As a specific material has not been found that meets every criterion, quality, and specification to date, there is much research still ongoing. Such requirements are: to form a stable metal hydride compound that possesses high gravimetric and volumetric storage density (for example MgH_2 contains 7.6 wt.% H_2 and $111 \text{ kg m}^{-3} \text{H}_2$, respectively [2]) has convenient thermodynamic and kinetic properties and should be relatively cheap [3]. Indeed, materials with these properties, such as magnesium-based metal hydrides, have been identified for potential application in a variety of technologies including thermal energy storage and hydrogen storage materials [4-8]. To date, materials that meet all of these conditions have been targeted as stationary hydrogen storage materials and thermochemical energy storage materials (TCES) due to their relatively high thermal stability [2].

Complex metal hydrides are a subgroup of metal hydrides that have been demonstrated to be promising candidates for solid-state storage, which include NaAlH_4 , NaBH_4 and NaMgH_3 [9]. Furthermore, studies have been carried out on complex metal hydride compounds to improve thermodynamic properties and reversibility. This includes LiBH_4 , which when mechanically milled with MgH_2 and 2 - 3 mol.% TiCl_3 has been demonstrated to reversibly store 8 - 10 wt.% hydrogen [10-12]. It has also been noted that many of these complex hydrides are synthesised or decompose in multiple steps forming a variety of hydrides. Complex hydrides with the formula ABX_3 are interesting materials for hydrogen storage. One material widely studied belonging to this group is the perovskite-type NaMgH_3 , which contains the lightweight elements Na and Mg [13].

NaMgH_3 has a theoretical volumetric hydrogen density of 88 g L^{-1} and a theoretical gravimetric hydrogen density of 6 wt.%, however, in practice only 4 wt.% of H_2 is reversible [14]. This is due to the fact that NaMgH_3 follows a two-step decomposition reaction (equations 6.1 and 6.2), with only the first one being reversible [14]. Another advantage of NaMgH_3 is its relatively low cost (3.50 US\$ per kg) [15], and high thermal stability ($\Delta H = 86.6 \text{ kJ/mol.H}_2$ and $\Delta S = 132.2 \text{ J/(mol.H}_2 \text{ K)}$ for equation 6.1) [13]. NaMgH_3 exists in the space group $Pnma$, N°. 62 with GdFeO_3 as the prototype structure, a twisted perovskite with a primarily orthorhombic unit cell [14]. Due to the smaller radius of Na, the octahedral MgH_6 groups are tilted, generating distortion in the structure. Figure 5.1 represents the NaMgH_3 structure. One H anion occupies two different Wyckoff sites (4c, 8d) in the structure and each is coordinated by 4 Na and 2 Mg cations. In turn, one Na cation is coordinated with 12 H anions.

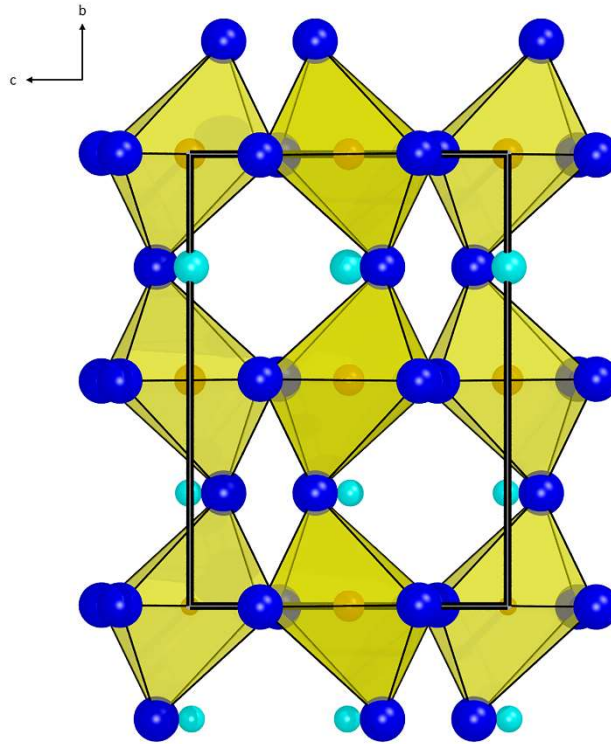
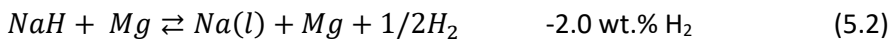


Figure 5.1. NaMgH_3 crystal structure, space group $Pnma$, No. 62. Lattice $a = 5.463 \text{ \AA}$, $b = 7.703 \text{ \AA}$, $c = 5.411 \text{ \AA}$ [16]. Na atoms are represented with the light blue spheres, Mg with orange and H with the blue spheres.



In recent years, partial fluorine substitution of hydrogen has been considered as a possible solution to improve the thermal stability of metal hydrides as hydrogen storage materials for next-generation concentrating solar power (CSP), which requires a temperature of decomposition of the metal hydride of $> 600^\circ\text{C}$ [17]. Studies have been carried out on the hydrogen storage properties of NaMgH_2F (fluorine substituted NaMgH_3) [15]. It presents a practical hydrogen capacity of 2.5 wt.% (theoretical: 2.95 wt.% H_2), a desorption enthalpy of $\Delta H_{des} = 96.8 \text{ kJ/mol.H}_2$ and a thermal storage capacity of 1416 kJ/kg. Although the theoretical thermal storage capacity of NaMgH_2F is $\sim 18\%$ less than the theoretical values for NaMgH_3 (1721 kJ/kg) and $\sim 50\%$ lower than MgH_2 (2814 kJ/kg) [18], the high enthalpy and operating temperatures of NaMgH_2F implies less hydrogen is needed so less gas needs to be stored, which lowers the cost of the installed system.

As the thermodynamics of NaMgH_2F have been measured to have a $\Delta H_{des} = 96.8 \text{ kJ/(mol.H}_2)$ and $\Delta S_{des} = 138.7 \text{ J/(mol.H}_2 \text{ K)}$ it is potentially suitable for CSP thermal storage applications operating between 600 and 800°C [15]. Both thermodynamic values are larger than for NaMgH_3 implying NaMgH_2F is more stable. Further

fluorine substitution into the NaMgH₃ system has been proposed to be experimentally measured in order to determine feasibility to be used and implemented as a thermochemical energy storage material (TCES). This will also determine the thermodynamic properties for the entire NaMg(H_{1-x}F_x)₃ series. Indeed, a previous theoretical study determined, by the reaction of the hydride with HCl in a colorimeter, the standard enthalpies of formation of NaMgH₃, NaMgH₂F and NaMgHF₂ to be -231 kJ mol⁻¹, -720 kJ mol⁻¹ and -1221 kJ mol⁻¹, respectively at 25°C [19]. These values provide an indication on the stability of the series. Other, examples of fluorine substitution in metal hydrides are NaH-NaF [20] and MgH₂-MgF₂ [2]. In both cases, the formation of a solid solution by the replacement of H atoms for F atoms makes for a more thermodynamically stable material. The NaH-NaF system has a higher temperature of hydrogen release than pure NaH, with a maximum rate of desorption at 443 °C for NaH_{0.5}F_{0.5} compared to 408 °C for pure NaH [20]. Additionally, NaH_{0.5}F_{0.5} has a ΔH_{des} of 106 kJ mol⁻¹ H₂ and ΔS_{des} of 143 J K⁻¹ mol⁻¹ H₂, compared to pure NaH ($\Delta H_{\text{des}} = 117$ kJ mol⁻¹ H₂ and $\Delta S_{\text{des}} = 167$ J K⁻¹ mol⁻¹ H₂). Although the enthalpy is lower and therefore a lower stabilisation would be expected, the fact that the entropy is much lower also leads to a reduction in hydrogen equilibrium pressures. Another system that has been studied is Mg(H_{0.85}F_{0.15})₂ which has an enthalpy (ΔH_{des}) of 73.6 kJ mol⁻¹ H₂ and an entropy (ΔS_{des}) of 131. J K⁻¹ mol⁻¹ H₂, which is slightly lower than MgH₂ with ΔH_{des} of 74.06 kJ mol⁻¹ H₂ and $\Delta S_{\text{des}} = 133.4$ J K⁻¹ mol⁻¹ H₂ [2]. In addition, cycling studies of Mg(H_{0.85}F_{0.15})₂ over six absorption/desorption cycles between 425 and 480 °C show an increased usable cycling temperature of ~ 80 °C compared to bulk MgH₂, increasing the thermal operating temperatures for technological applications. In this chapter, NaH has been mechanically mixed with MgF₂ via ball milling to successfully form a series of solid solutions NaMg(H_{1-x}F_x)₃ ($x = 0, 1, 2, 3$) and elucidate their structural and thermodynamic properties. *In situ* synchrotron radiation powder, X-ray diffraction (SR-XRD) studies have been carried out on all ranges of compositions to study their structures as well as to ascertain the thermal decomposition pathways of these compounds. Moreover, thermal analysis of this Na-Mg-H-F system using differential scanning calorimetry (DSC) and temperature-programmed-desorption mass spectrometry (TPD-MS), has also been measured and compared with the SR-XRD data.

The thermodynamic and kinetic properties of NaMgHF₂ were also determined by PCI analysis using the van't Hoff method. Indeed, to determine its applicability in the CSP system, cycling studies have also been carried out for the NaMgHF₂ compound. A cost analysis has also been carried out to determine the feasibility of this material for industrial applications.

5.2 Results and Discussion

5.2.1 Structure and Composition

The $\text{NaMg}(\text{H}_{1-x}\text{F}_x)_3$ ($x = 0, 1, 2, 3$) systems were prepared by ball milling NaH, NaF, MgH_2 and MgF_2 in various ratios (Table 5.1) at room temperature. Once the starting materials were ball milled, the samples (except for NaMgF_3) were then annealed at various temperatures under a hydrogen atmosphere to promote F atoms to substitute into the 4c and 8d sites and form single-phase compositions. Annealing samples under H_2 also prevents hydrogen release from the material [20].

Table 5.1. Mixing molar ratios and preparation conditions of $\text{NaMg}(\text{H}_{1-x}\text{F}_x)_3$. The compositions were determined by SR-XRD analysis and Rietveld refinement. Uncertainties are in parentheses.

Sample	NaH	NaF	MgH_2	MgF_2	Annealing conditions			Compositions (wt.%)						
					H_2 Pressure (bar)	Time (h)	Temperature ($^\circ\text{C}$)	$\text{NaMg}(\text{H}_{1-x}\text{F}_x)_3$	NaH	Mg	NaF	Fe	Fe_2O_3	MgO
NaMgH_3	1	-	1	-	30	5	350	96.20(4)	0.88(3)	2.91(3)	-	-	-	-
NaMgH_2F	-	1	1	-	50	12	450	99.48(9)	-	-	0.52(9)	-	-	-
NaMgHF_2	1	-	-	1	65	24	400	95.51(6)	-	-	3.77(6)	0.72(1)	-	-
NaMgF_3	-	1	-	1	-	5	750	98.75(5)	-	-	-	-	0.64(4)	0.61(4)

Fig 5.2 illustrates the SR-XRD patterns for each of the solid solutions at room temperature. Due to the fact that the NaMgH_3 and NaMgF_3 both exist in an orthorhombic crystal structure ($Pnma$, space group number 62) [21], the solid solutions of $\text{NaMg}(\text{H}_{1-x}\text{F}_x)_3$ also possess identical structures, as predicted by Messer [22]. The quantitative analysis of the data by Rietveld refinement for NaMgHF_2 indicates that the composition is $\text{NaMgH}_{0.83}\text{F}_{2.17}$ and shows the presence of some impurities such as NaF and Fe, but these are less than 5 wt.% in total. The Fe is introduced during ball milling.

In the diffraction patterns illustrated in Fig. 5.2, it is noticed that the central Bragg peak II of the triplet at $\sim 21.2^\circ 2\theta$ for $\text{NaMg}(\text{H}_{1-x}\text{F}_x)_3$ decreases in intensity as the F content in the compounds increases. At the same time, the two satellite peaks on either side (I and III) shift away from the central peak. As the F content increases, Bragg peaks II and III move towards higher angles, while peak I shifts to lower angles, so as F content increases the triplet peak becomes less intense and broader. In addition, it is noted that the in the triplet the peaks are equidistant, meaning that the distance between peaks I to II is identical to the distance between peaks II to III and is consistent for all of the $\text{NaMg}(\text{H}_{1-x}\text{F}_x)_3$ series (Table 5.2). The opposite trend occurs for the peak at $15^\circ 2\theta$ and $16.7^\circ 2\theta$, of which the intensity increases with the F content.

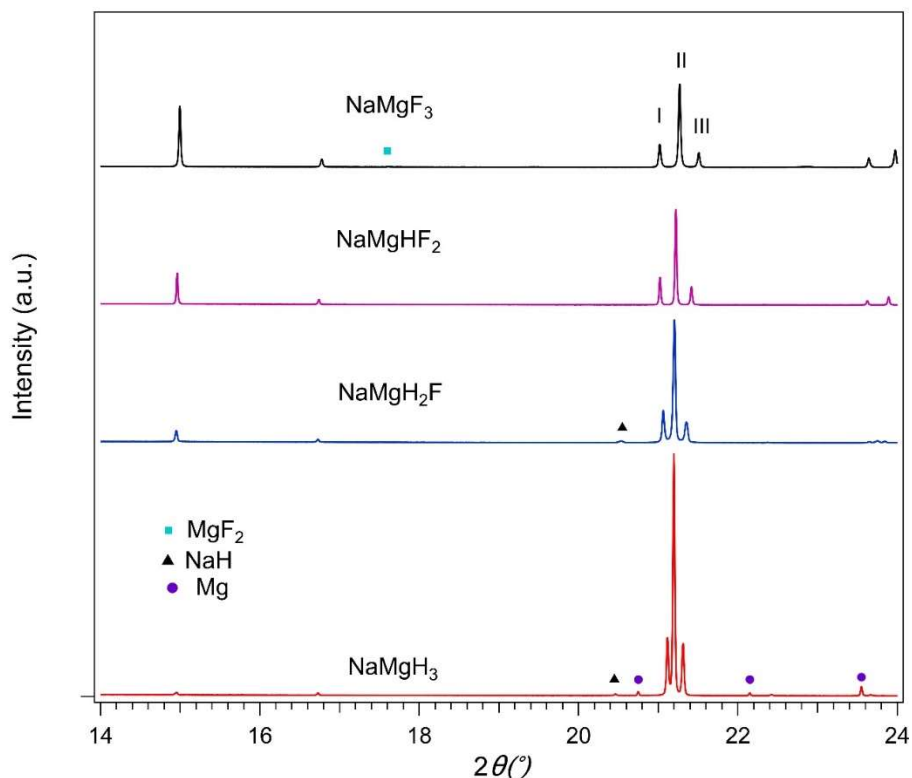


Figure 5.2. SR-XRD data at room temperature for $\text{NaMg}(\text{H}_{1-x}\text{F}_x)_3$ samples after ball milling and annealing. All other Bragg peaks are associated with the $\text{NaMg}(\text{H}_{1-x}\text{F}_x)_3$ mixtures. $\lambda = 1.000389(1) \text{ \AA}$.

Table 5.2. Peak positions for triplet at $2\theta = \sim 21.2$. I: left peak, II: middle peak, and III: right peak.

	Peak positions (2θ)			Difference between peak positions (2θ)	
	I	II	III	II - I	III - I
NaMgH₃	21.12	21.20	21.31	0.08	0.12
NaMgH₂F	21.06	21.20	21.35	0.14	0.15
NaMgHF₂	21.02	21.22	21.42	0.20	0.20
NaMgF₃	21.017	21.268	21.51	0.25	0.24

The shift in Bragg peak to higher angles with increasing F content, has a concomitant decrease in unit cell volume from $227.4541(4) \text{ \AA}^3$ for NaMgH_3 to $225.4794(3) \text{ \AA}^3$ for NaMgF_3 (Table 5.3). The lattice parameters for the Na-Mg-H-F solid solution are illustrated in Fig. 5.3 a and b and clearly show that the a , b and c lattice parameter values change (a increases, while b and c decrease) with increasing fluorine content, with b and c having a dominant influence on the unit cell contraction and therefore its crystallographic density mainly due to the F mass instead of H mass. Also, this figure manifests that lattice parameters as well as density and volume cells present a quadratic relationship with F content. The greatest difference in lattice parameters is experienced in the c lattice parameter which decreases from NaMgH_3 to NaMgF_3 by 0.89% (Fig. 5.4) compared to a 0.43% decrease in the b -axis and a 0.46% increase in a . This is evidenced by an overall decrease in unit cell volume of 0.87% for the NaMgF_3 .

In regard to bond distances, it is observed that upon fluorination the axial Mg-H(F) bond distances decrease, while the equatorial Mg-H(F) bond distances in the octahedron increase. The changes are both in the region of 1%. Correlating the lattice parameters and Mg-H(F) bond distances, the decrease in axial bond lengths coincides with the contraction of lattice parameter *b*, while the expansion on the equatorial bonds is spread between the contraction of *c* and expansion of *a*.

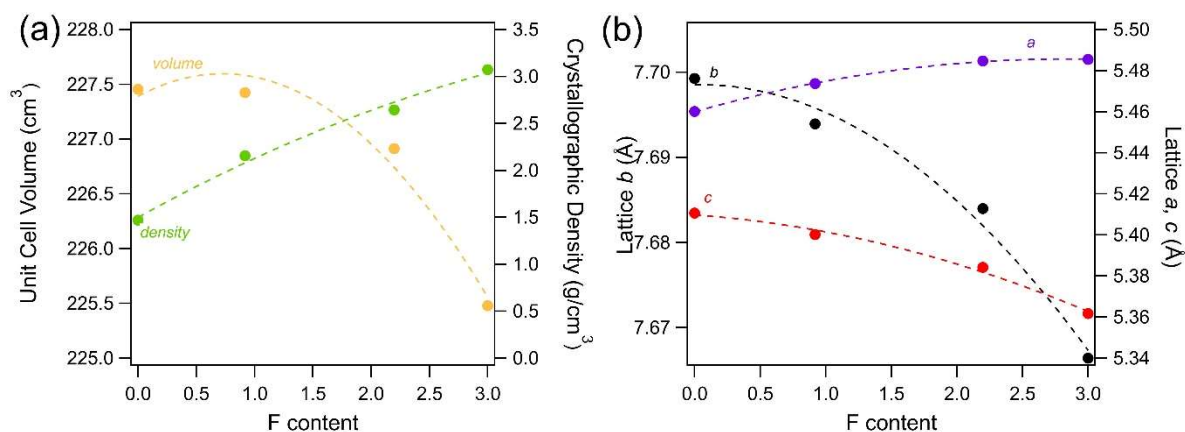


Figure 5.3. a) Represents the Crystallographic Density (g/cm³) and Unit Cell volume (cm³) of NaMg(H_{1-x}F_x)₃ solution and b) represents the lattice parameters *a*, *b* and *c* of the NaMg(H_{1-x}F_x)₃ series determined by Rietveld analysis of the SR-XRD data. Lattice *a*: $y = -0.0032x^2 + 0.018x + 5.46$. $R^2 = 0.9977$; Lattice *b*: $y = -0.0036x^2 - 0.00033x + 7.6985$. $R^2 = 0.9994$; Lattice *c*: $y = -0.0037x^2 - 0.0045x + 5.4097$. $R^2 = 0.9999$.

Table 5.3. Structural properties of NaMg(H_{1-x}F_x)₃ mixtures (Pnma) at room temperature. Estimated standard deviations (esd's) are in parentheses.

Sample Name	NaMgH ₃	NaMgH ₂ F	NaMgHF ₂	NaMgF ₃	
Lattice Parameter (Å)	<i>a</i>	5.46008(2)	5.47364(3)	5.48465(1)	5.48546(1)
	<i>b</i>	7.69926(2)	7.69392(4)	7.68399(2)	7.66643(2)
	<i>c</i>	5.41060(2)	5.40022(2)	5.38421(1)	5.36168(1)
Unit cell volume (Å ³)	227.4541(4)	227.4236(5)	226.9123(8)	225.4794(3)	
Theoretical H ₂ capacity (wt.%)	4.2	2.95	1.17	---	
Density (g/cm ³)	1.4694(1)	2.157(6)	2.7192(2)	3.07212(1)	
Bond distances	Mg-H ₁ (F ₁) (apical)	2.0086(5)	1.9804(8)	1.9821(3)	1.9816(8)
	Mg-H ₂ (F ₂) (equatorial)	1.9238(3)	1.978(3)	1.9840(9)	1.9780(3)

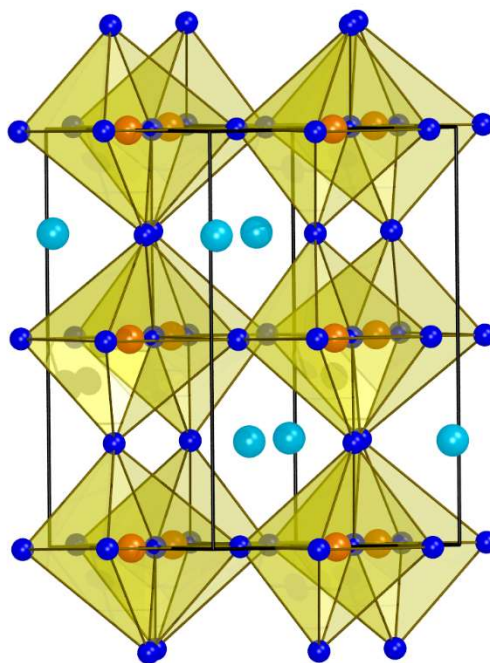


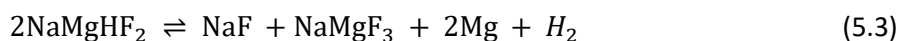
Figure 5.4. Representation of the NaMgHF_2 crystal structure. Na atoms are represented with the light blue spheres, Mg with orange and H (and F) with the blue spheres.

5.2.2 Temperature dependant powder X-ray diffraction studies

In situ synchrotron powder diffraction studies have been undertaken on the $\text{NaMg}(\text{H}_{1-x}\text{F}_x)_3$ samples to study the structural transitions and reactions which occur upon heating the sample in a capillary, under a dynamic vacuum, from room temperature to 595 °C. The experiments were undertaken at the Australian Synchrotron and analysed via a parametric distortion-mode refinement [23-25] in Topas [26]. $\text{NaMg}(\text{H}_{1-x}\text{F}_x)_3$ exists in a perovskite-type structure in the space group $Pnma$, but can be modelled as a distortion of a parent structure, e.g. neighborite, in space group $Pm-3m$. This type of refinement, in comparison to conventional crystallographic analysis can provide detail about crystal defects as it takes into account the distortion in the shapes of diffraction peaks. The distorted structure was generated by applying the $Pnma$ transformation matrix, as suggested by Howard and Stokes [27], to a generic structure of neighborite using the program Isodistort [24]. This then provides an output to be refined using Topas [26]. There are two distortion modes associated with Na, and five with the $\text{Mg}(\text{H}/\text{F})$ octahedra. The Mg positions are fixed by symmetry. Rather than allowing atom positions to freely refine in three-dimensional space, distortion-mode refinements allow only rigid distortions of structural units, the amplitude of which is a refinable parameter. This allows for important modes to be refined, and others to be fixed at zero, whilst maintaining the necessary degrees of freedom, stabilising the refinement. Furthermore, the change in the mode amplitudes with temperature can be further stabilised by utilising parametric refinements, where the amplitude is further defined as a function of temperature, and the function coefficients are refined, rather than the individual mode amplitudes. Such

a parameterisation can speed up refinements but should initially be undertaken with totally free parameters to ensure that the parameterisations introduced are supported by the data.

The *in situ* synchrotron data can be used to understand the decomposition process of a material. For example, a complete decomposition reaction for NaMgHF₂ is expected to be as follows (equation 5.3):



This material (NaMgHF₂) was heated from room temperature to 595 °C (Figure 5.5) and the lattice parameters expanded *a*: from 5.48465 (1) to 5.53524 (2) Å, *b*: from 7.68399(2) to 7.79782(1) Å and *c*: from 5.38421(1) to 5.48489(4) Å.

The NaMgHF₂ phase is stable from room temperature to ~ 320 °C. From this point, defined as the onset of decomposition, NaF, Mg/MgO and NaMgF₃ are formed. MgO is not expected to form, only Mg, but this is likely being formed from unknown amorphous impurities. At ~ 320 °C the amount of MgO (~ 9.2 wt.%) and NaF (~ 4.5 wt.%) increases gradually, while the formation of NaMgF₃ also begins (~ 6.5 wt.%) along with a concomitant reduction in NaMgHF₂ (~ 79 wt.%) (Table 5.4). As the temperature increases, a shift in peak position to lower 2θ occurs that is associated with thermal expansion and as consequence, the unit cell volume increases by ~ 4% from 226.9123(8) to 236.7434 (7) Å³ (Fig 5.6b).

After 320 °C it is evident that there are two kinetic regimes of decomposition: from 320 °C to ~ 400 °C, where the composition of the sample changes to 55 wt.% NaMgHF₂, 9 wt.% NaF, 14 wt.% MgO and 21 wt.% NaMgF₃ at 400 °C; and then the other regime from 450 °C to 595 °C, where at 450 °C the composition is 47 wt.% NaMgHF₂, 12 wt.% NaF, 17 wt.% MgO and 23 wt.% NaMgF₃. At ~ 565 °C the NaMgHF₂ unit cell decreases indicating an enrichment of fluorine within the structure. The material reaches full hydrogen desorption at 595 °C with NaMgF₃ (~ 51 wt.%), NaF (~ 22 wt.%), and MgO (~ 26 wt.%).

Table 5.4. Composition of NaMgHF₂ determined by SR-XRD as a function of temperature.

Temperature (°C)	NaMgHF ₂ (wt.%)	NaF (wt.%)	MgO (wt.%)	NaMgF ₃ (wt.%)
320	79(2)	4.5(3)	9.2(4)	6.5(6)
400	55(3)	9(2)	14(9)	21(2)
450	47(1)	12(7)	17(5)	23(8)
595	-	22 (7)	26(5)	51(3)

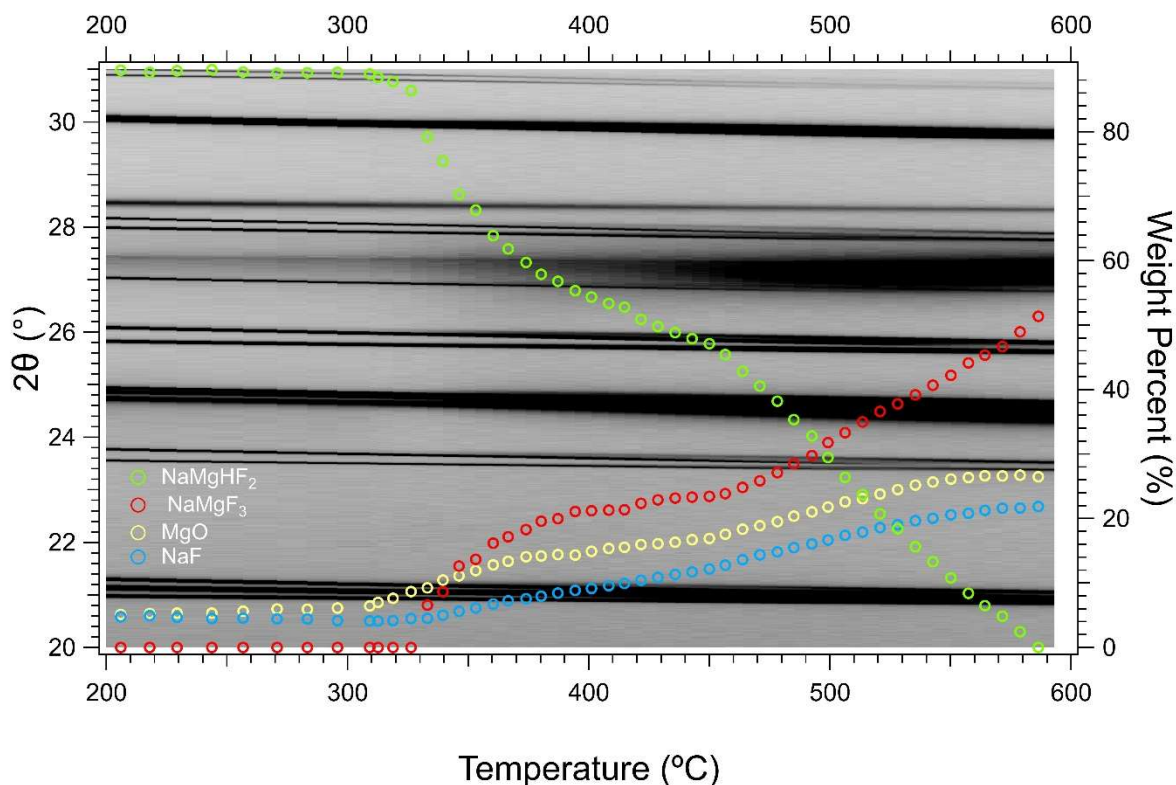


Figure 5.5. *In situ* SR-XRD data and quantitative refinement plot of NaMgHF₂. Heated from room temperature to 595 °C ($\Delta T/\Delta t = 6$ °C min⁻¹, $\lambda = 0.775227$ Å) under dynamic vacuum. Colour code: ● NaMgHF₂, ● NaMgF₃, ● MgO, ● NaF.

Figure 5.6 represents the *in situ* SR-XRD data for NaMgHF₂ as a function of F occupancy and unit cell parameters in NaMgHF₂ during heating to 595 °C. The F occupancy (Fig. 5.6a) does not alter from ~ 2.2 from room temperature to 450 °C (Fig 5.4 a). After 450°C, this behaviour changes rapidly and the F occupancy grows exponentially, meaning that H occupancy tends to zero very quickly, and the lattice contracts whilst still being heated. This could be due to the fact that up to 450 °C the NaMgHF₂ decomposes directly into NaMgF₃, while after 450 °C the initial NaMgHF₂ material becomes richer in F until the end (595 °C) allowing the formation of numerous solid-solution compositions in between (eq 5.3).

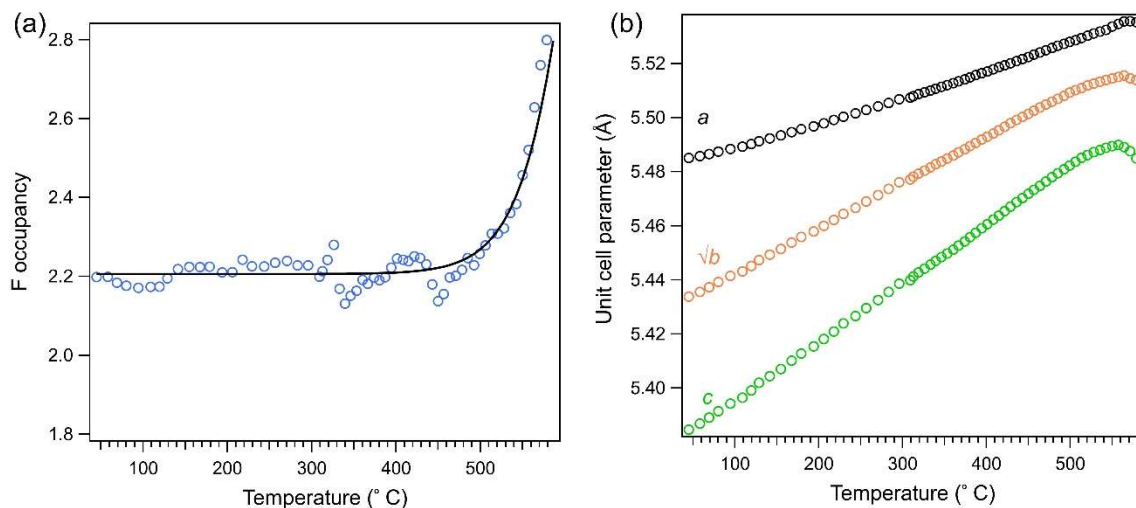


Figure 5.6. (a) NaMgHF₂ F occupancy as a function of temperature from synchrotron analysis. (b) Rietveld refined lattice parameters of NaMgHF₂ as a function of temperature.

5.2.3 Thermal analysis

Thermal analysis was undertaken for all samples of the Na-Mg-H-F system. The differential scanning calorimetry (DSC) and Temperature programmed desorption mass spectrometry (TPD-MS) analyses are illustrated in figure 5.7. The conditions of these measurements are described in chapter 2: Experimental.

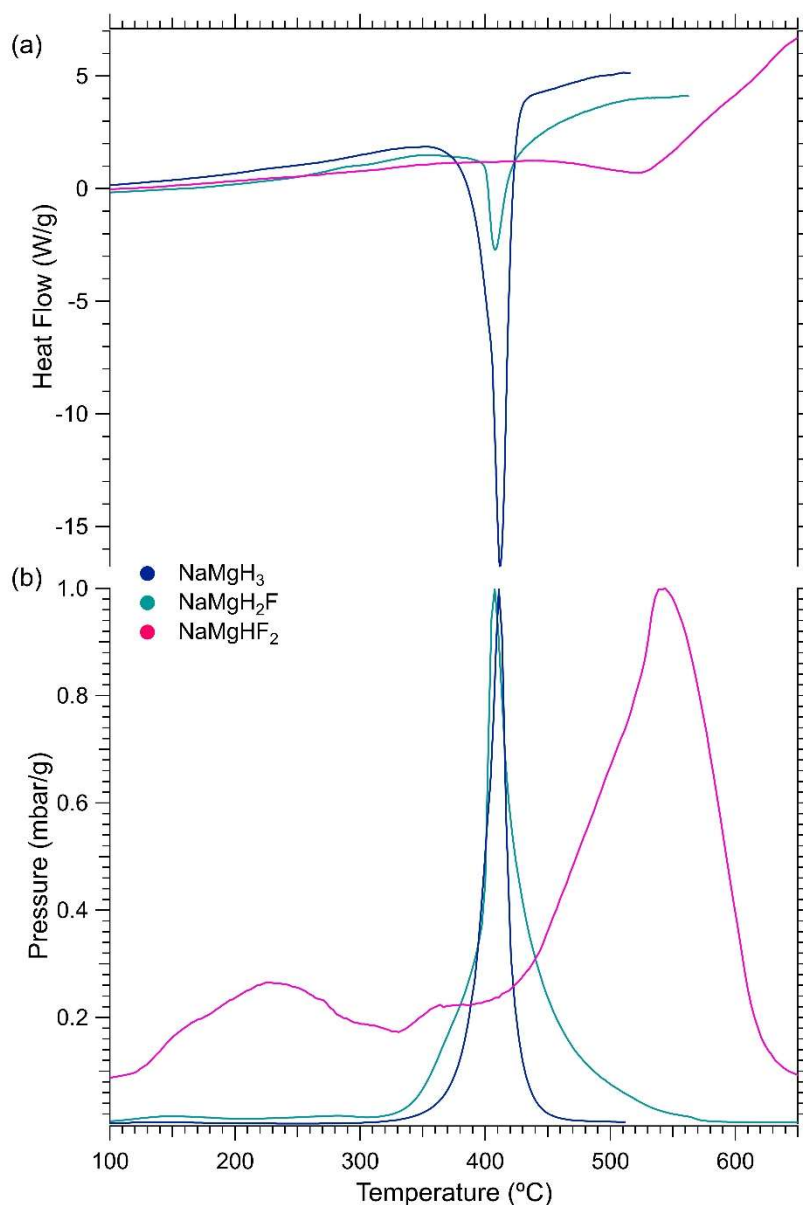


Figure 5.7. Simultaneous thermal analysis of $\text{NaMg}(\text{H}_{1-x}\text{F}_x)_3$ samples by (a) DSC, (b) TPD-MS. Ramp rate = $10^\circ\text{C}/\text{min}$. DSC and TPD-MS data are normalised to the mass of the samples.

The DSC and TPD-MS data measured for the $\text{NaMg}(\text{H}_{1-x}\text{F}_x)_3$ systems each show a single endothermic event. For DSC, the onset occurs between $350 - 450^\circ\text{C}$ (Fig 5.7a), while for TPD-MS the onset temperature is $\sim 315^\circ\text{C}$ except for NaMgHF_2 which is $\sim 370^\circ\text{C}$ (Table 5.5). The peaks for NaMgH_2F and NaMgHF_2 are clearly asymmetric for both techniques and so corroborates the SR-XRD conclusion that there are two regimes of decomposition, which may overlap here. The NaMgHF_2 curve shows at least two different regimes, the rate of H_2 release changes at ~ 440 and again at $\sim 515^\circ\text{C}$, while for NaMgH_2F this rate change occurs at $\sim 400^\circ\text{C}$. The onset and the maximum temperature of hydrogen release are expected to increase with increasing F content in the sample. This hypothesis is correct as NaMgHF_2 has a peak temperature of H_2 release that is significantly greater than NaMgH_3 and NaMgH_2F . For DSC the peak temperature for NaMgHF_2 is 525°C

compared to 411 and 408 °C for NaMgH₃ and NaMgH₂F, respectively. For TPD-MS the peak temperatures are 545 °C for NaMgHF₂ compared to 411 and 408 °C for NaMgH₃ and NaMgH₂F, respectively. It is noted that the peak values for NaMgH₃ and NaMgH₂F are similar, within error, while the NaMgHF₂ peak is broad. This is a testament to its increased stability and that decomposition may be slower due to the formation of a range of F containing phases. The same phenomenon that has also been observed for Mg(H_{0.95}F_{0.05})₂ versus MgH₂ [25]. It is also noted that in the decomposition process occurs faster for NaMgH₃, then NaMgH₂F and finally NaMgHF₂ with a temperature range of ~ 150, ~ 275 and ~ 300 °C, respectively (by TPD-MS).

Table 5.5. Decomposition temperatures determined by DSC and TPD-MS for NaMg(H_{1-x}F_x)₃ mixtures (ramp rate = 10 °C/min).

Sample	Onset/Peak Temperature of H ₂ desorption (DSC, °C)	Maximum Peak Temperature of H ₂ desorption (TPD-MS, °C)
NaMgH ₃	362/411	411
NaMgH ₂ F	385/408	407.5
NaMgHF ₂	430/525	545

In summary, the thermal data for NaMgHF₂ indicates it would be an ideal candidate for further studies as an HTMH for TES applications. Although its H₂ content (1.16 theoretical wt.% H₂) is lower than for NaMgH₃ (6 wt.% H₂) and NaMgH₂F (2.95 wt.% H₂), DSC and TPD-MS measurements (Fig. 5.7) show that NaMgHF₂ is the most stable of the NaMg(H_{1-x}F_x)₃ systems and could operate at higher temperatures. As such, NaMgHF₂ has been deemed an ideal candidate to be studied by PCI to determine its thermodynamics of decomposition. The PCI curves in Fig. 5.8a, measured between 505 and 554 °C, show that decomposition follows a single-step process that releases an average of ~ 1.14 wt.% H₂. The equilibrium pressures for the six temperatures measured were between 0.1 and 9 bar. Each of the curves exhibit a sloping plateau which is highly characteristic of a solid solution of this type, and correlates with the NaH_{0.50}F_{0.50} [20], MgH_{0.85}F_{0.15} [2], or NaMgH₂F systems [15, 20]. Sloping plateaus are not ideal in practical applications because hydrogen absorption and desorption do not occur in an isobaric process [15], and the range of operating system pressures becomes larger. This is because lower pressures are required to completely dehydrogenate the material, while higher pressures are required for hydrogenation. One way to avoid this situation is to increase the volume of the reactor as well as the temperature range for absorption and desorption [20]. The gradient of the plateaus in the PCI curves begins to increase at ~ -0.6 wt.% H₂. This can be indicative of different decomposition regimes (solid solution formation) that are occurring in the sample [2]. As the sample increases in F content there are at least two behaviours observed in the PCI curves (figure 5.6). The first is the main equilibrium plateau where desorption of H₂ from NaMgHF₂ occurs forming NaMgF₃, and the second, the tail end of the PCI's after 0.8 wt.% H₂ has been desorbed, where the desorption of H₂ from NaMgHF₂ forms various solid solutions between NaMgHF₂ and NaMgF₃.

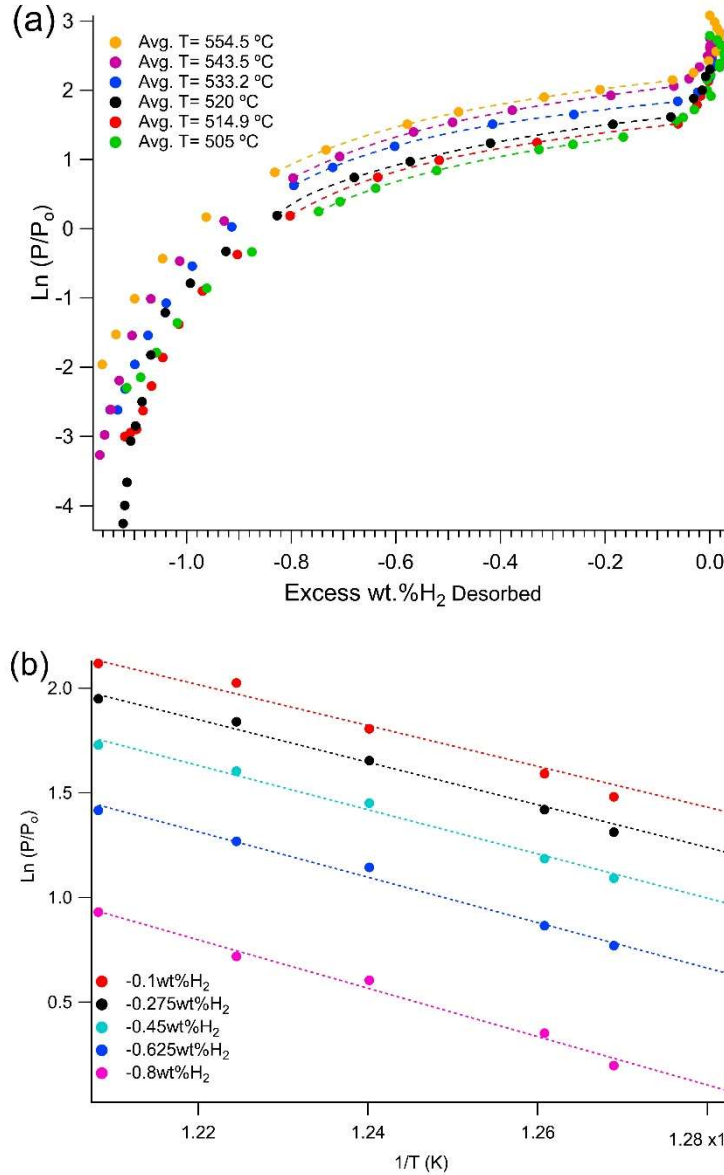


Fig 5.8. (a) Pressure–Composition–Isotherms (PCI) for NaMgHF₂ performed between 505 °C and 554 °C. (b) van't Hoff plot of respective H₂ desorption equilibrium pressures, where T is the temperature (K). $P_0 = 1$ bar. $\bullet \ln(P/P_0)_{-0.1\text{wt}\%H_2} = -9764.1x + 13.929$, $\bullet \ln(P/P_0)_{-0.275\text{wt}\%H_2} = -10176x + 14.265$, $\bullet \ln(P/P_0)_{-0.45\text{wt}\%H_2} = -10565x + 14.52$, $\bullet \ln(P/P_0)_{-0.625\text{wt}\%H_2} = -10855x + 14.558$, $\bullet \ln(P/P_0)_{-0.8\text{wt}\%H_2} = -11557x + 14.898$, where $x = 1/\text{Temperature (K)}$. $P_0 = 1$ bar.

Generally, the thermodynamics of sorption are determined by measuring the pressure at the midpoint of the equilibrium plateau and plotting this as a function of temperature in a van't Hoff plot. In this study, due to the sloping plateau (Fig 5.8a), each of the six curves were numerically fitted throughout the plateau, with a double exponential distribution equation 5.4.

$$\ln(P/P_0) = y_0 + A_1 \exp \frac{-(x-x_0)}{\tau_1} + A_2 \exp \frac{-(x-x_0)}{\tau_2} \quad (5.4)$$

where $x = \text{wt.}\% \text{ H}_2 \text{ desorbed}$, $x_0 = \text{is a constant}$, and A_1, A_2, τ_1, τ_2 , and y_0 are fit coefficients.

This allowed the enthalpy and entropy to be determined at variable hydrogen contents over the plateau region (Fig. 5.8b) [15]. The enthalpy (ΔH_{des}) and entropy (ΔS_{des}) of hydrogen desorption are presented in Table 5.6.

Table 5.6. Thermodynamic properties at 5 different hydrogen contents for NaMgHF₂

At H ₂ wt.%	ΔH_{des} (kJ/mol H ₂)	ΔS_{des} (J/K/mol H ₂)	R ²	ΔG (kJ/mol H ₂)
-0.1	81 ± 12	115 ± 15	0.9737	-11.67
-0.275	85 ± 12	118 ± 15	0.9894	-10.48
-0.45	87 ± 12	120 ± 16	0.9936	-8.95
-0.58 ^a	89 ± 12	121 ± 16	0.9932	-7.43
-0.625	90 ± 13	121 ± 16	0.9932	-6.79
-0.8	96 ± 14	123 ± 17	0.9924	-3.22
NaMgH ₃ ^b	86.6	132.20	-	-19.39
NaMgH ₂ F ^c	96.8	~139	-	-14.64

*^a middle point of full desorption

*^b [13] middle point of temperature is 418.6 °C

*^c [15] middle point of full desorption, values above 470 °C

The change in enthalpy, ΔH_{des} , increases from 81 ± 12 to 96 ± 14 kJ/mol H₂ between - 0.1 wt.% to - 0.8 wt.% H₂ (Figure 5.9). The values for the change in entropy also show the same trend, as they increase in value from 115 ± 15 to 123 ± 17 J/K/mol H₂ between - 0.1 wt.% to - 0.8 wt.% H₂. This means that at -0.58 wt.% H₂ (middle point of the plateau of full desorption), $\Delta H_{\text{des}} = 89 \pm 12$ kJ/mol H₂ and $\Delta S_{\text{des}} = 121 \pm 16$ J/K/mol H₂, are 3.58% higher and 8.37% lower than for NaMgH₃, respectively. Moreover, there is also a difference between NaMgH₂F and NaMgHF₂, with NaMgHF₂ being lower in ΔH_{des} by 7.91% and ΔS by 14.74% (Fig 5.9). This indicates that the equilibrium pressure at which decomposition will occur is significantly higher than for NaMgH₃ and NaMgH₂F at the same temperature (5.9c), e.g. at 1 bar of pressure NaMgH₃ will decompose at 385 °C, NaMgH₂F at 425 °C and NaMgHF₂ at 470 °C.

The nature of the sloping plateau is mainly explained by changes occurring gradually during decomposition, possibly as the H₂ is being released the sample is being fluorine substituted forming a range of compositions and, because of this, the thermodynamics of decomposition changes gradually during the measurement.

Figure 5.9 compares the change in enthalpy and entropy for NaMgHF₂ with NaMgH₃, and NaMgH₂F at different wt.% along the plateau, where the equilibrium pressures change (from the sloping plateau) and as a consequence the thermodynamics vary. In terms of ΔH (Fig 5.9a), the NaMgHF₂ behaviour can be divided into two parts at -0.38 H₂wt.%. If the H₂ wt.% is lower than -0.38 H₂wt.% $\Delta H_{\text{NaMgH}_3} > \Delta H_{\text{NaMgHF}_2}$, which implies that NaMgH₃ is more stable than NaMgHF₂. However, when H₂wt.% is above -0.38% the situation for ΔH changes, so that $\Delta H_{\text{NaMgHF}_2} > \Delta H_{\text{NaMgH}_2\text{F}} > \Delta H_{\text{NaMgH}_3}$, implying that at greater fluorine substitution the more stable the sample.

In regards to the NaMgHF₂ entropy (Fig 5.9b) it is < the entropy of NaMgH₃ and NaMgH₂F for all H₂ wt.% (-0.1 to -0.8), resulting in the trend that the > F⁻ content the lower the ΔS_{des} . Thermodynamically it is observed that as F⁻ content increases the ΔH_{des} and ΔS_{des} decrease (below -0.38 wt.% H₂), but the value of ΔS_{des} for NaMgHF₂ decreases substantially more with F substitution than does the ΔH_{des} compared to the other two compounds of the Na-Mg-H-F system. By consequence as the fluorine content increases ΔG_{des} is less negative, implying that the material becomes more stable (decomposition will happen at higher temperatures), similar to what occurs for MgH_{0.85}F_{0.15} compared to MgH₂ [28]. In fact, ΔS_{des} has a larger impact on the temperature of decomposition than ΔH_{des} . To sum up, as the fluorine content increases in the sample, decomposition will occur at higher temperatures resulting in an increase of thermal stability. This is also demonstrated in the DSC and TPD-MS analysis (Fig 5.7).

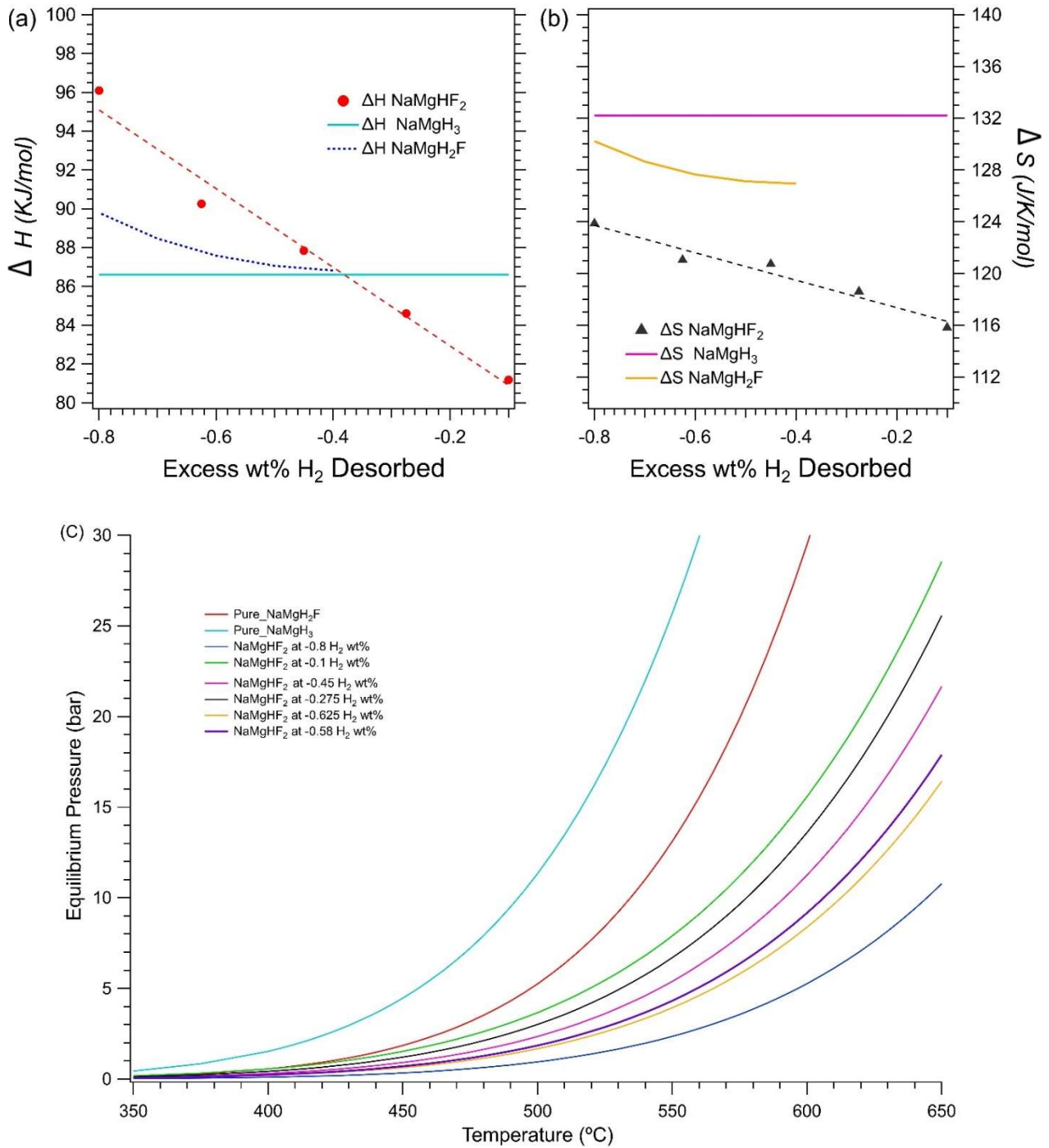


Figure 5.9. (a) Enthalpy of hydrogen desorption for NaMgHF₂, $\Delta H_{\text{des}} = 78.876 \cdot (\text{wt.}\% \text{ H}_2) - 20.268$. (b) Entropy of hydrogen desorption for NaMgHF₂ $\Delta S_{\text{des}} = 115.24 \cdot (\text{wt.}\% \text{ H}_2) - 10.599$. Enthalpy and Entropy is compared with NaMgH₃^{*1} and NaMgH₂F^{*2}. (c) Predicted equilibrium pressures of NaMgH₃, NaMgH₂F and NaMgHF₂ at 6 different values of wt.% H₂ along the plateau. For Fig 6b: pure NaMgH₃ [13] and NaMgH₂F [15]. Graph constructed with values above 470 °C.

5.3.4 Cycling studies

The hydrogen cyclability of NaMgHF₂ was investigated to characterise its reversibility and its potential use in technological applications. Pressure cycling studies were conducted over four sorption cycles at 508 °C (desorption and absorption). To ensure full absorption and desorption occurs during the cycling studies a

system pressure was set at 16 bar for absorption and 1 bar for desorption. Throughout the four consecutive sorption cycles (Fig. 5.10), the hydrogen capacity of the sample decreased gradually with the hydride desorbing 1.07(6) wt.% H₂ for the first cycle and then only reabsorbing 0.82(1) wt.% H₂. After the first cycle, the capacity of NaMgHF₂ was reduced by 9.4 % and a total of ~ 18 % capacity was lost during the 4 cycles (Table 5.7). Cycling was stopped after the fourth absorption, at which point XRD was undertaken (Fig. 5.11). Quantitative analysis shows that NaMgH_{0.63}F_{2.37} and MgO phases were present in 95.06(2) wt.%, 4.94(2) wt.%, respectively. Si was used as an internal standard.

Table 5.7. NaMgHF₂ cycling measurement of 4 cycles at 508 °C between 1 and 16 bar, sorption H₂ wt.%

Cycle number	1	2	3	4
Desorption (H ₂ wt.%)	-1.07(6)	-0.97(5)	-0.95(7)	-0.94(1)
Absorption (H ₂ wt.%)	0.82(1)	0.76(1)	0.72(5)	0.67(3)

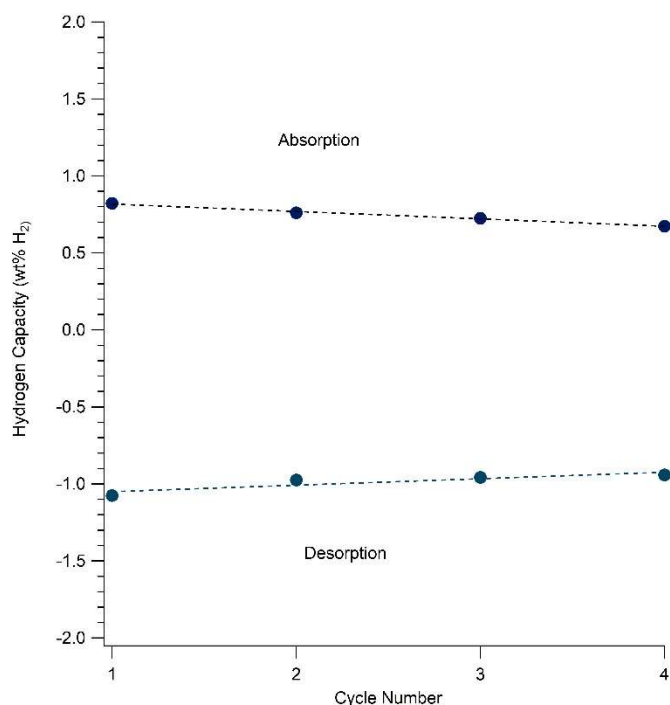


Fig.5.10. Cycling capacity of NaMgHF₂ cycled at 508 °C. Each absorption and desorption were carried out at 1 to 16 bar for 3 h each.

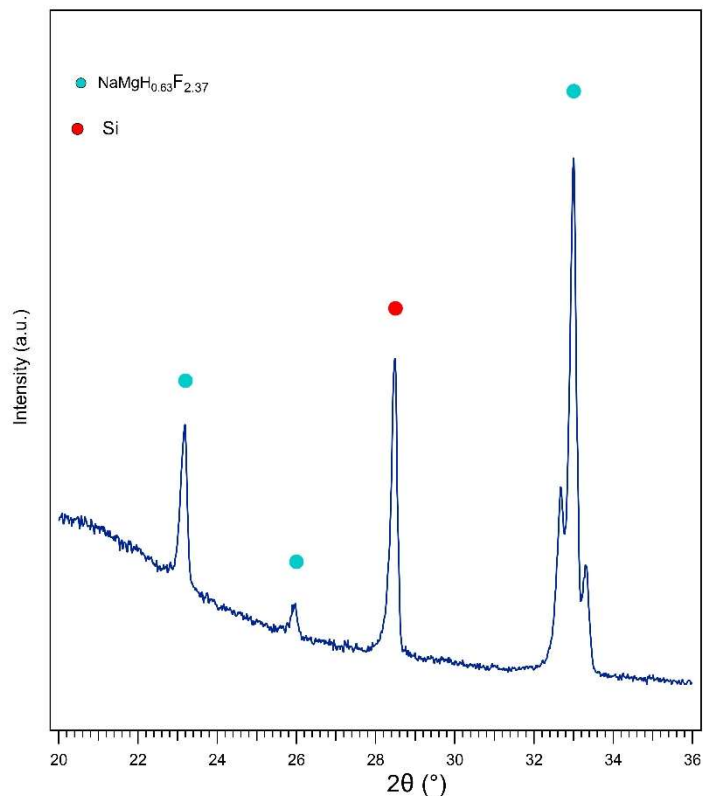


Fig 5.11. XRD data at room temperature of $\text{NaMg}(\text{H}_{1-x}\text{F}_x)_3$ after cycling at 508°C 4 times ending in absorption stage. $\lambda = 1.540596(1)$ Å. Being Si = ● and $\text{NaMgH}_{0.63}\text{F}_{2.37}$ = ●

5.3 Conclusions

A range of $\text{NaMg}(\text{H}_{1-x}\text{F}_x)_3$ ($x = 0, 1, 2, 3$) solid solutions have been synthesised by ball milling stoichiometric ratios of NaH, NaF, MgH_2 and MgF_2 followed by annealing under hydrogen backpressure. Their potential use as hydrogen storage or thermal energy storage materials has been examined by *in situ* synchrotron XRD, DSC-TGA-MS and PCI analysis.

Thermal studies carried out on all $\text{NaMg}(\text{H}_{1-x}\text{F}_x)_3$ mixtures determined that the thermal stability of Na-Mg-H-F solid solutions increases with increased F content. Decomposition occurs in a single endothermic event step with DSC data showing a maximum temperature of H_2 desorption of 525°C for NaMgHF_2 . As regards to TPD-MS measurements, the NaMgHF_2 curve shows at least two different regimes with a maximum temperature peak of hydrogen desorption observed at 545°C . *In situ* synchrotron data shows that NaMgHF_2 reaches full decomposition at 595°C forming NaMgF_3 , NaF and MgO. The decomposition reaction commences at $\sim 320^\circ\text{C}$.

PCI measurements of NaMgHF_2 determined an enthalpy of decomposition of 89 ± 12 kJ/mol H_2 and entropy of 121 ± 16 J/K/mol H_2 . In comparison with NaMgH_3 , these values increased from 86.60 kJ/mol H_2 and decreased from 132.20 J/K/mol H_2 , respectively [29]. Cycling of NaMgHF_2 has been investigated over four cycles at 508°C , with a reduction of $\sim 18\%$ of the practical hydrogen capacity.

Using NaMgHF₂, less hydrogen will be required to be stored to generate electrical power for solar thermal storage, compared to other Mg-based hydrides, such as MgH₂, Mg₂FeH₆, NaMgH₃, due to its high enthalpy (such as 89 compared to 74, 77 and 86.6 kJ mol⁻¹ H₂ respectively), theoretical H₂ wt.% (such as 1.16 compared to 7.66, 5.47 and 4.01 H₂ wt.% respectively) and high operating temperatures. Further research on NaMgHF₂ is needed to address H₂ loss during cycling. Once these problems are fixed this material can be evaluated as a candidate for solar thermal energy.

5.4 References

- [1] D.P. Broom. Hydrogen storage materials: the characterisation of their storage properties. Springer 2011.
- [2] M.S. Tortoza, T.D. Humphries, D.A. Sheppard, M. Paskevicius, M.R. Rowles, M.V. Sofianos, et al. Thermodynamics and performance of the Mg-H-F system for thermochemical energy storage applications. *Physical Chemistry Chemical Physics*. 20 (2018) 2274-83.
- [3] D. Abbott. Keeping the Energy Debate Clean: How Do We Supply the World's Energy Needs? *Proceedings of the IEEE*. 98 (2010) 42-66.
- [4] Q. Lai, M. Paskevicius, D.A. Sheppard, C.E. Buckley, A.W. Thornton, M.R. Hill, et al. Hydrogen Storage Materials for Mobile and Stationary Applications: Current State of the Art. *Chemsuschem*. 8 (2015) 2789-825.
- [5] J.-C. Crivello, R.V. Denys, M. Dornheim, M. Felderhoff, D.M. Grant, J. Huot, et al. Mg-based compounds for hydrogen and energy storage. *Applied Physics A*. 122 (2016) 85.
- [6] T.D. Humphries, D.A. Sheppard, C.E. Buckley. Recent advances in the 18-electron complex transition metal hydrides of Ni, Fe, Co and Ru. *Coordination Chemistry Reviews*. 342 (2017) 19-33.
- [7] McPhy Energy, <http://www.mcphy.com/en/products/solid-hydrogen-storage/>; [accessed 17/02/2016].
- [8] D.A. Sheppard, T.D. Humphries, C.E. Buckley. Sodium-based hydrides for thermal energy applications. *Applied Physics A*. 122 (2016) 406.
- [9] B. Bogdanović, M. Felderhoff, G. Streukens. Hydrogen storage in complex metal hydrides. *Journal of the Serbian Chemical Society*. 74 (2009) 183-96.
- [10] P. Chen, Z. Xiong, J. Luo, J. Lin, K.L. Tan. Interaction of hydrogen with metal nitrides and imides. *Nature*. 420 (2002) 302.
- [11] G. Barkhordarian. patent pending, German Pub. No: DE102004/061286 (priority 2004); Barkhordarian G, Klassen T, Dornheim M, Bormann R. *Journal of Alloys and Compounds*. 440 (2007) L18.
- [12] J.J. Vajo, S.L. Skeith, F. Mertens. Reversible storage of hydrogen in destabilized LiBH₄. *Journal of Physical Chemistry B*. 109 (2005) 3719-22.
- [13] D.A. Sheppard, M. Paskevicius, C.E. Buckley. Thermodynamics of Hydrogen Desorption from NaMgH₃ and Its Application As a Solar Heat Storage Medium. *Chemistry of Materials*. 23 (2011) 4298-300.
- [14] D. Pottmaier, E.R. Pinatel, J.G. Vitillo, S. Garroni, M. Orlova, M.D. Baró, et al. Structure and Thermodynamic Properties of the NaMgH₃Perovskite: A Comprehensive Study. *Chemistry of Materials*. 23 (2011) 2317-26.
- [15] D.A. Sheppard, C. Corgnale, B. Hardy, T. Motyka, R. Zidan, M. Paskevicius, et al. Hydriding characteristics of NaMgH₂F with preliminary technical and cost evaluation of magnesium-based metal hydride materials for concentrating solar power thermal storage. *RSC Advances*. 4 (2014) 26552-62.
- [16] A. Bouamrane, J. Laval, J.-P. Soulie, J. Bastide. Structural characterization of NaMgH₂F and NaMgH₃. *Materials Research Bulletin*. 35 (2000) 545-9.
- [17] U.D.o. Energy. D.O.E. ARPA-E High Energy Advanced Thermal Storage – DE-FOA-0000471.
- [18] A. Reiser, B. Bogdanović, K. Schlichte. The application of Mg-based metal-hydrides as heat energy storage systems. *International Journal of Hydrogen Energy*. 25 (2000) 425-30.
- [19] A. Bouamrane, C. De Brauer, J.-P. Soulié, J. Létouffé, J. Bastide. Standard enthalpies of formation of sodium–magnesium hydride and hydridofluorides NaMgH₃, NaMgH₂F and NaMgF₂H. *Thermochimica Acta*. 326 (1999) 37-41.
- [20] T.D. Humphries, D.A. Sheppard, M.R. Rowles, M.V. Sofianos, C.E. Buckley. Fluoride substitution in sodium hydride for thermal energy storage applications. *Journal of Materials Chemistry A*. 4 (2016) 12170-8.
- [21] E. Rönnebro, D. Noréus, K. Kadir, A. Reiser, B. Bogdanovic. Investigation of the perovskite related structures of NaMgH₃, NaMgF₃ and Na₃AlH₆. *Journal of Alloys and Compounds*. 299 (2000) 101-6.
- [22] C.E. Messer. Hydrides versus fluorides: Structural comparisons. *Journal of Solid State Chemistry*. 2 (1970) 144-55.
- [23] G.W. Stinton, J.S. Evans. Parametric Rietveld refinement. *Journal of Applied Crystallography*. 40 (2007) 87-95.
- [24] H.T. Stokes, D.M. Hatch, B.J. Campbell, D.E. Tanner. ISODISPLACE: a web-based tool for exploring structural distortions. *Journal of Applied Crystallography*. 39 (2006) 607-14.

- [25] B.J. Campbell, J.S. Evans, F. Perselli, H.T. Stokes. Rietveld refinement of structural distortion-mode amplitudes. *IUCr Comput Comm Newsl.* 8 (2007) 81-95.
- [26] A. Coelho. TOPAS-Academic, Brisbane. Australia 2016.
- [27] C.J. Howard, H.T. Stokes. Group-theoretical analysis of octahedral tilting in perovskites. *Acta Crystallographica Section B: Structural Science.* 54 (1998) 782-9.
- [28] T.D. Humphries, J. Yang, R.A. Mole, M. Paskevicius, J.E. Bird, M.R. Rowles, et al. Fluorine Substitution in Magnesium Hydride as a Tool for Thermodynamic Control. *The Journal of Physical Chemistry C.* 124 (2020) 9109-17.
- [29] M. Paskevicius, D.A. Sheppard, C.E. Buckley. Thermodynamic Changes in Mechanochemically Synthesized Magnesium Hydride Nanoparticles. *Journal of the American Chemical Society.* 132 (2010) 5077-83.

6. Conclusions, future work and outlook

According to the United Nations, climate change started to occur as early as the 1800s and is mainly due to human activities such as burning fossil fuels (coal, oil and gas), which generates greenhouse gas emissions (GHG). The use of renewable energies such as solar, wind, tidal, hydropower, biomass, biofuels, geothermal and hydrogen, all seem to be attractive solutions to limit the CO₂ emissions. However, the problem is to store this energy so it is available 24/7.

Currently, energy produced from fossil fuels is abundantly utilised as they have been used for centuries, so therefore, they are easy to transport, and are easily transformed into energy. In contrast, the energy generated by renewable sources, such as solar and wind, is intermittent and often reliant on the weather and season. As renewables are becoming increasingly prominent on the electrical grid, there is growing interest in systems that store clean energy.

Currently the majority of development and investigations on solar thermal energy storage (TES) are focused on high-temperature reactions. One type of TES is thermochemical energy storage (TCES), which is the storage of heat by an endothermic reaction of a substance at given conditions of pressure and temperature into two (or more) compounds. The energy delivered breaks the chemical bond between the atoms. This reaction must be reversible, so that the stored thermal energy can be recovered through the reverse exothermic reaction. Metal hydrides offer a wide range of high-operational temperatures and attractive energy densities with the ability to absorb and release hydrogen at specific temperatures and pressures.

The focus of this thesis is the investigation, analysis, development, and synthesis of metal hydrides to be used as TECS, by using the thermochemical reaction of their formation as a source of heat to store energy. Metal hydrides are reversible, the metal reacts with gaseous hydrogen forming the hydride through an exothermic reaction that releases heat, on the other hand the metal hydride absorbs heat through an endothermic reaction and releases hydrogen gas. This property can be exploited to release and store heat on demand. However, the reaction to form metal hydrides from metal and hydrogen involves large quantities of thermal energy, but in some cases, this reaction happens at temperatures below 565 °

C. As a consequence, the work presented herein explored the stabilisation of metal hydrides through fluorine substitution so that the decomposition temperature of such materials is increased. The substitution of fluorine into metal hydrides allows the stabilisation of the metal hydrides, in turn requiring higher temperatures of decomposition, therefore incurring greater amounts of thermal energy to be released during the reaction between the metal fluoride and hydrogen. This means they can be used for high-temperature thermal storage (> 565 °C). The work published in this thesis explored a range of different metal hydrides substituted with fluorine including MgH₂ and NaMgH₃ forming Mg(H_xF_{1-x})₂ and NaMg(H_{1-x}F_x)₃ systems, respectively. Moreover, in all cases, it was confirmed that the exchange of H and F in metal hydrides and metal fluorides with similar characteristics and crystalline structure generates a material with increased

thermal stability that will permit hydrogen cycling at higher temperatures and therefore greater efficiency for thermal energy storage, despite the reduction in hydrogen-storage capacity.

Magnesium hydride (MgH_2) is discussed in chapters three and four. It can generally operate as a hydrogen storage material between 300 °C and 420 °C as sintering starts to occur above the upper temperature. However, fluorine substitution for hydrogen in magnesium hydride increases the operating temperature of the metal hydride whilst limiting degradation. The substitution of fluorine for hydrogen in MgH_2 forms a range of $\text{Mg}(\text{H}_x\text{F}_{1-x})_2$ ($x = 1, 0.95, 0.85, 0.70, 0.50, 0$) composites. This is achieved by ball milling quantitative ratios of MgH_2 and MgF_2 followed by annealing under hydrogen backpressure. This substitution is utilised to thermodynamically stabilise the material, so it can be used as a thermochemical energy storage material with the potential to replace molten salts in concentrating solar thermal plants.

The potential use of these $\text{Mg}(\text{H}_x\text{F}_{1-x})_2$ composites as hydrogen storage materials was examined by in situ synchrotron powder XRD, DSC-TGA-MS and PCI analysis. The physical properties of these solid solutions have also been studied by powder X-ray diffraction, inelastic neutron spectroscopy, and thermal conductivity. In addition, these measurements have been verified by density functional theory calculations. Regarding the thermal studies, they were carried out on the $\text{Mg}(\text{H}_x\text{F}_{1-x})_2$ mixtures, which inferred that F content and thermal stability are proportionally related, although a decrease in the absorption/desorption kinetics compared to pure MgH_2 was observed. Using powder X-ray diffraction, it was discovered that the tetragonal unit cell volume MgH_2 to MgF_2 expands by 5.4 %. Overall, an increment in F⁻ content increases the average Mg–H(F) bond strength, allowing the thermal stability of the material to increase, enabling fluorine-rich $\text{Mg}(\text{H}_x\text{F}_{1-x})_2$ compounds to be potentially used as thermochemical energy storage materials. In fact, this was the first time that the $\text{Mg}(\text{H}_x\text{F}_{1-x})_2$ system had been studied by inelastic neutron diffraction, and together with GDOS data, it was confirmed that these materials had an expansion in lattice parameters and bond distances due to a trend in vibrational frequencies and intensities from MgH_2 towards MgF_2 .

$\text{Mg}(\text{H}_{0.85}\text{F}_{0.15})_2$ exhibited a maximum rate of H_2 desorption at 434 °C, with a practical hydrogen capacity of 4.6 ± 0.2 wt.% H_2 (theoretical 5.4 wt.% H_2). During the decomposition of each $\text{Mg}(\text{H}_x\text{F}_{1-x})_2$ composition, a stable phase of $\text{Mg}(\text{H}_{0.43}\text{F}_{0.57})_2$ was formed causing the remaining H_2 in the composites not to be released until above 505 °C. The enthalpy (ΔH_{des}) of $\text{Mg}(\text{H}_{0.85}\text{F}_{0.15})_2$ was determined to be 73.6 ± 1.2 kJ mol⁻¹ H_2 and entropy (ΔS_{des}) 131.2 ± 2 J K⁻¹ mol⁻¹ H_2 through PCI measurements. These values are slightly lower than for pure MgH_2 which has ($\Delta H_{\text{des}} = 74.06$ kJ mol⁻¹ H_2 and $\Delta S_{\text{des}} = 133.4$ J K⁻¹ mol⁻¹ H_2). $\text{Mg}(\text{H}_{0.85}\text{F}_{0.15})_2$ was investigated over six absorption/desorption cycles, between 420 and 480 °C at ~ 27 bar, and demonstrated a reduction of 27 % of the practical hydrogen capacity of 4.6 wt% H_2 . This entails an increased usable cycling temperature of ~ 80 °C compared to bulk MgH_2 , increasing the thermal operating temperatures for technological applications.

In chapter five, fluorine substitution into the NaMgH₃ system was performed to develop NaMg(H_{1-x}F_x)₃ ($x = 0, 1, 2, 3$) systems. In this chapter, a range of NaMg(H_{1-x}F_x)₃ solid solutions were synthesised by ball milling, varying mixtures of NaH, NaF, MgH₂ and MgF₂ followed by annealing under hydrogen backpressure. Their potential use as hydrogen storage or thermal energy storage materials were examined by *in situ* synchrotron XRD, DSC-TGA-MS and PCI analysis.

Thermal studies were carried out on NaMg(H_{1-x}F_x)₃ compounds concluding that the thermal stability of Na-Mg-H-F solid solutions increases with increased F content. For example, NaMgHF₂ in DSC measurement showed a maximum rate of H₂ desorption at 525 °C, and in TPD-MS measurement the curve shows at least two different rates with a maximum peak observed at 545 °C. *In situ* synchrotron data shows that NaMgHF₂ commences decomposition at ~ 320 °C and reaches full decomposition at 595 °C forming NaMgF₃, NaF and Mg.

As predicted, NaMgHF₂ is more thermodynamically stable. The enthalpy of decomposition was determined as $\Delta H = 89 \pm 12$ kJ/mol H₂, with an entropy of $\Delta S = 121 \pm 16$ J/K/mol H₂ by PCI measurements. Indeed, in comparison with NaMgH₃, these values increased for $\Delta H = 86.60$ kJ/mol H₂ and decreased for $\Delta S = 132.20$ J/K/mol H₂, respectively. Hydrogen cycling of NaMgHF₂ was demonstrated over four cycles at 508 °C, with a reduction of ~ 18 % of the practical hydrogen capacity, confirming that this material holds potential as a TES material for multiple applications. Overall, the crystallographic studies and thermodynamics properties are measured for NaMg(H_{1-x}F_x)₃ system, and it is found that NaMgHF₂ has attractive thermodynamics properties, making it a potential candidate as a high temperature metal hydride (HTMH).

All this data demonstrates that the substitution of hydrogen by fluorine in metal hydrides (MgH₂ and NaMgH₃) permits a relationship between the amount of F substituted with an increment in Mg–H bond strength, making the samples F substituted more thermally stable, therefore improving the hydrogen absorption and desorption properties by increasing the operational temperature. These hydrides can release and uptake hydrogen, improving kinetics and reversibility with little to no hysteresis, enhancing their potential use as TCES materials.

Based on the research in this thesis fluorine substitution into metal hydrides can help to develop new materials with F-rich content to be considered as a potential HTMH for TCES applications. This class of materials store heat, with an energy density of between 5 and 30 times higher than molten salts, and also have the potential to reduce heat storage cost because the increased thermal stability of the fluorine substituted hydride means less H₂ is needed to generate the same amount of heat. With less H₂ in the system, the cost to store this H₂ (until it is needed to generate heat) is reduced and the raw material cost of the high temperature metal hydride is reduced as metal fluorides are cheaper than the metal hydrides they partially replace. Indeed, one major advantage of CSP plants is that, when paired with a thermal energy storage (TES) module, electricity can be generated when the sun is not shining.

Also, more experiments need to be done with $\text{MgH}_{0.5}\text{F}_{0.5}$ that exhibits a high stability, abundant and low cost, and probably could be an interesting candidate to scale up and be used as a HTMH, and it has similar composition to the stable phase of $\text{Mg}(\text{H}_{0.43}\text{F}_{0.57})_2$ formed during sorption measurements, so it can be inferred that despite the lowest hydrogen content this sample has potential to be an interesting candidate for energy storage.

I believe that these materials will be useful in TCES applications in the future. The world needs to stop using fossil fuels and this is a promising way to do so. Metal hydrides are ideal materials for heat storage with high energy density. There is no doubt that this technology requires further innovation and development, but it is promising and has a lot of potential. It has been proven that they can function as energy storage materials in a wide range of temperatures from low to high. However, metal hydrides have been developed and tested on a small scale (lab scale). Therefore, the next step will be to scale to a prototype scale of 10 – 1000 kg according to the amount of energy required to store and deliver. Although these materials and this technology have a great future, to successfully achieve the technological implementation on a commercial scale there are significant challenges that must be addressed before thermochemical energy storage can become a fundamental part of the energy infrastructure. Efficiency, types of materials, stability and durability, corrosivity, safety, scalability, economic factors, and environmental impact, are some aspects that need to be addressed to overcome the roadblocks. It is clear that new questions will appear and will be solved in the future, but now it is imperative to test the system at large scale, in order to commence heat storage system commercialisation.

It is important not to lose focus on global challenges, and that is to preserve the environment and its resources while developing humanity and its progress, which is why it is important to generate energy through a system of renewable sources, continuous production, and low cost, with wide coverage, safe, sustainable and with constant availability.

6.1 Outlook

As it was mentioned previously, the use of these fuels has caused many problems, among which are: 1) global warming or the greenhouse effect caused mainly by the release of CO_2 and subsequent climate change; 2) deterioration of air quality in large cities where fossil fuel-based transportation, industry (such as agro-industry, cement manufacture), and electricity is used; 3) increase in fossil fuel prices as a result of the sustained increase in demand with a supply that in certain periods does not meet the demand.

It is critical to scale up clean energy power to avoid the potential catastrophes humanity faces if global warming increases. Leveraging solar energy is essential to achieve this, with available technologies such as solar photovoltaics (PV) and solar thermal electricity or concentrated solar power (CSP). For solar energy the low-tech method and most efficient in terms of sunlight used to produce electricity is CSP. CSP has the

convenience of TES, an energy storage system capable of storing large amounts of energy (heat) from the sun for a long time and at a low cost. TES is a significant advantage of CSP to combat fluctuating supplies of energy on the grid.

Most modern CSP plants operate between 290 °C and 565 °C using a 60/40 wt% mixture of sodium and potassium nitrate, where molten salt acts as the heat transfer fluid (HTF) and sensible heat store, which is coupled to a Rankine steam cycle [1]. However, the most efficient CSP plants are those with higher temperatures, this implies lower costs and, as a consequence, competitiveness, with a typical temperature range between 600 °C and 750 °C, with a storage time span of 12 - 14 h (at night) [2, 3]. Chloride salts give the possibility to reach these higher temperatures at > 700 °C, generating corrosion and being more expensive. For example, a two-tank nitrate system costs US \$ 20 - 33 kWh_{th}⁻¹, while MgCl₂/KCl is estimated at US \$ 58 kWh_{th}⁻¹, above the CSP-TES target of < US \$ 15 kWh_{th}⁻¹ [2] Phase change materials (PCM) and TCES materials, are a higher energy density technology that is used in TES allowing one to have smaller stores and also to use less material. For example, a multi-tube heat exchanger using latent heat (chlorides) was estimated at US \$ 39 kWh_{th}⁻¹, and this is also higher than the target value of CSP-TES [1]. Of the three TES technologies (sensible heat, PCM, and TCES), TCES has the lowest thermal energy losses and the highest material energy density, hence the cost is potentially low.

The advantages of TCES materials over molten, salts such as nitrate salts (60% NaNO₃ + 40% KNO₃) are high thermal and electric efficiency due to their high energy density 1657 kJ/kg for CaCO₃ (413 kJ/kg for nitrate salts). Also, due to a more extensive range of working temperature, for example 890 °C for CaCO₃ and nitrate salts it is limited at <565°C due to chemical instability (Table 1.1) [4-6], and for TCES less volumes are required to store energy for several hours.

Molten salts used in CSP technology also have some drawbacks, as the molten salts (60% NaNO₃ and 40% KNO₃, for example) have low thermal and electric efficiency due to their low mass energy density 413 kJ/kg [7], are corrosive, and tend to freeze below 200 °C [8]. In addition, large volumes are required to store energy for several hours, and the operating temperature is limited to 565 °C [9, 10]. In all, these factors result in high costs.

For TCES the main issue is reversibility and cyclability and a small operating temperature gap between the forward and backward reaction (small reaction hysteresis). Of these, MHs could become a promising system as they have a high energy density and can store energy and release it reversibly when it is required [1]. The main objective is to develop TCES materials with improved efficiency and reduced cost for use in a CSP system. MHs can operate at a wide range of target temperatures for solar energy (operating at higher

temperatures such as 565 °C Na/Mg based and around 700 °C (e.g., Ca/Sr based) [6]. These MH are fully reversible and have low hysteresis. The great advantage of TCES MHs is the possibility through stabilization or destabilization techniques to tailor the properties to the required temperatures.

A relevant point to consider is the storage of the hydrogen gas that is released during the endothermic process (hydrogen desorption). Hydrogen can be stored in a closed or open loop system. In a closed system, H₂ storage is sized exclusively for the CSP plant. One solution could be the sorption of H₂ by a low temperature metal hydride (LTMH) forming a pair of HTMH and LTMH. However, it is not the only option, and each alternative has its advantages and disadvantages.

These materials can be integrated into large scale system. For instance, the materials studied in this thesis are stabilized metal hydrides that can be used as HTMH and be paired with an LTMH such as NaAlH₄ integrated strictly into a system such as a typical power plant. This can include a CSP plant with integrated storage unit (in the centre) that is connected to both the solar collector and the thermal cycle. In case of strong solar radiation, i.e. in the charging process, the heat from the collector is transferred to the thermal cycle, and the surplus thermal energy is fed into the storage unit. In case of weak solar radiation or in other time periods, i.e., in the unloading process, the working fluid of the thermal cycle is heated with energy from the thermal storage system [11]. Usually, incorporating storage with a parabolic dish is challenged by that the energy needs to be stored either on the dish or on the ground, for which the high-temperature thermal energy should be moved efficiently from the dish by other devices. The thermal energy needs to be carried away from the dish in the storage form of lower temperature chemical reaction products. The energy can be added to the system via a reversible endothermic reaction to produce the heated reaction products. Then, the reaction products can be cooled in a counter flow heat exchanger in terms of preheating the chemical reactants. After that, it can be sent to storage until the sorption reaction is reversed to produce the heat and thus generate a thermal power cycle. Another example of application is the integration of a TCES system to a coal-fired power station. The basic principles are that the heat stored in the materials converts boiler water to steam, which is then used to spin turbines that turn the generators.

The large-scale use of CSP integrated with TES systems is an effective and sustainable option to alleviate fossil fuel scarcity and pollution problems, reducing global climate change.

6.2 References

- [1] M. Adams, C.E. Buckley, M. Busch, R. Bunzel, M. Felderhoff, T.W. Heo, T. Humphries, T.R. Jensen, J. Klug, K.-H. Klug. Hydride-based thermal energy storage. *Progress in Energy*. 4 (2022) 032008.
- [2] M. Mehos, C. Turchi, J. Vidal, M. Wagner, Z. Ma, C. Ho, W. Kolb, C. Andraka, A. Kruizenga. Concentrating solar power Gen3 demonstration roadmap. National Renewable Energy Lab.(NREL), Golden, CO (United States)2017.
- [3] A. Palacios, C. Barreneche, M. Navarro, Y. Ding. Thermal energy storage technologies for concentrated solar power—A review from a materials perspective. *Renewable Energy*. 156 (2020) 1244-65.
- [4] T.D. Humphries, M. Paskevicius, A. Alamri, C.E. Buckley. Thermodynamic destabilization of SrH₂ using Al for the next generation of high temperature thermal batteries. *Journal of Alloys and Compounds*. 894 (2022) 162404.
- [5] K.T. Møller, A. Ibrahim, C.E. Buckley, M. Paskevicius. Inexpensive thermochemical energy storage utilising additive enhanced limestone. *Journal of Materials Chemistry A*. 8 (2020) 9646-53.
- [6] K. Manickam, P. Mistry, G. Walker, D. Grant, C.E. Buckley, T.D. Humphries, M. Paskevicius, T. Jensen, R. Albert, K. Peinecke. Future perspectives of thermal energy storage with metal hydrides. *International Journal of Hydrogen Energy*. 44 (2019) 7738-45.
- [7] T.D. Humphries, K.T. Møller, W.D. Rickard, M.V. Sofianos, S. Liu, C.E. Buckley, M. Paskevicius. Dolomite: A low cost thermochemical energy storage material. *Journal of Materials Chemistry A*. 7 (2019) 1206-15.
- [8] D.N. Harries, M. Paskevicius, D.A. Sheppard, T.E.C. Price, C.E. Buckley. Concentrating Solar Thermal Heat Storage Using Metal Hydrides. *Proceedings of the IEEE*. 100 (2012) 539-49.
- [9] M. Fellet, C.E. Buckley, M. Paskevicius, D.A. Sheppard. Research on metal hydrides revived for next-generation solutions to renewable energy storage. *Mrs Bulletin*. 38 (2013) 1012-3.
- [10] SunShot Vision Study, Chapter 5: Concentrating Solar Power Technologies, Cost, and Performance. US Department of Energy2012.
- [11] G. Li, X. Zheng. Thermal energy storage system integration forms for a sustainable future. *Renewable and Sustainable Energy Reviews*. 62 (2016) 736-57.

Supporting information

Belonging to the manuscript

Thermodynamics and stability of the Mg-H-F system for thermochemical energy storage applications

M. S. Tortoza,^a T. D. Humphries,^{a*} D. A. Sheppard,^a M. Paskevicius,^a M. R. Rowles,^a M. V. Sofianos,^a K. F. Aguey-Zinsou^b and C. E. Buckley^a

- ^a. Department of Physics and Astronomy, Fuels and Energy Technology Institute, Curtin University, GPO Box U1987, Perth, WA 6845, Australia.
- ^b. Merlin Group, School of Chemical Engineering, The University of New South Wales, Sydney, NSW 2052, Australia.

* E-mail: terry_humphries81@hotmail.com

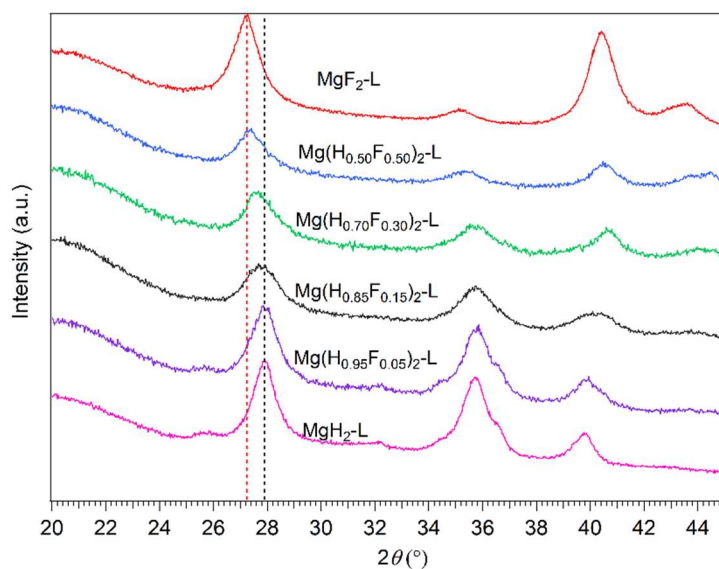


Figure I.1. Ex-situ XRD data for samples ball milled for 40 hours (L) collected at room temperature. $\lambda=1.5418 \text{ \AA}$. Red and black dot line's refers to main peaks of MgF_2 and MgH_2 respectively.

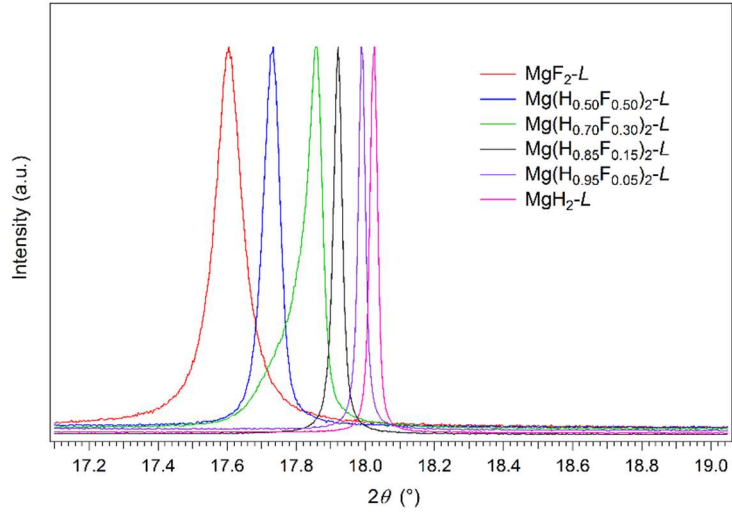


Figure I.2. In situ SR-XRD at room temperature of $Mg(H_xF_{1-x})_2-L$ samples ball milled for 40 hours and annealed. $\lambda = 1.0003896$.

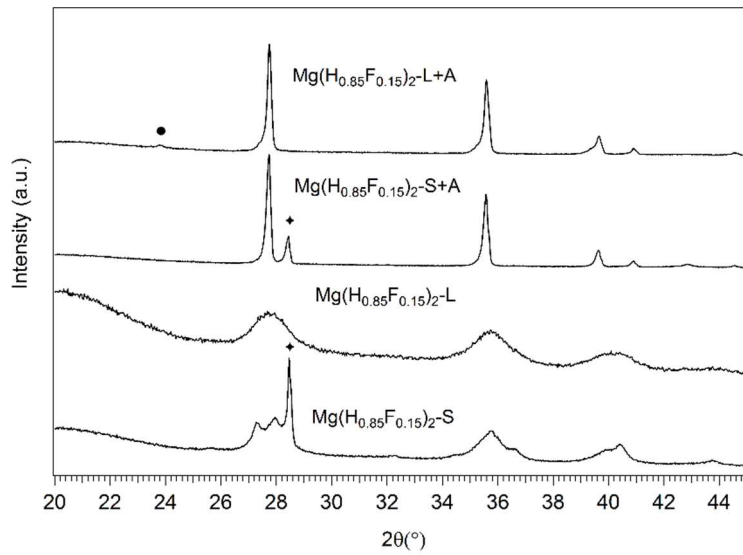


Figure I.3. Comparison between SR-XRD of samples ball milled for 10 and 40 hours and then annealed (A). ● = Mg_2FeH_6 , ◆ = Si. $\lambda = 1.5418 \text{ \AA}$, at room temperature

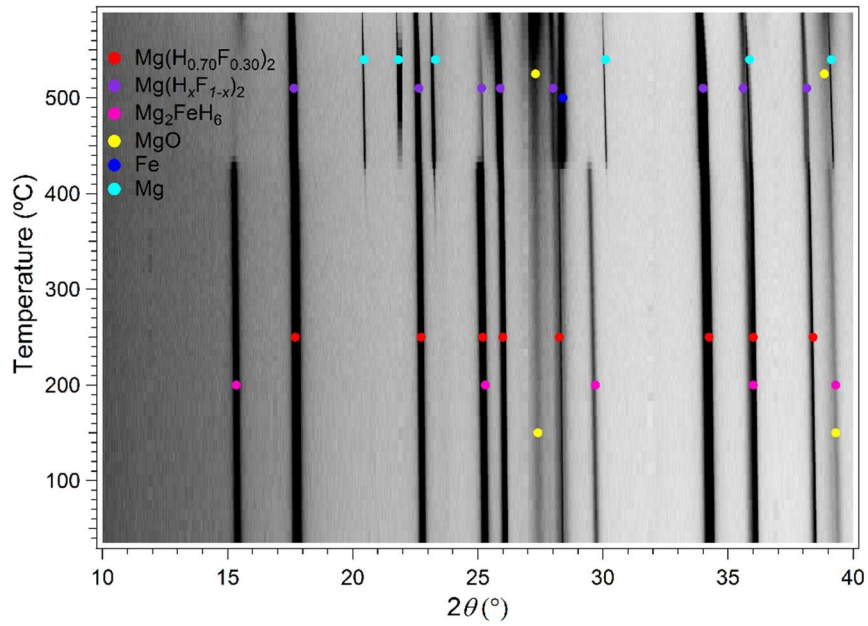


Figure I.4. In-situ XRD for $\text{Mg}(\text{H}_{0.70}\text{F}_{0.30})\text{-L}$ performed under vacuum using a heating rate of $10^\circ\text{C}/\text{min}$ before 200°C and $5^\circ\text{C}/\text{min}$ after 200°C . $\lambda = 1.0003896 \text{ \AA}$.

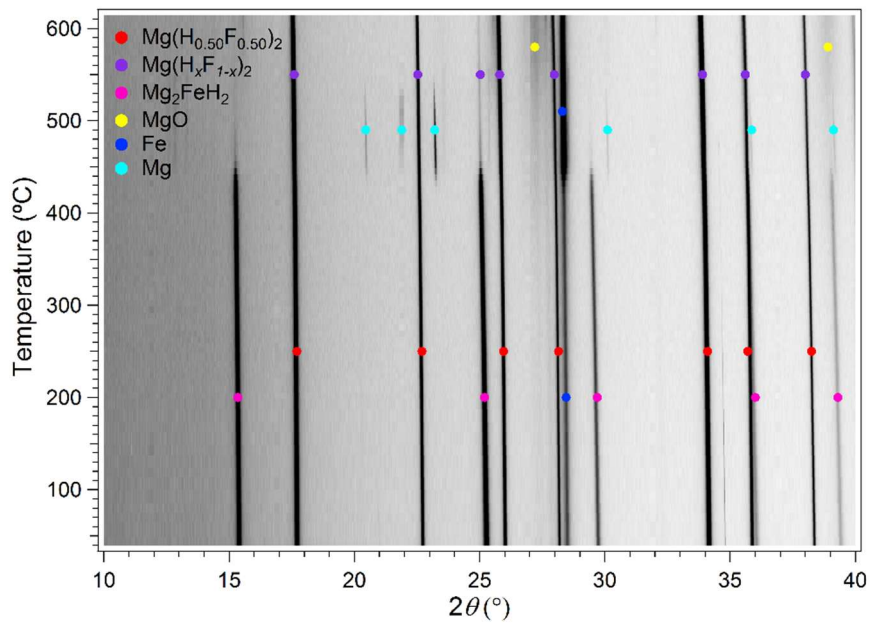


Figure I.5. In-situ XRD for $\text{Mg}(\text{H}_{0.50}\text{F}_{0.50})\text{-L}$ performed under vacuum using a heating rate of $10^\circ\text{C}/\text{min}$ before 200°C and $5^\circ\text{C}/\text{min}$ after 200°C . $\lambda = 1.0003896 \text{ \AA}$.

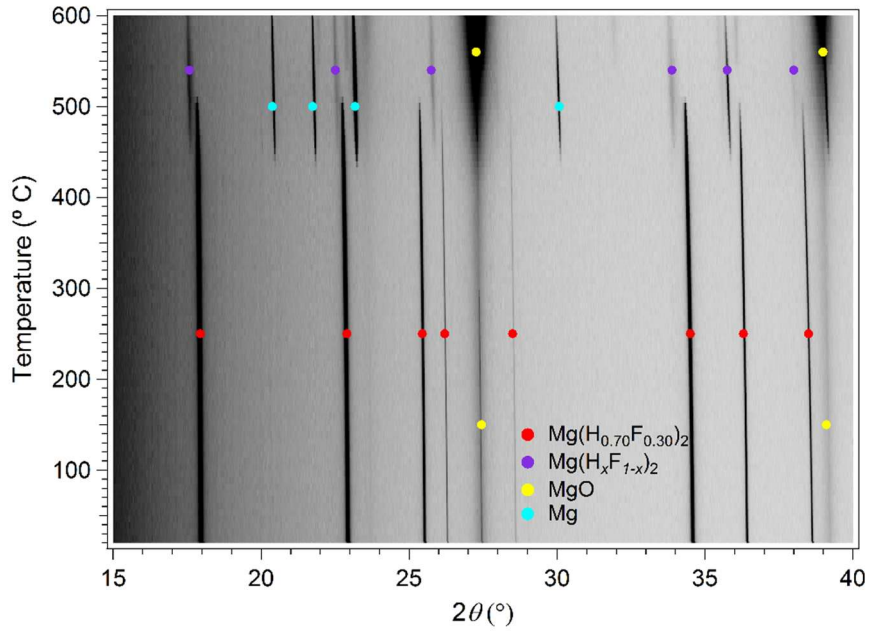


Figure I.6. In-situ XRD for Mg(H_{0.95}F_{0.05})-L performed under vacuum using a heating rate of 10°C/min before 200 °C and 5 °C/min after 200 °C. $\lambda = 1.0003896 \text{ \AA}$

Table I.1. Summary of parameters and data collected from PCT desorption measurements of Mg(H_{0.85}F_{0.15})₂-S Pressure and H₂ wt% uncertainties

Temperature (°C)	Observed Desorption H ₂ (wt%)	Final Pressure (bar)	Theoretical H ₂ wt%	Difference between observed vs theoretical H ₂ wt%
437.7	4.57 ± 0.14	14.5 ± 0.014	5.4	0.83
444.2	4.37 ± 0.29	24.1 ± 0.014	5.4	1.03
450.1	4.85 ± 0.19	4 ± 0.014	5.4	0.55
461	4.61 ± 0.15	19.8 ± 0.014	5.4	0.79

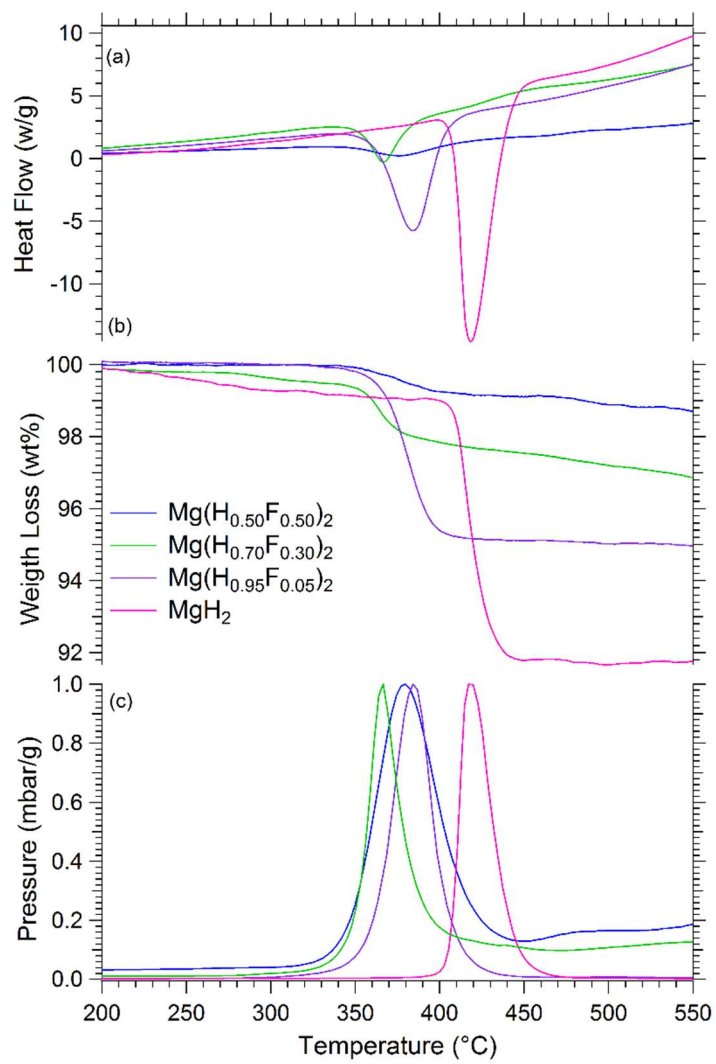
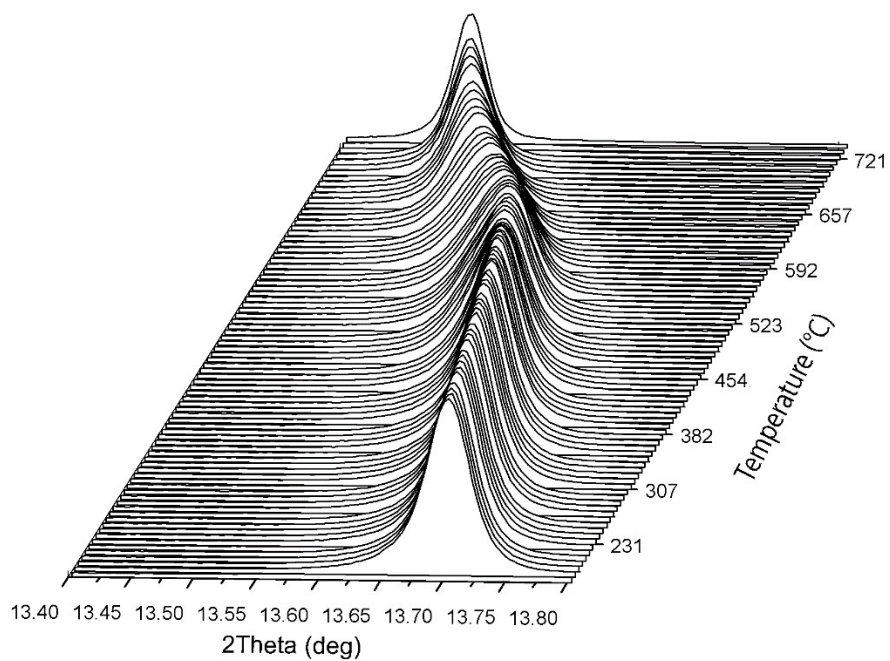
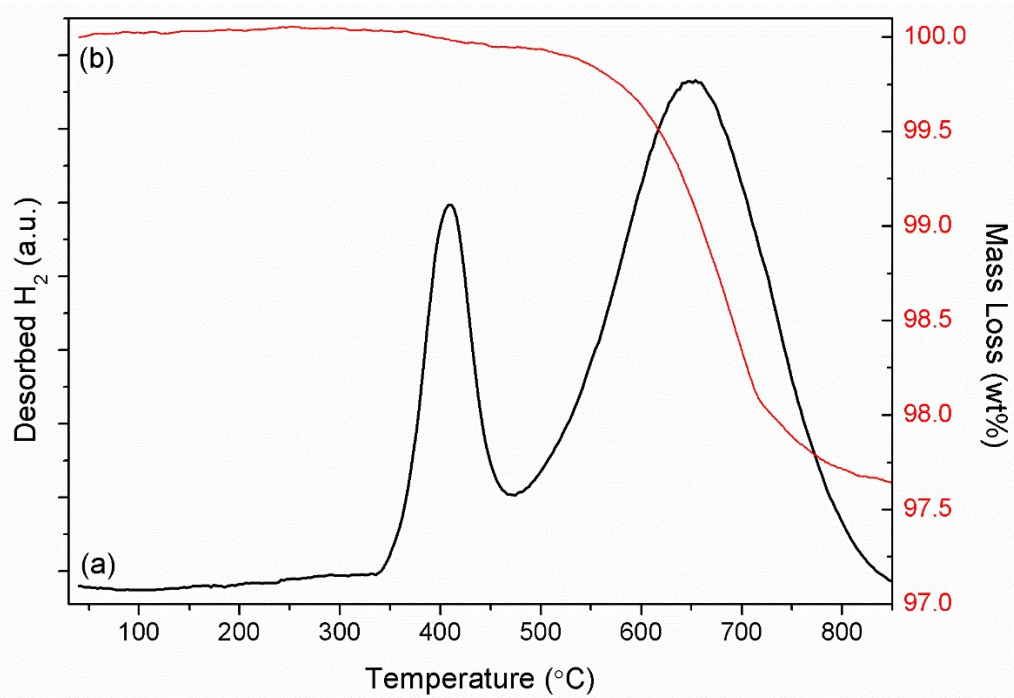


Figure I.7. Simultaneous thermal analysis of $\text{Mg}(\text{H}_{1-x}\text{F}_x)_2\text{-L}$ samples by (a) DSC, (b) TGA and (c) MS. Ramp rate = $10\text{ }^\circ\text{C}/\text{min}$. DSC and MS data are normalised to the mass of the sample.



Supporting Information

Belonging to the manuscript

Fluorine Substitution in Magnesium Hydride as a Tool for Thermodynamic Control

Terry D. Humphries,^{*a} Jack Yang,^{b,c} Richard Mole,^b Mark Paskevicius,^a Julianne Bird,^a Matthew R. Rowles,^{a,d} Mariana S. Tortoza,^a M. Veronica Sofianos,^a Dehong Yu,^b Craig. E. Buckley^a

^a Physics and Astronomy, Fuels and Energy Technology Institute, Curtin University, GPO Box U1987, Perth, WA 6845, Australia

^b Australian Nuclear Science and Technology Organisation, Locked Bag 2001, Kirrawee DC NSW 2232 Australia

^c School of Material Science and Engineering, University of New South Wales, Sydney, New South Wales, 2052 Australia

^d John De Laeter Centre, Curtin University, GPO Box U1987, Perth, WA 6845, Australia

*E-mail: terry_humphries81@hotmail.com

Table II.1. Quantitative Rietveld analysis of SR-XRD data for $Mg(H_xF_{1-x})_2$ solid solutions. Errors are in parentheses. The phases in shaded grey were used in the weight averaged calculations.

MgF ₂	wt%	Lattice Parameter (Å)				Axial Mg-H(F) distance (Å)		Equatorial Mg-H(F) distance		Refined H occupancy factor
		<i>a</i>	<i>c</i>	Wt. av. <i>a</i>	Wt. av. <i>c</i>	Wt. av.	Wt. av.			
1	0.72	4.55822	2.98699(5)	4.62337(5)	3.05214(5)	1.95323(2)	1.98114(2)	1.96041(2)	1.99700(2)	0.76
2	0.00	4.56322	2.99199(5)			1.95537(2)		1.96322(2)		0.78
3	0.18	4.56822	2.99699(5)			1.95751(2)		1.96603(2)		0.80
4	0.18	4.57322	3.00199(5)			1.95966(2)		1.96884(2)		0.82
5	0.13	4.57822	3.00699(5)			1.96180(2)		1.97164(2)		0.84
6	0.17	4.58322	3.01199(5)			1.96394(2)		1.97445(2)		0.86
7	0.17	4.58822	3.01699(5)			1.96608(2)		1.97726(2)		0.89
8	0.12	4.59322	3.02199(5)			1.96823(2)		1.98007(2)		0.90
9	0.25	4.59822	3.02699(5)			1.97037(2)		1.98287(2)		0.92
10	0.16	4.60322	3.03199(5)			1.97251(2)		1.98568(2)		0.94
11	0.99	4.60822	3.03699(5)			1.97465(2)		1.98849(2)		0.96
12	0.88	4.61322	3.04199(5)			1.97680(2)		1.99130(2)		0.98
13	12.59	4.61822	3.04699(5)			1.97894(2)		1.99411(2)		0.99
14	67.93	4.62322	3.05199(5)			1.98108(2)		1.99692(2)		1.01
15	15.52	4.62822	3.05699(5)			1.98322(2)		1.99973(2)		1.03
MgH _{0.95} F _{0.05}										
1	0.59	4.51452	3.01339(1)	4.52458(1)	3.02345(1)		1.946(3)		1.964(2)	0.87
2	2.11	4.51952	3.01839(1)				1.944(3)	1.961(2)		0.89

3	92.56	4.52452	3.02339(1)			1.946(3)		1.964(2)		0.91
4	3.22	4.52952	3.02839(1)			1.948(3)		1.967(2)		0.93
5	0.67	4.53452	3.03339(1)							0.95
6	0.28	4.53952	3.03839(1)							0.97
7	0.17	4.54452	3.04339(1)							0.99
8	0.09	4.54952	3.04839(1)							1.01
9	0.08	4.55452	3.05339(1)							1.03
10	0.09	4.55952	3.05839(1)							1.05
11	0.01	4.56452	3.06339(1)							1.07
12	0.04	4.56952	3.06839(1)							1.09
13	0.03	4.57452	3.07339(1)							1.11
14	0.00	4.57952	3.07839(1)							1.12
15	0.05	4.58452	3.08339(1)							1.14
MgH_{0.85}F_{0.15}										
1	0.00	4.52775	3.01473(1)	4.54284(1)	3.02982(1)		1.946637(1.974027(4)	0.75
2	0.00	4.53275	3.01973(1)							0.77
3	1.82	4.53775	3.02473(1)			1.944456(4)		1.971164(4)		0.79
4	94.53	4.54275	3.02973(1)			1.946598(4)		1.973976(4)		0.80
5	3.65	4.54775	3.03473(1)			1.948741(4)		1.976787(4)		0.82
6	0.00	4.55275	3.03973(1)							0.84
7	0.00	4.55775	3.04473(1)							0.86
8	0.00	4.56275	3.04973(1)							0.88
9	0.00	4.56775	3.05473(1)							0.90
10	0.00	4.57275	3.05973(1)							0.92
11	0.00	4.57775	3.06473(1)							0.94
MgH_{0.70}F_{0.30}										
1	0.00	4.52842	3.00351(3)	4.56514(4)	3.04023(3)		1.95619(2)		1.98201(1)	0.46
2	0.00	4.53342	3.00851(3)							0.48
3	0.00	4.53842	3.01351(3)							0.50
4	0.00	4.54342	3.01851(3)							0.52
5	0.00	4.54842	3.02351(3)							0.54
6	0.00	4.55342	3.02851(3)							0.56
7	46.96	4.55842	3.03351(3)			1.95331(2)		1.97827(1)		0.57
8	22.22	4.56342	3.03851(3)			1.95545(2)		1.98108(1)		0.59
9	10.39	4.56842	3.04351(3)			1.95759(2)		1.98389(1)		0.61
10	7.19	4.57342	3.04851(3)			1.95973(2)		1.98670(1)		0.63
11	4.98	4.57842	3.05351(3)			1.96188(2)		1.98951(1)		0.65
12	3.38	4.58342	3.05851(3)			1.96402(2)		1.99232(1)		0.67
13	2.33	4.58842	3.06351(3)			1.96616(2)		1.99514(1)		0.69
14	1.11	4.59342	3.06851(3)			1.96830(2)		1.99795(1)		0.71
15	1.47	4.59842	3.07351(3)			1.97045(2)		2.00076(1)		0.73

MgH _{0.50} F _{0.50}										
1	0.00	4.53171	2.98387(2)	4.59225(3)	3.04441(2)		1.9716(8)		1.9860(5)	0.16
2	0.00	4.53671	2.98887(2)							0.18
3	0.00	4.54171	2.99387(2)							0.20
4	0.00	4.54671	2.99887(2)							0.22
5	0.00	4.55171	3.00387(2)							0.24
6	0.00	4.55671	3.00887(2)							0.26
7	0.00	4.56171	3.01387(2)							0.28
8	0.00	4.56671	3.01887(2)							0.30
9	0.00	4.57171	3.02387(2)							0.32
10	0.00	4.57671	3.02887(2)							0.34
11	0.00	4.58171	3.03387(2)							0.36
12	12.56	4.58671	3.03887(2)			1.9692(8)		1.9829(5)		0.38
13	66.89	4.59171	3.04387(2)			1.9714(8)		1.9857(5)		0.40
14	17.71	4.59671	3.04887(2)			1.9735(8)		1.9885(5)		0.41
15	2.83	4.60171	3.05387(2)			1.9757(8)		1.9913(5)		0.43
MgH ₂										
1	99.31	4.51795	3.02257(1)	4.51795(1)	3.02257(1)	1.935973(6)	1.935973(6)	1.966804(5)	1.966804(5)	0.96
2	0.69	4.52295	3.02757(1)							0.98
3	0.00	4.52795	3.03257(1)							1.00
4	0.00	4.53295	3.03757(1)							1.02
5	0.00	4.53795	3.04257(1)							1.04
6	0.00	4.54295	3.04757(1)							1.06
7	0.00	4.54795	3.05257(1)							1.08
8	0.00	4.55295	3.05757(1)							1.10
9	0.00	4.55795	3.06257(1)							1.12
10	0.00	4.56295	3.06757(1)							1.14
11	0.00	4.56795	3.07257(1)							1.16
12	0.00	4.57295	3.07757(1)							1.18
13	0.00	4.57795	3.08257(1)							1.20
14	0.00	4.58295	3.08757(1)							1.22
15	0.00	4.58795	3.09257(1)							1.24

Table II.2. Atomic coordinates and thermal parameters of Mg(H_xF_{1-x})₂ solid solutions. Errors are in parentheses.

Sample	Mg coordinates (x, y, z)	H coordinates (x, y, z)	F coordinates (x, y, z)	Mg Thermal parameter (beq)	H Thermal parameter (beq)	F Thermal parameter (beq)
MgF ₂	0, 0, 0	---	0.303, 0.303, 0	0.21(1)	---	0.52(2)
Mg(H _{0.5} F _{0.5})	0, 0, 0	0.303, 0.303, 0	0.303, 0.303, 0	0.97(1)	3	1.23(3)
Mg(H _{0.7} F _{0.3})	0, 0, 0	0.303, 0.303, 0	0.303, 0.303, 0	0.92(2)	3	2.38(8)
Mg(H _{0.85} F _{0.15})	0, 0, 0	0.303, 0.303, 0	0.303, 0.303, 0	1.215(7)	3	2.10(8)
Mg(H _{0.95} F _{0.05})	0, 0, 0	0.303, 0.303, 0	0.303, 0.303, 0	1.088(8)	3	2.7(2)
MgH ₂	0, 0, 0	0.303, 0.303, 0	---	1.45(2)	3	---

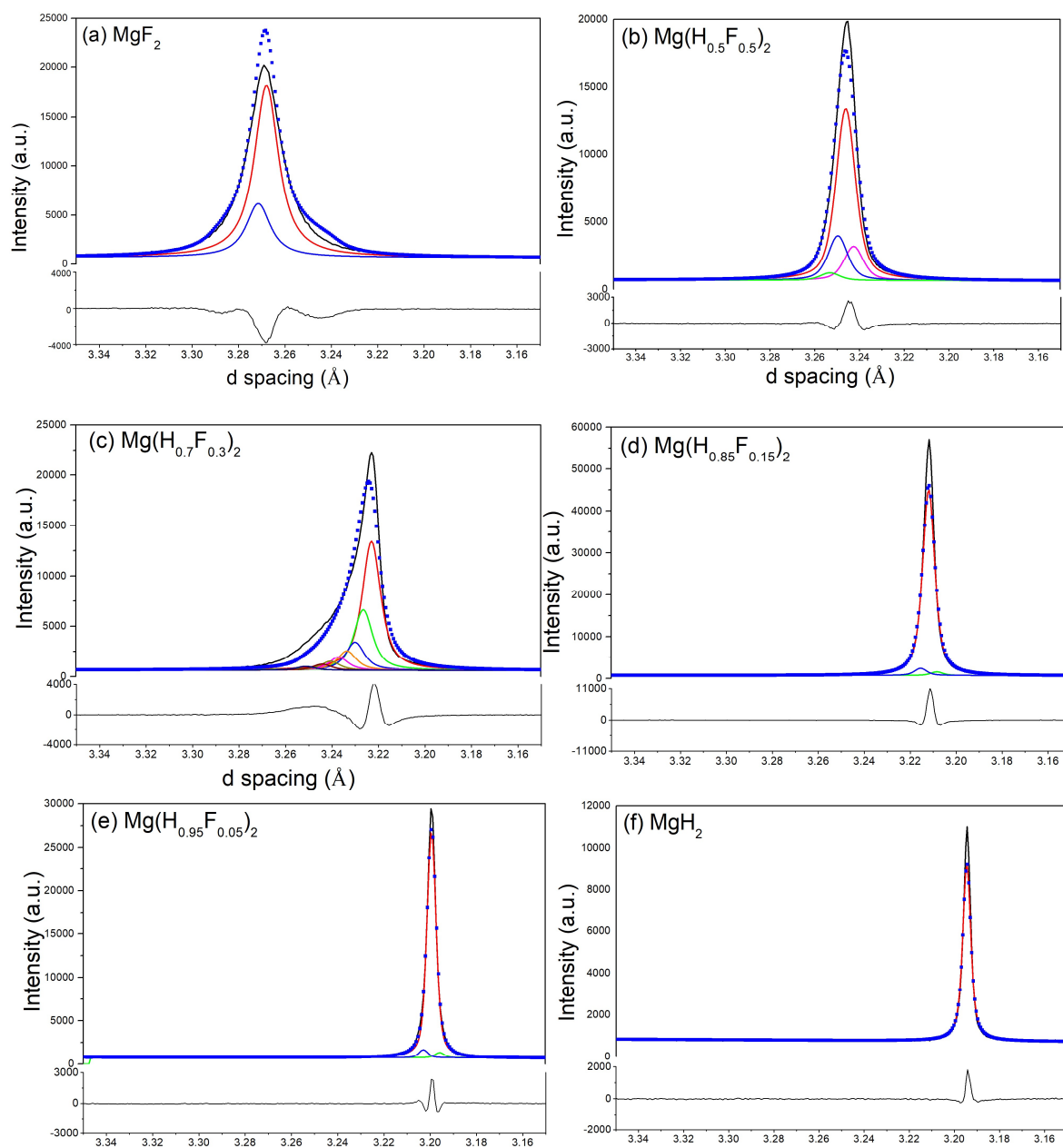


Figure II.1. SR-XRD pattern, Phase distribution and Rietveld refinement plot of $\text{Mg}(\text{H}_x\text{F}_{1-x})_2$ solid solutions focused on the (110) Bragg peak. the Experimental data illustrated as black line, calculated diffraction pattern as blue squares, calculated phase distribution as multi-coloured lines and the difference plot in black at the bottom of the plot. $T = 27^\circ\text{C}$.

Table II.3. Crystallographic parameters for Mg(H_xF_{1-x})₂ compounds optimized by DFT calculations. Percentage difference compared to experimental values given in parentheses.

Sample name	MgH ₂	Mg(H _{0.95} F _{0.05}) ₂	Mg(H _{0.90} F _{0.10}) ₂	Mg(H _{0.85} F _{0.15}) ₂	Mg(H _{0.80} F _{0.20}) ₂	Mg(H _{0.75} F _{0.25}) ₂	Mg(H _{0.70} F _{0.30}) ₂	Mg(H _{0.50} F _{0.50}) ₂	MgF ₂
Super cell size	1x1x1	1x1x5	1x1x5	1x1x5	1x1x5	1x1x5	1x1x5	1x1x1	1x1x1
Atoms in unit cell	6	30	30	30	30	30	30	6	6
Unit cell volume (Å)	61.07028	309.24927	311.51702	313.79404	315.95886	317.97643	319.55212	64.94474	67.27904
Volume/atom	10.17838 (1.01)	10.30831 (0.07)	10.3839 (N/A)	10.4598 (0.37)	10.53196 (N/A)	10.59921 (N/A)	10.65174 (1.31)	10.82412 (1.17)	11.21317 (3.08)
α (Å)	4.50589 (0.27)	4.52701 (0.06)	4.54044 (N/A)	4.55194 (0.2)	4.56547 (N/A)	4.57608 (N/A)	4.58461 (0.55)	4.61052 (0.4)	4.67321 (1.08)
c (Å)	3.00794	15.09009	15.11153	15.14244	15.15988	15.18472	15.20716	3.0579	3.0807
α (°)	90	90	89.9996	90.0006	89.9754	89.9763	89.9755	90	90
β (°)	90	90	89.9996	89.9982	90.019	90.0221	90.0175	90	90
γ (°)	90	89.6908	89.4224	89.7289	89.3277	89.6027	89.4074	87.6092	90
Average Mg-H(F) bond distance (Å)	1.94984 (0.08)	1.95653 (0.16)	1.95983 (N/A)	1.96521 (0.26)	1.96834 (N/A)	1.97319 (N/A)	1.97888 (0.65)	2.00472 (1.34)	2.01258 (1.17)

Table II.4. Thermodynamics of $\text{Mg}(\text{H}_x\text{F}_{1-x})_2$ compounds determined by DFT calculations and physical measurements. ΔH_{form} is the enthalpy of formation of $\text{Mg}(\text{H}_x\text{F}_{1-x})_2$ determined by DFT calculations. ΔH_{des} is the enthalpy of desorption determined experimentally.

Sample (x)	ΔH_{form} DFT (kJ/mol compound)	ΔH_{des} measured (kJ/mol compound)	ΔS_{des} measured (J/K/mol compound)	ΔG_{des} measured (kJ/mol compound, @ 448 °C)
1	-204.4	74.06 ^a	133.4 ^a	-22.1
0.95	-250.7	---	---	---
0.9	-298.3	---	---	---
0.85 ^b	-346.0	62.6 ^b	112 ^b	-17.8
0.8	-393.7	---	---	---
0.75	-441.3	---	---	---
0.7	-489.3	---	---	---
0.5	-681.4	---	---	---
0	-1177.5	1124 ^c	57.17 ^d	---

^a Ref [1]; ^b ref [2]; ^c ref [3]; ^dref [4].

NEXAFS

Near-Edge X-Ray Absorption Fine Structure (NEXAFS) spectroscopy measurements were performed at the Soft X-ray (SXR) beamline of the Australian Synchrotron [5]. All measurements were carried out at room temperature with the ultra-high vacuum (UHV) analysis chamber being maintained at a base pressure of $\leq 9 \times 10^{-10}$ mbar. Powdered samples were loaded in an argon-filled glovebox onto sample mounts and then transferred to the SXR beamline using a purpose-built vacuum transfer vessel. The vacuum transfer vessel is a sealed chamber that ensures that the samples are not exposed to air or moisture in the process of introducing them to the UHV chamber of the beamline. The NEXAFS spectra were recorded at the magnesium K-edge (1280 – 1360 eV). All spectra were obtained in total electron yield (TEY) mode and all NEXAFS spectra were processed and normalised using the QANT software program developed at the Australian Synchrotron [6]. Intensities have been normalised with respect to impinging photon flux.

Figure 8.2 shows the NEXAFS data collected for the $\text{Mg}(\text{H}_x\text{F}_{1-x})_2$ samples with the MgF_2 pattern showing excellent agreement with literature data [7, 8]. MgF_2 has a relatively simple spectrum with two predominant peaks at 1313 and 1318 eV in the full multiple scattering region, followed by several minor features in the intermediate multiple scattering region (IMS).³⁹ The NEXAFS spectrum of MgH_2 in contrast, has a predominant peak at 1308 eV followed by a number of broad features at higher energy. The $\text{Mg}(\text{H}_x\text{F}_{1-x})_2$ spectra each bear resemblance to the parent MgH_2 and MgF_2 spectra and vary depending on the stoichiometry of the solid solution. It has been noted that the spectra of six-coordinate Mg compounds are

the weighted sums of all the independent partial spectra generated by the absorber when located in each different environment within the investigated structure [8].

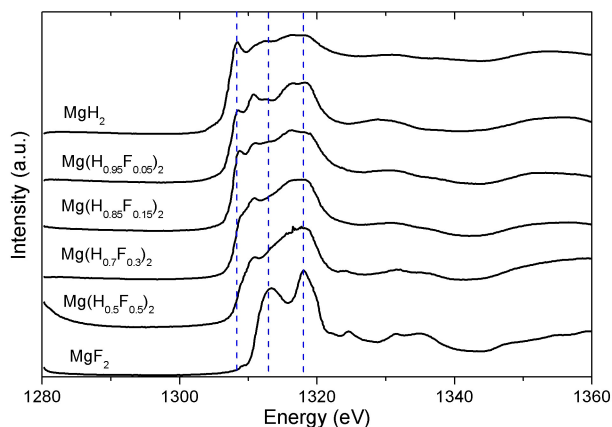


Figure II.2. NEXAFS data collected near the magnesium K-edge for the $Mg(H_xF_{1-x})_2$ system.

References

- [1] M. Paskevicius, D.A. Sheppard, C.E. Buckley. Thermodynamic Changes in Mechanochemically Synthesized Magnesium Hydride Nanoparticles. *Journal of the American Chemical Society*. 132 (2010) 5077-83.
- [2] M.S. Tortoza, T.D. Humphries, D.A. Sheppard, M. Paskevicius, M.R. Rowles, M.V. Sofianos, et al. Thermodynamics and performance of the Mg-H-F system for thermochemical energy storage applications. *Physical Chemistry Chemical Physics*. 20 (2018) 2274-83.
- [3] J.D. Cox, D.D. Wagman, V.A. Medvedev. CODATA key values for thermodynamics. Hemisphere Pub. Corp., New York, 1989.
- [4] M.W. Chase. NIST-JANAF thermochemical tables for oxygen fluorides. *Journal of Physical and Chemical Reference Data*. 25 (1996) 551-603.
- [5] B. Cowie, A. Tadich, L. Thomsen. The current performance of the wide range (90–2500 eV) soft x-ray beamline at the Australian Synchrotron. *AIP Conference Proceedings*. AIP2010. pp. 307-10.
- [6] E. Gann, C.R. McNeill, A. Tadich, B.C.C. Cowie, L. Thomsen. Quick AS NEXAFS Tool (QANT): a program for NEXAFS loading and analysis developed at the Australian Synchrotron. *Journal of Synchrotron Radiation*. 23 (2016) 374-80.
- [7] S.-i. Naoé, T. Murata, T. Matsukawa. Mg K-XANES studies in magnesium halides. *Physica B: Condensed Matter*. 158 (1989) 615-6.
- [8] G. Cibir, A. Marcelli, A. Mottana, G. Giuli, G. Della Ventura, C. Romano, et al. Magnesium X-ray absorption near-edge structure (XANES) spectroscopy on synthetic model compounds and minerals. 19th International Conference on X-ray and Inner-Shell Processes 2003. pp. 95-150.

Appendix III. Ammonium chloride-metal hydride based reaction cycle for vehicular applications

Ammonium chloride-metal hydride based reaction cycle for vehicular applications†

Helen G. Stewart,[‡] Terry D. Humphries,^{‡*} Drew A. Sheppard,[§] Mariana S. Tortoza,[§] M. Veronica Sofianos,[§] Shaomin Liu,[§] and Craig E. Buckley[§]

Received 00th January 20xx,
Accepted 00th January 20xx

DOI: 10.1039/x0xx00000x

www.rsc.org/

Hydrogen and ammonia have attracted attention as potential energy vectors due to their abundance and minimal environmental impact when used as a fuel source. To be a commercially viable alternative to fossil fuels, gaseous fuel sources must adhere to a wide range of standards specifying hydrogen delivery temperature, gravimetric capacity and cost. In this article, an ammonium chloride-metal hydride reaction cycle that enables the solid thermal decomposition products to be recycled using industrial processes is proposed. A range of metal hydrides and metal amides were reacted with ammonium chloride to determine the reaction pathways, products and overall feasibility of the cycle. The $\text{NH}_4\text{Cl-MH}$ (MH = metal hydride) and $\text{NH}_4\text{Cl-MNH}$ (MNH = metal amide) mixtures were heated to temperatures of up to 500 °C. The resulting products were experimentally characterised using temperature program desorption residual gas analysis, simultaneous differential scanning calorimetry and thermogravimetric analysis and *in situ* powder X-ray diffraction. Similar analysis was undertaken to determine the effect of catalyst addition to the starting materials. A maximum yield of 41 wt% of hydrogen and ammonia gas mixtures were released from the $\text{NH}_4\text{Cl-MH}$ materials. This exceptional gravimetric capacity allows for volumetric gas densities (363 – 657 kg/m³) that are much higher than pure NH_3 , H_2 or metal hydride materials. Overall, the reaction cycle potentially allows carbon-neutral regeneration of the starting materials, making it a sustainable energy option.

Introduction

With world energy consumption projected to exceed 18,000 TWh by 2035,¹ it has never been more important to invest in the development of sustainable energy technologies to meet this demand. Hydrogen is an attractive potential energy vector. It is universally abundant on earth, and its combustion has minimal environmental impact as it does not produce any carbon dioxide or nitrous oxides. Storing hydrogen in a high volumetric density format that flexibly links its production and use as an energy source is a critical part of developing a hydrogen economy.²⁻⁴

Hydrogen is traditionally stored in cylinders as a liquid at cryogenic temperatures or as a gas at high pressure.⁵ Storage of hydrogen as a high-pressure gas is preferable in industrial facilities and laboratories, where weight and volume capacities are not limiting factors. Storage of hydrogen as a liquid is also not suitable for energy applications as liquefaction can lead to a loss of up to 40% of hydrogen's energy content, while boil-off and safety concerns (through high-pressure build up upon cooling failure) are also factors to consider.⁶ Overcoming these

barriers and developing a system that can store hydrogen efficiently would provide a long term solution to meeting global energy demands in a sustainable manner.

Metal hydrides are of special interest to the hydrogen storage community. They have the capacity to be developed from inexpensive or abundant materials such as sodium, magnesium, calcium and titanium and form a variety of hydrogen containing species including ionic hydrides, complex hydrides and interstitial hydrides.⁷⁻¹¹ The thermal energy density of metal hydrides is up to thirty times more than molten salts, currently used to store solar energy.^{3, 12, 13} They also have the potential to reversibly absorb large amounts of hydrogen which makes them ideal for fuel cell applications.

When in the form of metal hydrides, light metals such as lithium, sodium, magnesium and aluminium are appealing hydrogen storage candidates due to their low atomic weight and high gravimetric hydrogen content.^{3, 4, 7-9, 11, 13} The higher the hydrogen-metal ratio and the lighter the metal elements incorporated into these compounds, the higher the hydrogen capacity of the material. Increasing the hydrogen capacity of a material is in effect, increasing its gravimetric energy density. Complex hydrides containing these lightweight metals such as borohydrides, transition metal hydrides, amides, imides and alanates are under investigation for use in hydrogen storage applications due to their potential high hydrogen weight capacities.^{2-4, 8, 9}

Ammonia has also been receiving heightened attention as a potential medium of indirect hydrogen storage and as an independent fuel source.¹⁴⁻¹⁶ Ammonia releases 316.80 kJ/mol

[§] Department of Physics and Astronomy, Fuels and Energy Technology Institute, Curtin University, GPO Box U1987, Perth, WA 6845, Australia.

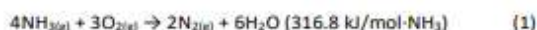
[‡] Department of Chemical Engineering, Curtin University, GPO Box U1987, Perth, WA, 6845, Australia.

* E-mail: terry_humphries81@hotmail.com

† Electronic Supplementary Information (ESI) available: Phase Identification of *in situ* XRD data. See DOI: 10.1039/x0xx00000x

‡ These authors contributed equally to this study.

of energy during combustion.¹⁷ This high energy release inspired Green to propose it as an energy vector by Green in 1982.¹⁸ Ammonia's combustion reaction simply releases nitrogen and water (eq. 1), both naturally present in the earth's atmosphere, although a small amount of NO_x may be produced as a by-product.¹⁹ Providing the nitrogen and hydrogen used to synthesise the ammonia are derived from clean and renewable sources, this reaction does not result in the release of hazardous air pollutants such as CO₂, SO₂ and soot.²⁰ Generally NH₃ has a narrow flammability limit of 15.5% to 27% volume in air,²⁰ which leads to a low combustion rate. However, recent studies have shown that the presence of hydrogen during ammonia combustion can lower combustion temperatures and increase the burning velocity of ammonia flames. In addition, ammonia-fueled solid oxide fuel cells (SOFC) have been developed that can directly utilise ammonia without the requirement for cracking.²¹



The Haber-Bosch process²² has made ammonia readily available at a cost ranging from US\$385 to \$770 per tonne.²³ In fact, global ammonia production is projected to exceed 150 mega tonnes per annum by the end of the decade.²⁴ Infrastructure for large-scale ammonia transportation also exists in the form of trucks, tank carriage, barge, ships and pipelines.²⁵ Therefore, an ammonia based fuel cycle could be expanded to an industrial scale without the need for any new infrastructure. Many factors have prevented the utilisation of ammonia as a large scale commercial fuel source as it is acutely toxic if inhaled, and highly harmful if released into marine environments.²⁶ The risk associated with ammonia's toxicity can be mitigated by storing it as a solid in the form of metal amines, ammonium chlorides, ammonium carbonates or urea, although infrastructure to retrieve the ammonia from the solid (such as thermal treatment) still needs further development.²⁷

In recent studies, ammonium complexes of metal hydrides or metal ammine complexes and metal amines have been under scrutiny as a means of high-density ammonia and hydrogen storage.^{14, 16, 28-31} Upon thermal treatment, these complexes produce either NH₃ and/or H₂. Rather than using ammonia directly as a fuel source, David *et al.* have reported a promising method of extracting hydrogen from ammonia or "ammonia cracking".¹⁴ By passing ammonia through a sodium amide catalyst powder they achieved a 99.2% ammonia decomposition efficiency at a temperature of 530 °C. Another technology for an ammonia cracking fuel cell using a zirconium based catalyst has also been patented.³²

More recently, high purity H₂ (99.99 %) has been produced using a two-step process with initial decomposition using 1 wt % Ru on Al₂O₃ catalyst, followed by purification using Pd-coated tubular vanadium membranes.³³ The catalyst and membrane are operated at temperatures of 450 and 340 °C, respectively. Other reported hydrogen separation membrane systems include Pd, Pd-Ag, vanadium alloys and Nb.³⁴ Additionally, adsorption of ammonia into zeolites has been shown to be an efficient method to purify H₂ produced from ammonia.³⁴

Li and Hurley investigated the effect of the presence of palladium (II) and palladium (IV) chlorides and ammonium chloride on the reaction between ammonia and magnesium hydride.³⁵ Their results showed that the addition of palladium (II) chloride and ammonium chloride increased the concentration of hydrogen in the released ammonia by up to 20 % compared to a non-doped system. This article, along with a study on the effect of La³⁺ on the dehydrogenation of LiAlH₄-NH₄Cl,³⁶ is one of the few articles in current literature that examines ammonium chloride in a metal hydride system.

For the ammonia cycle to be feasible and especially allow ammonia based materials to be used in vehicular or stationary applications, cracking of ammonia must be achieved at a temperature lower than the current limit of 450 °C in order to reduce energy costs.¹⁷ In fact, for vehicular applications, a conversion temperature of ~100 °C would be ideal, with high density storage of ammonia/hydrogen a necessity. In addition, the cycle must use cost-effective materials that can be reprocessed.

In this study, the reactions of ammonium chloride with sodium, magnesium, lithium and calcium hydrides and sodium and lithium amides have been experimentally characterised to determine the temperature at which gas release occurs. An evolved gas composition of N₂ and H₂ would be ideal for technical applications as this would allow technological applications using a PEM fuel cell. To promote the formation of H₂ rather than NH₃, addition of PdCl₂ as a catalyst has been explored. A number of complementary analysis techniques have been employed to determine the reaction pathway and products including temperature program desorption residual gas analysis, simultaneous differential scanning calorimetry and thermogravimetric analysis and *in situ* powder X-ray diffraction. In addition, a cost-effective cycle has been proposed, demonstrating the recyclability of the reaction products.

Experimental

All handling of chemicals was undertaken in an argon-atmosphere Mbraun Unilab glovebox to minimise oxygen (O₂ < 1 ppm) and water (H₂O < 1 ppm) contamination. NH₄Cl (>99.5 %), NaH (>95 %), LiH (~30 mesh, >95.5 %), MgH₂ (hydrogen storage grade), LiNH₂ (>99.5 %) and PdCl₂ (>99.9 %), all purchased from Sigma Aldrich and NaNH₂ (>95 %, Fluka) were used as supplied with no further purification. CaH₂ powder was prepared by the hydrogenation of Ca powder (99%, granular, Sigma Aldrich) under a H₂ pressure of 30 bar and a temperature of 400 °C for 18 h.

The ammonium chloride and metal hydride (MH)/metal amide (MNH₂) powders were mixed by ball milling at 450 rpm in a PQ-NO4 Planetary Ball Mill employing tempered steel vials and balls in an Ar atmosphere. A ball-to-powder mass ratio of 15:1 was employed, in 15 cycles of two minutes milling and a two-minute pause, giving a total milling time of 30 minutes. The stoichiometry of the mixed samples are presented in Table 1. The sample catalysed with PdCl₂ was prepared by combining the previously BM NH₄Cl + NaH powder with either 1 or 10 mol%

PdCl₂ using an agate mortar and pestle for 2 to 3 minutes under an argon atmosphere.

Table 1. Summary of sample compositions and measured decomposition temperatures, mass loss during thermal treatment and reaction products along with calculated costs. The costs are calculated from the cost of the raw materials and the energy produced from the combustion of the relative molar equivalents of NH₃ and H₂ produced during reaction.

Sample	Reaction Onset Temperature (°C) (RGA)	Total Theoretical/ Experimental (TGA) Gravimetric capacity (wt%)	Solid Reaction Products	Gaseous Reaction Products	Theoretical/ Experimental volumetric gas density (kg gas/m ³)	Cost (US\$/kWh) ⁴⁸	Theoretical enthalpy of combustion (kJ/kg reactant)
NH ₄ Cl + NaH	90	24.6/ 24.8	NaCl	H ₂ + NH ₃	360/363	0.6	7209
NH ₄ Cl + NaNH ₂	94	36.8/ 34.0	NaCl	2NH ₃	558/496	1.4	6849
2NH ₄ Cl + MgH ₂	125	28.6/ 40.4	MgCl ₂	2H ₂ + 2NH ₃	430/607	0.3	8381
NH ₄ Cl + LiH	115	31.0 / 37.6	LiCl	H ₂ + NH ₃	364/442	5.2	9092
NH ₄ Cl + LiNH ₂	72	44.5 / 38.3	LiCl	2NH ₃	640/519	15.7	8287
2NH ₄ Cl + CaH ₂	120	25.5 / 41.4	CaCl ₂	2H ₂ + 2NH ₃	406/657	0.5	7494
NH ₄ Cl + NaH + PdCl ₂ (1 mol%)	60	24.3/ 28.8	NaCl + Pd	H ₂ + NH ₃	—	—	—

X-Ray diffraction (XRD) was performed using the Bruker AXS D8 Advance Discover XRD System ($\lambda = 1.5406 \text{ \AA}$) set at 40 kV and 40 mA. The data was collected with a proportional counter, using a step scan from 2° to $80^\circ 2\theta$ with 0.03 degree steps for 0.6 s/step. XRD sample holders covered with a poly(methylmethacrylate) (PMMA) airtight dome were used to prevent oxygen/moisture contamination during data collection. The PMMA airtight bubble results in a broad hump in XRD patterns centred at $\sim 20^\circ 2\theta$. *In situ* synchrotron powder X-ray diffraction (SR-XRD) was performed at the Australian Synchrotron in Melbourne, Australia.⁴⁹ Powdered samples were loaded in a quartz capillary (outer diameter 0.7 mm, wall thickness 0.01 mm) that were then, using graphite ferrules, mounted in 1/16" tube fittings in a glove box filled with purified argon ($< 1 \text{ ppm O}_2$ and H₂O). The sample holder was then connected to a H₂ gas filling/vacuum manifold and the capillary heated with a hot air blower with a heating rate of 5 °C/min *in vacuo*. The temperature of the hot-air blower was calibrated against the known thermal expansion coefficients for NaCl and Ag.^{40, 41} One-dimensional SR-XRD patterns (monochromatic X-rays with $\lambda = 1.0003896(1) \text{ \AA}$) were collected using a Mythen, microstrip detector with an exposure time of 54 s per pattern. The capillary was rotated 120° during exposure to improve the powder averaging. The crystalline phases were identified by reference to the ICDD PDF database. Diffraction patterns were quantitatively analysed with the Rietveld method using the TOPAS software (Bruker-AXS).

TPD-MS (Temperature Programmed Desorption-Mass Spectrometry) was performed on a quadrupole mass spectrometer residual gas analyser (Stanford Research Systems RGA 300). For each measurement, approximately 0.5 mg of sample was outgassed at below 4×10^{-7} mbar over a minimum of 3 hours. While still under vacuum, the samples were heated up to 480 °C at a heating rate of 2 °C/min. Interpretation of the MS data was carried out using RGA Version 3.218.004 (SRS) using $m/e = 2$ for H₂ and 17 for NH₃. Simultaneous Differential Scanning Calorimetry - Thermal Gravimetric Analysis (DSC-TGA) was performed on a Mettler Toledo DSC 3+ using sample masses of ~ 10 mg at a heating rate of 5 °C/min under an argon

flow of 20 mL/min. The temperature accuracy of this instrument is ± 0.2 °C, while the balance has an accuracy of $\pm 20 \mu\text{g}$.

Results and Discussion

Thermal analysis and decomposition pathway

The NH₄Cl and metal hydride mixtures were ball-milled for 30 mins to maximise homogeneity but also minimise any potential reaction that could occur due to the heat generated during the milling process. Any reaction would result in capacity loss of gases evolved during thermal analysis. Table 1 summarises each of the mixtures employed in this study along with primary results of thermal experiments including DSC-TGA-RGA and also theoretical thermodynamic calculations.

Thermal decomposition of pure NH₄Cl

The decomposition of commercial ammonium chloride was measured by *in situ* SR-XRD and DSC-TGA (Figs. 1 and S1†) to allow direct comparison against the decomposition pathway of the measured NH₄Cl-MH and NH₄Cl-MNH₂ powder mixtures. The DSC data shows two endothermic events with peak maxima at 190 °C (corresponding to the phase II (LT-NH₄Cl) and phase I (HT-NH₄Cl) solid-solid phase transition), and 310 °C (corresponding to the decomposition of NH₄Cl), which was in agreement with literature values.^{42, 43} The TGA shows a distinct sublimation onset at ~ 208 °C, ending at ~ 330 °C, with a total

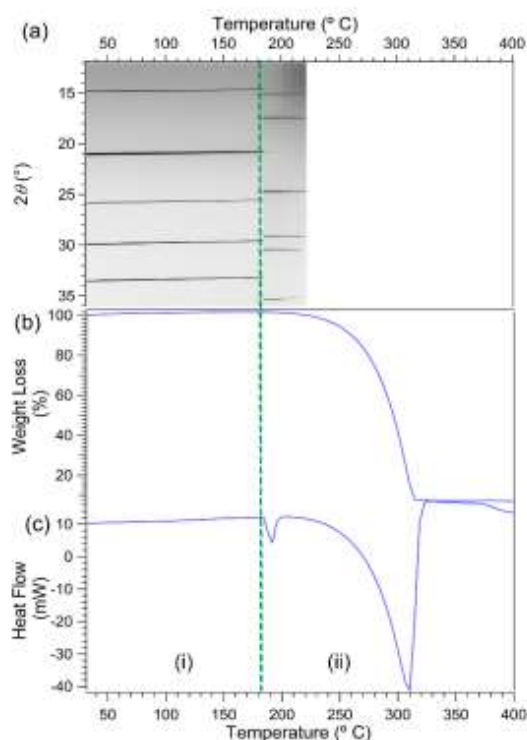


Fig. 1. (a) *in situ* SR-XRD data, (b) TGA and (c) DSC data for NH_4Cl . Region (i): contains LT- NH_4Cl phase. Region (ii) contains HT- NH_4Cl phase. For complete phase identification of XRD data see Fig. S1. $\Delta T/t = 5^\circ\text{C}/\text{min}$. $\lambda = 1.0003896(1) \text{ \AA}$. Endothermic heat flow in the down direction for DSC data.

mass loss of 94 wt%, allowing for the purity of the starting material.

The *in situ* SR-XRD data corroborates the thermal analysis results. Phase analysis of the material shows that the material at room temperature has Bragg peaks corresponding to LT- NH_4Cl only (space group (SG) $Pm\bar{3}m$). At $\sim 190^\circ\text{C}$ there is a phase change corresponding to the solid-solid phase transition from the LT- NH_4Cl to HT- NH_4Cl (SG $Fm\bar{3}m$) followed by the subsequent start of decomposition at $\sim 200^\circ\text{C}$.

Thermal decomposition of $\text{NH}_4\text{Cl} + \text{NaH}$

Quantitative analysis of the SR-XRD data of the starting material at room temperature (RT) indicates that the BM material consists of NH_4Cl (66.3(2) wt%), NaH (29.3(2) wt%), NaOH (2.2(2) wt%) and NaCl (2.1(1) wt%) (Figs. 2a and S2[†]). The small quantity of NaCl observed at RT can only be distinguished by the [022] reflection at $2\theta = 29.0^\circ$ due to the [002] ($2\theta = 20.4^\circ$) reflection being overlapped by the [111] peak of NaH. At $\sim 100^\circ\text{C}$ the [022] reflection for NaCl clearly starts to increase in intensity corresponding to the onset of decomposition with a corresponding initial gas detection at $\sim 90^\circ\text{C}$ for the RGA and TGA (Fig. 2b, d, Region (i) and Fig. S2). The first decomposition

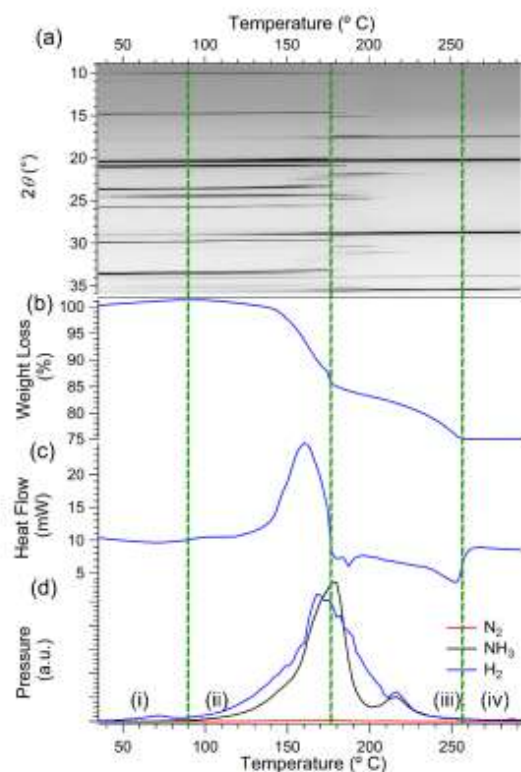


Fig. 2. (a) *in situ* SR-XRD data, (b) TGA, (c) DSC and (d) RGA data for $\text{NH}_4\text{Cl} + \text{NaH}$. Region (i): contains NaH, LT- NH_4Cl , NaOH and NaCl phases. Region (ii): contains NaH, LT- NH_4Cl , NaOH and NaCl phases. Region (iii) contains NaCl, NaOH and HT- NH_4Cl phases. Region (iv) contains NaCl. For complete phase identification of XRD data see Fig. S2. $\Delta T/t = 5^\circ\text{C}/\text{min}$. $\lambda = 1.0003896(1) \text{ \AA}$. Endothermic heat flow in the down direction for DSC data.

event is exothermic having a maximum heat flow at 161°C and ending at $\sim 180^\circ\text{C}$ (Fig. 2c). Coincidentally, NaH is no longer observed by SR-XRD after $\sim 185^\circ\text{C}$, while any remaining LT- NH_4Cl transitions to the HT phase, which is denoted by an endothermic peak by DSC (peak max = 187°C). In addition, a splitting of the NaH Bragg peaks is observed to occur above 100°C which is associated with the dissolution of NaOH impurities into the NaH lattice.¹³ From TGA, the mass loss in the first decomposition step was measured as 16.8%, while quantitative Rietveld refinement determined that 85 wt% of NH_4Cl has been consumed along with 100% NaH, giving a weight loss of 16% consisting of 0.85NH_3 and 0.925H_2 .

The remaining NH_4Cl decomposes in an endothermic process, with a maximum rate of H_2 and NH_3 release at $\sim 215^\circ\text{C}$, leaving NaCl as the only crystalline product. For the remaining HT- NH_4Cl to not decompose into HCl and NH_3 , a Na source, other than NaCl, must be present in order to form NaCl, H_2 and NH_3 . Crystalline NaOH is still present up to $\sim 200^\circ\text{C}$ allowing for a Na source. Beyond this temperature, it is likely that an amorphous NaOH species may exist. This is corroborated by the fact that only H_2 and NH_3 were observed by RGA above 200°C . Overall, a

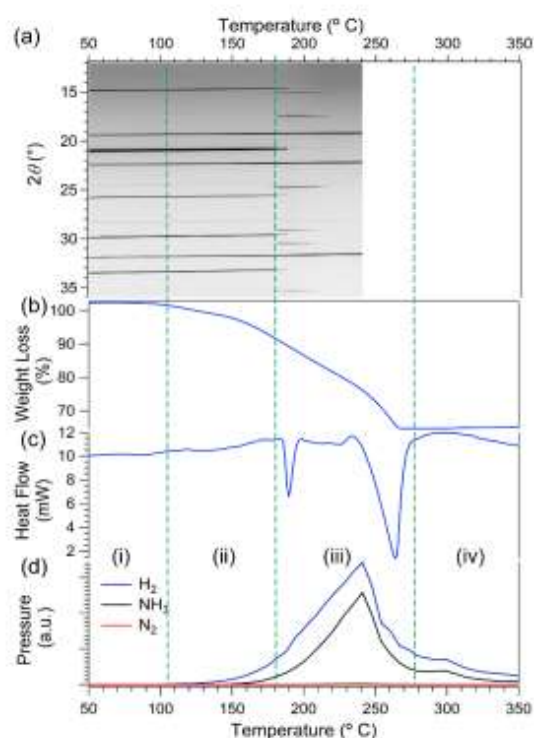


Fig. 3. (a) *In situ* SR-XRD data, (b) TGA, (c) DSC and (d) RGA data for $\text{NH}_4\text{Cl} + \text{LiH}$. Region (i) and (ii) contains LiH , $\text{LT-NH}_4\text{Cl}$ and LiCl phases. Region (iii) contains LiCl and $\text{HT-NH}_4\text{Cl}$ phases. Region (iv) contains LiCl . For complete phase identification of XRD data see Fig. S4†. $\Delta T/t = 5^\circ\text{C}/\text{min}$. $\lambda = 1.0003896(1) \text{ \AA}$. Endothermic heat flow in the down direction for DSC data.

total mass loss of 24.8 wt% was measured before 260 °C, which is close to the expected mass loss of 24.6 wt%.

Thermal decomposition of $\text{NH}_4\text{Cl} + \text{LiH}$

Initial laboratory based XRD of the $\text{NH}_4\text{Cl} + \text{LiH}$ starting material at *RT* directly after BM indicates that the material consisted of $\text{LT-NH}_4\text{Cl}$ (89(2) wt%), LiH (10(2) wt%) and LiCl (1.0(2) wt%) (Fig. S3†), indicating that negligible decomposition occurred during the process. After eight months of storage at *RT* under an Ar atmosphere SR-XRD was conducted. At this point some decomposition had occurred with a composition of NH_4Cl (78.2(5) wt%), LiH (8.4(5) wt%) and LiCl (13.4(1) wt%) being determined (Figs. 3a, S3 and S4†). This suggests that the mixture of these two materials is only metastable. According to the RGA data (Fig. 3d), onset of H_2 desorption occurs at 115 °C, while NH_3 was not detected until 145 °C. The SR-XRD data shows that at $\sim 135^\circ\text{C}$ the LiCl phase ([111] Bragg peak at $\sim 2\theta = 19.2^\circ$), by observation of the data, starts to increase in intensity while at 182 °C the $\text{LT-NH}_4\text{Cl}$ phase disappears ([011] Bragg peak at $\sim 2\theta = 20.8^\circ$) with some undergoing a phase transformation to $\text{HT-NH}_4\text{Cl}$. At $\sim 200^\circ\text{C}$ quantitative Rietveld refinement determines that the sample consists of $\text{HT-NH}_4\text{Cl}$ (38.9(4) wt%), LiCl (58.1(5) wt%) and LiH (3.0(6) wt%). The initial quantity of

LiH may be diminished compared to the theoretical value due to the reduced X-ray scattering of the light Li and H atoms compared to N and Cl. As a result, the peaks for LiH are barely visible in the initial diffraction pattern thus quantification by XRD may not be totally dependable throughout.

The remaining $\text{HT-NH}_4\text{Cl}$ decomposes in an endothermic process having a maximum heat flow at 264 °C (Fig. 3c) and a peak desorption rate measured by RGA for both H_2 and NH_3 at 241 °C. The final crystalline product is LiCl although 2.5(6) wt% LiH was also observed upon completion of the XRD experiment. Overall a total mass loss of 35.5 wt% was measured below 268 °C by TGA (Fig. 3b), which is close to the theoretical mass loss of 31.0 wt%. There are subtle variations of an otherwise linear weight change in this region which are most easily observed in the derivative of the TGA pattern (Fig. S5†). As LiH is still observable at the end of the *in situ* SR-XRD experiment, the exaggerated mass loss of an additional 4.5 % may be attributed to the direct decomposition of NH_4Cl into NH_3 and HCl . Although HCl was not detected by RGA, the gas release profile of NH_3 and H_2 appear to be similar and it may be assumed that the HCl may react with the stainless steel tubing producing H_2 at the same rate as NH_3 is detected.

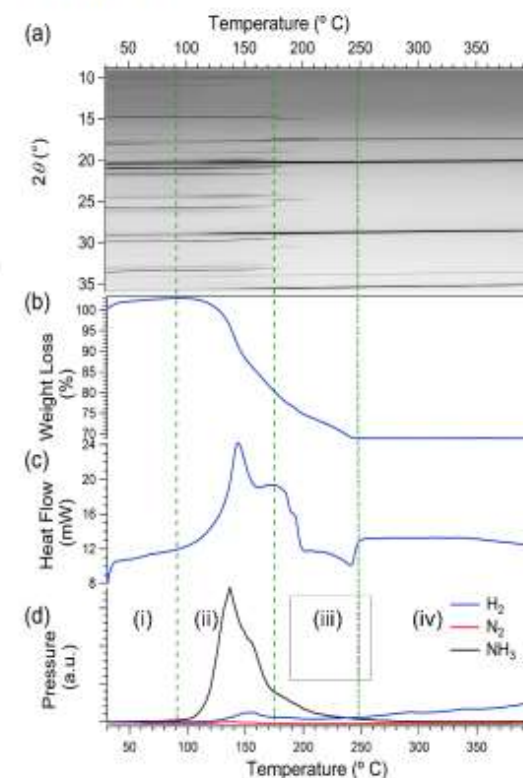


Fig. 4. (a) *In situ* SR-XRD data, (b) TGA, (c) DSC and (d) RGA data for $\text{NH}_4\text{Cl} + \text{NaNH}_2$. Region (i) and (ii) contains NaNH_2 , $\text{LT-NH}_4\text{Cl}$, NaOH , an unknown and NaCl phases. Region (iii) contains NaCl and $\text{HT-NH}_4\text{Cl}$ phases. Region (iv) contains NaCl . For complete phase identification of XRD data see Fig. S6†. $\Delta T/t = 5^\circ\text{C}/\text{min}$. $\lambda = 1.0003896(1) \text{ \AA}$. Endothermic heat flow in the down direction for DSC data.

Thermal decomposition of $\text{NH}_4\text{Cl} + \text{NaNH}_2$

The SR-XRD pattern of the initial BM mixture of NH_4Cl and NaNH_2 indicates that some decomposition has occurred during milling with the observation of NaCl along with the NH_4Cl and NaNH_2 starting materials (Figs. 4a and S6[†]). In addition, impurity NaOH and another unknown phase were identified. Upon reaching $\sim 146^\circ\text{C}$ during *in situ* SR-XRD measurements, all remnants of NaNH_2 had disappeared. At this point, excluding the unknown phase, the composition of the material determined by quantitative phase analysis is $\sim 42.7(5)$ wt% of NH_4Cl , $28.7(4)$ wt% NaCl and $28.5(8)$ wt% NaOH . The LT to HT phase change for NH_4Cl begins at $\sim 164^\circ\text{C}$, while the HT-phase undergoes decomposition and is unidentifiable by $\sim 215^\circ\text{C}$. The NaOH and the unknown phase are no longer detected by ~ 190 and $\sim 200^\circ\text{C}$, respectively, leaving NaCl as the only crystalline phase. While it was not possible to index the Bragg peaks for the unknown phase, it is believed that it is a $\text{Na}(\text{OH})_{1-x}(\text{NH}_2)_x$ phase.⁴⁴ The formation of this material during BM would also ascertain why NaCl is observed in the initial material.

Thermal decomposition of $\text{NH}_4\text{Cl} + \text{LiNH}_2$

The SR-XRD pattern of the ball milled mixture of NH_4Cl and LiNH_2 contains $57.4(1)$ wt% NH_4Cl , $20.3(1)$ wt% LiNH_2 , $21.8(1)$ wt% LiCl , and $0.43(9)$ wt% Li_2O indicating that some decomposition

occurred during the milling process (Figs. 5a and S7[†]). This assumption is corroborated by TGA data, in which a 38 wt% loss is observed rather than the theoretical value of 44.5 wt% (Fig. 5b). As the BM initial sample contained $21.8(1)$ wt% LiCl , assuming a 1:1 reaction product of $\text{LiCl}:\text{NH}_3$ (Table 1), this equates to 8.8 wt% NH_3 desorbed during milling, which is close to the difference between the measured and theoretical TGA capacities.

Thermal analysis of the material by TGA indicates that the onset temperature of decomposition occurs at 80°C (Fig. 5b). The broad exothermic event in the DSC data originating at 90°C , with a maxima of 143°C , is attributed to a slow reaction between NH_4Cl and LiNH_2 , producing NH_3 gas (Fig. 5c). This step produces 9 wt% NH_3 between 80 and 152°C . NH_3 , along with a minuscule quantity of H_2 , continues to be desorbed until 175°C (Fig. 5d), at which point *in situ* XRD indicates that the phase change from LT- NH_4Cl to HT- NH_4Cl occurs with subsequent decomposition between ~ 180 and 210°C (Figs. 5a and S7[†]). An endothermic peak is also observed in this regime, with a peak heat flow at 190°C . The decomposition of LiNH_2 appears to be present until $\sim 280^\circ\text{C}$ as observed in the *in situ* SR-XRD experiment, even after the decomposition of NH_4Cl at $\sim 220^\circ\text{C}$. In addition, three Bragg peaks of a minor unknown phase are observed at 14.6 , 19.5 , 20.8 , 22.7 and $29.5^\circ 2\theta$. This phase increases in crystallinity from $\sim 60^\circ\text{C}$ until disappearing at $\sim 280^\circ\text{C}$. The decomposition of NH_4Cl , LiNH_2 and the unknown phase explain the broad endothermic peak in the DSC data between 200 and 280°C along with a concomitant slow release of NH_3 . The decomposition temperature of lithium amide is therefore greatly reduced compared to that of the pure material, an effect that was also noted when exploring the effect of Cl^- on LiNH_2 with the addition of LiCl .⁴⁵

Thermal decomposition of $2\text{NH}_4\text{Cl} + \text{MgH}_2$

The initial composition of the BM material measured by SR-XRD indicates that NH_4Cl , MgH_2 and Mg are present in the powder (Figs. 6a and S8[†]). *In situ* SR-XRD of the powder shows that the phase transition onset of LT- NH_4Cl to HT- NH_4Cl begins at $\sim 176^\circ\text{C}$ with no more LT- NH_4Cl being observed at 197°C . Any remnants of HT- NH_4Cl disappears at 248°C . In addition to the NH_4Cl phase change and decomposition, a new phase emerges at 170°C , which has a maximum intensity at $\sim 242^\circ\text{C}$ and a decomposition temperature of 258°C . This phase can be indexed to a tetragonal phase with lattice parameters of $5.01746(2)$, $5.01746(2)$, $16.2398(1)$ Å at $\sim 240^\circ\text{C}$ corresponding to a possible space group of $I4/mmm$. A possible structure is $(\text{NH}_4)_2\text{MgCl}_4$ which is isomorphous with K_2MgCl_4 .⁴⁶ MgH_2 appears to start decomposing at 190°C and is last observed at 294°C . During the decomposition regime of MgH_2 and the $(\text{NH}_4)_2\text{MgCl}_4$ phase, two unknown phases begins to appear at $\sim 248^\circ\text{C}$ and disappear by 311 and 330°C . Due to the analogous nature of $(\text{NH}_4)_2\text{MgCl}_4$ to the K_2MgCl_4 system, the unit cells for $\text{K}_3\text{Mg}_2\text{Cl}_7$ and KMgCl_4 were evaluated but not match either of the unknown phases.⁴⁷ In addition, $\text{Mg}(\text{NH}_3)_x\text{Cl}_2$ ($x = 1, 2, 4, 6$) were considered as potential side products in the reaction. Within this temperature range $\text{Mg}(\text{NH}_3)_2\text{Cl}_2$ is the only likely

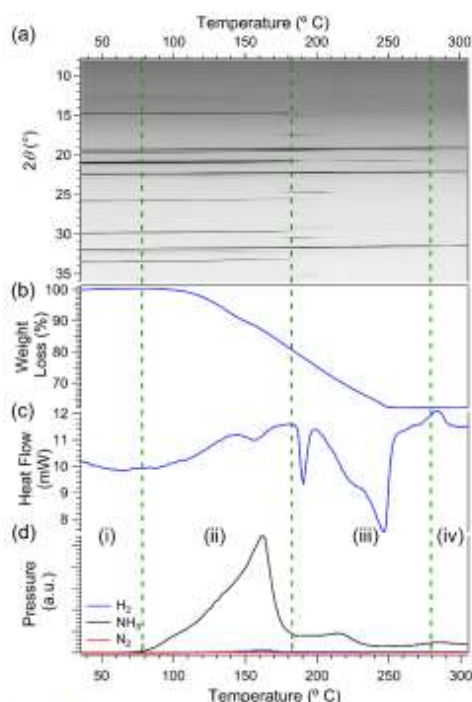


Fig. 5. (a) *In situ* SR-XRD data, (b) TGA, (c) DSC and (d) RGA data for $\text{NH}_4\text{Cl} + \text{LiNH}_2$. Region (i) and (ii) contains LiNH_2 , LT- NH_4Cl , Li_2O , unknown and LiCl phases. Region (iii) contains LiNH_2 , LiCl , Li_2O , unknown and HT- NH_4Cl phases. Region (iv) contains LiCl . For complete phase identification of XRD data see Fig. S7[†]. $\Delta T/t = 5^\circ\text{C}/\text{min}$. $\lambda = 1.0003896(1)$ Å. Endothermic heat flow in the down direction for DSC data.

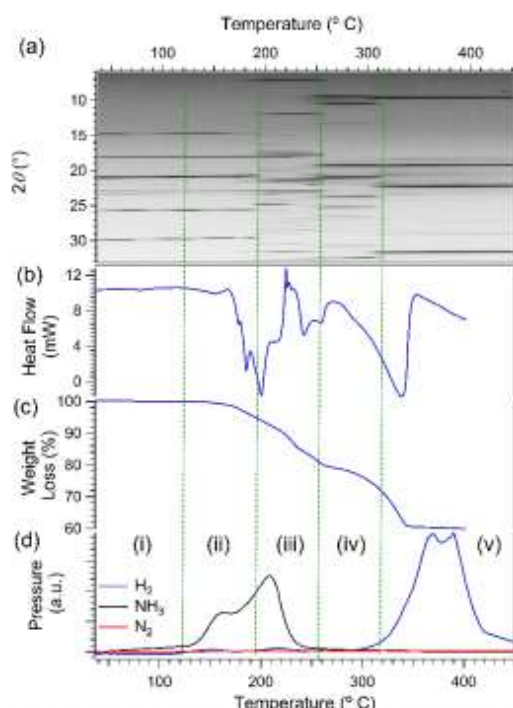


Fig. 6. (a) *in situ* SR-XRD data, (b) DSC, (c) TGA and (d) RGA data for $2\text{NH}_4\text{Cl} + \text{MgH}_2$. Region (i): contains MgH_2 , Mg and LT- NH_4Cl phases. Region (ii): contains MgH_2 , Mg, $(\text{NH}_4)_2\text{MgCl}_4$ and LT- NH_4Cl phases. Region (iii) contains MgH_2 , $(\text{NH}_4)_2\text{MgCl}_4$, Mg and HT- NH_4Cl phases. Region (iv) contains MgH_2 , Mg and two unknown phases. Region (v) contains MgCl_2 , an unknown and Mg. For complete phase identification of XRD data see Fig. S8†. $\Delta T/t = 5^\circ\text{C}/\text{min}$. $\lambda = 1.0003896(1) \text{ \AA}$. Endothermic heat flow in the down direction for DSC data.

compound to exist⁴⁸ and unfortunately none of the unknown phases match the measured lattice parameters or unit cell.⁴⁹ MgCl_2 is not observed until $\sim 300^\circ\text{C}$ and is the major crystalline phase after 330°C , along with another unknown phase. The thermal analysis data correlates extremely well with the crystallographic data, which shows that there are three distinct decomposition events, each containing multiple components (Fig. 6(b-d)). The first event releases NH_3 and H_2 between ~ 125 to $\sim 250^\circ\text{C}$, as determined by RGA. DSC analysis identifies four endothermic maxima (177, 185, 200 and 215°C), while TGA indicates a corresponding mass loss of 10.5 wt%. Between 225 and 238°C , a mass loss of 4.5 wt% is observed, along with a triplet of exothermic peaks at 225, 228 and 232°C . Between 238 and 264°C a doublet of endothermic events 243 and 259°C and an associated mass loss of 5.2 wt% is observed. After 264°C a large exothermic peak is determined with a maximum heat flow at 334°C . The event continues until 355°C where 10.8 wt% of NH_3 and H_2 is released. Overall, 40.4 wt% loss is detected by TGA despite a theoretical loss of 28.6 wt%. This would indicate a loss of a quarter of the Cl content, although analysis of the RGA for HCl and N_2 indicated no loss of gaseous Cl containing products. As construed in the reaction between $\text{NH}_4\text{Cl} + \text{LiH}$, it is possible that HCl may be produced during the decomposition

of NH_4Cl causing a continued detection of H_2 throughout the remaining experiment.

Thermal decomposition of $2\text{NH}_4\text{Cl} + \text{CaH}_2$

Compared to the $2\text{NH}_4\text{Cl} + \text{MgH}_2$ mixture, the decomposition of $2\text{NH}_4\text{Cl} + \text{CaH}_2$ is relatively simple. The initial mixture was determined to contain only NH_4Cl (71.8(1) wt%) and CaH_2 (28.2(1) wt%), as expected, by SR-XRD (Figs. 7a and S9†). NH_3 and H_2 are observed by RGA starting at $\sim 120^\circ\text{C}$ and both having maxima at 230°C (Fig. 7b). A second NH_3 peak is observed at 273°C and is no longer detected after 365°C . H_2 meanwhile, is continuously evolved throughout experiment. The first indication of decomposition by TGA occurs at 152°C , in which a mass loss of 30.1 wt% is achieved before 284°C (Fig. 7b). The second mass loss step releases 8.6 wt% before 335°C giving a total of 38.7 wt% mass loss. As observed with $2\text{NH}_4\text{Cl} + \text{MgH}_2$, the measured mass loss is greater than the theoretical value of 25.5 wt% and may be attributed to the loss of a quarter of the Cl content. Again, the RGA data indicated no evolution of HCl or N_2 although H_2 is observed throughout the experiment even after mass loss from the sample is complete.

During the DSC measurement, three endothermic events are observed with peak heat flows at 195, 280 and 329°C (Fig. 7b). The peak at 195°C corresponds to the decomposition of LT-

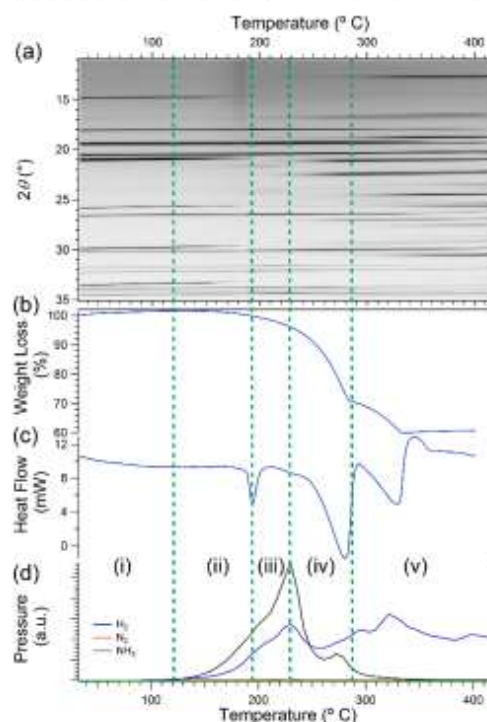


Fig. 7. (a) *in situ* SR-XRD data and (b) DSC-TGA-RGA data for $2\text{NH}_4\text{Cl} + \text{CaH}_2$. Region (i) and (ii): contains CaH_2 and LT- NH_4Cl phases. Region (ii): contains CaH_2 , LT- NH_4Cl and NH_4CaCl_2 phases. Region (iii) contains CaH_2 , HT- NH_4Cl and NH_4CaCl_2 phases. Region (iv) contains CaH_2 , and two unknown phases. Region (v) contains CaH_2 , CaHCl and CaCl_2 . For complete phase identification of XRD data see Fig. S9†. $\Delta T/t = 5^\circ\text{C}/\text{min}$. $\lambda = 1.0003896(1) \text{ \AA}$.

NH_4Cl , which is no longer observable by XRD after 203 °C. On this occasion, no phase change is observed from LT- NH_4Cl to HT- NH_4Cl by *in situ* SR-XRD. NH_4CaCl_3 (space group $Pm\bar{3}m$, isomorphous to KCaCl_3)³⁰ is observed from ~170 °C. This phase has a maximum intensity at ~207 °C and disappears by 227 °C. CaH_2 is observed from RT to 400 °C although the corresponding Bragg peaks begin to diminish at ~239 °C. CaH_2 is most likely to be the largest contribution to the second endotherm at 280 °C (see Fig. 7b). This temperature is considerably lower than that observed for pure CaH_2 ,³¹ likely caused by the destabilising effect of the added NH_4Cl . The onset of decomposition for CaH_2 coincides with the onset of formation of CaHCl (space group $P4/nmm$)³² and an unknown phase which are thermally stable up to at least 500 °C. CaCl_2 is observed to commence formation at 286 °C along with another unknown phase. One exothermic event is observed at 345 °C although the cause is unclear, it is most likely attributed to a phase change. The identity of the unknown phases were considered and attempts to index the peaks were made. Materials that were considered also include $\text{CaCl}_2(\text{NH}_3)_x$ ($x = 2, 8$).

Addition of Pd catalyst to NH_4Cl + NaH

In attempt to alter the reaction kinetics between the NH_4Cl and NaH and to cause preferential formation of H_2 and N_2 over NH_3 ,

palladium (II) chloride was added (1 mol% and 10 mol%) as a potential catalyst to the NH_4Cl + NaH powder (Figs. 8, S10 and S11†). From *in situ* SR-XRD data, the NH_4Cl , NaH and 1 mol% PdCl_2 material does not show any observable Bragg peaks for PdCl_2 as it is below the limit of detection (Figs. 8a and S10†). LT- NH_4Cl phase transitions to the HT phase at ~176 °C, which also decomposes before ~206 °C. NaH is no longer visible in the XRD pattern by 214 °C. On the contrary, analysis of the BM mixture of NH_4Cl , NaH and 10 mol% PdCl_2 shows that minimal reaction has occurred between the starting reagents and only 3 wt% NaCl is present. As the sample is heated *in situ*, the intensity of PdCl_2 starts to decrease at ~130 °C and has disappeared by 155 °C (Figs. 8e and S11†). At the same time, Pd metal is observed and increases in intensity. The observed intensity of NaH begins to decrease from ~95 °C while it is no longer detected at the temperature of the LT- NH_4Cl to HT phase change at 176 °C. Once the HT- NH_4Cl has decomposed, ~227 °C, no further reaction occurs. Overall, the increment of 1 mol% PdCl_2 to 10 mol% does not alter the reaction pathway, but the temperatures at which reactions occur.

A comparison of the thermal analysis data (DSC-TGA and RGA) shows a stark contrast between the catalysed and uncatalysed NH_4Cl + NaH samples. The pure sample shows a peak gas desorption at ~170 °C while 1 mol% and 10 mol% have a

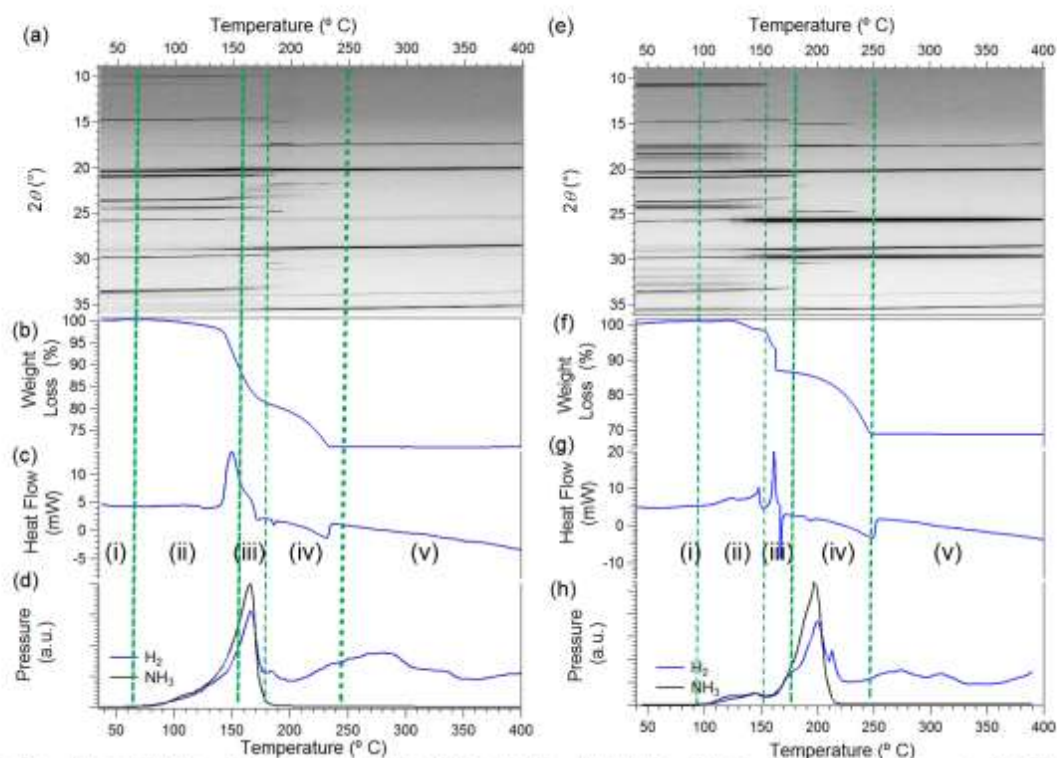


Fig. 8. (a – d) *In situ* SR-XRD data and DSC-TGA-RGA data for NH_4Cl + NaH + 1 mol% PdCl_2 , and (e – h) NH_4Cl + NaH + 10 mol% PdCl_2 . Region (i) and (ii): contains NaH, LT- NH_4Cl , PdCl_2 and NaCl phases. Region (iii) contains NaH, LT- NH_4Cl , Pd and NaCl phases. Region (iv) contains HT- NH_4Cl , Pd and NaCl phases (also NaH for 1 mol% PdCl_2 containing material). Region (v) contains NaCl. For complete phase identification of XRD data see Figs. S10 and S11†. $\Delta T/t = 5$ °C/min for SR-XRD. $\lambda = 1.0003896(1)$ Å. Endothermic heat flow in the down direction for DSC data



maximum H₂ release at 166 and 198 °C, respectively. In addition, for the catalysed samples, H₂ continues to be detected until the end of the experiment. This is surprising as no crystallographic events at these temperatures during *in situ* SR-XRD. In addition, the measured mass loss for the 1 mol % and 10 mol % catalysed systems is much greater than the theoretical mass loss. The 1 mol % PdCl₂ system loses 28.8 wt% while the theoretical mass loss is 24.3, whereas 31.2 wt% is measured compared to a theoretical quantity of 20.0 wt% for the 10 mol% system. As mentioned previously for the NH₄Cl mixed with MgH₂ or CaH₂, the elevated practical mass loss may be attributed to HCl loss. This gaseous acid reacts with the stainless-steel tubing producing hydrogen. It is noted that elevated mass loss occurs with increased addition of PdCl₂, with no difference in mass loss being observed when catalyst is not added to NH₄Cl + NaH. This is attributed to the NaH reacting with PdCl₂ rather than the intended NH₄Cl. The remaining NH₄Cl then decomposes as observed for the pure material (Fig. 1) producing HCl, although NH₃ is not observed during this process. Overall, this suggests that the addition of PdCl₂ does not incur splitting of NH₃ during desorption as discussed previously in the literature.³⁵

The DSC data exhibits the largest contrast between samples. The pure and 1 mol% samples have a large exothermic peak between ~125 and 175 °C (Figs. 2c and 8c), whereas the 10 mol % sample exhibits two exothermic peaks in the same region with an additional sharp endothermic peak at ~165 °C (Fig. 8g). The mass loss for all three samples is completed between 225 and 250 °C.

Technological feasibility assessment

For energy storage materials to be utilised in technological applications, they must have a high energy density, be inexpensive, and usable within a practical temperature range. The materials employed in this study hold great potential for technological applications as they meet these demands. The US DOE has provided targets that hydrogen storage materials must meet to be used for vehicular applications, one of which is that the gas should be released between 40 and 85 °C.³³ The mixture of NH₄Cl + NaH has a decomposition onset temperature of ~90 °C, although peak gas evolution is not achieved until ~170 °C. Addition of 1 mol% PdCl₂ to NH₄Cl-NaH has a similar, albeit increased, onset decomposition temperature of ~65 °C although this incurs an increase in monetary price. The other MH's and MNH₂'s investigated in this study have increased decomposition onset temperatures, compared to NH₄Cl-NaH, of between 72 and 125 °C, which is potentially useful. 2NH₄Cl + MgH₂ has the highest onset operating temperature of above 125 °C, making it the least likely to find application.

The cost of a fuel is a very important consideration when examining its viability compared to current fuel options. The US DOE has set an energy target cost of US\$10/kWh. The energy target cost of these materials compare favourably to the US DOE target. NH₄Cl-NaH for instance, would cost US\$1.25/kg of raw material.^{36, 34} A 50:50 NH₃:H₂ combustion ratio would produce 14.7 MJ/kg (4.1 kWh/kg) of gas produced giving an overall cost of US\$0.6/kWh (Table 1).³⁸ The cost of the other mixtures would be of similar size although sourcing industrial prices for these materials is troublesome. These prices would diminish further for large scale production of the materials. The 2NH₄Cl-MH₂ (M = Mg, Ca) materials show excellent gravimetric capacity (40.4 and 41.4 wt%, respectively) and practical volumetric gas densities (607 and 657 kg/m³, respectively). The cost of these MH's is also low with 2NH₄Cl-CaH₂ and 2NH₄Cl-MgH₂ costing US\$0.5/kWh and US\$0.3/kWh, respectively. LiH, LiNH₂ and NaNH₂ may have agreeable energy densities and decomposition temperatures but the price of the raw materials excludes them from contention. In addition, the long term utilisation of a lithium based material as a fuel source is not sustainable.³⁵

A weakness of these materials is that they decompose over multiple steps. This may have a detrimental effect on the energy storage capacity because if the fuel is operated at lower temperatures, the onset of decomposition for the next step will not be reached resulting in a major reduction in efficiency.

The decomposition pathway and thermodynamics of these materials have been determined using HSC Chemistry software (Table S1†). Unfortunately, the database for this software did not contain many of the by-products experimentally observed including e.g. the Mg and Ca amides/imides, (NH₄)₂MgCl₄ and NH₄CaCl₃. The thermodynamic properties of many of these compounds are generally unknown and as a result accurate thermodynamic predictions could not be obtained. Theoretically the reactions are all exothermic with NH₄Cl + NaH having the largest predicted reaction enthalpy of -86.1 kJ/mol NH₄Cl. Experimentally many of the systems exhibit endothermic reactions although a precise determination of the thermodynamics could not be achieved due to the multiple steps of reaction and impurities within the samples. Comparing the Ca and Mg systems, it is clear that the experimental pathway is predominantly endothermic rather than exothermic. This is due to the mismatch between the theoretical and experimental reaction pathway.

Since the NH₄Cl-MH and NH₄Cl-MNH₂ materials form NH₃/H₂ gas mixtures during decomposition, the fuel produced could be burnt in an internal combustion engine to avoid poisoning of fuel cell membranes. Generally NH₃ has a narrow flammability limit of 15.5% to 27% volume in air,²⁰ which leads to a low

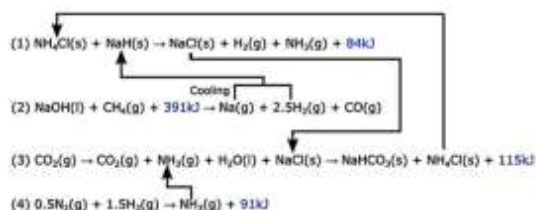


Fig. 9. Proposed reaction cycle for sodium chloride and ammonium chloride starting materials.

combustion rate. However, recent studies have shown that the presence of hydrogen during ammonia combustion can lower combustion temperatures and increase the burning velocity of ammonia flames.⁵⁶ These mixtures are theoretically producing a 50 mol% ratio of H_2 and NH_3 apart from LiNH_2 and NaNH_2 which are producing nearly 100 % NH_3 . Therefore, these mixtures will allow efficient conversion of the gas fuel to energy to propel a vehicle without the formation of large quantities of NO_x or other products usually associated with combustion engines using petrol or diesel.

Upon refuelling the vehicle, the waste product removed would be the solid metal salt, e.g. NaCl , which is non-hazardous. Off-board regeneration of the waste product can also be considered to recycle this material using methods that are already used in large scale commercial processes. An example of a viable fuel cycle utilising commercial processes is exhibited in Fig. 9 with the reactions incorporated into the scheme outlined below. Ideally the hydrogen would be produced using renewable energy sources.

- NH_3 , H_2 and NaCl are produced from the reaction between NH_4Cl and NaH . NH_3 and H_2 are used for on-board fuel applications while NaCl is reprocessed.
- Production of NaH from NaOH and CH_4 using the Power Ball process.⁵⁷ $\text{NaOH}(\text{l})$ is first reacted with $\text{CH}_4(\text{g})$ to form $\text{Na}(\text{g})$, $\text{H}_2(\text{g})$ and $\text{CO}(\text{g})$. The $\text{Na}(\text{g})$ and $\text{H}_2(\text{g})$ are then cooled and combined to form $\text{NaH}(\text{s})$. This method has the potential to reduce production costs compared to synthesis by common electrolysis. The left over $\text{CO}(\text{g})$ and $\text{H}_2(\text{g})$ could then be used to produce $\text{CO}_2(\text{g})$ and more $\text{H}_2(\text{g})$ via the Water Shift reaction.⁵⁸
- Regeneration of NH_4Cl from NaCl via the Solvay process using NH_3 , CO_2 and H_2O .⁵⁹
- NH_3 generated from N_2 and H_2 using the Haber-Bosch process²² or electrochemical synthesis.⁶⁰

Conclusions

This study has explored the reactions of four ammonium chloride – metal hydride ($\text{NH}_4\text{Cl-MH}$) and two ammonium chloride – metal amide ($\text{NH}_4\text{Cl-MNH}_2$) powders for potential use as solid-state ammonia and hydrogen fuel sources for vehicular applications. Comparison of the results to US DOE guidelines for vehicles running on gas reveals that these materials exceed targets with respect to cost of materials, fuel capacity and operating temperature. DSC-TGA and RGA analysis indicates

that the onset of H_2 and/or NH_3 release occurs at $\sim 90^\circ\text{C}$ for $\text{NH}_4\text{Cl-NaH}$ with an average of 97°C for all materials in the study. TGA analysis revealed a high gravimetric gas evolution ranging between 24.8 wt% for $\text{NH}_4\text{Cl-NaH}$ and 41.4 wt% for $2\text{NH}_4\text{Cl-CaH}_2$ providing exceptional volumetric gas densities of 363 and 657 kg/m^3 , respectively. This far exceeds densities of pure NH_3 , H_2 or metal hydride materials such as Mg_2FeH_6 .

In situ synchrotron powder X-ray diffraction of each of the materials shows that the metal hydrides decompose at significantly lower temperatures compared to their pure counterparts with the reaction with NH_4Cl enhancing the decomposition process. The final products after a full reaction are the metal hydride salts with no other by-products. This will allow for the products to be recycled in an off-board process.

Each of the $\text{NH}_4\text{Cl-MH}$ or $\text{NH}_4\text{Cl-MNH}_2$ materials released NH_3 and H_2 upon reaction apart from NaNH_2 and LiNH_2 . To determine if the $\text{NH}_4\text{Cl-NaH}$ mixture could be catalytically prevented from forming NH_3 , PdCl_2 was added. Unfortunately, this resulted in a slight increase in the onset temperature of desorption with NH_3 still being released. Further investigation into alternative catalysts such as Ru based compounds may alter the decomposition pathway. NH_4Cl alone could not be used in a system as the decomposition process involves the formation of HCl . No acid was identified in the decomposition process of the $\text{NH}_4\text{Cl-MH}$ or $\text{NH}_4\text{Cl-MNH}_2$ systems.

The high gravimetric capacity of the materials along with the low cost of NH_4Cl allows for the overall cost to meet US DOE targets of US\$10/kWh. $\text{NH}_4\text{Cl-NaH}$ has a material cost of US\$0.6/kWh while $2\text{NH}_4\text{Cl-CaH}_2$ and $2\text{NH}_4\text{Cl-MgH}_2$ cost US\$0.5/kWh and US\$0.3/kWh, respectively. A recycling process has been identified for the $\text{NH}_4\text{Cl-NaH}$ material using industrial processes already developed. This will decrease the overall cost of the system, which is already estimated to meet targets set by the US DOE. If the industrial process is to be scaled up further, the cost of these metal hydrides should decrease causing this fuel to be even more competitive in the future. Overall, the reaction cycle potentially allows carbon-neutral regeneration of the starting materials, making it a sustainable energy option.

Conflicts of interest

There are no conflicts to declare.

Acknowledgements

CEB, TDH, DAS and VS acknowledge the financial support of the Australian Research Council (ARC) for ARC Linkage grant LP120101848, LP150100730 and ARC LIEF grant LE0989180. HS acknowledges the Department of Physics and Astronomy at Curtin University for providing support through the Summer Physics and Astronomy Scholarship. DAS acknowledges the financial support of a Curtin University Postdoctoral Research Fellowship. The authors also acknowledge funding from the Australian Synchrotron (ANSTO), which enabled the research at the powder diffraction beamline to be undertaken.

Notes and references

- H. Khatib, *Energy policy*, 2012, **48**, 737-743.
- L. Schlapbach and A. Züttel, *Nature*, 2001, **414**, 353-358.
- D. A. Sheppard, M. Paskevicius, T. D. Humphries, M. Felderhoff, G. Capurso, J. Bellosta von Colbe, M. Dornheim, T. Klassen, P. A. Ward, J. A. Teprovich, C. Corgnale, R. Zidan, D. M. Grant and C. E. Buckley, *Appl. Phys. A*, 2016, **122**, 395.
- K. T. Møller, T. R. Jensen, E. Akiba and H.-w. Li, *Prog. Nat. Sci.*, 2017, **27**, 34-40.
- A. Züttel, A. Remhof, A. Borgschulte and O. Friedrichs, *Phil. Trans. R. Soc. A*, 2010, **368**, 3329-3342.
- G. W. Crabtree, M. S. Dresselhaus and M. V. Buchanan, *Physics Today*, 2004, **57**, 39-44.
- B. R. S. Hansen, M. Paskevicius, H.-W. Li, E. Akiba and T. R. Jensen, *Coord. Chem. Rev.*, 2016, **323**, 60-70.
- T. D. Humphries, D. A. Sheppard and C. E. Buckley, *Coord. Chem. Rev.*, 2017, **342**, 19-33.
- S. Orimo, Y. Nakamori, J. R. Eliseo, A. Züttel and C. M. Jensen, *Chem. Rev.*, 2007, **107**, 4111-4132.
- C. Frommen, M. H. Sørby, M. Heere, T. D. Humphries, J. E. Olsen and B. C. Hauback, *Energies*, 2017, **10**, 2115.
- T. D. Humphries, D. A. Sheppard, G. Li, M. R. Rowles, M. Paskevicius, M. Matsuo, K.-F. Aguey-Zinsou, M.-V. Sofianos, S.-I. Orimo and C. E. Buckley, *J. Mater. Chem. A*, 2018, **6**, 9099-9108.
- M. Fellet, C. E. Buckley, M. Paskevicius and D. A. Sheppard, *MRS Bulletin*, 2013, **38**, 1012-1013.
- D. A. Sheppard, T. D. Humphries and C. E. Buckley, *Appl. Phys. A*, 2016, **122**, 406.
- W. I. F. David, J. W. Makepeace, S. K. Callear, H. M. A. Hunter, J. D. Taylor, T. J. Wood and M. O. Jones, *J. Am. Chem. Soc.*, 2014, **136**, 13082-13085.
- A. Klerke, C. H. Christensen, J. K. Norskov and T. Vegge, *J. Mater. Chem.*, 2008, **18**, 2304-2310.
- Z. Zhang, H. Miyaoka, H. Miyaoka, T. Ichikawa and Y. Kojima, *ACS Applied Energy Materials*, 2018, **1**, 232-242.
- Outokumpu, HSC Chemistry, 6.1, 2006.
- L. Green, *Int. J. Hydrogen Energy*, 1982, **7**, 355-359.
- J. Lee, S. Lee and O. Kwon, *Int. J. Hydrogen Energy*, 2010, **35**, 11332-11341.
- J. Li, H. Huang, N. Kobayashi, Z. He, Y. Osaka and T. Zeng, *Energy*, 2015, **93**, 2053-2068.
- A. Afif, N. Radenahmad, Q. Cheok, S. Shams, J. H. Kim and A. K. Azad, *Renew. Sustainable Energy Rev.*, 2016, **60**, 822-835.
- J. M. Modak, *Resonance*, 2002, **7**, 69-77.
- Indicative Chemical Prices A-Z, <http://www.icis.com/chemicals/channel-info-chemicals-a-z/>, (accessed 12/02/2018).
- E. Matthews, *Global Biogeochem. Cycles*, 1994, **8**, 411-439.
- P. J. Feibelman, *Physics Today*, 2005, **58**, 13-14.
- Praxair, Ammonia, anhydrous. Safety Data Sheet P- 4562, <http://www.praxair.com/-/media/documents/sds/ammonia-nh3-safety-data-sheet-sds-p4562.pdf>, (accessed 12/02/2018).
- R. Lan, J. T. Irvine and S. Tao, *Int. J. Hydrogen Energy*, 2012, **37**, 1482-1494.
- J. Yang, P. R. Beaumont, T. D. Humphries, C. M. Jensen and X. Li, *Energies*, 2015, **8**, 9107.
- L. H. Jepsen, M. B. Ley, Y.-S. Lee, Y. W. Cho, M. Dornheim, J. O. Jensen, Y. Filinchuk, J. E. Jørgensen, F. Besenbacher and T. R. Jensen, *Mater. Today*, 2014, **17**, 129-135.
- L. H. Jepsen, M. B. Ley, Y. Filinchuk, F. Besenbacher and T. R. Jensen, *ChemSusChem*, 2015, **8**, 1452-1463.
- J. W. Makepeace, T. J. Wood, H. M. Hunter, M. O. Jones and W. I. David, *Chemical Science*, 2015, **6**, 3805-3815.
- US Pat., US7157166B2, 2007.
- K. E. Lamb, D. M. Viano, M. J. Langley, S. S. Hla and M. D. Dolan, *Ind. Eng. Chem. Res.*, 2018, **57**, 7811-7816.
- H. Miyaoka, H. Miyaoka, T. Ichikawa, T. Ichikawa and Y. Kojima, *Int. J. Hydrogen Energy*, 2018, **43**, 14486-14492.
- L. Li and J. A. Hurley, *Int. J. Hydrogen Energy*, 2007, **32**, 6-10.
- Z. Xueping, M. Qijuhua, F. Zhen, M. Feng, L. Shenglin, F. Xin, X. Guo and Z. Jiaojiao, *Rare Metal Materials and Engineering*, 2014, **43**, 2075-2078.
- S. Mukherjee, S. V. Devaguptapu, A. Sviripa, C. R. F. Lund and G. Wu, *Applied Catalysis B: Environmental*, 2018, **226**, 162-181.
- Price of chemicals, <https://www.alibaba.com>, (accessed 19/08/2018).
- K. S. Wallwork, B. J. Kennedy and D. Wang, *Synchrotron Radiation Instrumentation: Ninth International Conference on Synchrotron Radiation Instrumentation*, 2007, **879**, 879-882.
- P. D. Pathak and N. G. Vasavada, *Acta Crystallogr A*, 1970, **26**, 655-658.
- I.-K. Suh, H. Ohta and Y. Waseda, *J. Mater. Sci.*, 1988, **23**, 757-760.
- R. Farasat, B. Yancey and S. Vyazovkin, *J. Phys. Chem. C*, 2013, **117**, 13713-13721.
- N. W. Luft, *Industrial Chemistry*, 1955, **31**, 502.
- L. H. Jepsen, P. Wang, G. Wu, Z. Xiong, F. Besenbacher, P. Chen and T. R. Jensen, *Phys. Chem. Chem. Phys.*, 2016, **18**, 25257-25264.
- J. Zhang and Y. H. Hu, *Ind. Eng. Chem. Res.*, 2011, **50**, 8058-8064.
- C. S. Gibbons, V. C. Reinsborough and W. A. Whitla, *Can. J. Chem.*, 1975, **53**, 114-118.
- G. S. Perry and H. Fletcher, *J. Phase Equilib.*, 1993, **14**, 172-178.
- H. Zhu, X. Gu, K. Yao, L. Gao and J. Chen, *Ind. Eng. Chem. Res.*, 2009, **48**, 5317-5320.
- A. Leineweber, M. W. Friedriszik and H. Jacobs, *J. Solid State Chem.*, 1999, **147**, 229-234.
- H. J. Seifert, H. Fink, G. Thiel and J. Uebach, *Z. Anorg. Allg. Chem.*, 1985, **520**, 151-159.
- R. W. Curtis and P. Chiotti, *J. Phys. Chem.*, 1963, **67**, 1061-1065.
- P. Ehrlich, B. Alt and L. Gentsch, *Z. Anorg. Allg. Chem.*, 1956, **283**, 58-73.
- DOE Technical Targets for Onboard Hydrogen Storage for Light-Duty Vehicles, <https://www.energy.gov/eere/fuelcells/doe-technical-targets-onboard-hydrogen-storage-light-duty-vehicles>, (accessed 12/03/2018).
- J. P. DiPietro and E. G. Skolnik, 2000.
- D. Abbott, *Proc. IEEE*, 2010, **98**, 42-66.
- J. Li, H. Huang, N. Kobayashi, Z. He and Y. Nagai, *International Journal of Energy Research*, 2014, **38**, 1214-1223.
- E. Skolnik, *Proceedings of the DOE*, 2000.
- J. Xu and G. F. Froment, *AIChE J.*, 1989, **35**, 88-96.
- G. Steinhäuser, *Journal of Cleaner Production*, 2008, **16**, 833-841.
- S. Giddey, S. P. S. Badwal, C. Munnings and M. Dolan, *ACS Sustainable Chemistry & Engineering*, 2017, **5**, 10231-10239.

Electronic Supplemental Information for:

Ammonium chloride-metal hydride based reaction cycle for vehicular applications

Helen G. Stewart,^a Terry D. Humphries,^a Drew A. Sheppard,^a Mariana S. Tortoza,^a M. Veronica Sofianos,^a Shaomin Liu,^a and Craig E. Buckley^a

- Department of Physics and Astronomy, Fuels and Energy Technology Institute, Curtin University, GPO Box U1987, Perth, WA 6845, Australia
- Department of Chemical Engineering, Curtin University, GPO Box U1987, Perth, WA, 6845, Australia.

Table S1. Predicted reaction pathways and calculated standard enthalpy of reaction for each of the systems studied.

Sample Reaction Path	Calculated ΔH° at 25°C/mol NH_4Cl of reaction (kJ/mol)	Theoretical reaction weight loss (%)		
		H_2	NH_3	Total
$\text{NH}_4\text{Cl}_{(s)} + \text{NaH}_{(s)} \rightarrow \text{NaCl}_{(s)} + \text{H}_{2(g)} + \text{NH}_{3(g)}$	-86.1	2.6	21.9	24.6
$\text{NH}_4\text{Cl}_{(s)} + \text{NaH}_{(s)} + \text{PdCl}_{2(s)} \rightarrow \text{NaCl}_{(s)} + \text{H}_{2(g)} + \text{NH}_{3(g)} + \text{PdCl}_{2(s)}$ (1mol% / 10 mol %)	-86.1	2.6/2.1	21.7/17.9	24.3/20.0
$\text{NH}_4\text{Cl}_{(s)} + \text{NaNH}_{2(s)} \rightarrow \text{NaCl}_{(s)} + 2\text{NH}_{3(g)}$	-64.6	0.0	36.8	36.8
$2\text{NH}_4\text{Cl}_{(s)} + \text{MgH}_{2(s)} \rightarrow \text{MgCl}_{2(s)} + 2\text{H}_{2(g)} + 2\text{NH}_{3(g)}$	-15.7	3.0	25.6	28.6
$\text{NH}_4\text{Cl}_{(s)} + \text{LiH}_{(s)} \rightarrow \text{LiCl}_{(s)} + \text{H}_{2(g)} + \text{NH}_{3(g)}$	-49.1	3.3	27.7	31.0
$\text{NH}_4\text{Cl}_{(s)} + \text{LiNH}_{2(s)} \rightarrow \text{LiCl}_{(s)} + \text{H}_{2(g)} + \text{NH}_{3(g)}$	-6.1	0.0	44.5	44.5
$2\text{NH}_4\text{Cl}_{(s)} + \text{CaH}_{2(s)} \rightarrow \text{CaCl}_{2(s)} + 2\text{H}_{2(g)} + 2\text{NH}_{3(g)}$	-40.6	2.7	22.8	25.5

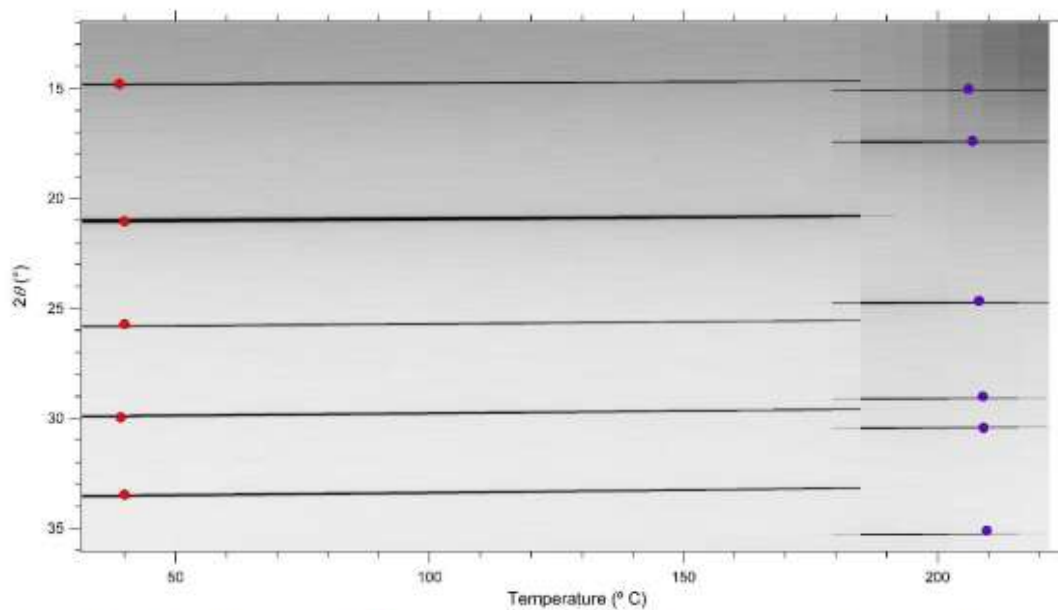


Fig. S1. In situ SR-XRD data for NH_4Cl . ● LT- NH_4Cl and ● HT- NH_4Cl . $\Delta T/t = 5$ °C/min. $\lambda = 1.0003896(1)$ Å.

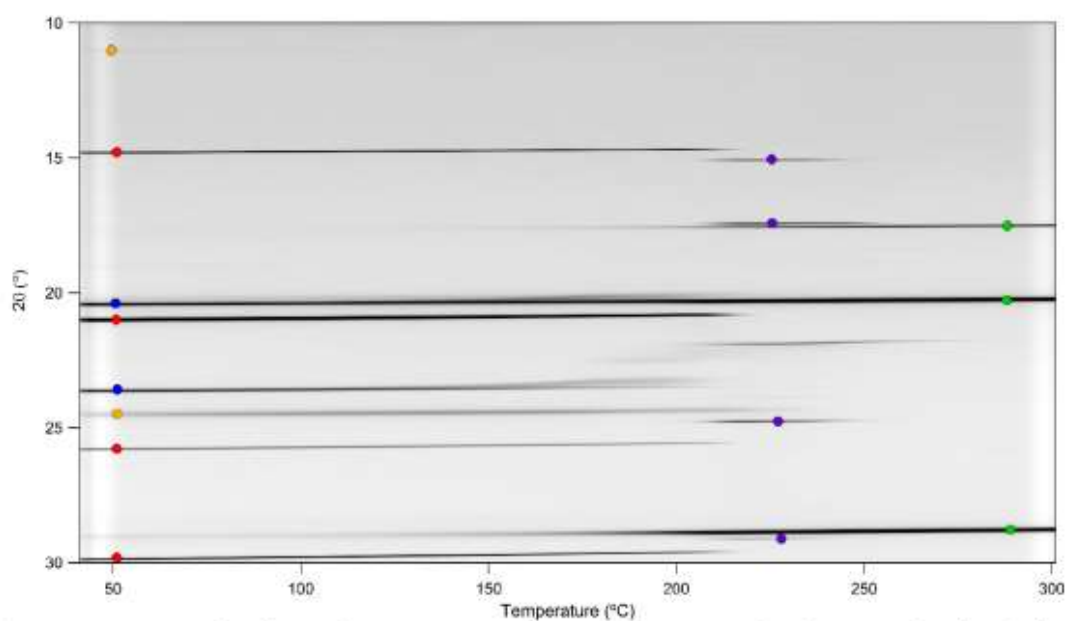


Fig. S2. In situ SR-XRD data for $\text{NH}_4\text{Cl} + \text{NaH}$. ● LT- NH_4Cl , ● NaH, ● NaOH, ● NaCl and ● HT- NH_4Cl . $\Delta T/t = 5$ °C/min. $\lambda = 1.0003896(1)$ Å.

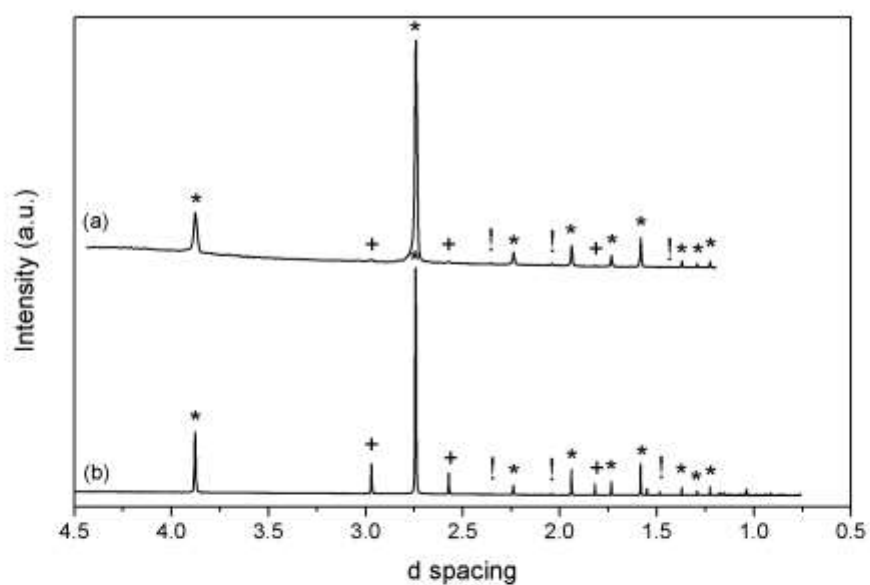


Fig. S3. XRD data for $\text{NH}_4\text{Cl} + \text{LiH}$ collected at room temperature. (a) Data collected directly after ball milling on Bruker AXS D8 Advance Discover XRD System ($\lambda = 1.5406 \text{ \AA}$), (b) data collected 8 months after ball milling using synchrotron radiation ($\lambda = 1.0003896(1) \text{ \AA}$). * = NH_4Cl , ! = LiH , + = LiCl .

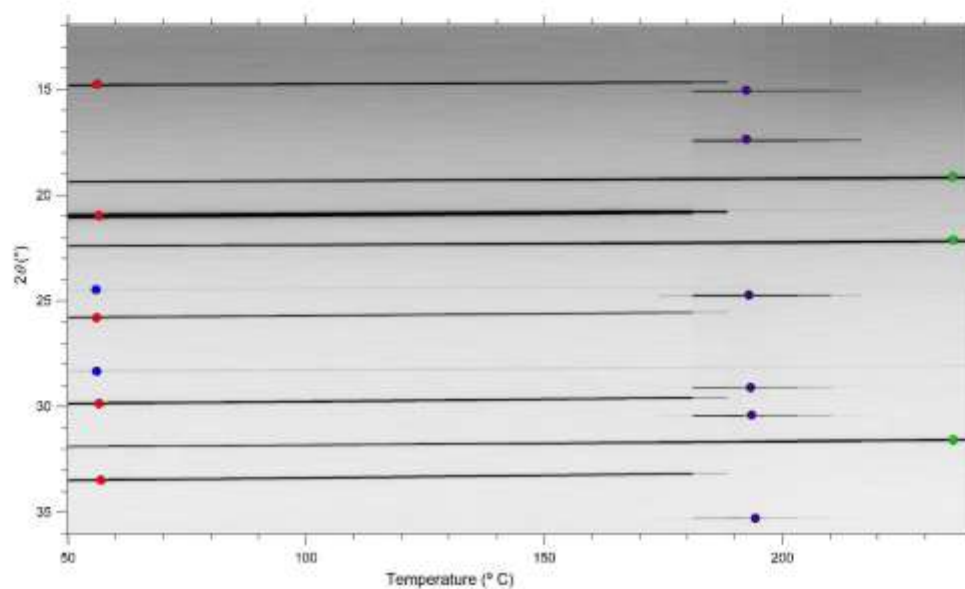


Fig. S4. In situ SR-XRD data for $\text{NH}_4\text{Cl} + \text{LiH}$. • LT- NH_4Cl , • LiH , • LiCl and • HT- NH_4Cl . $\Delta T/t = 5 \text{ }^\circ\text{C}/\text{min}$. $\lambda = 1.0003896(1) \text{ \AA}$.

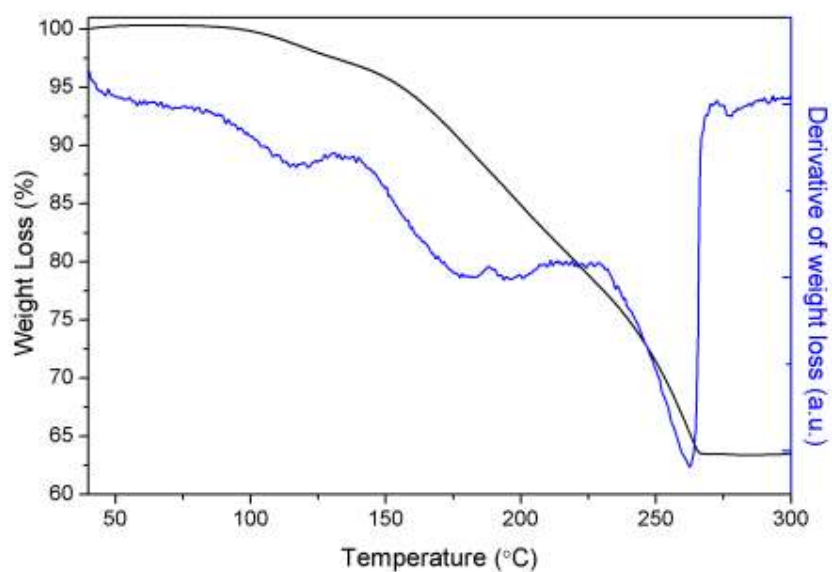


Fig. S5. TGA and first derivative of the TGA data for $\text{NH}_4\text{Cl} + \text{LiH}$. $\Delta T/t = 5 \text{ }^\circ\text{C}/\text{min}$.

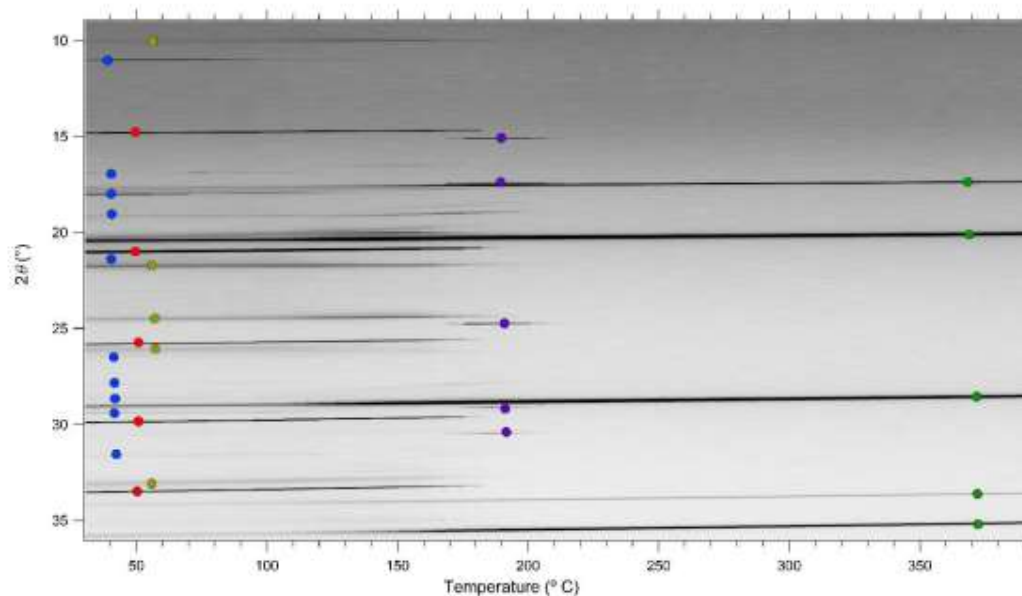


Fig. S6. In situ SR-XRD data for $\text{NH}_4\text{Cl} + \text{NaNH}_2$. ● $\text{LT-NH}_4\text{Cl}$, ● NaNH_2 , ● NaCl , ● NaOH , and ● $\text{HT-NH}_4\text{Cl}$. $\Delta T/t = 5 \text{ }^\circ\text{C}/\text{min}$. $\lambda = 1.0003896(1) \text{ \AA}$.

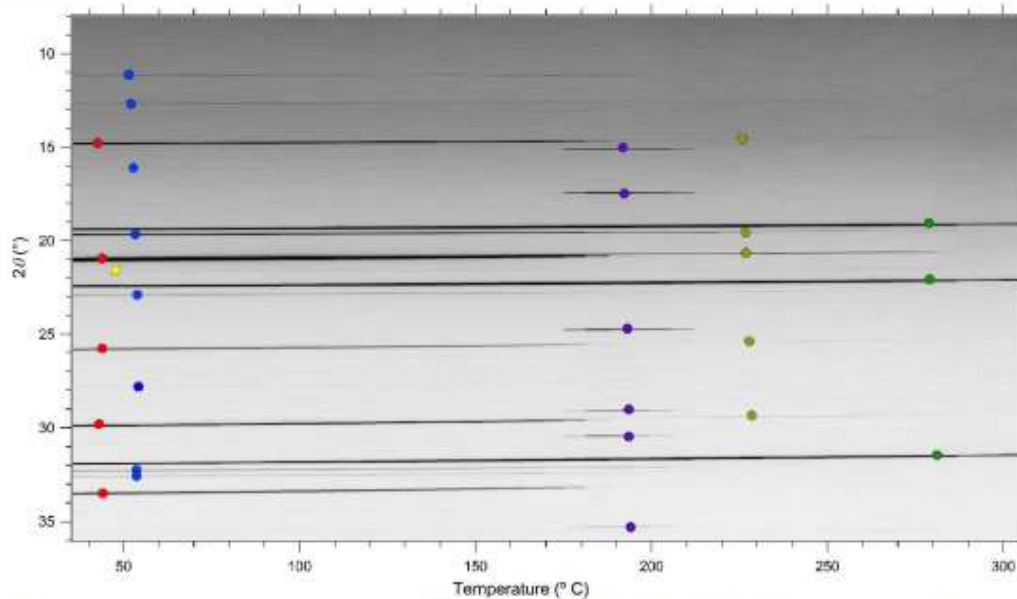


Fig. S7. In situ SR-XRD data for $\text{NH}_4\text{Cl} + \text{LiNH}_2$. ● LT- NH_4Cl , ● LiNH_2 , ● Li_2O , ● LiCl , ● HT- NH_4Cl and ● unknown. $\Delta T/t = 5^\circ\text{C}/\text{min}$. $\lambda = 1.0003896(1) \text{ \AA}$.

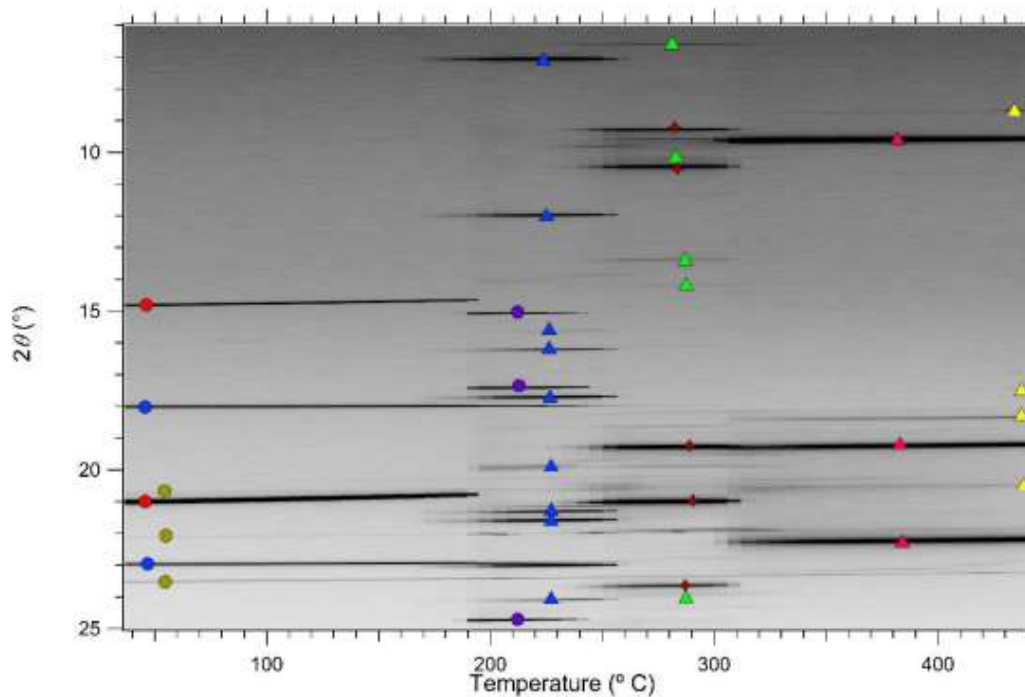


Fig. S8. In situ SR-XRD data for $\text{NH}_4\text{Cl} + \text{MgH}_2$. ● LT- NH_4Cl , ● MgH_2 , ● Mg , ▲ $(\text{NH}_4)_2\text{MgCl}_4$, ● HT- NH_4Cl , ▲ unknown, ▲ unknown, ▲ unknown and ▲ MgCl_2 . $\Delta T/t = 5^\circ\text{C}/\text{min}$. $\lambda = 1.0003896(1) \text{ \AA}$.

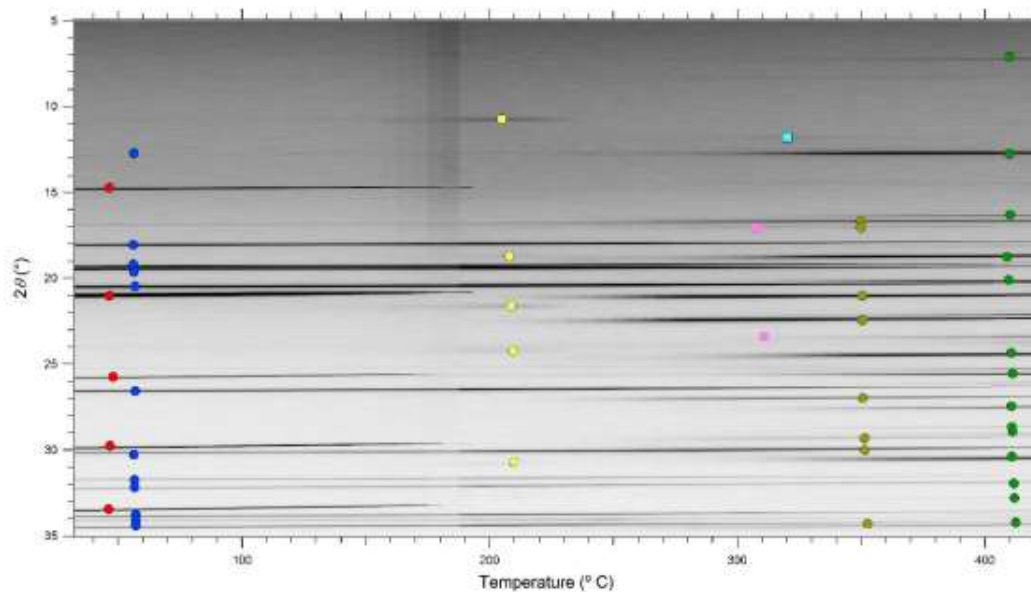


Fig. S9. In situ SR-XRD data for $\text{NH}_4\text{Cl} + \text{CaH}_2$. ● LT- NH_4Cl , ● CaH_2 , ▲ NH_4CaCl_3 , ■ unknown, ■ unknown, ● CaHCl and ● CaCl_2 . $\Delta T/t = 5^\circ\text{C}/\text{min}$. $\lambda = 1.0003896(1) \text{ \AA}$.

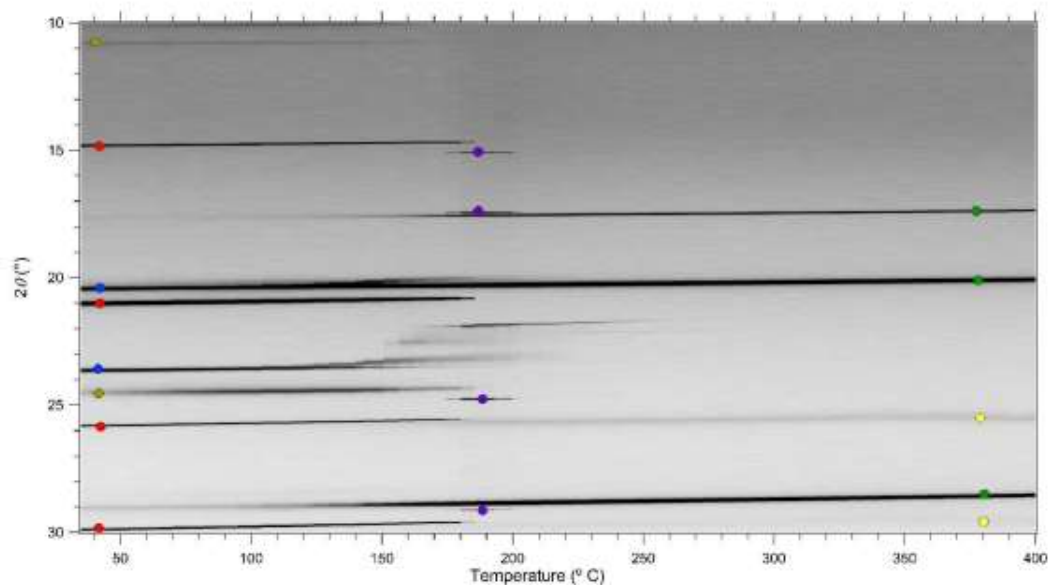


Fig. S10. In situ SR-XRD data for $\text{NH}_4\text{Cl} + \text{NaH} + \text{PdCl}_2$ (1 mol%). ● LT- NH_4Cl , ● NaH , ● NaOH , ● NaCl , ● Pd and ● HT- NH_4Cl . $\Delta T/t = 5^\circ\text{C}/\text{min}$. $\lambda = 1.0003896(1) \text{ \AA}$.

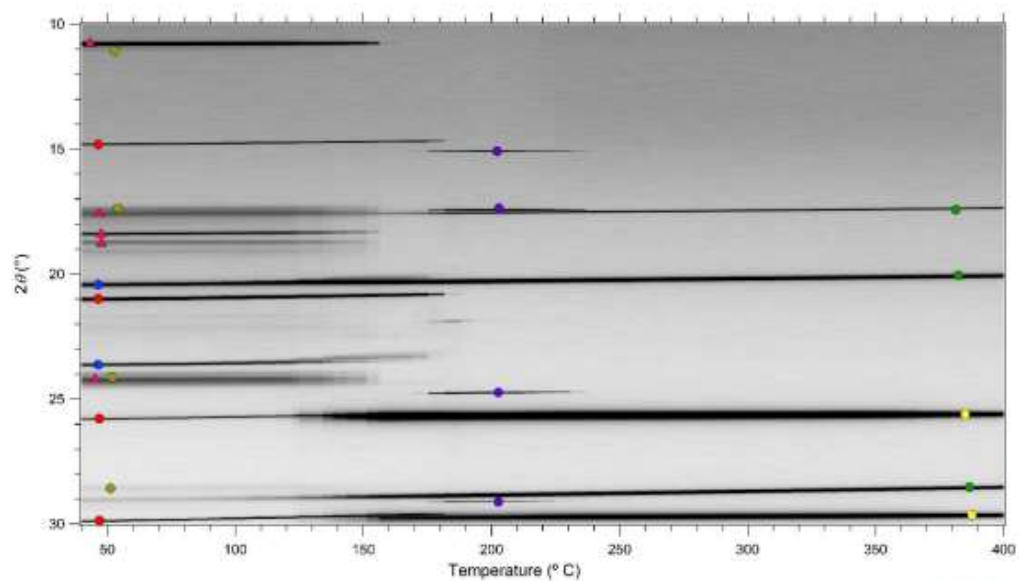
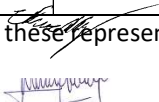













Fig. S11. In situ SR-XRD data for $\text{NH}_4\text{Cl} + \text{NaH} + \text{PdCl}_2$ (10 mol%). ● LT- NH_4Cl , ● NaH, ● NaOH, ● NaCl, ▲ PdCl₂, ● Pd and ● HT- NH_4Cl . $\Delta T/t = 5$ °C/min. $\lambda = 1.0003896(1)$ Å.

Appendix IV. Statement of contributions

Chapter 3: Tortoza Mariana S, Humphries Terry D, Sheppard Drew A, Paskevicius Mark, Rowles Matthew R, Sofianos M Veronica, Aguey-Zinsou Kondo-Francois and Buckley Craig E, Thermodynamics and performance of the Mg–H–F system for thermochemical energy storage applications, Physical Chemistry Chemical Physics, 2018. DOI: 10.1039/c7cp07433f

	Conception & design	Experiments conduction & data acquisition	Data processing & analysis	Interpretation & discussion	Manuscript writing, revision
Mariana Tortoza	x	x	x	x	x
I acknowledge these represent my contribution to the above research output Signature: 					
Terry Humphries	x	x	x	x	x
I acknowledge these represent my contribution to the above research output Signature: 					
Drew Sheppard	x		x	x	x
I acknowledge these represent my contribution to the above research output Signature: 					
Mark Paskevicius				x	x
I acknowledge these represent my contribution to the above research output Signature: 					
Matthew Rowles		x	x	x	x
I acknowledge these represent my contribution to the above research output Signature: 					
M. Veronica Sofianos		x			x
I acknowledge these represent my contribution to the above research output Signature: Not contactable.					
Francois Aguey-Zinsou		x			x
I acknowledge these represent my contribution to the above research output Signature: Not contactable.					
Craig E Buckley	x			x	x
I acknowledge these represent my contribution to the above research output Signature:					

Chapter 4: Terry D. Humphries, Jack Yang, Richard A. Mole, Mark Paskevicius, Julianne E. Bird, Matthew R. Rowles, Mariana S. Tortoza, M. Veronica Sofianos, Dehong Yu, and Craig. E. Buckley. "Fluorine substitution in magnesium hydride as a tool for thermodynamic control". The Journal of Physical Chemistry C 124 (2020) 9109 – 9117. DOI: <https://dx.doi.org/10.1021/acs.jpcc.9b11211>

	Conception & design	Experiments conduction & data acquisition	Data processing & analysis	Interpretation & discussion	Manuscript writing, revision
Terry Humphries	X	x	x	x	x
I acknowledge these represent my contribution to the above research output Signature: 					
Jack Yang		x	x	x	x
I acknowledge these represent my contribution to the above research output Signature: 					
Richard A. Mole		x	x	x	x
I acknowledge these represent my contribution to the above research output Signature: 					
Mark Paskevicius		x		x	x
I acknowledge these represent my contribution to the above research output Signature: 					
Julianne E. Bird		x	x	x	x
I acknowledge these represent my contribution to the above research output Signature: 					
Matthew R. Rowles		x	x	x	
I acknowledge these represent my contribution to the above research output Signature: 					
Mariana Tortoza	x	x	x		x
I acknowledge these represent my contribution to the above research output Signature: 					
M. Veronica Sofianos					x

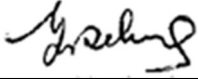
I acknowledge these represent my contribution to the above research output

Signature: Not contactable

Dehong Yu					x
-----------	--	--	--	--	---

I acknowledge these represent my contribution to the above research output

Signature:



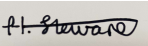




Craig E Buckley				x	x
-----------------	--	--	--	---	---

I acknowledge these represent my contribution to the above research output

Signature:



Annex III: Helen G. Stewart, Terry D. Humphries, Drew A. Sheppard, Mariana S. Tortoza, M. Veronica Sofianos, Shaomin Liu, and Craig E. Buckley. "Ammonium chloride-metal hydride based reaction cycle for vehicular applications". Journal of Materials Chemistry A, 2019. DOI: 10.1039/C9TA00192A

	Conception & design	Experiments conduction & data acquisition	Data processing & analysis	Interpretation & discussion	Manuscript writing, revision
Helen Stewart		x	x	x	x
I acknowledge these represent my contribution to the above research output					
Signature: 					
Terry Humphries	x	x	x	x	x
I acknowledge these represent my contribution to the above research output					
Signature: 					
Drew Sheppard	x			x	x
I acknowledge these represent my contribution to the above research output					
Signature: 					
Mariana Tortoza		x			x
I acknowledge these represent my contribution to the above research output					
Signature: 					
M. Veronica Sofianos		x			x
I acknowledge these represent my contribution to the above research output					
Signature: Not contactable.					
Shaomin Liu					x
I acknowledge these represent my contribution to the above research output					
Signature: 					
Craig E Buckley					x
I acknowledge these represent my contribution to the above research output					
Signature: 